Multiscale modeling of chemical stability and transportation of OH^- ion for chitosan-based biocomposite anion exchange membrane fuel cells

Mirat Karibayev, MSc in Chemical and Materials Engineering

Submitted in fulfillment of the requirements for the degree of PhD in Chemical Engineering

NAZARBAYEV UNIVERSITY

School of Engineering and Digital Sciences
Department of Chemical and Materials Engineering
Nazarbayev University

53 Kabanbay Batyr Avenue,
Astana, Kazakhstan, 010000

Supervisors: Dr. Yanwei Wang
Dr. Almagul Mentbayeva
Dr. Li Xi

September, 2024

Declaration

I certify that, with the exception of correctly referenced quotes and references, the manuscript "*Multiscale modeling of chemical stability and transportation of OH^- ion for chitosan-based biocomposite anion exchange membrane fuel cells*" is entirely my original work. I further affirm that, to the best of my knowledge, no other academic degree at Nazarbayev University or elsewhere has accepted this work in whole or in part.

Name: Mirat Karibayev

Data: 16.09.2024

Abstract

Anion Exchange Membrane Fuel Cells are obtaining popularity in current research due to their promising advancements, which include low production costs, the ability to use catalysts free of platinum group metals, moderate operating temperatures, and high power densities. However, the primary challenge of Anion Exchange Membranes is associated with chemical instability of the quaternary ammonium head groups in alkaline conditions and elevated temperatures, which also led to a decrease in the diffusion of hydroxide ions. This study used Density Functional Theory calculations, ab initio Molecular Dynamics simulations, and conventional all-atom Molecular Dynamics simulations to examine the chemical stability of different chemical structures, including quaternary ammonium head groups, quaternized chitosan head groups, and Deep Eutectic Solvent supported quaternized chitosan head groups as well as the diffusion of hydroxide ions. This research work consisted of the following four main objectives: i) the degradation mechanisms of different quaternary ammonium head groups under different hydration levels via the Density Functional Theory method, ii) the diffusion of hydroxide ion via different quaternary ammonium head groups under different hydration levels via conventional all-atom Molecular Dynamics simulations, iii) the degrataion mechanisms of various quaternized chitosan head groups and the diffusion of hydroxide ions under different hydration levels and temperatures via the Density Functional Theory method and conventional all-atom Molecular Dynamics simulations, and finally iv) explore the degradation mechanisms and diffusion mechanisms of hydroxide ion via Deep Eutectic Solvents supported tetramethylammonium head group and quaternized chitosan head group under different hydration levels and temperatures via Density Functional Theory calculations and ab initio Molecular Dynamics simulations.

Firstly, the following increasing order of chemical stability of the various quaternary ammonium head groups based on the Lowest Unoccupied Molecular Orbital energy, reaction energy, reaction free energy, activation energy, and activation free energy values was obtained using the Density Functional Theory method: (a) pyridinium < (b) 1,4-diazabicyclo [2.2.2] octane ~(c) benzyltrimethylammonium < (d) n-methyl piperidinium ~ (e) guanidium < (f) trimethylhexylammonium at the hydration level 0. The transition state calculation for the nucleophilic substitution reaction showed that, notably, (f)

trimethylhexylammonium had more chemical stability than (c) benzyltrimethylammonium at the different hydration levels from 0 to 3.

Secondly, the findings of the conventional all-atom Molecular Dynamics simulations on distinct quaternary ammonium head groups indicated that the hydroxide ion had similar vehicular diffusion behavior via (c) benzyltrimethylammonium and (f) trimethylhexylammonium head groups, as shown by the diffusion coefficients determined from mean square displacement versus time graphs. Additionally, as the hydration level increased from 3 to 15, the vehicular diffusion of hydroxide ion for (c) and (f) quaternary ammonium head groups increased monotonically.

Thirdly, Lowest Unoccupied Molecular Orbital energies, reaction energies, reaction free energies, activation energies, and activation free energies from Density Functional Theory calculations suggested an increasing stability trend: (C) propyl trimethyl ammonium chitosan < (B) oxy propyl trimethyl ammonium chitosan < (A) 2-hydroxy propyl trimethyl ammonium chitosan at the different hydration levels from 0 to 3. Following the conventional all-atom Molecular Dynamics results, diffusion coefficient of hydroxide ions was shown to rise monotonically with the increase of hydration levels (3-15) and temperatures (298-350 K) for quaternized chitosan types (A, B, and C). Notably, for the vehicular diffusion of hydroxide ions over various hydration levels and temperatures, all three quaternized chitosan variations showed similar diffusion coefficients.

Lastly, the Density Functional Theory calculations of transition state for key degradation mechanisms, ylide formation and nucleophilic substitution, suggested that the presence of Deep Eutectic Solvent enhances the stability of the tetramethylammonium head groups compared to systems without Deep Eutectic Solvent. From the results of ab initio Molecular Dynamics simulation, in the absence of Deep Eutectic Solvent, the nucleophilic substitution mechanism predominated at hydration level 3 and 310 - 350 K, while ylide formation emerged as the major degradation mechanism pathway at various hydration levels, including 1 and 3, and at 298 K. Nevertheless, Density Functional Theory and ab initio Molecular Dynamics simulations showed that the addition of Deep Eutectic Solvent improved the chemical stability of head groups. Afterward, it was discovered that incorporating Deep Eutectic Solvent resulted in comparable diffusion behavior of hydroxide ions through quaternized chitosan head groups at various hydration levels and temperatures, when compared to scenarios without Deep Eutectic Solvent.

These insights from multiscale molecular modeling and simulation are helping us to understand the molecular structure, chemical instability of head groups, degradation mechanisms, and diffusion mechanisms of hydroxide ions via Anion Exchange Membrane for boosting of alkaline fuel cells performance.

Acknowledgements

Firstly, I would like to express my gratitude towards my supervisors *Dr. Yanwei Wang*, *Dr. Almagul Mentbayeva*, and *Dr. Li Xi*. Their guidance and oversight during my studies have enabled me to complete my PhD thesis successfully. I am thankful for the support and motivation that pushed me to grow as a PhD candidate, as well as for the thorough discussions and ongoing feedback on my work. I extend my thanks for instructing me in the techniques of computational modeling and simulations concerning advanced energy materials.

Secondly, this work was supported by the research grant 080420FD1906 titled "Development of composite anion exchange membranes with improved chemical and mechanical stability", which has been sponsored by Nazarbayev University's Faculty development competitive research grant (2020-2022), and AP09057868 titled "High performance polymer-based anion exchange membranes for alkaline fuel cells", which has been sponsored by MES RK (2021-2023), and AP14869880 titled "Deep eutectic solvent supported polymer-based high performance anion exchange membrane for alkaline fuel cells", which has been sponsored by MES RK (2022-2024).

Thirdly, I want to convey my gratitude to Nazarbayev University and its community for their support.

Finally, I am grateful to my family and extended relatives for their unwavering encouragement and assistance.

Table of contents

List of abbreviations

AFCs – Alkaline Fuel Cells

BTMA – Benzyltrimethylammonium

BSSE – Basis set superposition error

DABCO – 1,4-diazabicyclo [2.2.2] octane

TMHA – Trimethylhexylammonium

PEMFCs – Proton Exchange Membrane Fuel Cells

SOFCs – Solid Oxide Fuel Cells

MCFCs – Molten Carbonate Fuel Cells

DES – Deep Eutectic Solvents

EFCs – Enzymatic (Bio)Fuel Cells

PAFCs – Phosphoric Acid Fuel Cells

AEMFCs – Anion Exchange Membrane Fuel Cells

QA – Quaternary Ammonium head groups

QM – Quantum Mechanics

QCS – Quaternized Chitosan head groups

OH^- – Hydroxide ion

HLs – Hydration Levels

DFT – Density Functional Theory

PCM – Polarizable Continuum Model

MD – Molecular Dynamics

MM – Molecular Mechanics

MSD – Mean Square Displacement

RDF – Radial Distribution Function

MEA – Membrane Electrode Assembly

GDL – Gas Diffusion Layers

CL – Catalyst Layers

HOR – Hydrogen Oxidation Reaction

ORR – Oxygen Reduction Reaction

$\mathbf{E_2}$ – Hoffman elimination

$\mathbf{S_N2}$ – Nucleophilic substitution

YF – Ylide formation

$\mathbf{\Delta E_{activation}}$ – Activation energy

$\mathbf{\Delta G_{activation}}$ – Activation free energy

$\mathbf{\Delta E_{reaction}}$ – Reaction energy

$\mathbf{\Delta G_{reaction}}$ – Reaction free energy

$\mathbf{\Delta E_{Binding}}$ – Binding energy

List of figures

Figure 7.11: RDFs for N atom of QCS with OH^- ion in the absence and presence of the DES at the different HLs including (a) HL 1 K, (b) HL 3, and (c) HL 5.

Figure 7.12: Snapshot of vehicular diffusion mechanism surrounding QCS head group in the presence and absence of DES at various HLs.

Figure 7.13: Snapshot of Grotthuss diffusion mechanism surrounding QCS head group in the presence and absence of DES at various HLs.

Figure 7.14: MSD vs. time curves and waiting time distribution histogram at different HLs ((a) 298 K, (b) 320 K, and (c) 350 K) for OH^- ions for QCS head group in the absence and presence of DES.

List of tables

Table 7.1: $\Delta E_{reaction}$, $\Delta G_{reaction}$, $\Delta E_{activation}$, and $\Delta G_{activation}$ values for our designed systems, in the absence and presence of DES. Unit kJ/mol.

Table 7.2: Diffusion coefficients of OH^- ions for DES supported QCS head groups of AEM at the different temperatures.

Table 7.3: Diffusion coefficients of OH^- ions for DES supported QCS head groups of AEM at the different HLs.

Chapter 1: Introduction

1.1 Anion exchange membrane

An electrochemical device known as a fuel cell makes it possible to convert chemical energy into electric energy [1-3]. Anion exchange membrane fuel cells (AEMFCs), solid oxide fuel cells (SOFCs), molten carbon fuel cells (MCFCs), enzymatic (bio) fuel cells (EFCs), phosphoric acid fuel cells (PAFCs), and proton exchange membrane fuel cells (PEMFCs) are the six main types of fuel cells in this regard. The electrolyte type used in AEMFCs is solid (polymeric backbone with positively charged QA head groups) [4–9]. AEMFCs also provide several benefits, including low production costs, the ability to use catalysts free of platinum group metals, moderate operating temperatures, and high power densities [7]. For AEM to be widely commercialized for fuel cell applications, several obstacles must be overcome. Because of the chemical breakdown of QA head groups, AEM's limited chemical stability is one of its key limitations. The decreased OH^- ion diffusion is also a result of the reduced chemical stability of the QA [8, 9].

Biopolymers based on polysaccharides are a plentiful resource on our planet and have been extensively researched as a potential substitute for conventional plastics derived from petroleum. Several polysaccharide-based biopolymer options, including chitosan, cellulose, starch, and xyloglucan, demonstrate their superiority in terms of both structural characteristics and practical and commercial considerations [10], [11]. As a result, millions of tons of crustacean shell waste are used to extract chitosan, a derivative from chitin, the second most plentiful material. In addition, chitosan is stiffer than other biopolymers due to the presence of an acetyl side group. As one of the most popular cationic polymers, it has a great deal of promise for creating high-quality composites. Modified chitosan is a polysaccharide that possesses strong mechanical and chemical resistant qualities, along with excellent film-forming abilities for AEM applications.

More significantly, chitosan does not require the extremely hazardous chloromethylation process and may be readily quaternized thanks to its functional groups (e.g., $-NH_2$, -OH) [12–14]. Furthermore, the incorporation of Deep Eutectic Solvents (DES) into quaternized chitosan (QCS) can enhance its ionic conductivity and chemical stability. Within this framework, adding DESs to QCS head group is a viable way to enhance its characteristics and maybe boost AEM performance.

This PhD work computationally investigated the chemical stability, degradation mechanisms, and molecular structures of QCS head groups, as well as the diffusion of OH^- ions through these head groups when supported by DES for AEM applications, using multiscale molecular modeling and simulation approaches.

1.2 Thesis objectives and hypothesis

The main challenge of AEM is related to the chemical instability of QA head groups at alkaline conditions and elevated temperatures, which also affect the diffusion of OH^- ions. This PhD work was devoted to understanding the degradation mechanisms of the QCS head groups and the diffusion mechanisms of OH^- ion in detail via multiscale molecular modeling and simulation techniques. Our main objectives are shown below:

- Explore the effect of HLs on the chemical stability and degradation mechanism reactions of various QA head groups of AEM via DFT method.
- Study the effect of HLs on the vehicular diffusion mechanism of OH^- ions via different QA head groups by conventional all-atom MD method.
- Study the chemical stability, degradation mechanism of QCS head groups, and vehicular diffusion of OH^- ions at various HLs and temperatures via DFT, and conventional all-atom MD methods.
- Understand the chemical stability, and degradation mechanism of DES supported QCS head groups and vehicular/Grotthuss diffusion mechanisms of OH^- ions at different HLs and temperatures via DFT and ab initio MD methods.

The main hypothesis of the thesis research is that multiple factors, such as various structures of QCS head groups, HLs, and temperatures, could affect the degradation mechanism and diffusion mechanism of OH^- ions. Additionally, it is hypothesized that the addition of DES could improve the chemical stability of QCS head groups and the vehicular/Grotthuss diffusion mechanisms of OH^- ions at higher HLs and temperatures.

1.3 Research contributions

The list of published research papers and submitted research manuscripts:

1. **M., Karibayev**, Bauyrzhan Myrzakhmetov, Yanwei Wang, Almagul Mentbayeva, *Atomistic modeling of tetramethylammonium head groups supported by Deep Eutectic*

Solvents for Anion Exchange Membranes. **Being prepared for submission to journal in 2024. (Original Article, Q1/Q2)**

2. **M., Karibayev,** Bauyrzhan Myrzakhmetov, Dias Bekeshov, Yanwei Wang, Almagul Mentbayeva, Atomistic Modeling of Quaternized Chitosan Head Groups: Insights into the Chemical Stability and Ion Transport for Anion Exchange Membranes Applications. **Molecules** 2024, 29(13), 3175; https://doi.org/10.3390/molecules29133175. (**Original Article, Q1, 83%**)

3. Bauyrzhan Myrzakhmetov, **M., Karibayev**, Yanwei Wang, Almagul Mentbayeva, *Density Functional Theory Investigation of Intermolecular Interactions for Hydrogen-Bonded Deep Eutectic Solvents*. **Eurasian Chemico-Technological Journal** 2024**,** 26(1), 29; https://doi.org/10.18321/ectj1563 **(Original Article, Q3, 29%)**

4. Bauyrzhan Myrzakhmetov, Aktilek Akhmetova, Aiman Bissenbay, **Mirat Karibayev**, Xuemiao Pan, Yanwei Wang, Zhumabay Bakenov, Almagul Mentbayeva, *Review: chitosan-based biopolymers for anion exchange membrane fuel cell application*. **Royal Society Open Science** 2023**,** 10(11), 230843; https://doi.org/10.1098/rsos.230843 **(Review Article, Q1, 88%)**

5. **M., Karibayev**, Dias Bekeshov, Bauyrzhan Myrzakhmetov, Sandugash Kalybekkyzy, Yanwei Wang, Almagul Mentbayeva, *Effect of hydration on the intermolecular interaction of various quaternary ammonium based head groups with hydroxide ion of anion exchange membrane studied at the molecular level*. **Eurasian Chemico -Technological Journal** 2023, 25(2), 89; https://doi.org/10.18321/ectj1499 **(Original Article, Q3, 29%)**

6. **M., Karibayev**, Sandugash Kalybekkyzy, Yanwei Wang, Almagul Mentbayeva, *Molecular Modeling in Anion Exchange Membrane Research: A Brief Review of Recent Applications*. **Molecules** 2022, 27(11), 3574; https://doi.org/10.3390/molecules27113574 **(Review Article, Q1, 83%)**

7. **M., Karibayev,** Bauyrzhan Myrzakhmetov, Sandugash Kalybekkyzy, Yanwei Wang, Almagul Mentbayeva, *Binding and Degradation Reaction of Hydroxide Ions with Several Quaternary Ammonium Head Groups of Anion Exchange Membranes Investigated by the DFT Method*. **Molecules** 2022, 27(9), 2686; https://doi.org/10.3390/molecules27092686 **(Original Article, Q1, 83%)**

The list of presentations on international conferences, seminars and research days:

1. **M., Karibayev**, Aida Barlybayeva, Bauyrzhan Myrzakhmetov, Yanwei Wang, Almagul Mentbayeva, *Deep eutectic solvent supported polymer-based high performance anion exchange membrane for alkaline fuel cells*. "**First Annual Nazarbayev University Research Conference**", September **2024** (poster presentation), Astana, Kazakhstan.

2. **M., Karibayev**, Bauyrzhan Myrzakhmetov, Yanwei Wang, Almagul Mentbayeva, *Deep eutectic solvent supported quaternized chitosan head groups for anion exchange membranes: insight from atomistic modeling*. "**INESS - 2024**", August **2024** (poster presentation), Astana, Kazakhstan.

3. Aida Barlybayeva, Bauyrzhan Myrzakhmetov, **M., Karibayev**, Yanwei Wang, Almagul Mentbayeva, *Deep eutectic solvent supported poly(vinyl) alcohol electrospun anion exchange membrane for alkaline fuel cells*. "**INESS - 2024**", August **2024** (poster presentation), Astana, Kazakhstan.

4. Aida Barlybayeva, Bauyrzhan Myrzakhmetov, **M., Karibayev**, Yanwei Wang, Almagul Mentbayeva, *Deep eutectic solvent supported polymer-based high performance anion exchange membrane for alkaline fuel cells*. "**245th ECS Meeting**", May **2024** (poster presentation), San Francisco.

5. **M., Karibayev**, Bauyrzhan Myrzakhmetov, Sandugash Kalybekkyzy, Yanwei Wang, Almagul Mentbayeva, *Deep eutectic solvent supported polymer-based high performance anion exchange membrane for alkaline fuel cells*. "**NU Research Day 2023**", October **2023** (poster presentation), Astana, Kazakhstan.

6. **M., Karibayev**, Bauyrzhan Myrzakhmetov, Sandugash Kalybekkyzy, Yanwei Wang, Almagul Mentbayeva, *Deep eutectic solvent supported polymer-based high performance anion exchange membrane for alkaline fuel cells*. "**NU SEDS RESEARCH WEEK 2023**", April **2023** (poster presentation), Astana, Kazakhstan.

7. **M., Karibayev,** Bauyrzhan Myrzakhmetov, Sandugash Kalybekkyzy, Yanwei Wang, Almagul Mentbayeva, *Intermolecular Interaction and Chemical Degradation mechanism of Hydroxide Ions with Various Quaternary Ammonium Head groups of Anion Exchange Membrane Studied via the DFT Calculations*. "**8th International Congress on Energy Efficiency and Energy Related Materials (ENEFM 2022)**", October **2022** (poster presentation), Mugla, Turkey.

8. **M., Karibayev,** Bauyrzhan Myrzakhmetov, Sandugash Kalybekkyzy, Yanwei Wang, Almagul Mentbayeva, *Binding, Reaction, and Activation Energies of OH^- Ions interacting and reacting to Some Head Groups of Anion Exchange Membrane explored via the DFT method*. "**INESS 2022**", August **2022** (oral presentation), Astana, Kazakhstan.

9. **M., Karibayev,** Bauyrzhan Myrzakhmetov, Sandugash Kalybekkyzy, Yanwei Wang, Almagul Mentbayeva, *Binding and Degradation mechanism Reaction of Hydroxide Ions with Different Quaternary Ammonium Head Groups of AEM studied at the molecular level*. "**NU HPC AI**", 8 December **2022** (oral presentation), Astana, Kazakhstan.

10. **M. Karibayev**, Y. Wang, A. Mentbayeva, *Computational and theoretical studies on the transport of hydroxide ions through the anion exchange membrane based on imidazolium and nitrogenous cyclohexane*, "**80^{th} anniversary of the academician of NAS RK Edil Ergozhaevich Yergozhin**", November **2021** (oral presentation), Almaty, Kazakhstan.

1.4 Thesis organization

The PhD thesis consists of eight chapters. Chapter 1 is the introduction that provides an overview of the research, thesis objectives and hypothesizes, and key contributions. Chapter 2 includes a review of literature on the relevant research work. The multiscale molecular modeling and simulation details were provided in Chapter 3. The main work was related to examining the chemical stability and degradation mechanism, vehicular/Grotthuss diffusion mechanism of OH^- ions for DES supported QCS head groups of AEM at different HLs, temperatures via DFT, ab initio MD, and conventional all-atom MD techniques, which were presented in Chapters from 4 to 7. Chapter 8 concludes the PhD thesis and offers recommendations for further research.

Chapter 2: Literature review

In this chapter, two major challenges in AEMs research are presented in detail, which are related to the chemical instability of QA and diffusion mechanisms of OH^- ions, along with DFT, ab initio MD, and conventional all-atom MD techniques.

2.1. Background of hydrogen fuel cells

Energy is crucially important and required to perform all human activities. Renewable energy sources are plentiful, sustainable, naturally replenished, and environmentally friendly, while non-renewable energy sources have a limited supply that we can obtain from mines or extract from the earth.

There has been a rapid increase in energy consumption around the world due to economic development and population growth. Global energy consumption doubled from 270.5 to 580.5 Exajoules during the period between 1978 and 2018 [15]. At the same time, global population growth reached from 4.30 to 7.63 billion [15]. In this regard, the energy crisis is the main challenge in the world. Mainly, a dramatic increase in energy consumption is expected for solar and wind energy sources. Among various types of renewable energy sources, solar energy could be the best alternative for the future world due to its low cost and lack of exhaustion. Although, its intermittent nature requires an efficient storage method. Consequently, the possible route for the usage of solar energy was storage in the form of a chemical bond as hydrogen fuel. At the same time, hydrogen fuel is another promising energy source and has applications in heating homes, vehicles, and others.

Hydrogen is a clean energy carrier with the following advantages, including: i) being the most abundant element in the world, ii) being sustainable, iii) being non-toxic, and iv) being environmentally friendly. There are many sources for the generation of hydrogen fuel, such as hydro, coal, wind, natural gas, wave, nuclear energy, solar, biomass, and geothermal [16]. Hence, there are many technologies for the production of hydrogen, including natural gas steam reforming (95 %), coal gasification, biomass gasification and pyrolysis, high-temperature water splitting, reforming of renewable liquid fuels, electrolyzers, and others [16]. The main applications of hydrogen fuel include heating homes and industry, as can be seen in **Figure 2.1**.

In **Figure 2.1**, the basic hydrogen house components are a hydrogen storage tank, water electrolyzer, and fuel cell stack [17]. Hence, a hydrogen storage tank keeps hydrogen

gas compressed. After that, the fuel cell stack is a major component that can transform the oxygen and hydrogen gas into electricity.

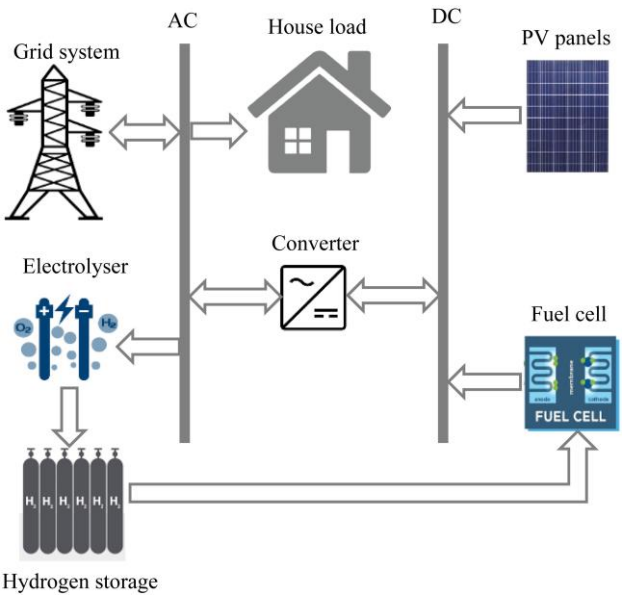

Figure 2.1: Basic hydrogen house component [17].

In this regard, the use of hydrogen fuels as a clean energy carrier is fraught with difficulties because of their high volumetric energy density, which makes them difficult to store, their high cost—which is currently four times that of conventional gasoline—and their current hydrogen fuel cell, which is ten times more expensive than an internal combustion engine [17].

Table 2.1: Different fuel cells.

Fuel Cell	T, ^{0}C	Fuel Type	Efficiency
AFC	50-200	H_2	~35-60 %
PEMFC	50-100	H_2/CO_2	~40-60 %
PAFC	180-220	H_2/CO_2	~ 40 %
MCFC	~650	H_2, CH_4, CO	~50 %
SOFC	500-1000	H_2, CH_4, CO	~45-65 %

With the use of a fuel cell, we may convert chemical energy directly into electrical energy without the need for a step-by-step combustion process. Moreover, fuel cells have the following benefits: i) high energy conversion efficiency; ii) modular design; iii) extremely low emission levels; iv) fuel flexibility; v) cogeneration capabilities; and, lastly,

vi) quick load response. Fuel cells could be divided into following categories: AFC, SOFC, PAFC, MCFC, and PEMFC (**Table 2.1**). Regretfully, SOFCs and MCFCs operate at the higher temperatures, while PEMFCs and PAFCs need expensive noble metal catalysts like platinum. Scientists have, however, started paying closer attention to AFC, which is likewise divided into liquid and solid categories depending on the electrolyte. A solid (polymeric) electrolyte is used in AEMFCs.

In the next subsections, the schematic structure of AEM, the chemical stability, and the diffusion of OH^- ions for AEM were discussed [17].

2.2 Anion exchange membrane

The basic AEMFCs design consists of electrode parts, including anode and cathode, which are separated by AEM, as can be seen in **Figure 2.2**. Membrane electrode assembly (MEA) and flow-field components make up the electrode part in this sense. We can supply pure hydrogen, oxygen from the air, and water to our fuel cell thanks to the flow-field component. Catalyst layers (CL) and gas diffusion layers (GDL) make up the MEA portion after that. GDL's primary roles in the cathode and anode are to support CL, provide a uniform reactant distribution, and transfer electrons to the current collector. The backing layer and the microporous layer are the two layers that make up the GDL layers.

Hydrogen is supplied as fuel to the anode of an AEMFC, while oxygen is supplied to the cathode via water and air. Subsequently, fuel is oxidized at the anode, and oxygen is reduced at the cathode. OH^- ions are produced at the cathode and are carried to the anode by the electrolyte. Water and electrons are produced at the anode by OH^- ions reacting with the fuel (equation 1 and 2). The circuit uses electrons to produce current [18–20].

At anode: $H_2 + 2OH^- \rightarrow 2H_2O + 2e^-$ (equation 1)

At cathode: $O_2 + 2H_2O + 4e^- \rightarrow 4OH^-$ (equation 2)

In addition, the overall composition of AEM is comprised of polymer chains that have been functionalized with several cationic groups. In general, the four types of polymers used in the creation of the AEM backbone are: (i) fluorinated polymers; (ii) hydrocarbon-based polymers; (iii) condensation polymers; and (iv) biopolymers.

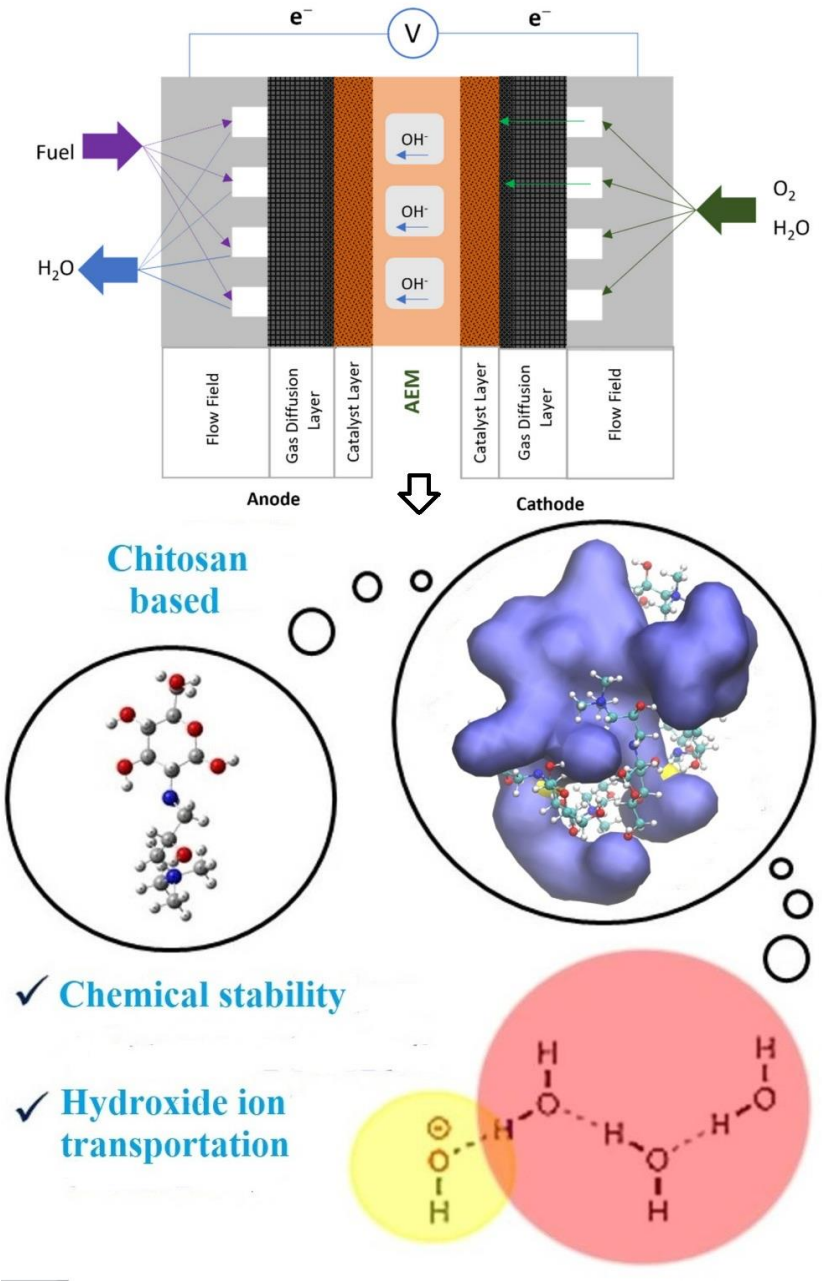

Figure 2.2: Basic design of QCS head groups based AEM.

Biopolymers based on polysaccharides have been extensively studied as potential substitutes for conventional plastics generated from petroleum. Biopolymers based on polysaccharides include chitin, xyloglucan, chitosan, starch, and cellulose.

The waste shells of millions of crustaceans are used to extract chitin. The primary natural sources of biopolymers are the exoskeletons of arthopods, mushrooms, fungi, and the shells of shrimp, crabs, krill, and prawns [20–22]. Because it has an acetyl side group, chitosan is more rigid than other biopolymers while remaining inexpensive and

environmentally friendly (**Figure 2.3**). Furthermore, to create its composites, chitosan is frequently altered to take on the form of a cationic polymer.

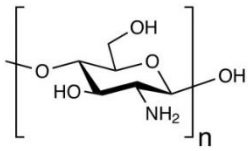

Figure 2.3: Chemical structure of chitosan monomer.

In assessing the performance of AEMs for fuel cells, it is crucial to evaluate various key characteristics, including tensile strength, thickness, water uptake, swelling degree, ionic conductivity, and chemical stability (**Table 2.2**).

Table 2.2: Desired and currently achieved values for AEM performance for fuel cell applications [23-27].

Characteristic	Description	Desired Value	Currently Achieved Value
Tensile strength	Measure tensile strength of AEM	≥ 20MPa	85 MPa
Thickness	Measure thickness of AEM	< 50 μm	26-34 μm
Water uptake	Changes in AEM mass when exposed to water	>50%	235%
Swelling degree	Dimensional change of the AEM when exposed to water	10 – 30 %	11-27 %
Ionic Conductivity	Measure OH^- ion conductivity	≥ 100 mS/cm	120 mS/cm
Chemical stability	AEM performance needs to be maintained over time when exposed to high pH environments	1000-5000 hours	1400 hours

These parameters significantly influence the efficiency, durability, and overall functionality of AEMs in practical applications. The desired values for these characteristics are established based on the requirements for optimal fuel cell performance. As shown in **Table 2.2**, the limited chemical stability of AEMs, due to the chemical breakdown of QA head groups, is one of their key limitations.

2.3 Chemical stability of quaternary ammonium head groups

Because of the instability of the positively charged cationic head group in alkaline environments, particularly at high temperatures, the stability of AEMFCs at high pH is a major concern. Three primary pathways for the breakdown of QA head groups at high pH were proposed as follows: E_2, S_N2, and YF.

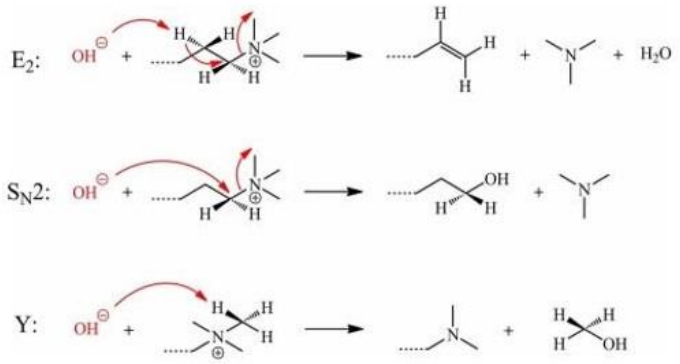

Figure 2.4: Degradation mechanism of QA head groups in alkaline conditions [8].

Figure 2.4 shows the potential ways in which E_2, S_N2, and YF could degrade positively charged QA at alkaline condition. As **Figure 2.4** [8] illustrates, there were three probable ways for the QA to degrade at alkaline condition, which contributed to the low chemical stability under alkaline circumstances. The HL is calculated as the number of H_2O molecules per QA ($\lambda = n_{H_2O}/n_{QA}$) [28]. There are various types of research on the degradation mechanisms of QA head groups under alkaline conditions in AEMs. Furthermore, low HL conditions were typically the cause of the QA degradation mechanism. Studying the OH^- ion diffusion at the lower HL and the degradation mechanism of the QA is therefore crucial [29–40].

2.4 Diffusion of OH^- ions

There are two major types of diffusion of OH^- ion mechanisms (**Figure 2.5**),

including: i) the Grotthuss mechanism, and ii) vehicular diffusion [34-41]. The details of those mechanisms are listed in the below paragraphs one by one.

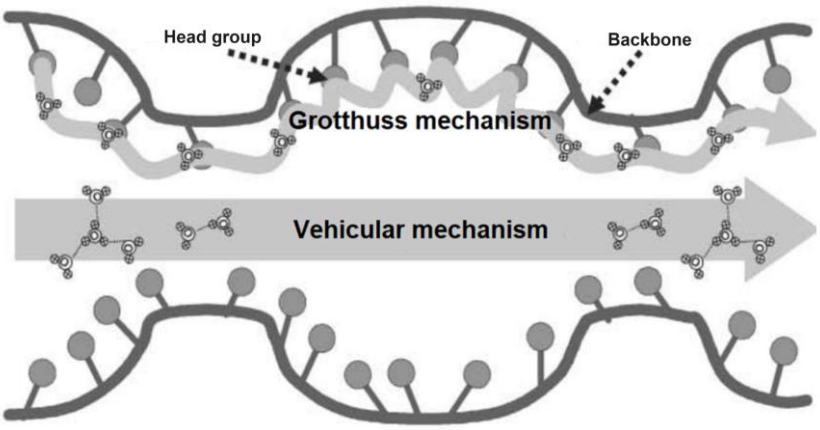

Figure 2.5: Schematic diagram of the Grotthuss and vehicular mechanisms of OH^- ion diffusion in AEMs. [9].

The Grotthuss diffusion mechanism involves a process known as proton hopping, where OH^- ions facilitate their movement by transferring protons between water molecules within the membrane. This mechanism enables rapid diffusion of OH^- ions through the AEM by leveraging the mobility of protons in water [34-40].

In contrast, the vehicular diffusion mechanism refers to the direct movement of OH^- ions through the membrane's water channels, bypassing the need for proton hopping. This form of diffusion relies on the physical movement of the ions within the aqueous channels of the membrane, which allows them to traverse the membrane more straightforwardly. Together, these mechanisms contribute to the overall efficiency of ion transport in AEMs, impacting their performance in fuel cell applications [34-42].

2.5 Molecular modeling of anion exchange membrane

Computational studies have been archived in numerous databases and archives in support of transferable and open research. Emerging as a new topic in recent years, material informatics assists us in selecting the important property of our developed material from extensive material databases [43–46].

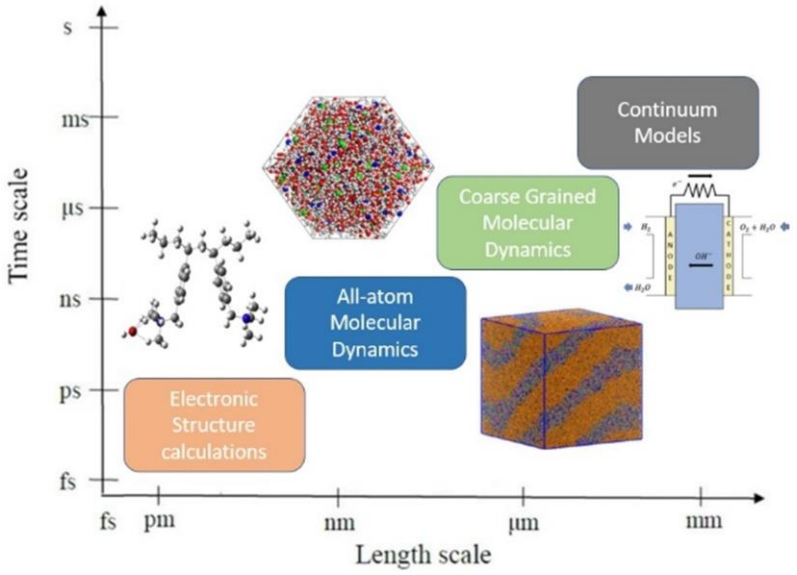

Figure 2.6: The hierarchy that extends from the atomic to the systemic levels [2].

Numerous outstanding reviews and perspective articles have already been published on the use of materials and molecular modeling techniques in advanced energy materials research [47–49]. These molecular and material modeling techniques have a wide range of applications at various scales (**Figure 2.6**) [50–79].

Computational investigations have been widely employed by researchers across various scales, enabling the examination of the chemical stability of AEM's QA head group-based polymeric matrix and the transport of OH^- ions in AEM through multiscale molecular modeling and simulations. Numerous models of typical AEM are available:

- The DFT calculation models were created to offer fundamental insights into the mechanisms that control local properties, including degradation mechanism processes and the chemical stability of QA.
- Ab initio MD techniques were formulated to explore the mechanism of vehicular/Grotthuss diffusion of OH^- ions and the molecular structure.
- All-atom MD techniques were created to explore the OH^- ion vehicular diffusion and the molecular structures within the AEM.

To our knowledge, limited efforts have been made to comprehensively assess all facets of modeling and simulation in the context of AEM systems [80]. This contribution seeks to present various computational works within the research community, focusing on AEM.

2.5.1 Density functional theory calculations

Ab initio calculations involve determining the ground state of a group of atoms by solving the Schrödinger equation, which forms the foundation of quantum mechanics for a multitude of atoms [81, 82]. The majority of computational investigations on the chemical stability of AEM rely on DFT. The subsequent sections delve into diverse DFT studies related to AEM, drawing from an extensive literature review as summarized in **Table 2.3**.

Table 2.3: DFT calculations on AEMs.

QA Head Group	Functional Used	Basis Set	Solvation Model	Ref.
Imidazolium	B3LYP	6-311++G(2d, p)	PCM	[26, 83-85]
Guanidimidazolium	B3LYP	6-311++G (d, p)	PCM	[86]
Imidazolium	B3LYP	6-311++G (2d, p)	PCM	[84, 85]
Phenyltrimethylammonium	B3LYP	6-311++g(2d, p)	PCM	[87]
Benzyltrimethylammonium	B3LYP	6-311++G (2d, p)	PCM	[88]
Tetraalkylammonium	B3LYP	6-311++G (2d, p)	PCM	[89, 90]
Imidazolium	B3LYP	6-311++G (d, p)	PCM	[91]
Vinyl benzyl	GGA-BLYP	—	COSMO	[92]
Trimethylammonium	B3LYP	6-311++G(d,p)	PCM	[93]

2.5.1.1 Imidazolium-based QA head groups of AEM

DFT methods were implemented for the imidazolium-based head group using Gaussian09 software [83–85]. Researchers looked at how C2-substitution affected the imidazolium-based head group alkaline stability and degradation mechanism processes. As shown in **Figure 2.7**, the main mechanism of degradation mechanism for head groups based on imidazolium and benzimidazolium is a nucleophilic addition–elimination pathway at the C–2 atom position on the imidazolium ring [84, 86].

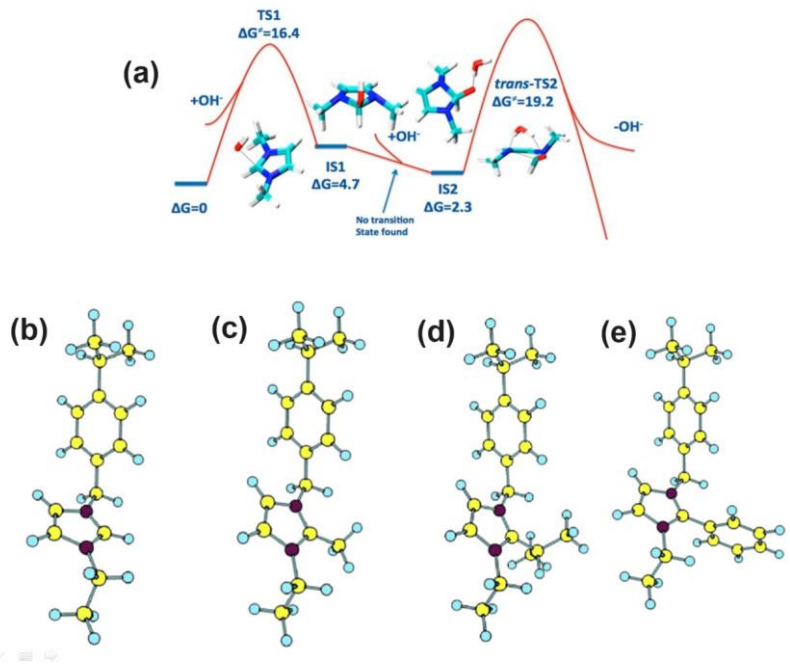

Figure 2.7: (a) Degradation mechanism for the benzimidazolium head group, and structural scheme of (b) EIIM (C2 unsubstituted), (c) EMIIM (phenyl), (d) EIIIM (isopropyl), and (e) EPhIIM (phenyl) [83, 85].

For the dehydrogenation reaction, DFT transition-state-energy calculations showed the following sequence of alkaline stability: EIIM (C2 unsubstituted) > EPhIIM (phenyl) > EMIIM (methyl) > EIIIM (isopropyl). EMIIM effectively hinders the deprotonation reaction, making it the most stable head group [83].

Designers use longer alkyl chains to improve the stability of cations, particularly about E_2. Because of the steric effect this elongation creates, Hofmann removal is more difficult. A different strategy is to replace the alpha and beta hydrogens with distinct functional groups [85, 86].

2.5.1.2 Alkylammonium-based QA head groups

Using the PCM in water and the B3LYP 6-311G (2d,p) level, the degradation mechanism mechanism of the substituted phenyltrimethylammonium head group under alkaline circumstances was investigated [87]. The stability of substituted phenyltrimethylammonium cations was examined about the orientation effect by varying the positions of various substituents on the benzene ring. The DFT calculations indicate that the ortho and para positions of the benzene ring are where the electron-donating substituents have the highest energy barriers. The results of the calculations indicate that the phenylTMA^+ that has been double-substituted with CH_3N is more stable than the benzylTMA^+ that has also

been double-substituted with CH_3N. These results provide insights into the possible use of substituents in AEM and illuminate how they affect the degradation mechanism of model cations [87].

DFT calculations on the AEM based on benzyltrimethylammonium showed that QA cations degraded at ambient temperature and lower HLs. However, the OH^- nucleophilicity was hindered as more water molecules solvated it [88].

According to DFT calculations, the main pathways of degradation mechanism for the tetraalkylammonium head group are YF and S_N2 [89, 90].

In addition, compared to the alpha carbon unsubstituted imidazole head groups, the imidazolium cation with alpha carbon-methyl substitution (TMIM) demonstrated higher stability. In addition to the methyl group's steric action, the hyperconjugation between the imidazole ring and the alpha carbon causes this increased stability. As a result, in alkaline circumstances, the imidazolium head group with methyl substitution exhibits enhanced stability [91].

2.5.1.3 Other Types of QA head groups

The head groups were found to be stable in the following order: DABCO < TMA < NMP < ABCO [92]. Furthermore, a multi-step AEM degrading mechanism was found that involves the complete vinyl benzyl head group dissociation. A nucleophilic attack is the first step that causes the molecule to lose its aromaticity and change into a quinodimethane moiety [92].

The transport of OH^- ions through QA-functionalized polystyrene (QAPS) was investigated [93]. It was determined that the OH^- transfer via QAPS-AEM happens in two stages. First, since hydrogen connections (H-bonds) between H_2O and OH^- form and break often, OH^- moved within the water channel [93]. Second, OH^- transfer in QAPS-AEM was determined by the pace at which the C-C single bond rotated, which occurred after OH^- was translated over the QA head groups.

Several DFT experiments have been carried out to look at the various QA head groups' degrading reactions in AEM. The electronic structure modeling approach based on DFT shows promise for optimizing structure and provides an in-depth investigation of the mechanisms behind degradation mechanism events and binding interactions.

2.5.2 Ab initio molecular dynamics

Ab initio MD has been used in many computational studies to investigate OH^- ion transport pathways and chemical stability in AEMs at both high and low HLs. **Table 2.4** lists a few recent ab initio MD investigations on AEMs that were discussed in the next paragraphs.

Table 2.4: Ab initio MD simulations on AEMs.

AEM Structure	Function Used	Ref.
TMA based polystyrene	GGA-BLYP	[94]
TMA based graphene	BLYP	[35-37]

2.5.2.1 Trimethylammonium-based poly(styrene)

The Quantum Espresso Package was used to model and simulate the AEM made up of quaternized polystyrene in the presence of OH^- ions and water to study OH^- ion transport [94]. The main conclusions of the study show that the precise positioning of OH^- ions and HLs are critical to ion transport. The findings provide many insights and demonstrate the Grotthuss mechanism's dominance in the hydrated state [94]. First, when HL is 4, competing donor-acceptor interactions cause OH^- ions to partially dissociate. Second, at water absorption of six, OH^- ions completely dissociate and take on a hypercoordinated structure [94].

2.5.2.2 Trimethylammonium-based Graphene Bilayer

The structural characteristics and diffusion patterns inside each water layer of AEMs based on graphene sheet were examined using the ab initio MDs simulation, especially at various HLs [35–38]. Remarkably, changes in HL, and shape resulted in notable modifications to the nanoconfined water structures (**Figure 2.8**). Each water layer had a variety of OH^- ion coordination patterns.

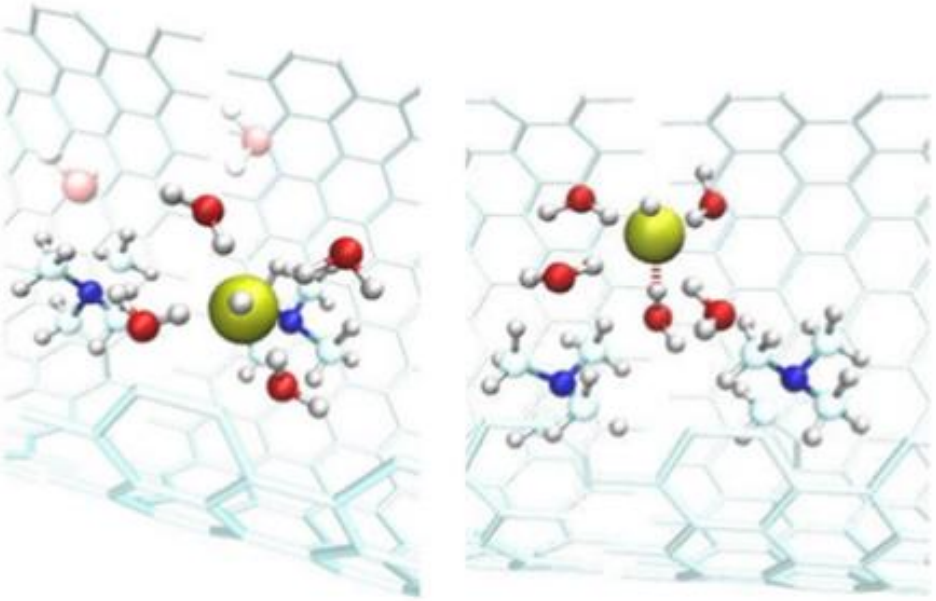

Figure 2.8: A section of the carbon nanotube containing a quaternary ammonium head group and the movement of hydroxide ions in the presence of coordinating water molecules [34].

Moreover, AEM's six different idealized water distribution models were developed using different head group spacing and HLs [36]. The results of the study underscored the importance of the various water distributions in AEM as a descriptor, which is more important than the degree of hydration in classifying the principles of operation of AEMs at reduced HLs [37].

2.5.3 Conventional all-atom molecular dynamics

To improve ion exchange capacity, a MD simulation research has been performed to investigate the OH^- ion diffusion mechanisms in different AEM matrices. Numerous polymers, such as poly(p-phenylene oxide) (PPO), poly(vinyl benzyl) (PVB), poly(arylene ether sulfone ketone) (PEEK), polysulfone (PS), and norbornene, have been computationally studied as possible backbones for the AEM matrix [13, 95]. Positive properties of these polymers include improved mechanical and chemical stability, affordability, and simplicity in functionalizing with cationic functional head groups [13, 95].

Many computational studies have been conducted utilizing conventional all-atom MD techniques to investigate the OH^- ion diffusion process in AEMs. The results of a comprehensive literature study including many conventional all-atom MD models of AEMs was presented in the next paragraphs, as indicated in **Table 2.5**.

Table 2.5: Conventional all-atom MDs simulations on AEMs.

AEM structure	Force field used	Ref.
Various QA	OPLS	[96]
PPO	CHARMM	[97]
Functionalized PPO	ReaxFF	[98]
Various QA head groups	ReaxFF and APPLE&P	[99]
Imidazolium based PPO	COMPASS II	[100]
Four types of PVB	AMBER	[101]
PVBTMA	OPLS-AA	[102]
Ethyl imidazolium functionalized PEEK	COMPASS	[103]
Fluorenyl group based PEEK	CVFF	[104]
PEEK	COMPASS	[105]
Tetramethylammonium based PS	DREIDING	[106]
Quaternarized PS	DREIDING	[107]
Tetraalkylammonium based norbornene	(not mentioned)	[108, 109]

2.5.3.1 Various QA head groups of AEM

With the OPLS force field, conventional all-atom MD methods were used to study various QA. The primary aim was to investigate the critical link between the chemical stability of QA head groups in AEM environments [96]. The simulations revealed that QA degrade rapidly under low HL, consistent with experimental observations. Moreover, elevated temperatures expedite this degradation process of QA under low HL [96].

2.5.3.2 Functionalized Poly(phenylene Oxide) based AEM

Allan Hay discovered PPO, an amorphous, high-temperature thermoplastic, which General Electric commercialized in 1960. It has a wide range of uses, such as electrolytes in household appliances, electronics, lithium-ion batteries, and as the foundation material for AEMs. According to Li and colleagues' proposal [110], chain scission that happens during exposure to alkaline solutions is the cause of the chemical instability of PPO-based AEMs. Parrondo and colleagues' study revealed that PPO-based AEMs degrade due to the electron-withdrawing action of a tethered QA head group [95]. As a result, these PPO-based AEM membranes have been the subject of MD simulations.

Zhang *et al.* investigated the polymer structure and the hydration of the imidazolium group [97]. The outcomes showed that a favorable equilibrium between the imidazolium group's affinity for OH^- ions and the diffusion of OH^- ions in PPO could be achieved under crucial water-saturation circumstances [97].

Additionally, simulations employing the COMPASS II force field showed that the PPO-based AEM, including 1,2,4,5-tetramethylimidazolium and an alkyl spacer chain with either six or eight aliphatic carbons at a HL of six, exhibited an optimal equilibrium between chemical stability and OH- ion diffusivity [100].

Moreover, different PPO AEMs featuring unique head groups were simulated and analyzed using the conventional polarizable force fields APPLE&P (non-reactive) and ReaxFF (reactive) [42, 98, 99, 111]. The formation of a water channel with increased water content facilitated the OH- ion transport. Substituting the methyl group of the QA head group with larger hydrophobic groups offered a means to enhance alkaline stability by impeding the access of OH- ions to the nitrogen in QA [42, 98, 99, 111].

2.5.3.3 Functionalized Poly(vinyl) based AEM

Among its many uses, polyvinyl chloride is the most commonly used plastic polymer. It is used to make food packaging, doors, and windows. There are several polyvinyl chloride derivatives, including polyvinyl alcohol and polyvinyl benzyl. Of particular note is the stable environment that poly(vinyl benzyl) trimethylammonium exhibits in alkaline solutions because of its advantageous anionic conductivity and lack of beta hydrogen atoms.

A thorough investigation was carried out by modeling and simulating four different kinds of PVB in the presence of F^- and Cl^- ions as well as the SPC/Fw water model. This work sought to clarify a new "co-ion effect" in which the presence of Cl^- ions significantly increases the transport of F^- ions in the AEM [101].

Chen *et al.* simultaneously used the universal AMBER force field to perform conventional all-atom MD techniques for PVB chains with 10 and 40 monomers [33]. Conventional all-atom MD techniques were also carried out by Dubey *et al.* in a related study for a single PVB polymer chain consisting of 40 monomers and 120–720 water molecules. In an AEM, the solvation structure and vehicular dispersion of OH^- ions were examined using the OPLSAA force fields [102].

2.5.3.4 Functionalized Poly(arylene Ether Sulfone) based AEM

Using the COMPASSII force field, a single chain of ethyl imidazolium-functionalized poly(arylene ether sulfone) was simulated to investigate how various functional group types affected the shape of the water channel [103]. Because of its better chemical stability and well-defined phase separation morphology, ethyl imidazolium-functionalized poly(arylene ether sulfone) exhibited higher OH^- ion conductivity than its QA-functionalized counterparts. The findings revealed that AEMs with ethyl imidazolium head groups had higher chemical stability and more effective water channels than AEMs with QA head groups.

In a different work, the diffusion of OH^- ions was investigated by simulating classical all-atom MD models of QA-substituted fluorenyl group-based poly(arylene ether sulfone ketone)s using the CVFF force field [104]. The results showed that OH^- diffusion was significantly influenced by surface diffusion processes [104].

2.5.3.5 Functionalized Poly(arylene Ether Ketone) based AEM

To simulate PEEK chains with different lengths (10–40 units), conventional all-atom MD models were used. This simulation was carried out to examine the impact of the polymer's QA head groups on the movement of hydronium and OH^- ions [105]. In this regard, the solvation impact of the water reduced the density of the polymer functional group in the simulated cell when the water concentration was high. As a result of this decrease in polymer density, there was less polymer density overall and there was less connection of ionic sites [105].

2.5.3.6 Functionalized Poly(Sulfone) based AEM

AEM based on trimethyl ammonium PS was simulated conventionally using all-atom MD methods. The impact of HL on diffusivity was investigated by simulations using the DREIDING force field [106]. The trimethylammonium groups, defined by fixed charges throughout the polymeric chain, tended to interact in a manner that maximizes electrostatic and hydrogen bonding interactions.OH^- ions showed poor hydration at low ion exchange capacity and water absorption circumstances, while trimethylammonium groups supplied two to three coordinating water molecules [106].

In a similar study, the DREIDING force field and LAMMPS software were used to simulate PS-based AEMs and PEM. The purpose of this simulation was to compare their transport properties and molecular structure [107]. In contrast to hydronium ions and

sulfonate groups of PEMs, the results showed that OH^- ions and the QA head groups of AEMs were more solvated with water [107].

2.5.3.7 Functionalized Poly(nonbornene)-based AEM

Conventional all-atom MD techniques were used to study the coordination numbers between OH^- ions, and poly(norbornene) polymer chains, as well as the OH^- ion diffusion mechanism [108]. The findings showed that temperature and water content improved the OH^- ion diffusivity, preferred continuous water channels and involved both vehicular and Grotthuss mechanisms [108].

Materials Studio software was used to simulate poly(norbornene) polymer chains to study the diffusion of OH^- ions [109]. The results implied that OH^- ions moved between two layers of water shells and were surrounded by them, and that the increased kinetic energy at higher temperatures caused the speed of OH^- ion movement to rise [109].

2.6 Related experimental works

A review of experimental works related to the chemical stability and hydroxide ionic conductivity of various quaternary ammonium head group-based polymeric backbones—including polyarylether ketone, polyetherether ketone, polypropylene oxide, poly(vinyl) alcohol, chitosan, and others—has been included in **Table 2.6**.

These studies, summarized in **Table 2.6**, highlight the performance of different quaternized polymers under alkaline conditions based on experimental results. Notably, quaternized chitosan demonstrates ionic conductivity comparable to other quaternary ammonium-based polymers, positioning it as a promising candidate for applications requiring efficient ion transport. However, the review also underscores that while some of these polymers exhibit satisfactory conductivity, their chemical stability often diminishes under alkaline conditions, posing a significant challenge for long-term durability in practical applications [8].

The alkaline stabilities of the head groups and corresponding AEMs were tested under different experimental conditions. These conditions included variations in solvent, alkaline concentrations, and relative humidity. Additionally, different methods such as NMR spectroscopy, FTIR, UV/Vis, and TGA were used. Due to these variations, it is challenging to directly compare the alkaline stability data reported in the literature.

Table 2.6: A review of the conducted experimental work on various head group-based AEMs.

AEM	Ionic conductivity (mS/cm)	Chemical Stability	Ref.
Polyarylether ketone with pyridinium based head group	15	96% ion exchange capacity after 4 weeks in 3 M NaOH at 60 ^{0}C	[110]
Polyetherether ketone with imidazolium head group	30	68% ion exchange capacity after 468 h in 1 M KOH at 60 ^{0}C	[111]
Polypropylene oxide with imidazolium head group	120	70% ion exchange capacity after 480 h in 2 M NaOH at 80 ^{0}C	[112]
Poly(vinyl) alcohol with gluteraldehyde head groups	18	80% ion exchange capacity after 120 h in 2 M NaOH at 60%	[113]
Chitosan with gluteraldehyde head groups	82	70% ion exchange capacity after 250 h in 1 M KOH at 80%	[114]
Heptamethyl phenolphthalein with imidazolim head group	14	50% ion exchange capacity after 800 h in 2M KOH at 80%	[115]
Copolymer of 1-vinyl imidazole and n-vinyl carbazole with tetramethylammonium head group	33	84% ion exchange capacity after 1400 h in 1 M KOH at 60 ^{0}C	[116]
Graphene oxide with tetramethylammonium head group	11	87% ion exchange capacity after 120 h in 1 M NaOH at 50 ^{0}C	[117]

At the same time, Mohanty and his research team developed an experimental procedure and conducted a series of experiments to determine the chemical stability trends

for more than six different head groups of AEM (**Figure 2.9**) [119]. Their findings revealed that benzyltrimethylammonium possesses reasonably good alkaline stability in fully hydrated conditions at 120 °C. Additionally, they identified a number of cation groups with even greater stability, with trimethylhexylammonium showing the greatest chemical stability among the tested groups. These results provide valuable insights into the design of more durable AEMs for various applications.

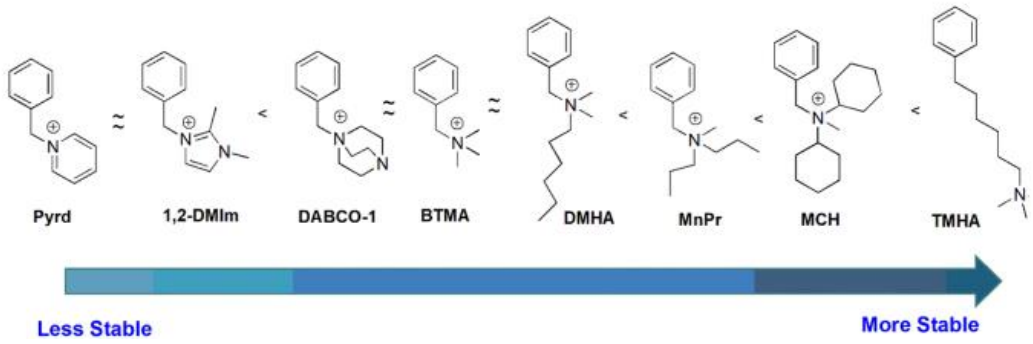

Figure 2.9: Experimentally obtained chemical stability trends for various quaternary ammonium head groups [119].

AEMs have been the subject of several computational investigations, as discussed in the sections above. Zhang and his research team studied ionic conductivity using diffusion coefficients calculated from the Nernst–Einstein equation, employing all-atom MD simulations [97]. They reported a computational ionic conductivity of 2.6 mS/cm, in contrast to the experimental value of 30 mS/cm. The researchers explained this discrepancy by noting that vehicular diffusion contributes to OH^- conductivity in bulk water. However, due to membrane confinement, the contribution of vehicular diffusion is likely lower in this context.

For molecular and material modeling, there are many different approaches and software programs available; nonetheless, using these approaches advances our knowledge of the chemical stability of functional head groups, OH^- ion diffusion pathways, and other relevant characteristics. Though there are still issues with accurately modeling genuine experimental circumstances and system scale, the incorporation of QM-based DFT computations offers valuable insights. The interpretation of DFT results is further influenced by idealized process parameters and implicit solvation models.

AEM-related problems, such as OH^- ion conductivity calculations utilizing the Nernst-Einstein equation, have been extensively studied through the use of ab initio and conventional all-atom MD techniques. Dynamic degradation mechanism reactions, AEM

chemical stability, and the mechanism of OH^- ion diffusion present difficulties, nevertheless. Chemical degradation mechanism reactions are not well-simulated by conventional all-atom MD techniques. The development of the QM/MM method, in particular reactive MD and ab initio MD, presents a viable method for simulating these reactions. Although there is a drive to use conventional all-atom MD to simulate large AEM systems, it is recognized that no single modeling technique can fully handle all of the difficulties associated with multiscale molecular and material modeling.

Chapter 3: Computational methods

In this chapter, the theories and fundamentals of three different atomistic simulations are presented, including DFT, ab initio MD, and conventional all-atom MD methods.

3.1. Density functional theory

3.1.1 Background of DFT

The Schrodinger equation must be solved to get the ground state for a set of atoms. A system's ground state is its most stable state. Equation 3.1 illustrates the Schrodinger equation, which forms the foundation of QM for collections of many atoms.

$$H \times \psi(\{r_i \ldots\}, \{R_i \ldots\}) = E \times \psi(\{r_i \ldots\}, \{R_i \ldots\}) \qquad (3.1)$$

The energy *E*, the wave function ψ, the electron position r_i, the Hamiltonian operator *H,* and the nucleus position R_i are all represented in the equation above. While a wave function in QMs depicts the quantum state of a group of particles or atoms in an isolated system, the Hamiltonian operator is based on kinetic and potential components. One of the most crucial aspects of QM is that a Hamiltonian operator behaves very differently in conventional systems. The Schrodinger equation's exact solution yields the wave function and energy, which provide a comprehensive description of the electronic properties.

In light of this, there are many quantum-chemical techniques for resolving Schrodinger equations. Schrodinger's equation for a collection of numerous atoms is extremely hard to solve [120].

The Born-Oppenheimer approximation is used to treat the nuclei as fixed, based on the aforementioned assertion [121]. The electron is small and quick in the Born-Oppenheimer approximation, whereas nuclei are large, heavy, and slow. As a result, we can distinguish between the movements of nuclei and electrons, as demonstrated by equation 3.2, which indicates that the electron perceives the external potential of static nuclei.

$$\psi(\{r_i \ldots\}, \{R_i \ldots\}) = \psi(\{r_i \ldots\}) * \psi(\{R_i \ldots\}) \qquad (3.2)$$

The wave function ψ, the electron position r_i, and the nucleus position R_i are all represented in the equation above.

Now, we can rewrite equation 1 for the collection of multi electrons as follows in equation 3.3:

$$H * \psi(\{r_i \ldots\}) = E * \psi(\{r_i \ldots\}) \qquad (3.3)$$

The energy *E*, the wave function ψ, the electron position r_i, and the Hamiltonian operator *H* are all represented in the equation above.

$$H = \hat{T} + \hat{V} + \hat{U} \qquad (3.4)$$

Next, we obtained a Hamiltonian operator for the multi-electron situation in equation 3.4, where $\hat{\hat{T}}$ is the electron's kinetic energy, $\hat{V}$ is the potential energy where the electron interacts with external static nuclei, and $\hat{U}$ is the electrons' mutual interaction energy (or electron repulsions).

There are 22 electrons in carbon dioxide, and each electron has three coordinates, which results in 66-dimensional issues. As such, it is challenging to solve the Schrodinger equation for the aggregation of many electrons. DFT then helps with the electron density term. The main application of DFT approaches, which are based on Schrodinger equation approximations, is in computational chemistry.

In terms of electron density, the j-th electron is considered as a singular charge within the influence of all other electrons. This simplification transforms the complex many-electron issue into multiple individual electron problems, as demonstrated in equation 3.5:

$$\psi(r_1, r_2, \ldots, r_N) = \psi(r_1) * \psi(r_2) * \ldots * \psi(r_N) \quad (3.5) \text{ (Hartree product)}$$

The wave function ψ, and the electron position r_i are both represented in the equation above.

Now, let us redefine the electron density by many one electron wave functions as follows in equation 3.6:

$$n(r) = 2 \sum_i \psi_i^*(r) \psi_i(r) \quad (3.6)$$

The electron density n, the wave function ψ, the complex conjugate wave function ψ^*, and the electron position r are all represented in the equation above.

The Hohenberg and Kohn theorems form the foundation of DFT. DFT, which was first presented by P. Hohenberg and W. Kohn in 1964, uses the likelihood of detecting an electron rather than just a wave function to solve the Schrodinger equation [122]. Moving

forward, knowing the electron density is enough to significantly minimize the degree of freedom and enable straightforward computer analysis of huge molecular systems.

Hohenberg and Kohn Theorem I: the ground state energy (E) is a unique functional of the electron density (equation 3.7).

$$E = E[n(r)] \quad (3.7)$$

The energy *E*, the electron density n, and the electron position r are all represented in the equation above.

Hohenberg and Kohn Theorem II: The electron density that minimizes the energy of the overall functional is the true ground state electron density (equation 3.8):

$$E[n(r)] > E_0\,[n_0\,(r)] \quad (3.8)$$

The energy *E*, the electron density n, and the electron position r are all represented in the equation above.

The energy functional consists of known and exchange correlation functionals as shown in equation 3.9:

$$E\{\psi_i\} = E_{known}\{\psi_i\} + E_{XC}\,\{\psi_i\} \quad (3.9)$$

The energy *E*, and the wave function ψ are both represented in the equation above.

In the given situation, the unknown part that needs to be estimated is represented by the exchange correlation functional E_{XC}, which contains all quantum mechanical terms.

Now equation 3.10 can be derived from equation 3.3 following the theorems of Hohenberg and Kohn:

$$[\frac{-\hbar^2}{2m_i}\nabla^2 + V(r) + V_H(r) + V_{XC}(r)]\psi_i(r) = \varepsilon_i * \psi_i(r) \quad (3.10)$$

Where $\frac{-\hbar^2}{2m_i}\nabla^2$ is the kinetic energy term, $\hbar$ is reduced Planck constant, m is the mass, ∇^2 is the Laplacian operator, $V(r)$ is the potential energy term, and $V_H(r)$ is the Hartree potential, $V_{XC}(r)$ is the exchange correlation potential, ε_i is the energy eigenvalue associated with the i-th wave function $\psi_i(r)$. Equation 3.10 above can be solved using the Kohn-Sham iteration approach, which is the foundation of most DFT computations.

Geometry optimization

Geometry optimization is an essential and fundamental stage in the field of computational chemistry and materials research. It involves precisely identifying the molecular system's most energetically advantageous atom configuration, and providing information about the system's structural stability and reactivity. In DFT calculations, selecting the B3LYP basis set is a well-known and frequently used alternative. Because B3LYP combines exchange-correlation functionals that balance computational efficiency and accuracy, it is especially well-suited for a wide variety of molecular systems.

Transition State calculations

Transition state calculations are an important part of your computational methodology in the context of this PhD research, offering crucial insights into the energetics and mechanisms of S_N2 and YF reactions involving different QA head groups within AEMs. The B3LYP basis set is used to make these computations easier to understand, which are essential for deciphering the complex complexities of chemical reactions [1-5, 123-125]. Understanding the reactivity of QA head groups inside AEMs requires an understanding of the processes including S_N2 and YF reactions. The energy barriers that reactants must cross to reach the transition state and the corresponding activation energies are revealed by transition state calculations. These data are essential for estimating the reactions' kinetics and figuring out whether they are energetically aided or hindered.

3.1.2 Software's for DFT calculations

Several software tools for DFT calculations have been created in the fields of computational science. These programs are vital resources for learning about the characteristics and electronic structure of molecules and other materials. A few popular software programs for DFT computations are NWChem, Quantum ESPRESSO, VASP, and Gaussian. These software programs are useful tools for academics across a range of fields because each one has particular advantages and uses [126-128]. The precision with which this software can forecast different spectroscopic characteristics, vibrational frequencies, and molecule structures is exceptional. Both specialists and beginners in the field of computational chemistry can easily utilize Gaussian16 thanks to its intuitive interface and comprehensive documentation.

Support for a wide variety of DFT functionals is one of Gaussian 16's best qualities; it enables researchers to select the functional that best suits their particular research

requirements. A set of tools for visualizing and interpreting electrical structure data is also offered by Gaussian 16, which is essential for learning about the characteristics of molecules.

3.1.3 Quantum chemical properties

Optimized structures

The electronic and geometric features of optimized molecule or material structures can be critically understood in the context of DFT simulations. Determining equilibrium bond lengths and angles as part of this study usually yields information about the stable configuration of the system. Moreover, DFT computations provide useful information on attributes associated to energy, including electronic density of states, frontier molecular orbitals, and total energy. Understanding the stability, reactivity, and electrical structure of the system under study depends on these values. Furthermore, the DFT output makes it possible to compute vibrational frequencies, which is helpful in evaluating molecular vibrations and predicting infrared and Raman spectra, which are essential for describing molecular species [1-5, 123-127].

Lowest Unoccupied Molecular Orbitals (LUMO)

The study of the LUMO in the framework of DFT research offers vital insights into the electronic structure and reactivity of molecular systems. Understanding a variety of occurrences depends on an investigation of the LUMO, which is the highest energy molecular orbital in a molecule. Researchers can evaluate the molecule's electron-accepting capacity by looking at its spatial distribution and LUMO energy; this makes the molecule a crucial sign of its electrophilic nature and reactivity in chemical reactions. Furthermore, the shape and spatial direction of the LUMO provides useful details about possible nucleophilic attack sites, which helps anticipate chemical bonding sites and reaction mechanisms [1-5, 125-130].

Degradation mechanism

The study of transition states is essential to comprehending molecular-level chemical reactions in the context of DFT computations. Calculations of the transition state offer crucial details about a reaction's energy environment, including the $\Delta E_{activation}$, $\Delta G_{activation}$, $\Delta E_{reaction}$ and $\Delta G_{reaction}$. The energy differential between the reactants and products is calculated to determine the $\Delta E_{reaction}$, which measures the thermodynamic favorability of a chemical transformation. This number provides important information about the reaction's overall

viability by indicating whether the reaction is exothermic (having a negative reaction energy) or endothermic (having a positive reaction energy) [1-5, 130-133].

3.1.4 Application of DFT

DFT is an extremely versatile computational method that finds extensive use in a multitude of scientific fields. DFT is essential to understanding the electronic structure, energetics, and characteristics of a wide range of systems in the context of materials science and quantum chemistry. It is widely used in the synthesis and characterization of materials, molecules, and surfaces, giving scientists new perspectives on how matter behaves at the atomic and molecular levels. It is also used to analyze electronic structure, dynamics of systems, and chemical interactions.

When developing AEM materials and comprehending the electrochemical processes that occur within these systems, DFT is a crucial technique. DFT simulations can offer vital information about the reactivity of QA head group of polymer materials, enabling the development of AEM that are both more economical and efficient. This skill is essential to developing high-performing, sustainable AEM and overcoming obstacles associated with alkaline environments. DFT's use in AEM research is crucial to the advancement of this clean energy technology and to solving problems with durability, cost, and efficiency [1-5, 130-134].

3.1.5 Advantages and disadvantages of DFT

Because DFT calculations require less computing power than other ab initio techniques, it is possible to examine systems with a high atom count or to filter materials with a high throughput. Furthermore, DFT offers a fair balance between computing cost and precision, which makes it appropriate for a variety of applications. It is very useful for exploring various scientific and technological difficulties since it can anticipate the electronic structure, geometries, and characteristics of chemical structure. Additionally, DFT offers a wide selection of exchange-correlation functionals, allowing researchers to choose the functional that best suits their particular research problems.

DFT is not without its restrictions, though. The correctness of the exchange-correlation functionals is one significant flaw. No single functional can offer high accuracy for all kinds of systems and attributes, despite the fact that they all exist and have advantages and disadvantages of their own. The functional choice has a significant influence on the outcomes, hence it is important to fully comprehend the system being studied. Additionally,

DFT has difficulty adequately modeling tightly coupled electron systems, which limits its applicability to specific material classes [130-135]. Regarding AEM, DFT presents several benefits as well as certain difficulties. Insights into the electrical structure of AEM components can be gained by DFT, which can aid in the improvement of chemical stability for QA head groups of AEM, and reaction processes. To overcome these constraints, scientists frequently integrate DFT with additional experimental or computational methods to produce more precise and thorough analyses of AEM performance.

3.2. Ab Initio molecular dynamics

3.2.1 Background

Another effective method is ab initio MD based on QM/molecular mechanics (MM) [136]. As the MD simulation moves forward, forces produced by ab initio calculations are implemented to derive trajectories of finite-temperature dynamics through an ab initio MD simulation. Furthermore, chemical bond creation and breaking events are made possible by ab initio MD simulation, which also takes electronic polarization effects into consideration. Although ab initio MD techniques and DFT are both regarded as ab initio methods, ab initio MD simulation also describes dynamics, which is crucial when investigating OH^- ion diffusion as well as chemical stability [120–122].

In its optimal state, an ab initio molecular dynamics (MD) simulation operates under the assumption that the system comprises *N* nuclei and *Ne* electrons, adheres to the Born-Oppenheimer approximation, and allows for the nuclei's dynamics to be traditionally handled on the electronic ground-state surface. This scenario is captured by the total Hamiltonian (equation 3.11).

$$H = T_e + V_{ee} + V_{eN} + T_N + V_{NN} \quad (3.11)$$

The Hamiltonian operator *H*, the electronic kinetic energy T_e, the electron-electron Coulomb repulsion V_{ee}, the electron-nuclear Coulomb attraction V_{eN}, the nuclear kinetic energy T_N, and the nuclear-nuclear Coulomb repulsion V_{NN} are all represented in the equation above. When the nuclear positions are represented as R1 ..., R2 = R, the dynamics of the nuclei are expressed through equation 3.12.

$$M_I \ddot{R}_I = -\nabla_I [\varepsilon_0(R) + V_{NN}(R)] \quad (3.12)$$

The mass M_I, the second derivative of position vector $\ddot{R}_I$, the gradient operator ∇_I, the corresponding ground-state energy eigenvalue $\varepsilon_0(R)$ at the nuclear configuration R, and the potential energy $V_{NN}(R)$ are all represented in the equation above.

Since the ground-state electronic problem cannot be solved exactly, approximate electronic structure methods are needed. In modern ab initio MD simulation, the electronic structure method most commonly used is the Kohn–Sham formulation of DFT, wherein the total energy is expressed as a functional of *n* mutually orthonormal single-particle electron orbitals $\psi_i(r), i = 1, \ldots . n$.

The total energy is given by equation 3.13:

$$E[\{\psi\}, R] = -\frac{1}{2}\sum_i f_i \int dr \psi_i^*(r)\Delta^2\psi_i(r) + \frac{1}{2}\int drdr' \frac{n(r)n(r')}{|r-r'|} + E_{XC}[n] + \int drn(r)V_{ext}(r,R)$$

(3.13)

The total energy $E[\{\psi\}, R]$, the i-th electron wavefunction $\psi_i(r)$, the complex conjugate of the wavefunction $\psi_i^*(r)$, the occupation number of the i-th orbital f_i, the laplacian operator Δ^2, the electron density n(r), the electron position r, the nuclei position R, the exchange-correlation energy E_{XC}, and the external potential V_{ext} are all represented in the equation above.

Generally speaking, such approximations are unable to manage dispersion effectively; however, a new family of nonlocal functionals appears to greatly ameliorate this drawback. The simplest kind of ab initio MD simulation is numerically integrating the above equation using a symplectic integrator. We refer to this kind of ab initio MD simulation as Born-Oppenheimer dynamics.

Researchers can model molecular system dynamics at the QM level using a sophisticated computer technique called ab initio MD simulations. In many scientific fields, this approach is especially useful for investigating chemical reactions, changes in electronic structure, and other quantum phenomena [121–125].

Selecting the right basis set is essential to getting correct results in ab initio MD simulations. Various basis sets are available for researchers to choose from, contingent on the required degree of precision and the computational capacity on hand. In ab initio MD simulations, atomic locations and velocities are updated by iterative stages where the electronic structure is solved at each time step. Until the specified simulation time is reached, these iterations keep going [120–128].

3.2.2 Software's for ab initio MD simulations

A range of software tools are used in the field of ab initio MD simulations, which allow scientists to investigate the dynamic behavior of atoms and molecules with a high degree of precision. The study of complicated systems, such as chemical processes, phase transitions, and biomolecular dynamics, has made these software programs essential. VASP, Quantum ESPRESSO, CPMD, and CP2K are notable software choices for ab initio MD simulations. Each has specific functions and uses. These software programs are frequently selected by researchers by their particular research requirements, system complexity, and the degree of simulation accuracy needed [127-130].

One popular software package that is well-known for its ability to do ab initio MD simulations is called CP2K [140]. To offer accurate descriptions of electronic structure and molecular dynamics, CP2K combines wave function-based techniques, such as Hartree-Fock theory, with first-principles techniques, such as DFT. The focus on hybrid functionals, which combine DFT with post-Hartree-Fock techniques and provide a high degree of accuracy for a variety of materials, is one of CP2K's unique characteristics. Scientists use CP2K to simulate a wide range of systems, such as solid-state materials, biomolecules, and organic and inorganic compounds. Moreover, CP2K offers sophisticated resources for researching attributes including vibrational spectra, thermodynamics, and NMR chemical shifts, which makes it an adaptable option for researchers working on ab initio MD simulations [126-131].

3.2.3 Quantum chemical and molecular mechanics based properties

RDF analysis

The examination of radial distribution functions (RDFs) is crucial for clarifying the spatial arrangement of atoms or molecules in a system when using ab initio MD simulations. The RDF is estimated by equation 3.14.

$$g(r) = \frac{\rho(r)}{\rho} \qquad (3.14)$$

The local density $\rho(r)$, and the system average bulk density ρ are both represented in the equation above.

RDF analysis offers important insights into the likelihood of locating a specific species at a given distance from a reference particle, hence disclosing vital details regarding the local order, intermolecular interactions, and structural structure of the system. Through close examination of RDFs, scientists can spot trends in atomic or molecular configurations,

pinpoint peaks that match distinctive bond lengths, coordination settings, and solvation shells, and ultimately advance our comprehension of the thermodynamic and structural characteristics of the system.

Distance between atoms

An essential method for examining the structural dynamics and interactions of a molecular system is the examination of interatomic distances within the context of Ab initio MD simulations. Through the course of a simulation, the distances between atom pairs are tracked in this research, which sheds light on bond lengths, atomic coordination, and the investigation of conformational spaces. Researchers can find significant structural alterations, bond breaking and formation events, and fluctuations in chemical environments by keeping an eye on these interatomic lengths. This information is crucial for comprehending the dynamic behavior of the system they are studying. This analysis adds to a thorough description of the behavior and reactivity of the molecular system by clarifying reaction processes, evaluating molecular conformations, and highlighting crucial structural transitions.

Diffusion Coefficients

A key component of describing the dynamic behavior of molecular systems in Ab initio MD simulations is the examination of diffusion coefficients obtained from the mean square displacement (MSD) vs time curve. The MSD is estimated by equation 3.15.

$$MSD\ (t) = \langle |r(t) - r(0)|^2 \rangle \qquad (3.15)$$

The position vector $r(t)$ at time t, and the initial position $r(0)$ are both represented in the equation above.

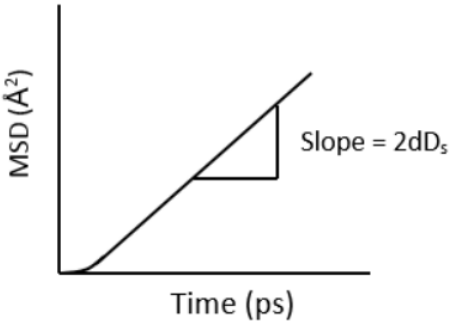

Figure 3.1: Plot of the MSD as a function of time.

Albert Einstein related the MSD to the self-diffusion coefficient in Equation 3.16.

$$D_s = \lim_{t\to\infty} \frac{1}{2dt} \langle |r(t) - r(0)|^2 \rangle \qquad (3.16)$$

The dimensionality of system d, the time t, the position vector $r(t)$ at time t, and the initial position $r(0)$ are both represented in the equation above.

The MSD is a critical metric used to quantify the extent of a molecular system as a function of time, providing a comprehensive numerical representation of the molecules' or ions' diffusive and mobility characteristics. By tracking the displacement of molecules over time, the MSD captures both the random motion of molecules, and the influence of external forces or constraints that may affect their movement [128-132].

The slope of the MSD curve over long time intervals is particularly informative, as it reflects the molecules' diffusive behavior. This slope is directly related to the diffusion coefficient, a fundamental parameter that quantifies the rate at which molecules spread out from their initial positions. The diffusion coefficient is essential for understanding the dynamics of the system, as it provides insights into how quickly molecules move and how their motion evolves over time.

Importantly, only the linear portion of the MSD plot, which corresponds to the diffusive regime, is utilized to calculate the self-diffusion coefficient. This linear region indicates a steady-state condition where the displacement of molecules is proportional to time, allowing for an accurate determination of the self-diffusion coefficient.

3.2.4 Application of ab initio MD simulations

Because ab initio MD simulations can offer comprehensive insights into the dynamic behavior of atoms and molecules, they are used in a wide range of scientific areas. The study of structural changes in materials, including phase transitions and flaws, benefits greatly from the application of ab initio MD techniques. Furthermore, ab initio MD technique is used in biophysics to simulate the dynamic behavior of biomolecules, providing information on their interactions with other molecules and conformational changes.

The use of ab initio MD techniques in the context of AEM is essential for clarifying important procedures. By providing a view into the chemical events taking place within the AEM, they aid in the identification of the mechanisms underlying material degradation mechanism by researchers. The Grotthuss mechanism, which describes the OH^- ion transport via the exchange of hydrogen ions within a network of water molecules, is best understood

through the use of ab initio MD techniques. This realization is crucial to maximizing AEM longevity and efficiency [129-133].

An essential component of AEM operation, the vehicular transfer of OH^- ions within the AEM, is another area in which ab initio MD simulation assists. By offering a microscopic picture of ion, QA head group, and water dynamics, ab initio MD simulations help researchers make well-informed decisions about fuel cell optimization and membrane design.

3.2.5 Advantages and disadvantages of ab initio MD simulations

Ab initio MD techniques provide atomic-level insights into the behavior of complicated systems with several important benefits. Their precision is one of the main benefits. Because ab initio MD simulations are based on first-principles techniques DFT, they guarantee extremely accurate representations of atomic interactions and electronic structure. Because of its accuracy, ab initio MD simulation is a great tool for studying complex processes like bond formation and chemical reactions.

Nevertheless, ab initio MD simulations come with certain drawbacks, with high computational cost being a significant concern. For instance, ab initio MD simulations typically require computational resources that scale with the cube of the system size. As a result, simulating a moderately sized system of around 100 atoms for a few picoseconds can demand several thousand CPU hours on high-performance computing clusters. For larger and more complex systems, or when using more accurate methods such as hybrid functionals, the computational cost can easily exceed tens of thousands of CPU hours, making such simulations prohibitively expensive and time-consuming [130-134].

3.3. Conventional all-atom molecular dynamics

3.3.1 Background of conventional all-atom MD

To simulate the dynamics of built systems using a shorter timescale and discrete integration of Newton's equations of motion, the total forces acting on all atoms are first determined. This allows for the determination of how each atom could respond to these forces. Let's take an example where the system's potential energy at the particle's position is known. As a result, the interaction between atoms depends on the interatomic distances, which can be computed if the positions of the atoms are known [135-140]. The equations used to estimate atomistic interactions, based on potential energies, are summarized below (equations 3.17-3.19):.

$$U_{total} = U_{non-bonded} + U_{bonded} \quad (3.17)$$

The total potential energy U_{total}, the intermolecular interactions $U_{non-bonded}$, and the intramolecular bonded interactions U_{bonded} are all represented in the equation above.

$$U_{non\text{-}bonded} = U_{LJ} + U_{electrostatic} \quad (3.18)$$

The intermolecular interactions $U_{non-bonded}$, the Lennard-Jones potential U_{LJ}, and the Coulombic interactions $U_{electrostatic}$ are all represented in the equation above.

$$U_{bonded} = U_{bond-stretching} + U_{angle} + U_{torsion} + U_{oop} \quad (3.19)$$

The intramolecular bonded interactions U_{bonded}, the bond stretching $U_{bond-stretching}$, the bond angle U_{angle}, the torsion $U_{torsion}$, and the out-of-the-pane U_{oop} are all represented in the equation above.

After that, we can calculate the forces on each atom from the potential energy function, and then we can calculate acceleration according to Newton's second law (equation 3.20). The second law of Newton's states that the forces on a particle equal to its mass times acceleration.

$$\overrightarrow{F_i} = -\frac{\partial U_{total}}{\partial \vec{r_i}} = m\frac{\partial^2 \vec{r_i}}{\partial t^2} \quad (3.20)$$

The force F, the total potential energy U_{total}, the mass m, the position r_i, and the time t are all represented in the equation above.

Next, the configurations are updated at each integration step, with atomic movements predicted using Newtonian dynamics. This process generates output parameters such as pressure, temperature, energies, atomic positions, and velocities.

3.3.2 Software's for conventional all-atom MD simulations

For doing conventional MD simulations, a variety of software programs are available, each with a range of features suited to specific research goals. In this category, some well-known software choices are AMBER, NAMD, LAMMPS, CHARMM, and Gromacs. These resources are frequently utilized by researchers to investigate a wide range of systems and phenomena in the domains of computational chemistry, biophysics, materials science, and other related topics [139-142]. The compatibility with force fields, and the particular

characteristics or behaviors being studied are some of the variables that influence the software selection.

Gromacs is effective for simulating complex materials and biological macromolecules, including lipids, proteins, and nucleic acids. Gromacs may be tailored to meet a wide range of research objectives because they support many input formats and integrate a vast range of force fields. Additionally, it offers an extensive collection of analysis tools that let academics examine a multitude of data produced by simulations [140-142]. Gromacs is still developing, and its capabilities are being added to by a passionate user base. Researchers of different skill levels can utilize the software thanks to its easy-to-use interface and comprehensive documentation, which increases its attractiveness as a useful tool for investigating the atomic-level dynamics of a variety of systems.

3.3.3 Molecular structural and molecular dynamic properties

Radial Distribution Function

RDF analysis is described in the previous sub-subsection 3.2.3

Diffusion Coefficient

Diffusion coefficient calculation is described in the previous sub-subsection 3.2.3

3.3.4 Application of conventional all-atom MD simulations

There are numerous uses for conventional all-atom MD simulations across numerous scientific fields. They are a priceless resource for researching the dynamic behavior of materials and molecules because they shed light on structural alterations, molecular interactions, and thermodynamic characteristics. Scholars have examined phase transitions, chemical processes, and the mechanical characteristics of materials using conventional all-atom MD simulations. These simulations have proven crucial in the field of biophysics to comprehend the conformational dynamics of biomolecules like proteins, DNA, and membranes [135-145].

AEM relies heavily on conventional all-atom MD techniques to shed light on essential processes at the microscopic level. They aid in the comprehension of OH^- ion diffusion process, which is essential to the functioning of an AEM. These simulations provide a thorough understanding of the dynamics of water and OH^- ions, clarifying the mechanics underlying OH^- ion diffusion and transport. Comprehending these procedures is essential for

enhancing the effectiveness and longevity of AEM since it facilitates the creation of better materials for AEM [1-5, 135-140].

3.3.5 Advantages and disadvantages of conventional all-atom MD simulations

MD techniques using all-atom conventional methods have significant benefits that make them useful for a wide range of applications. They are especially helpful in calculating the processes involved in vehicle motion, which enables scientists to learn more about the atomic-scale dynamics of OH^- ions and water molecules via QA head groups of AEM. Understanding ion transport processes, diffusion, and conduction in a variety of materials and systems depends on this capacity. Additionally, large-scale molecular simulations are a strength of conventional all-atom MD simulations, giving researchers the chance to examine complicated systems in great detail, including proteins, AEMs, and solvated molecules.

Conventional all-atom MD simulations do have certain drawbacks, though. Due to the use of non-reactive force fields, one major disadvantage is their inability to record chemical events involving bond creation and breaking. This constraint is especially important when modeling the chemical degradation mechanism events occurring within the fuel cell components in the context of AEM. Conventional all-atom MD simulations are useful for understanding the structural and dynamic properties of materials, but they are unable to represent the chemical events that lead to material degradation mechanism. When examining chemical reactions within AEM, researchers need to be aware of this constraint and take into account alternate computational techniques, including quantum mechanical simulations [1-5, 135-146].

3.4. Multiscale molecular modeling details implemented in this study

3.4.1 DFT calculation details

DFT with the B3LYP functional was employed for geometry optimization and transition state calculations. The initial geometries were constructed using GaussView software, and the algorithm for the DFT calculations is illustrated in **Figure 3.2**. The study focused on optimizing the structures of QA head groups, ensuring their stability by confirming that all stationary points corresponded to absolute minima on their respective potential energy surfaces. This verification was achieved through additional calculations of the second derivatives of the energy.

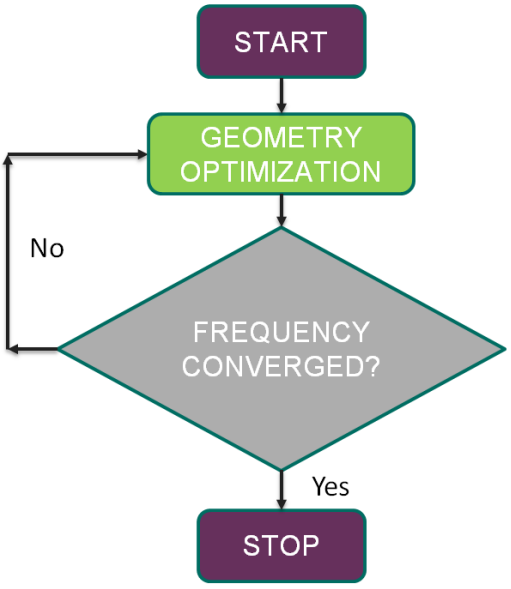

Figure 3.2: Algorithm of the DFT calculation used in this work.

After completing the geometry optimization and transition state calculations, key electronic properties such as the LUMO energy, reaction energy, and activation energy were computed for various QA head groups. These include the QA head groups (discussed in subsection 4.3), QCS head groups (discussed in subsection 6.3), and tetramethylammonium head groups (discussed in subsection 7.3). **Table 3.1** provides a comprehensive overview of the details and parameters used in the DFT calculations conducted for this study, including the methodologies and computational settings applied to optimize and analyze the geometries and transition states of the systems.

Table 3.1: Details of DFT calculations used in this work.

Details	Descriptions
Theoretical models	The various QA head group structures from literature were selected as a theoretical model for DFT [119]. The coordinates were obtained using GaussViewer software. The detailed structures of theoretical models for i) QA head group-based AEMs is discussed in subsection 4.2, ii) QCS head groups of AEMs is discussed in subsection 6.2, and iii) tetramethylammonium head group in subsection 7.2.
Optimization, and transition states	DFT optimization of QA head groups and transition state calculations were conducted to obtain the optimized geometries and transition states for nucleophilic substitution and ylide formation

	reactions. These calculations aimed to identify the most stable configurations of the reactants and to characterize the critical points along the reaction pathways, providing insights into the energy barriers and mechanistic details of these processes. More details on the DFT optimization and transition state calculations for i) QA head group-based AEMs are discussed in subsection 4.2, ii) QCS head groups of AEMs in subsection 6.2, and iii) tetramethylammonium head groups in subsection 7.2.
Analysis	After DFT optimization, and transition state calculations, the LUMO energy, reaction energy, reaction free energy, activation energy and activation free energy were computed for QA head groups (subsection 4.3), QCS head groups (subsection 6.3), and tetramethaylammonium head groups (subsection 7.3).
Validation of results	The B3LYP functional was used in this DFT calculation. Our choice of the B3LYP functional was influenced by the validation adopted from Dario Dekel's work [88], which focused on the chemical stability of quaternary ammonium-based benzylic head groups. We have also benchmarked this approach in our work. This functional was selected based on validations available in the literature and the verification of calculated reaction and activation energy values. The validation for i) QA head group-based AEMs is discussed in subsection 4.3, ii) QCS head groups of AEMs in subsection 6.3, and iii) tetramethylammonium head group in subsection 7.3.

The decision to use the B3LYP functional in these DFT calculations was informed by validation studies, particularly those referenced from Dario Dekel's work [88], which concentrated on the chemical stability of QA-based benzylic head groups. This choice was further validated by benchmarking in our work, confirming the reliability of the B3LYP functional for this purpose.

In this study, three designed systems were examined: i) QA head groups, ii) QCS head groups, and iii) tetramethylammonium head groups. These systems were carefully selected to explore the stability and reactivity of head groups, with a focus on their potential applications

in various chemical processes, particularly within the context of AEMs. The findings provide valuable insights into the reaction pathways of these QA-based systems.

3.4.2 Ab initio MD simulation details

The ab initio MD simulations conducted in this study provided critical insights into two key aspects: (i) chemical degradation reactions and (ii) the molecular structural diffusion of OH^- ions. These simulations utilized the BLYP functional, a choice substantiated by extensive validations in the literature [34-37] and the verification of density and diffusion coefficient values specific to this work, as detailed in Section 7.2.

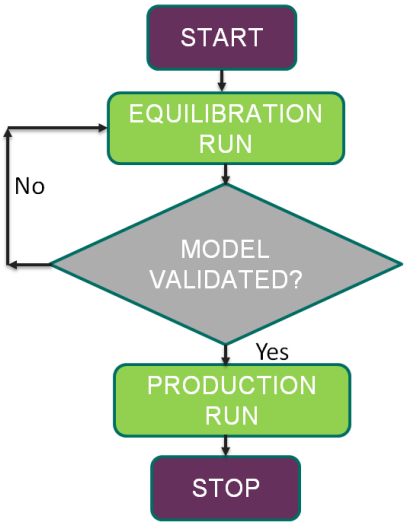

Figure 3.3: Algorithm of the MD simulation used in this work.

The simulation process was meticulously outlined and is depicted in **Figure 3.3**. It began with the creation of theoretical models to represent the systems under investigation. Following model construction, an initial configuration was set up to prepare the system for equilibration. This equilibration phase ensured that the system reached a stable state before transitioning to the production run. The production run involved the actual MD simulations that provided the data necessary for subsequent analysis. **Table 3.2** provides a comprehensive summary of the details and parameters used throughout the ab initio MD simulations.

Table 3.2: Details of ab initio MD simulations used in this work.

Details	Descriptions
Theoretical models	The coordinates of the selected theoretical models were generated using GaussViewer software. Positively charged

	tetramethylammonium head groups had a counter ion negatively charged OH^- ions. The detailed structure of theoretical model is discussed in subsection 7.2.
Equilibriation and production runs	Energy minimization was performed to optimize the initial configuration under conditions ranging from 298 to 350 K, at 1 bar pressure, and utilizing both NVE and NPT ensembles for 5-10 ps after the initial simulation box for the system was established. Following system equilibration, ab initio MD simulations were conducted using an NVT ensemble for 50 ps, with a reference temperature set at 298, 320, or 350 K. The equilibration and production run details for tetramethylammonium head groups of AEMs are discussed in subsection 7.2.
Analysis	After completing the ab intio MD simulations, the results were analyzed from various perspectives, including molecular structural analysis using bond distances and OH^- ion diffusivity analysis by calculating the diffusion coefficient from the MSD vs. time curve.
Validation	The BLYP functional was implemented in this work to perform ab intio MD simulations. Our choice of the BLYP functional was influenced by the methodology outlined in Zelovich et al.'s work [34]. These parameters were selected based on validations available in the literature [34-37] and the validation of density and diffusion coefficient values. The validation for i) tetramethylammonium head groups of AEMs is discussed in subsection 7.3.
Repeatability	To estimate the diffusion coefficient, an initial 50 ps simulation run was conducted for the system. However, due to significant statistical noise, even after performing three independent simulations, further refinement was deemed necessary. Consequently, 10 independent simulations for each system design were carried out to minimize statistical uncertainty and enhance the reliability of the results.

These simulations enabled several key analyses. Bond distances were calculated to understand the structural properties of the systems. Additionally, the simulations facilitated the visualization of vehicular and Grotthuss diffusion mechanisms of OH^- ions, which are critical for understanding ion transport and interactions within the system. MSD and waiting time distribution analyses were performed to quantify the diffusion behavior and dynamics of the OH^- ions. These analyses provided valuable insights into the mechanisms driving chemical reactions and ion mobility, contributing to a deeper understanding of the system's behavior under various conditions.

3.4.3 Classical all-atom MD simulation details

Classical all-atom MD simulations were employed to investigate OH^- ion diffusion at the atomic level, providing deeper insights into the mechanisms involved. The CHARMM36 force field parameters were utilized for these simulations, selected based on validations available in the literature [97, 105], which are further discussed in Sections 5.2 and 6.2. The algorithm used for the classical all-atom MD study is outlined in **Figure 3.3**, and the detailed methodology is presented in **Table 3.3**.

Table 3.3: Details of classical all-atom MD simulations used in this work.

Details	Descriptions
Theoretical models	The coordinates of the selected theoretical models were generated using GaussViewer software. Further, CHARMM forcefield parameters were obtained by Swiss Param tool [147-150]. Positively charged QA head groups had a counter ion negatively charged OH^- ions. The detailed structures of theoretical models for i) QA head group-based AEMs is discussed in subsection 5.2, and ii) QCS head groups of AEMs is discussed in subsection 6.2.
Equilibriation and Production run	The simulation protocol began with energy minimization, followed by 1 ns of NPT equilibration at each temperature setting (298, 330, and 350 K) and 1 bar pressure. Subsequent NVT equilibration at the same temperatures ensured system stability before running production MD simulations for 10 ns under the NVT ensemble. The equilibration and production run details for i) QA head group-based AEMs are discussed in subsection 5.2, and ii) QCS head groups of AEMs are discussed in subsection 6.2.

Analysis	After completing the MD simulations, the results were analyzed from various perspectives, including molecular structural analysis using RDF and OH^- ion diffusivity analysis by calculating the diffusion coefficient from the MSD vs. time curve.
Validation	The CHARMM36 force field parameters were implemented in this work to perform classical all-atom MD simulations. Our choice of the CHARMM36 force field was influenced by the methodology outlined in Zhang et al.'s work [97]. These parameters were selected based on validations available in the literature [97, 105] and the validation of density and diffusion coefficient values. The validation for i) QA head group-based AEMs is discussed in subsection 5.3, and ii) QCS head groups of AEMs is discussed in subsection 6.3.
Repeatability	To estimate the diffusion coefficient, an initial 10 ns simulation run was conducted for the system. However, due to significant statistical noise, even after performing three independent simulations, further refinement was deemed necessary. Consequently, 10 independent simulations for each system design were carried out to minimize statistical uncertainty and enhance the reliability of the results.

In this study, standard classical all-atom MD parameters were implemented, including NPT and NVT equilibration steps with periodic boundary conditions. A 10 ns production MD run was then conducted using the NVT ensemble. The selection of the CHARMM36 force field was guided by the validation presented in Zhang et al.'s work [97]. In line with Zhang et al.'s [97] approach to atomistic model construction, the same CHARMM36 force field was applied to QCS head groups in AEM, with densities and diffusion coefficients validated in subsections 5.3 and 6.3. The automatic topology-building tool Swiss Param was used to generate the necessary force field parameters for CHARMM36. Ten independent simulations were conducted for each system design to minimize statistical error. Additional details regarding the simulations and parameters can be found in Sections 5.2 and 6.2.

Chapter 4: Chemical stability of several quaternary ammonium head groups of anion exchange membranes

In this chapter, the DFT calculations were used to study the chemical stability and chemical degradation mechanism of various QA head groups found in AEM at the atomistic level.

The work presented in this chapter has been published in 2022 in the journal Molecules [147].

4.1. Introduction

Because QAs are easily synthesized and abundantly available, they are frequently used as cation head groups. Using small-molecule compounds such as pyridinium, 1,4-diazabicyclo [2.2.2] octane (DABCO), benzyltrimethylammonium (BTMA), n-methyl piperidinium, guanidium, and trimethylhexylammonium (TMHA), recent experimental studies have concentrated on the thermochemical stability of QA cation groups [147-149].

However, commercialization of AEM development has been restricted by various QA head groups degradation mechanism, which affects the diffusion of OH^- ions. Understanding the molecular degradation mechanism of different QA with OH^- ions is essential for the creation of high-performance AEMs. For different QA of AEM in alkaline condition, three degradation mechanisms have been proposed in this context: E_2, S_N2, and YF [1-3]. Nevertheless, a thorough knowledge of the chemical mechanisms underlying the degradation mechanism of different QA in alkaline condition is lacking.

To investigate the chemical breakdown and diffusion of OH^- ion around QA head groups of AEM, computational modeling, and simulations have emerged as a vitally important technique. In particular, to examine the molecular structure and molecular dynamic features, degradation mechanisms, chemical stability, and other topics, it is common practice to employ conventional all-atom MD, ab initio MD, and DFT methods [1-3, 83-93]. There is, however, little research on the various QA head group degradation mechanism with OH^- ion to relate to experimental features such as chemical stability in AEM. The degradation mechanisms of various QA head groups, such as (a) pyridinium, (b) DABCO, (c) BTMA, (d)

n-methyl piperidinium, (e) guanidium, and (f) TMHA, are investigated in this study using DFT.

In the next section, DFT calculations methodology, $\Delta E_{reaction}$, $\Delta G_{reaction}$, transition state, $\Delta E_{activation}$, $\Delta G_{activation}$, and LUMO energy for typical QA head groups of AEM are described.

4.2. Models and methods

4.2.1 System of interest

For our DFT calculations, six sample segments from AEMs—henceforth referred to as QA head groups—were chosen as theoretical models. They were (a) pyridinium, (b) DABCO, (c) BTMA, (d) n-methyl piperidinium, (e) guanidium, and (f) TMHA, as shown in **Figure 4.1**.

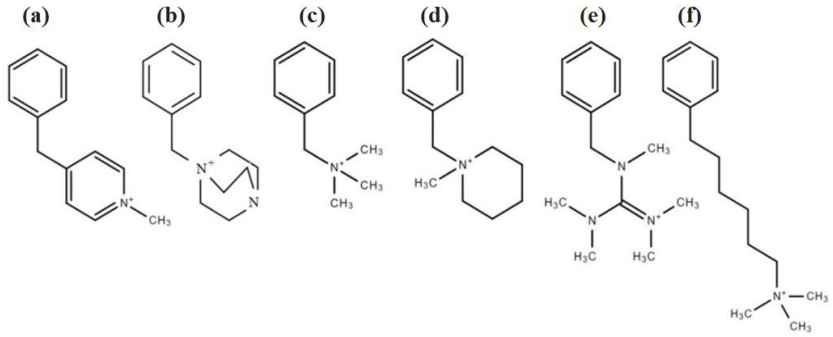

Figure 4.1: Illustration of typical segments for various QA head groups: The six QA head groups include (a) pyridinium, (b) DABCO, (c) BTMA, (d) n-methyl piperidinium, (e) guanidium, and (f) TMHA.

4.2.2 DFT calculations

DFT is used to calculate a wide range of attributes for practically any type of atomic system. The electronic ground state geometries were optimized and bond length, molecular orbital densities, binding energy ($\Delta E_{Binding}$), $\Delta E_{reaction}$, $\Delta G_{reaction}$, transition state, $\Delta E_{activation}$, and $\Delta G_{activation}$ were computed in this work using DFT-based computations. Covalent and noncovalent interactions were present in the molecular contacts between positively charged QA head groups and OH^- ions in the aqueous phase in our investigation. Using the PCM [150, 151] as an implicit solvation model, the electronic ground state geometries for the six QA head groups were optimized using DFT calculations, both in the presence and absence of OH^- ions.

As discussed in section 3.4, our choice of the B3LYP functional was influenced by the validation adopted from Dario Dekel's work [88]. One of the most widely used exchange functional types in quantum chemistry computations is known as B3LYP (Becke, 3-parameter, Lee–Yang–Parr). This functional is based on a hybrid functional where the exchange energy is computed using the HF approach [152-155].

4.2.2.1 LUMO Energies

LUMO distribution and energies were obtained by the B3LYP functional [89-93]. Here, as indicated in equation (4.1) and table A1 of Appendix A, $\Delta E_{binding}$ was calculated utilizing the variations in the total energy values as shown in equation 4.1.

$$\Delta E_{binding} = E_{QA\ with\ OH^-} - (E_{QA} + E_{OH^-}) \quad (4.1)$$

4.2.2.2 Degradation mechanism

The B3LYP DFT method was used to optimize the transition states for the S_N2 degradation mechanism reactions of two QA (c) and (f), at the various HLs (0–3). To determine $\Delta E_{activation}$ and $\Delta E_{reaction}$ for the S_N2 degradation mechanism reaction, DFT calculations were performed for the transition state structure of QA at the HLs 0, 1, 2, and 3. Furthermore, the amount of water molecules per OH^- ion was specified as HL.

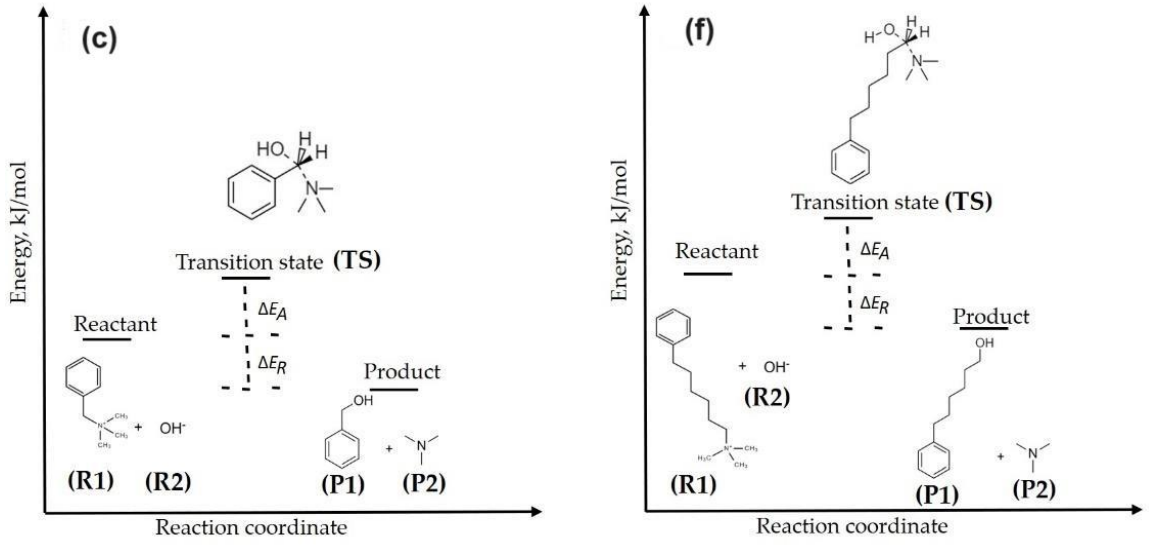

Figure 4.2: 2D representation of S_N2 mechanism for QA (c) and (f).

Here, equations (4.2), (4.3), (4.4) and (4.5) were used in conjunction with the methodology depicted in **Figure 4.2** to determine the $\Delta E_{reaction}$, $\Delta G_{reaction}$, $\Delta E_{activation}$ and $\Delta G_{activation}$. Additionally, for the optimized transition state structures, the counterpoise

correction approach was used to evaluate the basis set superposition error (BSSE). The transition state was split into the electrophile and nucleophile clusters (OH^-) for the BSSE evaluation.

$$\Delta E_{reaction} = \sum E_{(products)} - \sum E_{(reactants)} \quad (4.2)$$

$$\Delta G_{reaction} = \sum G_{(products)} - \sum G_{(reactants)} \quad (4.3)$$

$$\Delta E_{activation} = E_{(transition\ state)} - \sum E_{(reactants)} - E_{(BSSE)} \quad (4.4)$$

$$\Delta G_{activation} = G_{(transition\ state)} - \sum G_{(reactants)} \quad (4.5)$$

All stationary points were verified to be genuine minima on their corresponding potential energy surfaces by doing additional computations of the second energy derivatives.

GaussView (v6.0) (Gaussian, Inc., Wallingford, CT) was used for post-analysis after all DFT computations were completed using GAUSSIAN16 [156].

4.3. Results and discussion

In this section, DFT results related to the chemical stability of QA are presented. DFT properties including the $\Delta E_{reaction}$, $\Delta G_{reaction}$, transition state, $\Delta E_{activation}$, $\Delta G_{activation}$, and distribution of LUMO orbitals are analyzed and discussed to understand the chemical stability of QA (a)-(f) and their chemical degradation mechanism.

4.3.1 Degradation mechanism

The results of the molecular electrostatic potential (ESP) maps for the binding of OH^- ions with various QA head groups of the AEM via the B3LYP DFT method are displayed in Appendix A (**Figure A1**). The results show that the OH^- ions mainly interact with the nitrogen atoms of the QA head groups in the AEM to stabilize their positive charge. Structural optimizations for various QA head groups of the AEM, via B3LYP DFT method and $E_{Binding}$ calculations are presented in **Figure A2**, and **Table A1** of Appendix A. The results imply that the $E_{Binding}$ of different QA head groups to OH^- ions are quite different, indicating that further analysis of the degradation mechanism is needed.

In this regard, we present the results of $\Delta E_{reaction}$, transition state, and $\Delta E_{activation}$ for two QA head groups of the AEM by the B3LYP DFT method (**Table A2**, and **A3** Appendix A). OH^- ions have the potential to attack the benzylic carbon atoms of the two QA head

groups (c) and (f), which could lead to a chemical breakdown through the S_N2 degradation mechanism. For QA head groups (c) and (f), we looked at the S_N2 degradation mechanism in more detail. **Table 4.1, Figure 4.3** and **Figure 4.4** display the $\Delta E_{reaction}$, $\Delta G_{reaction}$, transition state, $\Delta E_{activation}$, and $\Delta G_{activation}$ results for the S_N2 degradation mechanism of the two QA head groups.

Table 4.1: $\Delta E_{reaction}$, $\Delta G_{reaction}$, $\Delta E_{activation}$ and $\Delta G_{activation}$ energy values for the S_N2 mechanisms of QA (c) - (f). Unit: kJ/mol.

QA	HL	$\Delta E_{reaction}$	$\Delta G_{reaction}$	$\Delta E_{activation}$	$\Delta G_{activation}$
(a)	0	-147.75	-219.33	27.97	42.07
(b)	0	-128.19	-193.72	32.20	75.83
(c)	0	-124.72	-139.55	41.56	91.01
	1	-69.67	-117.74	53.57	104.09
	2	-40.02	-93.47	64.91	110.66
	3	-19.7	-72.41	86.69	145.78
(d)	0	-122.84	-135.67	43.73	107.6
(e)	0	-122.24	-133.35	53.20	126.46
(f)	0	-121.20	-131.79	61.08	130.1
	1	-66.15	110.02	76.17	135.47
	2	-36.49	134.29	88.78	146.73
	3	-16.21	155.35	106.25	166

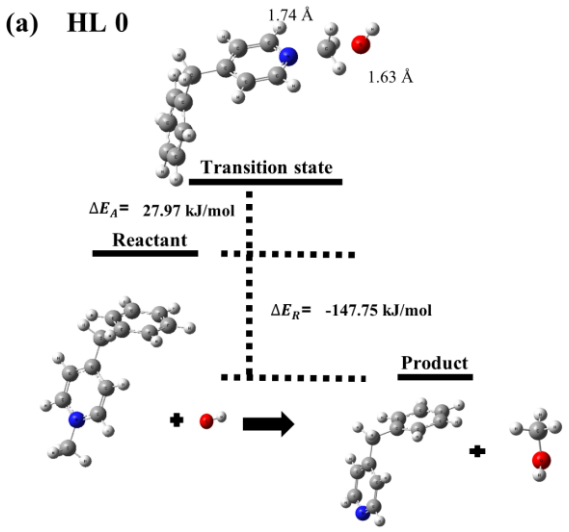

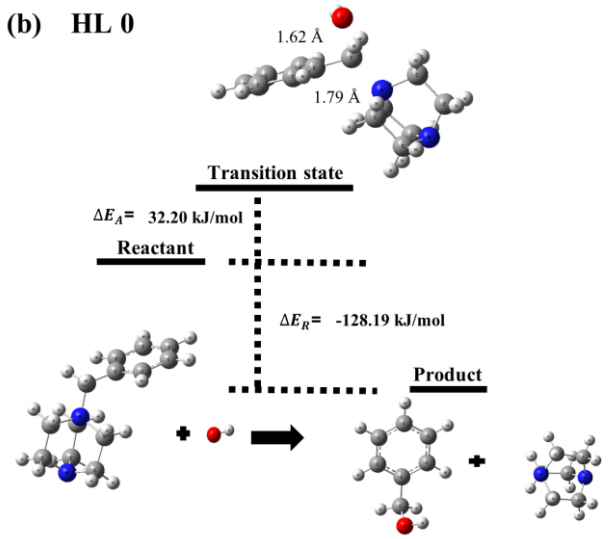
(b) HL 0
1.62 Å
1.79 Å
Transition state
ΔE_A= 32.20 kJ/mol
Reactant
ΔE_R= -128.19 kJ/mol
Product

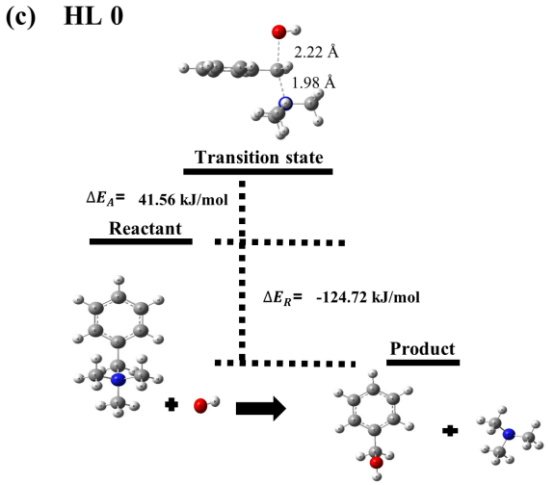
(c) HL 0
2.22 Å
1.98 Å
Transition state
ΔE_A= 41.56 kJ/mol
Reactant
ΔE_R= -124.72 kJ/mol
Product

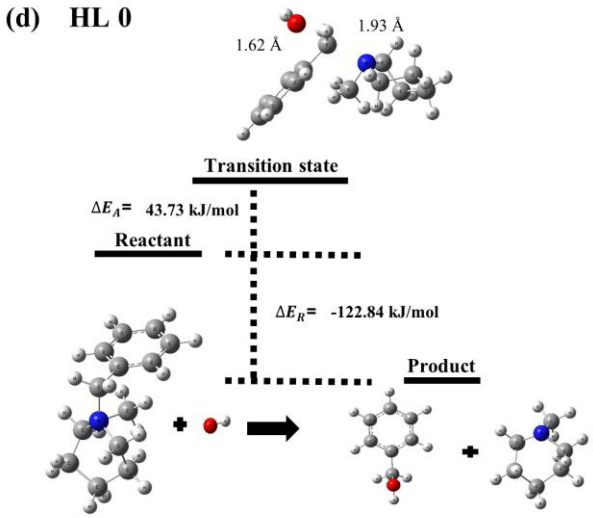
(d) HL 0
1.62 Å
1.93 Å
Transition state
ΔE_A= 43.73 kJ/mol
Reactant
ΔE_R= -122.84 kJ/mol
Product

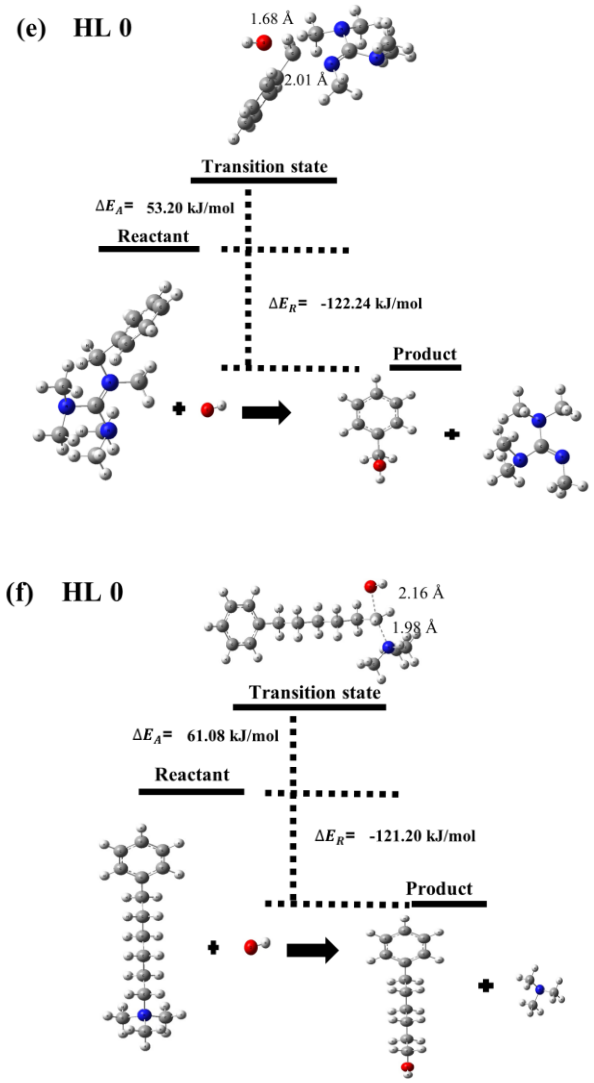

Figure 4.3: $\Delta E_{reaction}$ and $\Delta E_{activation}$ energies for S_N2 mechanism of QA (a) - (f).

The results of the transition state calculation ($\Delta E_{reaction}$, $\Delta G_{reaction}$, $\Delta E_{activation}$ and $\Delta G_{activation}$ energy values) for S_N2 mechanism of QA (a) - (f) indicate an increasing stability trend as follows: (a) pyridium < (b) DABCO ~ (c) BTMA < (d) n-methyl piperidinium < (e) guanidium < (f) TMHA (**Table 4.1, Figure 4.3**).

The QA head groups' (c) and (f) S_N2 degradation mechanism $\Delta E_{reaction}$ results show that the S_N2 degradation energy rises thermodynamically with HL from 0 to 3. Moreover, the value of S_N2 degradation mechanism $\Delta E_{reaction}$ for QA head group (f) is slightly higher to the value of S_N2 degradation mechanism $\Delta E_{reaction}$ for QA head group (c). The DFT transition state results implied that the QA (f) head group benefits from higher $\Delta E_{activation}$ values in comparison with QA (c) at the different HLs. The results of the transition state calculation ($\Delta G_{reaction}$, and $\Delta G_{activation}$ energy values) for the S_N2 mechanism of QA (c) and (f) at different

HLs indicate similarly that QA (f) is more chemically stable than QA (c), reinforcing the thermodynamic trend observed with rising HLs from 0 to 3.

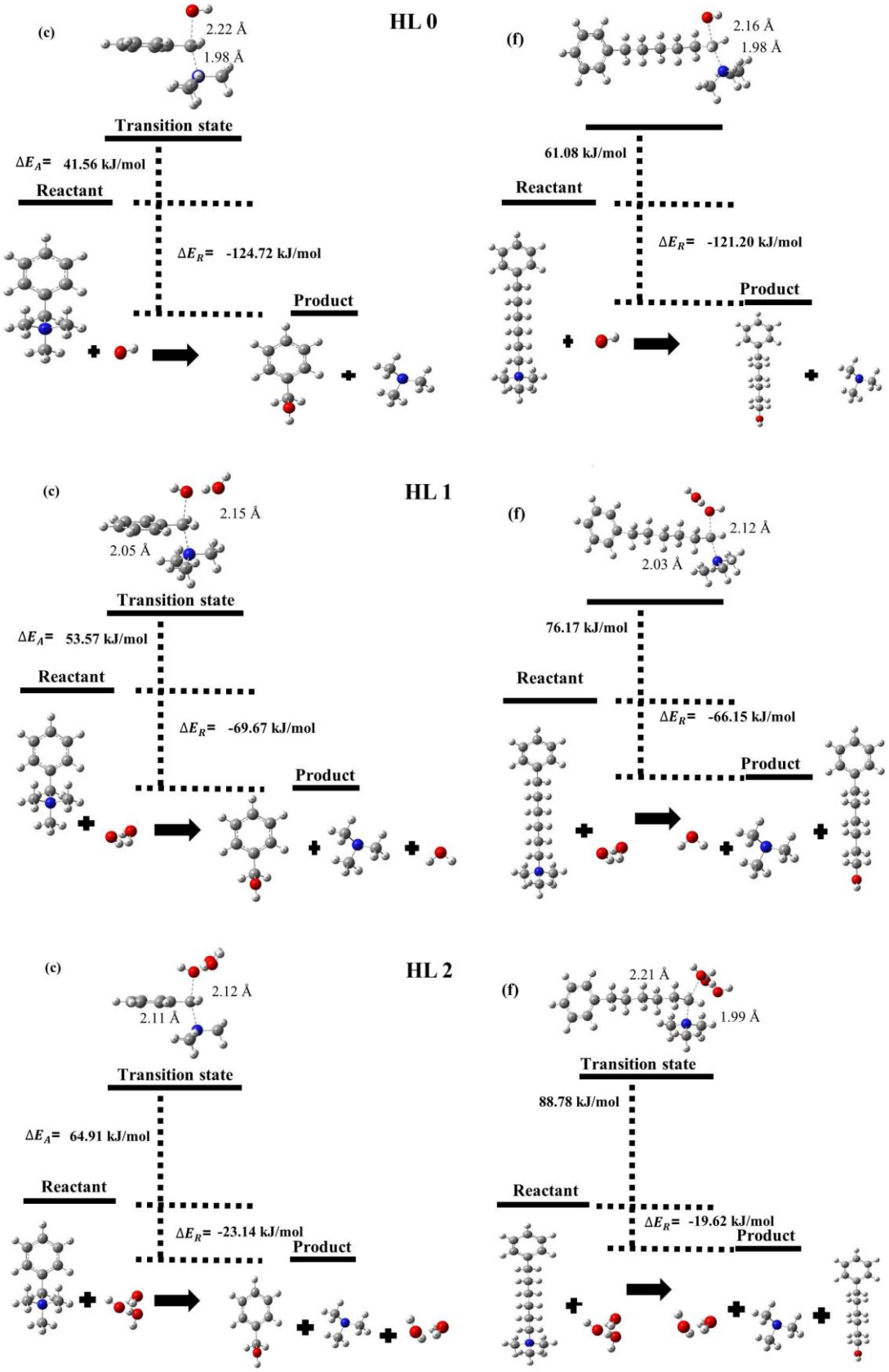

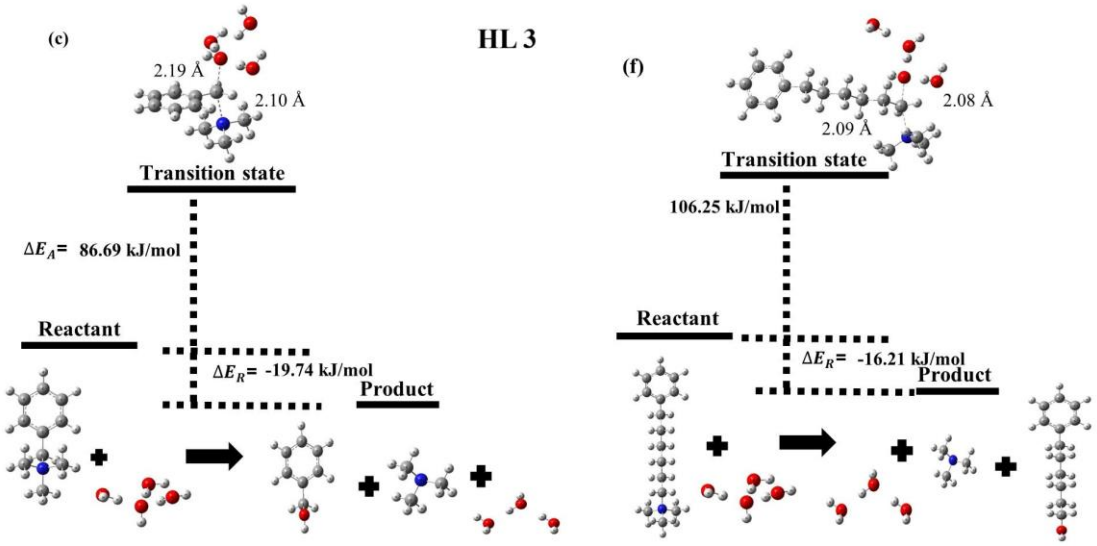

Figure 4.4: $\Delta E_{reaction}$ and $\Delta E_{activation}$ energies for S_N2 mechanism of QA (c) and (f).

These findings demonstrate that, in comparison to the vinyl carbon of QA head group (f), the vinyl carbon of QA head group (c) is significantly less chemically stable due to its extreme sensitivity to OH^- ion attack. Additionally, the activation energy barrier rises from HL 0 to 3, indicating that the stability of the QA (c) compared to (f) is greater at higher HLs. As a result, the S_N2 reaction slows down. Put otherwise, when there is no water present, the QA head group degrades very quickly through the S_N2 reaction pathway, in contrast to the situation with large HLs. In essence, at higher HLs, both QA (c) and (f) were more stable. As schematically shown in **Figure 4.4**, these results demonstrate that water molecules, which are tightly coupled to the OH^-, diminish its nucleophilicity, so "shielding" it from attacking the QA head group.

4.3.2 LUMO distribution and energy

Here, using the B3LYP DFT technique, we present the distribution of LUMO orbitals and their energy for each of the six QA head groups of the AEM. The LUMO energy of each QA head group can be used to evaluate chemical stability in alkaline environments. Essentially, because OH^- ions are strongly nucleophilic (electron rich), they might interact with the LUMOs of various QA head groups with ease. This means that the ability of LUMO orbitals to receive nucleophiles can be used to quantify the alkaline stability of QA head groups.

This implies that the difficulty of an OH^- ion assault increases with the LUMO energy of the QA head group, leading to increased stability. Stated differently, a lower LUMO energy indicates a higher probability of QA head group breakdown by OH^- ions via S_N2

mechanism. **Figure 4.5** demonstrates that for QA head groups (b), (c), (d), and (f), the benzyl group is the primary contributor to LUMOs. Furthermore, the LUMO for QA head group (a) is positioned around the pyridinium group's nitrogen atom, whereas for (e), it is situated on the DABCO nitrogen atom.

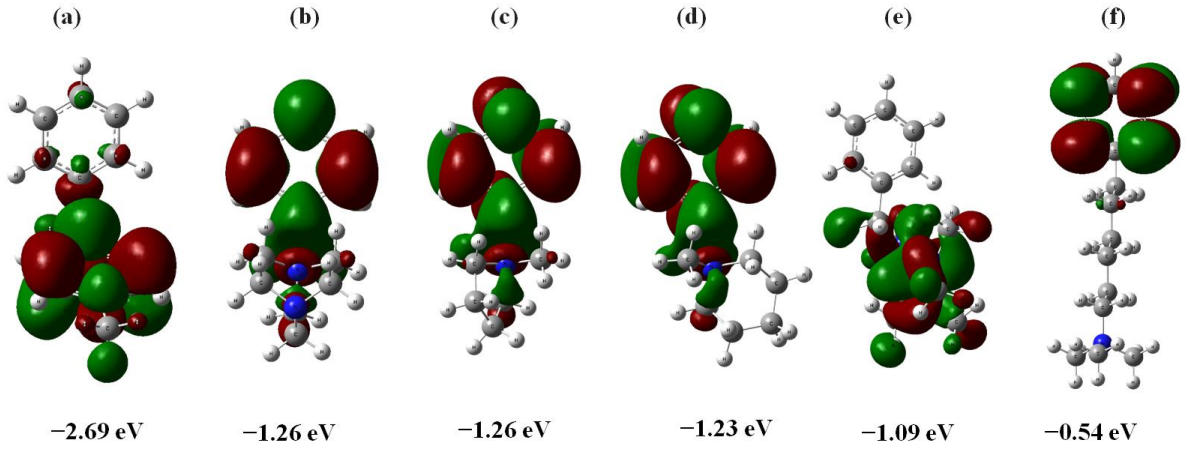

Figure 4.5: Visualization of the LUMOs' density for QA (a)–(f).

Additionally, **Figure 4.5** shows that, out of all the QA head groups examined, the TMHA head group had the highest LUMO energy (-0.548 eV), indicating that it was the most stable QA head groups among the other QA head groups investigated. The results of the LUMO energy values indicate an increasing stability trend as follows: (a) pyridium < (b) DABCO ~ (c) BTMA < (d) n-methyl piperidinium < (e) guanidium < (f) TMHA. Additionally, the alkaline stability trend in this work was validated by the experimental findings of Noh *et al.* [157, 158]. TMHA exhibited the highest alkaline stability among the sequences, similar to our findings. In particular, most of the benzyl-substituted QA head groups (f) in the presence of OH^- ions, as complexes, were observed to degrade via the S_N2 reaction, producing benzyl alcohols as the final product during GC–MS and NMR examinations. This discovery implies that the electron-withdrawing inductive effect of the aromatic ring makes the benzylic carbon vulnerable to nucleophilic attack by OH^- ions [157, 158].

4.4. Conclusions

From this study, the following conclusions can be made:

- The mechanism of chemical degradation for distinct QA head groups of AEM were investigated using DFT.

- From a methodological perspective, our work involved calculating the DFT of our developed systems to obtain optimal structures and to comprehend the molecular interaction and OH^- ion degradation mechanism response with six different QA head groups of AEM.
- Through the use of quantum chemical properties like LUMO distribution and energy, $\Delta E_{reaction}$, transition state, and $\Delta E_{activation}$ at the DFT level, this work may help understand the degradation mechanism of QA head groups of AEM.
- The following order for chemical stability was found by looking at the calculated LUMO energy values for six different QA head groups using the DFT method: (a) pyridium < (b) DABCO ~ (c) BTMA < (d) n-methyl piperidinium < (e) guanidium < (f) TMHA.
- $\Delta E_{activation}$, $\Delta G_{activation}$, $\Delta E_{reaction}$, and $\Delta G_{reaction}$ energy values were obtained for QA (c), and (f) head groups at the different HLs from 0 to 3 via transition state calculations by DFT.
- The results imply that the QA (f) head group exhibits higher chemical stability compared to QA (c) across HLs from 0 to 3.
- These DFT results were consistent with experimental findings, offering crucial insights into AEM degradation mechanism.

Chapter 5: Diffusion of hydroxide ions with several quaternary ammonium head groups of anion exchange membranes

In this chapter, conventional all-atom MD simulations were used to study the diffusion of OH^- ions within QA head groups of AEM at the atomistic level.

The work presented in this chapter was published in 2023 in the Eurasian Chemico-Technological Journal [159].

5.1. Introduction

The chemical stability of several QA head groups, including pyridinium, DABCO, BTMA, n-methyl piperidinium, guanidium, and TMHA was thoroughly studied in Chapter 4. Still, little is known about the mechanisms controlling OH^- ion transport at high pH levels, particularly at various HLs [159-162].

The use of computational modeling and simulations has become essential in examining the OH^- ion transport and chemical degradation mechanism occurring in the polymeric structure of AEMs through positively charged QA head groups. Specifically, OH^- ion diffusivity in AEM polymeric matrices, QA head group degradation mechanisms, and the impact of HLs on QA head group stability and OH^- ion diffusivity in the presence of implicit or explicit water are all investigated through the use of classical all-atom MD simulations and DFT calculations.

The purpose of this work was to clarify the shielding effect of water surrounding OH^- ions in different QA head groups using conventional all-atom MD methods. We looked into the intermolecular interactions at different HLs between OH^- ions and different QA-based head groups in AEMs.

5.2. Models and methods

5.2.1 System of interest

As shown in **Figure 5.1**, we chose to use the six distinct QA head groups of AEM as a computational model for conventional all-atom MD method. Initially, three water molecules and one molecule of the QA from **Figure 5.1** with one OH^- ion were chosen for conventional all-atom MD simulations.

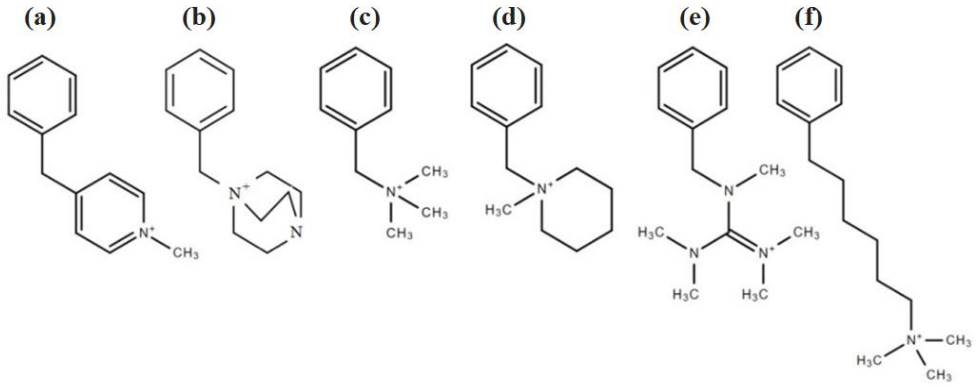

Figure 5.1 Illustration of typical segments for various QA head groups: The six QA head groups include (a) pyridinium, (b) DABCO, (c) BTMA, (d) n-methyl piperidinium, (e) guanidium, and (f) TMHA.

Using conventional all-atom MD, the novel systems were constructed with one/five QA head group molecules (c) and (f) and one/five OH^- ions as can be seen in **Table B1** (Appendix B). Additionally, 3/9/15/500 water molecules were simulated to investigate the impact of HLs and solvation on OH^- ion diffusion of AEM.

5.2.2 Conventional all-atom MD simulations

Initially, the Swiss Param tool was used to generate the optimized coordinates and force field parameters (partial charges, bonds, angles, and dihedrals) for QA head groups (**Figure 5.1**) from optimized ATB database structures [147-157]. Simultaneously, Lennard-Jones (LJ) parameters were derived from the force field CHARMM36 [147-158]. As discussed in section 3.4, the selection of the CHARMM36 force field was guided by the validation presented in Zhang et al.'s work [97]. In the presence of explicit TIP3P [160] (3/9/15/500) water molecules, each constructed system for conventional all-atom MD simulations contains a single representative segment of the characteristic QA head group with OH^- ion.

The bonded and non-bonded contributions to the potential energy of the systems in the CHARMM36 force field are included. Using the steepest descent method, initial simulation boxes were built with a 500 kJ/mol/nm maximum force constraint on each atom to reduce energy by optimizing the starting configuration at 1 bar and 298 K for 0.1 ns. The systems were first brought to equilibrium under NPT, and then NVT ensembles were run for one second at 1 bar and 298 K. Production runs for conventional all-atom MD simulations were carried out for 10 ns at 298 K, 1 bar, and with an NVT ensemble at a fixed volume once the system had reached equilibrium.

During the simulation, the LINCS constraint method was applied to every bond. Thus, for LJ and coulombic short-range interactions, a 0.5 nm cut-off was applied. In the meanwhile, Particle Mesh Ewald summation was used to compute long-range interactions. Furthermore, to maintain system pressure and temperature, a Berendsen pressure coupling and a Nose-Hoover thermostat were installed [160, 161]. It should be noted that all directions had periodic boundary conditions added. Gromacs and VMD software were implemented in this work [162].

The computationally obtained densities from classical all-atom MD simulation were calculated as 1.17 g/cm^3, 1.14 g/cm^3, and 1.10 g/cm^3 for HLs of 3, 9, and 15, respectively, aligning closely with the experimental values (1.15 g/cm^3 for HL 3, 1.12 g/cm^3 for HL 9, and 1.09 g/cm^3 for HL 15) reported in the literature [97]. Conventional all-atom MD methods were used to study the molecular interaction of the OH^- ion with six distinct QA, as shown in Appendix B of Table B1. In the end, the molecular interaction between the OH^- ion and distinct QA (a)-(f) was examined for RDF, MSD, the OH^- ion diffusion coefficient, and water cluster.

5.3. Results and discussion

The RDF, water clusters, and diffusion coefficients from MSD vs time curve are analyzed and discussed.

5.3.1 Effect of hydration levels on radial distribution functions

The RDFs profiles (**Figure 5.2**) for the nitrogen atoms of the QA head groups with the oxygen atom of OH^- ions were found in this investigation. The RDF results from conventional all-atom MD simulations, which were represented as a function of the distance between the nitrogen atoms of the six distinct QA head groups and the oxygen atom of OH^- ions, are used to assess the operation of AEM at HL 3. It was discovered that the QA head

group (a), which has OH^- ions surrounding it and a peak value of 230.39 at 2.95 Å, accounted for the strongest intermolecular interaction.

The chemical interaction of QA head group (c) with OH^- ions has the next highest peak value, 166.18 at 3.45 Å. The chemical interaction of the QA head group (f) with the OH^- ion was related to the higher peak value of 160.26 at 3.75 Å, which ranked third. The peak values of 148.98 for the QA head group (d) with OH^- ions at 3.45 Å came next. The QA head group (e) with OH^- ions has the fifth peak value, which is approximately 125.09 at 3.45 Å. The QA head group (b) containing OH^- ion has the smallest peak, with a peak value of 84.70 at 3.65 Å.

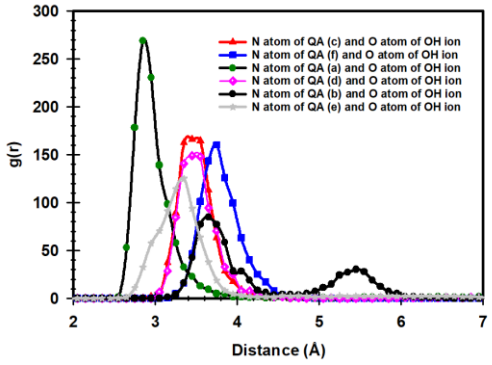

Figure 5.2: RDFs for N atom of QA with OH^- ion.

Accordingly, the following is the order of the OH^- ion's molecular contact strength with different QA head groups: The sequence (a) > (c) ≥ (f) > (d) > (e) > (b) suggests that (b) has a strong OH^- ion interaction via the nitrogen atom of the QA head group of AEM.

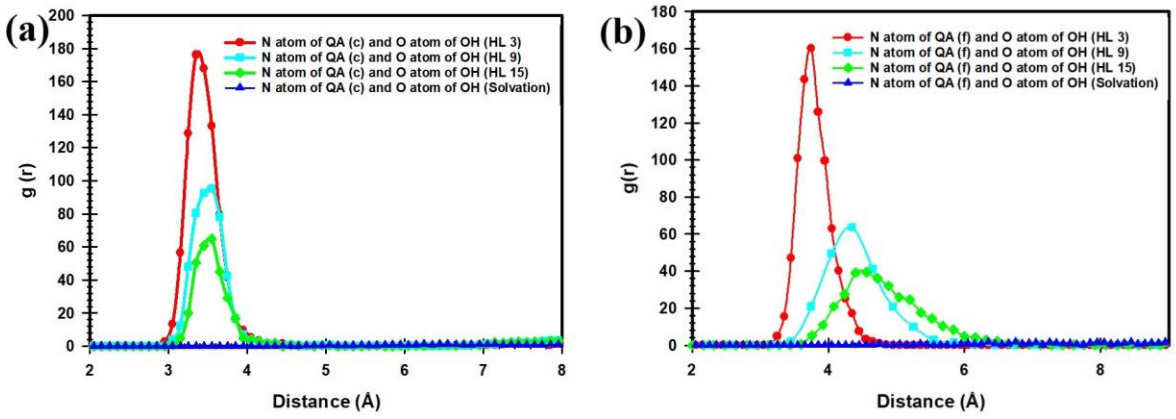

Figure 5.3: RDFs for a) N atom of QA (c) with OH^- ion, and b) N atom of QA (f) with OH^- ion at the different HLs.

Next, the RDF patterns between the OH^- ion and nitrogen atoms of QA head groups (c) and (f) at various HLs are shown in **Figures 5.3a** and **b**. As shown by **Figure 5.3a**, the oxygen of the OH^- ion near the nitrogen atom of a single QA head group (c) at the HL of 3 corresponds to the initial highest radial distribution peak value of 176.17 at 3.35 Å. Next, 95.26, at 3.55 Å, is the second-highest peak value and corresponds to HL 9. The OH^- ion with the head group QA (c) at HL 15 is more weakly bound, and 64.82 at 3.55 Å is the third highest peak value. As the HL increases, **Figure 5.3a** shows that the RDFs between the OH^- ion and the QA head group (c) become weaker. The OH^- ion interaction with QA head group (f) showed the same pattern, yielding 160.26 at 3.75 Å for HL 3, 63.66 at 4.35 Å for HL 9, and 39.33 at 4.56 Å for HL 15. **Figures 5.3a** and **b** show that there was no intermolecular contact between the OH^- ion and the nitrogen atom of the QA head group ((c) and (f)) during solvation. Because a high HL physically shields the OH^-, hydration restricts the OH^- ion's approach to the QA head group, resulting in a drop in the RDF peak.

This indicates that lower HL has higher OH^- ion interaction by nitrogen atom of QA based head group. The correlation of the nitrogen atom of QA based head group site with OH^- ion is lowered as increasing HL. Furthermore, it was observed that the RDF peaks corresponding to the OH^- ion and QA (c) and QA (f) head groups vanished in the aqueous media (solvation) stage, indicating the AEM breakdown state.

5.3.2 Effect of hydration levels on diffusion of OH^- ion

Figures 5.4 shows the MSD for OH^- ions, and H_2O at the different HLs, respectively.

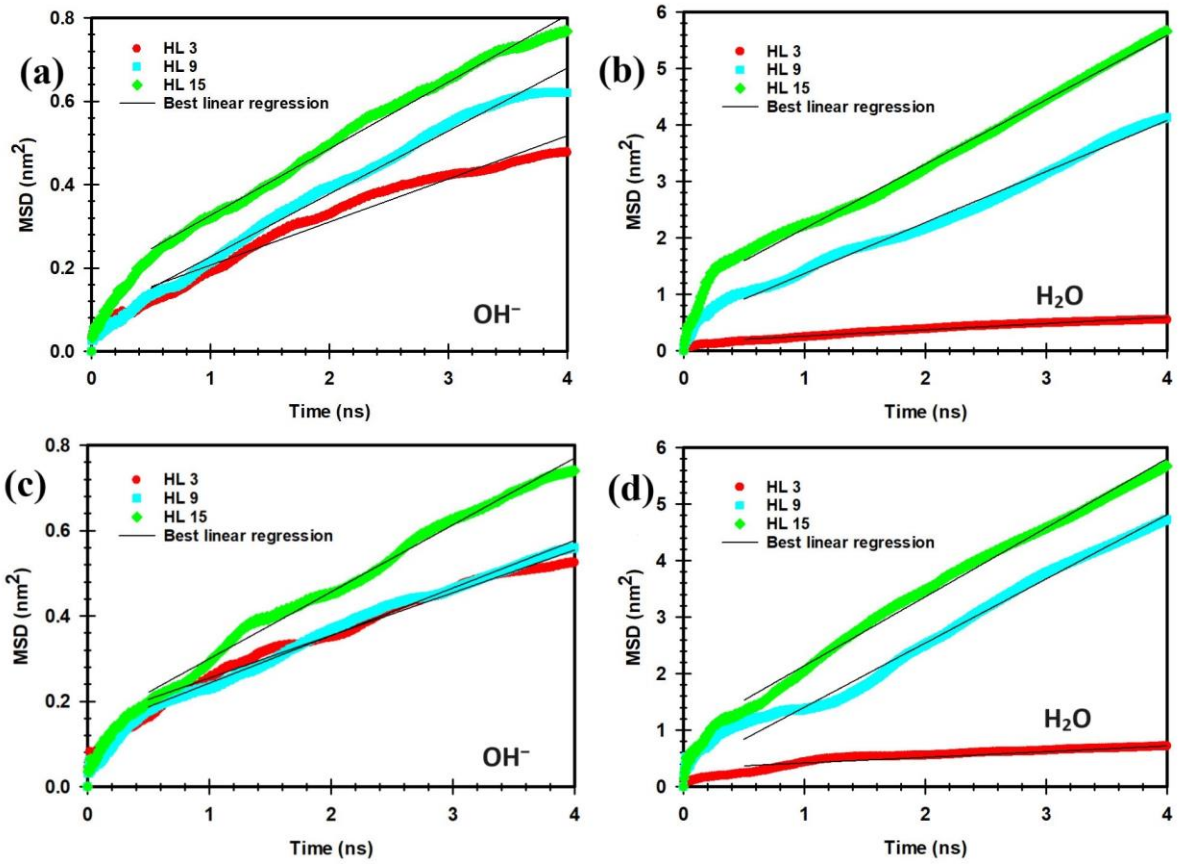

Figure 5.4: MSD plot for OH^- ions, and H_2O molecule in the presence of a), c) for QA (c), and b), d) for QA (f) at the different HLs.

As discussed in sub-subsection 3.2.3, the diffusion coefficients were calculated from the slope of the MSD curve for OH^- ions and H_2O at different HLs. To estimate the diffusion coefficient, we conducted 10 independent simulations for each of our systems to minimize statistical uncertainty, as shown in **Figures B1** to **B12** (Appendix B), which depict the complete MSD vs. time curves for both OH^- ions and water molecules. The data for the linear fitting of the MSD plot was selected based on the linear portion of the MSD plot, which corresponds to the diffusive regime. This linear region indicates a steady-state condition where the displacement of molecules is proportional to time, allowing for an accurate determination of the self-diffusion coefficient. The results of the obtained diffusion coefficients are illustrated in **Tables 5.1** and **5.2**.

Tables 5.1 and 5.2 show that from HL 3 to HL 15, the mobility of OH^- ion and H_2O molecules increased. As HLs rose in the presence of QA head group (c), the diffusion coefficients of OH^- ions and H_2O molecules increased from 0.017 to 0.027 nm^2/ns, and 0.018 to 0.19 nm^2/ns, respectively. The mobility of H_2O molecules and OH^- ion increased from HL

3 to HL 15 concerning the TMHA based head group of AEM. In the presence of QA head group (f), when HLs rose, the diffusion coefficient of OH^- ions and H_2O molecules increased from 0.016 to 0.026 nm^2/ns, and 0.018 to 0.203 nm^2/ns, respectively.

Table 5.1: Diffusion coefficients of OH^- ions across different QA structures and HLs.

D, nm^2/ns, (SE)		HL values		
		3	9	15
OH^-	QA (c)	0.017 (0.005)	0.025 (0.002)	0.027 (0.002)
	QA (f)	0.016 (0.003)	0.018 (0.002)	0.026 (0.002)

Table 5.2: Diffusion coefficients of H_2O molecules across different QA structures and HLs.

D, nm^2/ns, (SE)		HL values		
		3	9	15
H_2O	QA (c)	0.018 (0.003)	0.019 (0.003)	0.19 (0.024)
	QA (f)	0.018 (0.003)	0.189 (0.012)	0.203 (0.027)

For both QA (c) and QA (f), the mobility of the OH^- ion increased monotonically with increasing cell water content. It was noted that there was a negative link between the mobility of OH^- ions and the interaction between the OH^- ions and the nitrogen atom QA (c)/(f) based head group and a positive correlation with the HL.

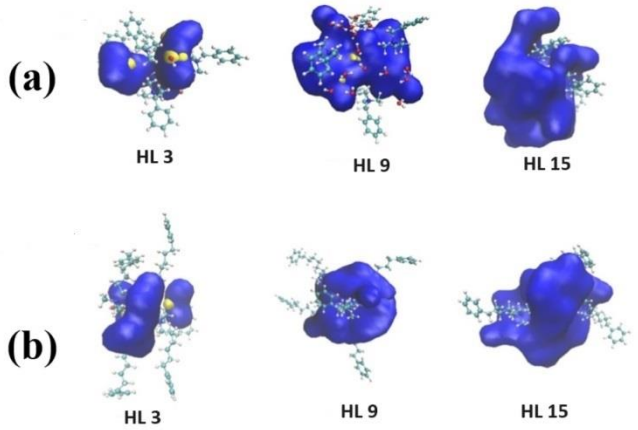

Figure 5.5: Water clusters surrounding a) QA (c) and b) QA (f) at the various HLs.

Moreover, the diffusion coefficients of OH^- ions and water molecules obtained from our MD simulations were validated against values reported in other studies [97, 105]. According to the literature, the diffusion coefficient of OH^- ions typically falls within the range of 0.016 to 0.037 nm^2/ns. Similarly, for water molecules, the diffusion coefficient has been reported to range from 0.005 to 0.18 nm^2/ns, depending on the HL from 3 to 15 [97, 105]. These values are consistent with the findings from our simulations, confirming the accuracy of our results.

A standard depiction of an AEM is shown in **Figures 5.5a** and **5.5b**. The development of interconnected water clusters expands as HLs increase, as evidenced by hydrogen bonding analysis.

5.4. Conclusions

From this study, the following conclusions can be made:

- The diffusion of OH^- ion around QA was studied by the results of the conventional all-atom MD methods at various HLs.
- QA (c) and (f) variations exhibited similar OH^- ion vehicular diffusion coefficients from MSD vs time curve at the varied HLs from 3 to 15.
- Higher water content was found to enhance OH^- ion mobility, emphasizing the importance of considering water content in QA (c) and (f) head groups.
- The underlying OH^- ion diffusion through the QA head groups of AEM is better understood via classical all-atom MD simulations, which can help develop more efficient AEM-based solutions for alkaline fuel cell applications.

Chapter 6: Chemical stability and hydroxide ion transport properties of quaternized chitosan head groups for anion exchange membranes applications

In this chapter, DFT calculations and conventional all-atom MD simulations were used to study the chemical stability and OH^- ion diffusion properties of QCS head groups within AEM at the atomistic level.

The work presented in this chapter has been published in 2024 in the journal Molecules [147].

6.1. Introduction

Notably, the extremely hazardous chloromethylation step is not required for the obtaining QCS [163-183]. Several experimental studies have been conducted on the applications of QCS in AEM. Jang *et. al* determined that the ionic conductivity of QCS-functionalized carbon nanotube composite-based AEM was 47 mS/cm at 353 K [186]. Nhung *et. al* found the ionic conductivity of the QCS/poly(vinyl benzyl chloride)/polysulfone blend was 49.6 mS/cm at 298 K and 130 mS/cm at 353 K [187]. Zhao *et. al* reported the ionic conductivity of QCS/poly(vinyl alcohol) was 25.7 mS/cm at 353 K [188]. Despite a wealth of experimental data, there aren't many computational studies that use atomistic modeling to rationalize the design of chitosan based AEMs [4]. Furthermore, our understanding of the diffusion of OH^- ions via QA-based head groups in the biopolymer is still lacking [1-5].

In this work, we investigate the chemical stability and diffusion of OH^- ions in QCS based AEMs using DFT and conventional all-atom MD methods. The computational models, DFT, and the conventional all-atom MD methods are described in depth in the ensuing sections. The chemical stability and transport mechanisms of OH^- ions are then covered, taking into account variables like the energy and distribution of the LUMO, $\Delta E_{activation}$, $\Delta G_{activation}$, $\Delta E_{reaction}$, $\Delta G_{reaction}$, and diffusion coefficients from the MSD vs. time curve. Variations in HLs, temperatures and QCS chemical structure are used in these analyses.

6.2. Models and methods

6.2.1 System of interest

As shown in **Figure 6.1**, different QCS-based monomeric structures (A-C) were designed in order to develop computational models for DFT computations and conventional all-atom MD simulations. The chemical stability of the QCS-based monomeric segment and OH^- ion diffusion were then examined using DFT calculations utilizing one QCS (A-C) based monomeric segment with one OH^- ion in the presence of implicit water as a computational model for AEM. Next, the conventional all-atom MD simulation setup was established by placing five OH^- counter ions and five QCS based monomeric segments (A-C). As shown in the Appendix C (**Table C1**), the temperature ranges were 298 K to 350 K, and the range of water molecules per OH^- ion was 15 to 75.

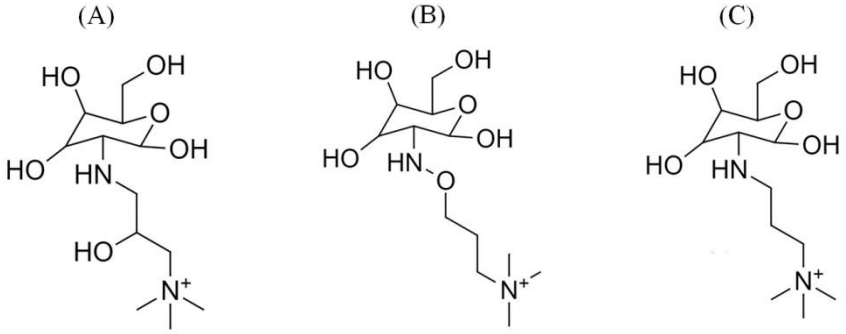

Figure 6.1: Representative structures of different QCS segments: (A) 2-hydroxy propyl trimethyl ammonium chitosan, (B) oxy propyl trimethyl ammonium chitosan, and (C) propyl trimethyl ammonium chitosan.

In this study, simulations were conducted on monomeric units of QCS to approximate the properties of the full polymer. This approach is widely used in computational chemistry [88, 96, 184, 185] to address the high computational costs associated with simulating entire polymer chains. By focusing on the QA head groups, where key chemical reactions are concentrated, this method provides critical insights into the chemical stability and degradation mechanisms within AEMs. However, while this targeted approach effectively captures localized chemical behaviors, it may not fully represent the broader dynamics of the entire polymer system. To bridge this gap, future research will explore oligomer simulations to better assess how these localized findings apply to more complex polymer structures.

6.2.2 DFT calculations

The electronic ground state geometries were optimized through the application of B3LYP DFT calculations, which also yielded information on bond length, LUMO energy, transition state, $\Delta E_{reaction}$, $\Delta G_{reaction}$, $\Delta E_{activation}$, and $\Delta G_{activation}$. As discussed in section 3.4, our choice of the B3LYP functional was influenced by the validation adopted from Dario Dekel's work [88]. The three QCS segments were optimized using DFT using the B3LYP functional in the PCM both in the presence and absence of OH^- ions [150, 151].

The transition states for the S_N2 reactions of the QCS (A), (B), and (C) at the HL 3 were optimized in implicit DMSO using the B3LYP 6-311++g(2d,p) level of theory [152-155]. The $\Delta E_{activation}$, $\Delta G_{activation}$, $\Delta E_{reaction}$, and $\Delta G_{reaction}$ were calculated using DFT calculations for the OH^- ion transition state structure, or QCS, in the implicit DMSO model at HL 3.

Moreover, HL is demonstrated by the quantity of water molecules per OH^- ion. Energies and free energies were estimated using the system shown in **Figure 6.2** (**Figure C1-C3**, Appendix C). Both electrophile and nucleophile fragments were present in the transition state, and the counterpoise correction method was used to estimate the BSSE.

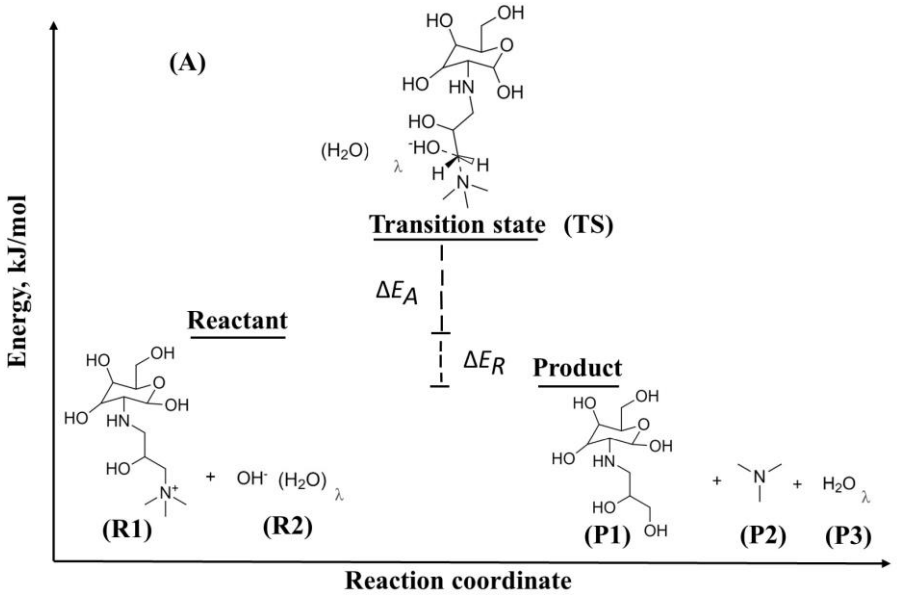

Figure 6.2: 2D representation for S_N2 mechanism for QCS (A).

Additional calculations of the second energy derivatives demonstrated that all stationary locations were absolute minima on their respective potential energy surfaces. For all DFT analysis and computations, GAUSSIAN16 and GaussView (v6.0) were used [156].

6.2.3 Conventional all-atom MD simulations

As illustrative models of AEM, a monomeric unit of QCS and an OH^- ion in water were chosen; they are shown in **Figure 6.1**. Following that, Swiss Param tool was used to generate the optimized coordinates for small segments of AEM and the optimized force field parameters [147-157]. Concurrently, the Lennard-Jones parameters were extracted from the CHARMM36 force field standard [147-158]. Because of this, the intended system's potential energy in the CHARMM36 force field consists of both bound and non-bonded contributions. The selection of the CHARMM36 force field was based on the validation provided in Zhang *et al.'s* work [97]. Moreover, the OH^- was modeled using the values given by Han *et al.* [105], and the water molecules were characterized by the TIP3P [159] model.

As can be seen in **Table C1** (Appendix C), each conventional all-atom MD simulation began with an initial configuration of QCS, OH^- ion, and water molecules at HL (3, 9, and 15) at temperatures ranging from 298 K to 350 K. The total amount of OH^- ions was selected to attain electric neutrality. The desired water uptake for the HL, which is also mentioned in the Appendix C, was used to calculate the water amount. The ratio of the total number of OH^- and water molecules to the total number of QCS was used to determine the HL.

To optimize the initial configuration at 298/330/350 K and 1 bar pressure for 0.1 ns, energy minimization was carried out using the steepest descent approach after the required system was created. The maximum force that could be applied to any atom was limited to 500 kJ/mol/nm. Both NPT and NVT equilibration were then carried out for 1 ns at 298/330/350 K and 1 bar of pressure. Following the system's equilibrium, conventional all-atom MD simulations using the NVT ensemble with a reference temperature of 298/330/350 K were run for 10 ns.

During the simulation, the LINCS constraint method was applied to every bond. Therefore, for Lennard-Jones and coulombic short-range interactions, a 1.0 nm cut-off was applied. In the meantime, fourth-order interpolation and 0.14 nm grid spacing were used in the Particle Mesh Ewald summation to calculate long-range interactions. Furthermore, temperature was maintained using the Nose-Hoover technique, and system pressure was maintained using the Berendsen pressure coupling. All directions were subjected to periodic boundary conditions [160, 161].

The densities obtained from classical all-atom MD simulations were 1.14 g/cm^3, 1.09 g/cm^3, and 1.07 g/cm^3 for HLs of 3, 9, and 15, respectively. These values closely match the

experimental densities reported in the literature [97], which were 1.15 g/cm³ for HL 3, 1.12 g/cm³ for HL 9, and 1.09 g/cm³ for HL 15. Using GROMACS software, conventional all-atom MD methods were performed. Additionally, the simulated box was visualized using VMD, after which the diffusion coefficients, MSD, and RDF were examined [145, 146, 162].

6.3. Results and discussion

6.3.1 DFT results

This section's DFT calculation results discuss the chemical stability of various QCS. Major analyses and discussions are focused on the study of quantum chemical features, such as $\Delta E_{activation}$, $\Delta G_{activation}$, $\Delta E_{reaction}$, and $\Delta G_{reaction}$ for the S_N2 degradation mechanism processes, and LUMO distribution and energies.

6.3.1.1 Degradation mechanism

As the current density of AEMFCs increases, the water molecules can be consumed more quickly and the cathode electrode dries up, and in this case OH^- can attack the QA head group.

The molecular ESP maps, illustrating the interaction between OH^- ions and various QCS head groups in the AEM, calculated using the B3LYP DFT method, are shown in Appendix C (**Figure C4**). These maps reveal that OH^- ions predominantly interact with the nitrogen atoms of the QCS head groups, stabilizing their positive charge. Structural optimizations of the different QCS head groups, along with binding energy ($\Delta E_{Binding}$) calculations, are provided in **Figure C5** and **Table C2** of Appendix C. The results suggest that the $\Delta E_{Binding}$ values for the QA head groups to OH^- ions vary significantly, highlighting the need for further investigation into the degradation mechanism.

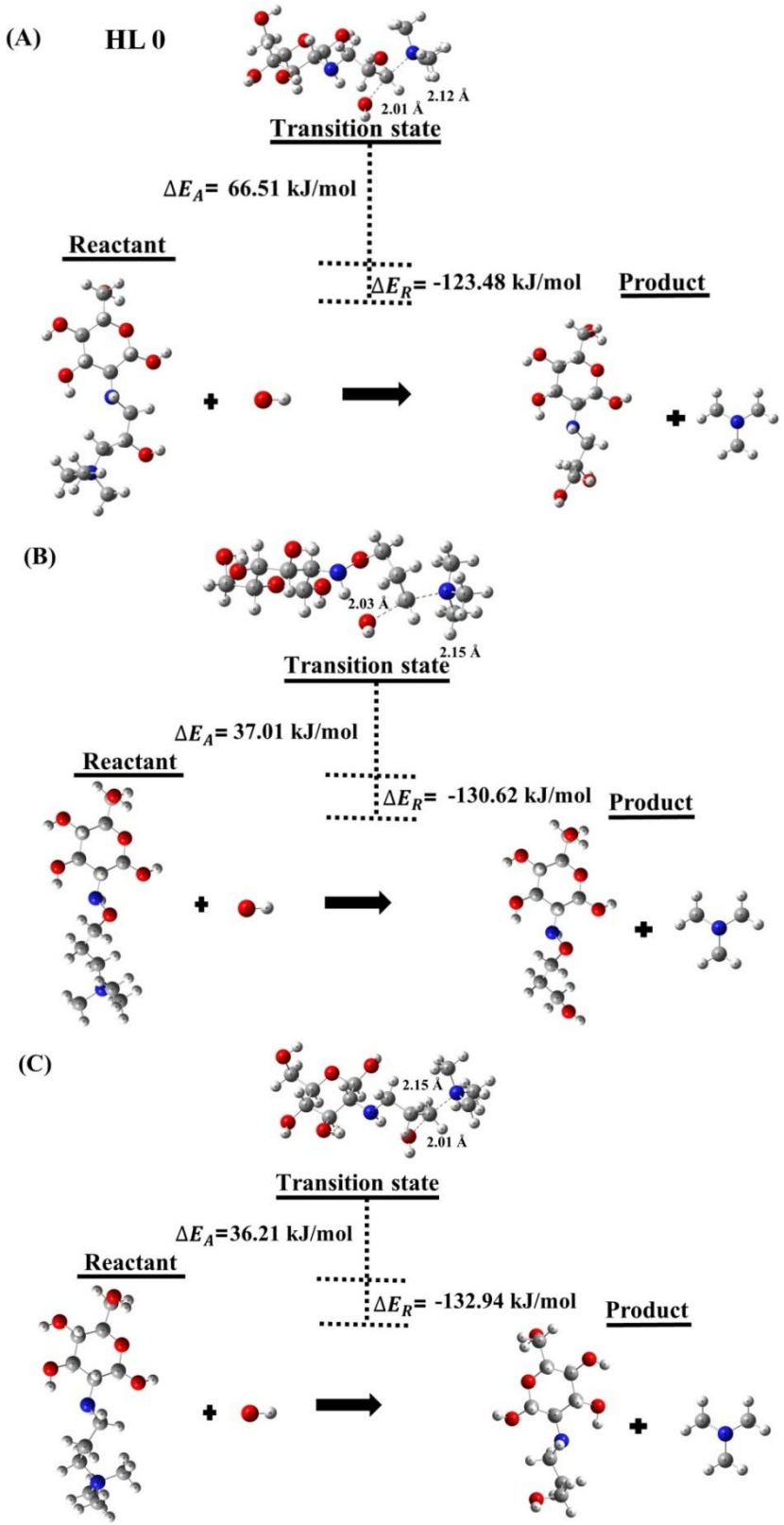

Figure 6.3: Depiction of S_N2 reactions for QCS segments (A), (B), and (C) at the HL 0.

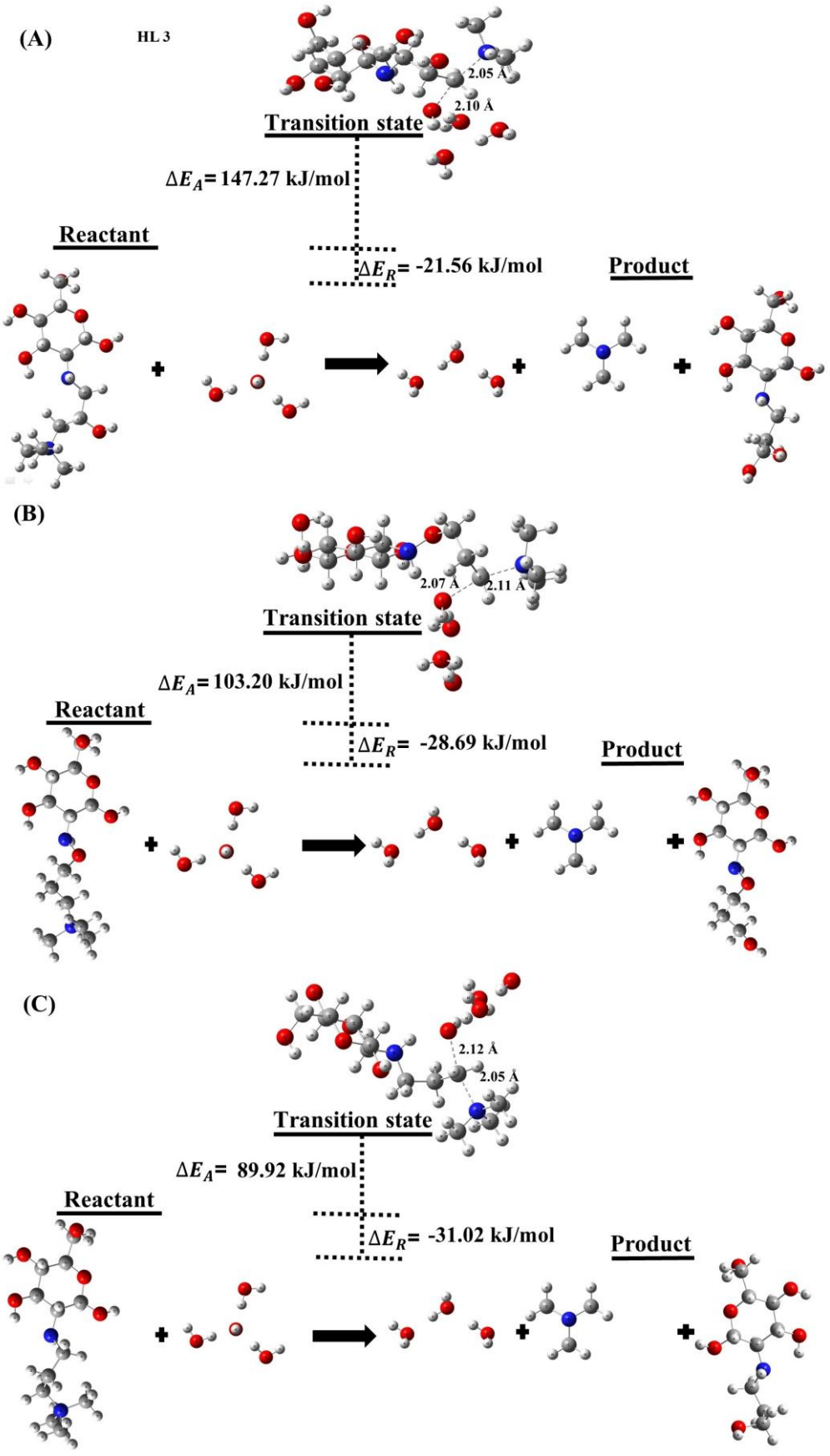

Figure 6.4: Depiction of S_N2 reactions for QCS segments (A), (B), and (C) at the HL 3.

In addition to calculating the $\Delta E_{activation}$, $\Delta G_{activation}$, $\Delta E_{reaction}$, $\Delta G_{reaction}$, and transition state for various QCS, the B3LYP DFT approach was utilized to evaluate the chemical degradation mechanism process between the OH^- ion and QCS in more detail (**Table C3-C6**, Appendix C). In this case, OH^- ions may target the QCS methylene carbon atoms, which could result in chemical degradation mechanism through the S_N2 reaction mechanism. The $\Delta E_{activation}$, $\Delta G_{activation}$, $\Delta E_{reaction}$, and $\Delta G_{reaction}$ for the S_N2 reaction of the QCS are shown in **Tables 6.1, 6.2** and **Figures 6.3, 6.4**.

Table 6.1: $\Delta E_{activation}$, $\Delta G_{activation}$, $\Delta E_{reaction}$, and $\Delta G_{reaction}$ values for our designed systems, measured at 298 K and 1 bar, HL 0. Units: kJ/mol.

QCS	$\Delta E_{reaction}$	$\Delta E_{activation}$	$\Delta G_{reaction}$	$\Delta G_{activation}$
(A)	-123.48	66.51	-226.93	106.83
(B)	-130.62	37.01	-182.39	87.07
(C)	-132.94	36.21	-156.04	76.3

Table 6.2: $\Delta E_{activation}$, $\Delta G_{activation}$, $\Delta E_{reaction}$, and $\Delta G_{reaction}$ values for our designed systems, measured at 298 K and 1 bar, HL 3. Units: kJ/mol.

QCS	$\Delta E_{reaction}$	$\Delta E_{activation}$	$\Delta G_{reaction}$	$\Delta G_{activation}$
(A)	-21.56	147.27	-159.79	163.16
(B)	-28.69	103.20	-115.25	126.16
(C)	-31.02	89.92	-88.9	122.94

A nucleophile, such as an OH^- ion, attacks the QCS in the S_N2 degradation mechanism pathway, causing bond breaking and AEM degradation mechanism. The findings have significant ramifications for AEM durability and stability (**Figures 6.3, 6.4**). When nucleophiles such OH^- ions attack AEMs with QCS (B) and QCS (C), they are more likely to break down than AEMs with QCS (A).

The activation energy for an OH^- ion nucleophilic attack on the QCS is also displayed in **Figures 6.3** and **6.4**. **Figures 6.3** and **6.4** indicate that QCS (B) and (C) of the AEM deteriorate far more quickly than QCS (A). In comparison to QCS (B) and QCS (C), the greater $\Delta E_{activation}$ for QCS (A) indicates that the quaternized head group of chitosan is more stable and resistant to OH^- ion assault. The fact that QCS (B) and (C) have lower $\Delta E_{activation}$

indicates that the quaternized head group of chitosan is less stable and more prone to degradation mechanism when attacked by OH^- ions. Similar trend is observed for $\Delta G_{activation}$.

This is in line with the findings of the $\Delta E_{reaction}$ computations, which also show that QCS (A) is more stable than QCS (B) and QCS (C). Similar trend is observed for $\Delta G_{reaction}$. The results can be utilized to direct the creation of more stable and long-lasting AEMs and offer insights into the mechanisms of AEM degradation mechanism.

Based on literature, it was observed that two isomeric forms of QCS, QCS (A) and QCS (B), were produced through the use of glycidyltrimethylammonium chloride precursors in the synthesis of QCS [189-193]. Compared to the studies of QCS (B) and QCS (C), QCS (A) has been studied in greater detail in the field of AEM applications. In our earlier work, we used DFT calculations to examine the $\Delta E_{activation}$, $\Delta G_{activation}$, $\Delta E_{reaction}$, and $\Delta G_{reaction}$ from HL 0 to 3 to study the degradation mechanism mechanism of two distinct QA head groups. When we compare our current study with our earlier research, we find that QCS has greater chemical stability than both TMHA and BTMA. It might be able to create AEMs with improved long-term stability and durability as well as increased resistance to nucleophilic attack by improving the chemical structure of the QCS [1-3, 189-193].

6.3.1.2 LUMO distribution and energy

To assess a QCS's chemical stability in alkaline circumstances, one can look at its LUMO energies. **Figure 6.5** shows that the chitosan group is the major contributor to LUMOs for various QCS. As seen in **Figure 6.5**, the computation for the other QCS of AEM reveals a tendency of increasing stability as follows: (C) < (B) < (A).

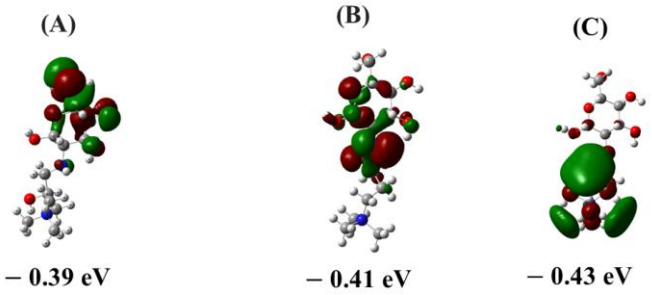

Figure 6.5: Visualization of the LUMO densities for QCS segments.

In our earlier study, we used DFT simulations to examine the LUMO distribution and energies in order to investigate the chemical stability of six distinct QA head groups. Consequently, the following sequence for chemical stability was discovered in the absolute

values of the LUMO energies for each of the six QA head groups: pyridinium < DABCO ~ BTMA < n-methyl piperidinium < guanidium < TMHA. A more thorough comparison of our new findings with our earlier findings suggests that QCS was the most stable QA head group under investigation, as evidenced by the highest LUMO energy. Better stability results as a result of the OH^- ion assault becoming more difficult as the QCS's LUMO energy rises. Additionally, the alkaline stability trend observed in this work was validated by the experimental findings of Wan *et al.* [191, 193]. Consistent with our results, QCS (A) demonstrated the highest alkaline stability among the sequences. Comparing our current study with our previous research on LUMO energy values, we find that QCS exhibits greater chemical stability than pyridinium, DABCO, BTMA, n-methyl piperidinium, guanidium, and TMHA.

6.3.2 Results from conventional all-atom MD simulation

6.3.2.1 Effect of hydration levels on radial distribution functions

Conventional all-atom MD simulations were used to calculate RDFs to investigate the interaction between the OH^- ion and the nitrogen atom of QCS. The RDF profiles (shown in **Figure 6.6**) were particularly calculated for QCS nitrogen atoms concerning OH^- ion oxygen atom at HL 3.

The RDF profiles illustrating the interaction between QCS's nitrogen atoms and OH^- ion oxygen atom at various HLs are shown in **Figure 6.6**. The first peak value in the RDF, as shown in **Figure 6.6**, is 70.43 at 4.35 Å, which represents the distance between the oxygen of the OH^- ion and the nitrogen atom of QCS (A) at HL 3. The second peak value, which corresponds to HL 9 for QCS (A), is 34.26 at 5.44 Å. A weaker binding of the OH^- ion with QCS (A) at HL 15 is indicated by the third peak value, which is 28.72 at 6.17 Å. A similar pattern was observed for the interaction of OH^- ion with QCS (B), yielding peak values of 71.08 at 4.55 Å (HL 3), 49.77 at 5.95 Å (HL 9), and 37.44 at 6.05 Å (HL 15). Similarly, for QCS (C), the peak values were 94.80 at 4.30 Å (HL 3), 54.21 at 5.9 Å (HL 9), and 41.95 at 6.10 Å.

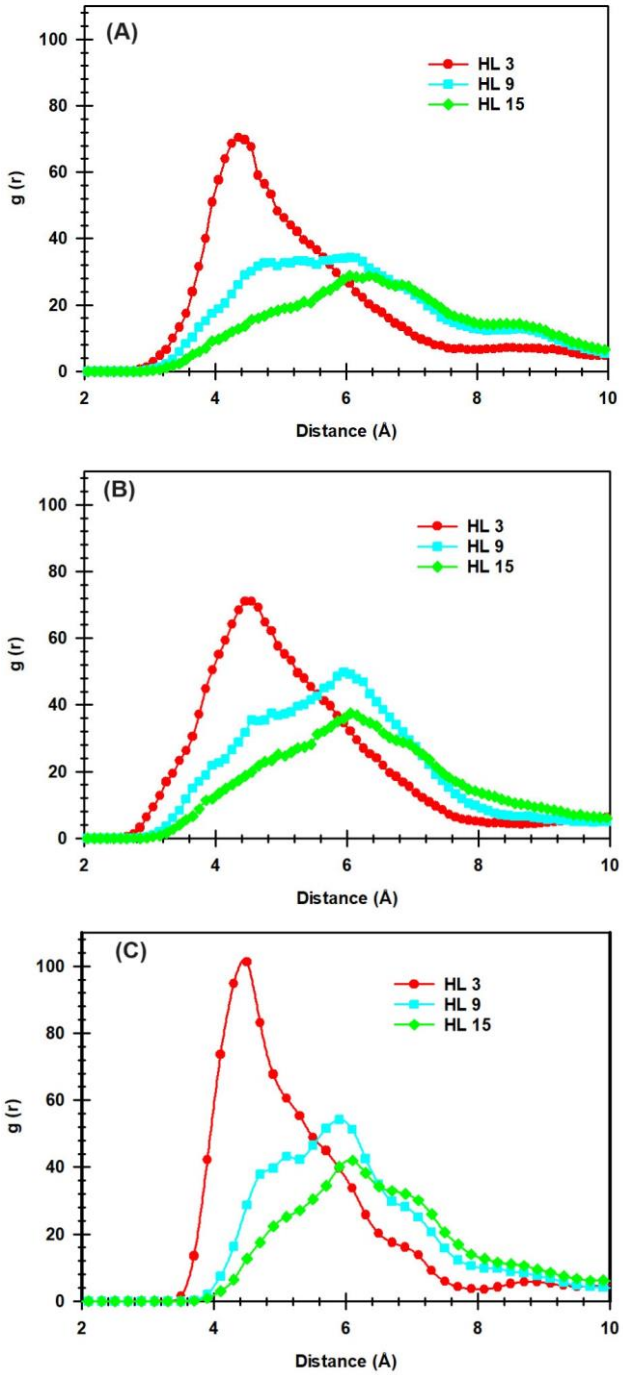

Figure 6.6: RDFs for N atom of QCS(type A, B, and C) with OH^- ion at the different HLs.

As the HL grows, the RDFs between the OH^- ion and QCS become weaker, as illustrated by the patterns shown in **Figure 6.6**. This data suggests that increased HL leads to increased hydration of AEM, which has a major effect on OH^- ions and facilitates their release from QCS's affinity. Reduced RDF peaks show that a high HL effectively protects the OH^- ion from the QCS.

6.3.2.1 Effect of hydration levels on diffusion of OH^- ion

The OH^- ion diffusion may be impacted by the molecular structure of AEM. Different molecular structures of AEM exist, including gyroid-like, bicontinuous, crossing lamella, perfect lamella, and non-regular molecular structures. As a result, **Figure 6.7** provides a typical AEM snapshot for additional molecular structural investigation. Consequently, it was discovered that the molecular structure of QCS is probably going to form a bicontinuous network at HL 3 through self-assembly with water clusters. Certain differences were found between HLs 3 and 9 to 15 structures after a more thorough comparison.

Water molecules have a significant role in the OH^- ion transport in AEM in this regard. By adding water molecules to AEM, one may increase the QCS's connection, which would increase the flow of the AEM's head groups and boost OH^- ion mobility. Regretfully, comprehensive and basic studies regarding how HL affects OH^- ion transport, how water clusters and channels form, and QCS-based AEM have not yet been published. Thus, using conventional all-atom MD simulations, the influence of HL on QCS (A, B, and C) was examined in this section based on diffusion coefficients of MSD vs. time curves.

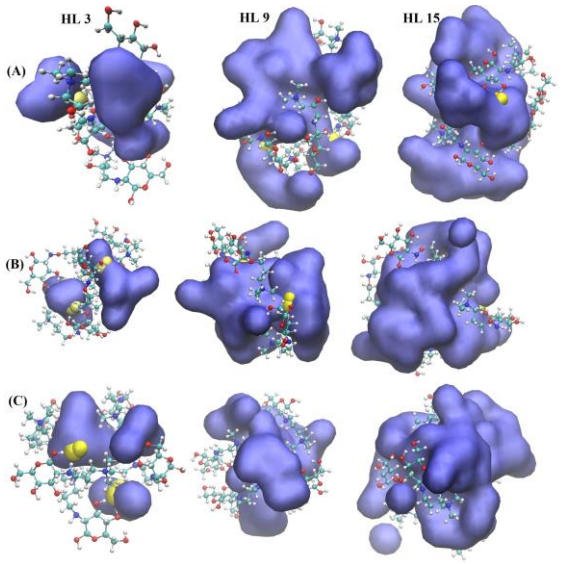

Figure 6.7: Snapshot of water clusters surrounding QCS type (A), type (B), and type (C) AEM at various HLs. Drawing method for water: Quick Surface and color scheme for water: blue; Drawing method for OH^- ion: VdW representation and color scheme for OH^- ion: yellow (oxygen), grey (hydrogen); Drawing method for QCS: CPK representation and color scheme for QCS: violet (carbon), grey (hydrogen), red (oxygen), blue (nitrogen).

To minimize statistical uncertainty, 10 independent classical all-atom MD simulations were conducted for each system. The complete MSD vs. time curves for OH^- ions and water

molecules at various HLs are shown in **Figures C6** to **C23** (Appendix C). The linear fitting of the MSD plot was based on the linear region corresponding to the diffusive regime, as illustrated in **Figure 6.8**.

Figure 6.8 shows the MSDs for H_2O and OH^- ions at different HLs. Moreover, the diffusion coefficients were obtained by calculating the slopes of the MSD curves for OH^- ions and H_2O at different HLs. The computed diffusion coefficient results are shown in **Tables 6.3** and **6.4**. In addition, the strong slope of the MSD plot characterizes the increased mobility of the AEM. Consequently, increased OH^- ion transport was caused by an increase in HLs. This indicates that the OH^- ion mobility in AEM is influenced by the amount of water present.

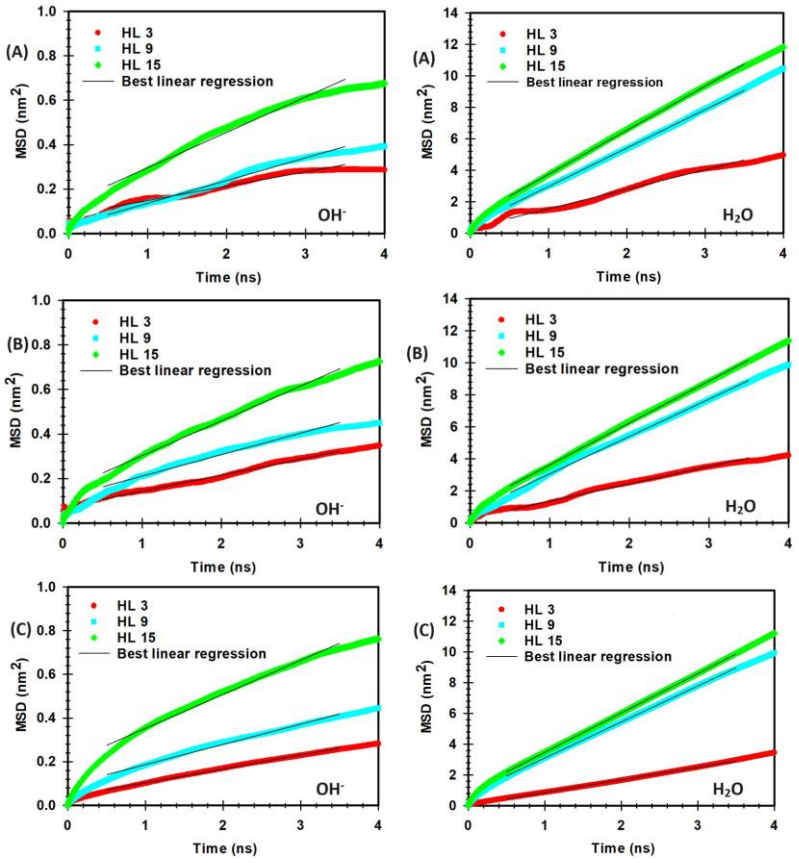

Figure 6.8: MSD vs. time curves at different HLs for OH^- ions and H_2O molecules in systems with QCS type (A), (B) and (C), respectively.

As shown in **Tables 6.3 and 6.4**, the mobility of OH^- ion and H_2O molecules increased from HL 3 to HL 15. The diffusion coefficients presented in **Table 6.3** include standard error (SE) values in parentheses, which indicate the variability and precision of the simulation data. A smaller SE reflects higher confidence in the reported diffusion coefficients, with less variation across the independent classical all-atom MD simulations.

According to the results in Table 6.3, 6.4 6.5, and 6.6, the SE for the diffusion coefficients from our MD simulations ranged between 1% and 5%. Although these values are relatively high, similar high errors have been reported previously in the literature [95-110].

In the presence of QCS type (A) of AEM, as HLs rose, the diffusion coefficients of OH^- ion and H_2O molecules increased monotonically from 0.011 to 0.027 nm^2/ns and 0.20 to 0.46 nm^2/ns, respectively. The diffusion coefficients of OH^- ions and H_2O molecules increased monotonically from HL 3 to HL 15, according to the QCS (B) of AEM. The OH^- ion and H_2O molecules' diffusion coefficients increased in the presence of QCS (B) from 0.011 to 0.026 nm^2/ns and 0.18 to 0.43 nm^2/ns, respectively. The diffusion coefficients of H_2O molecules rose from 0.13 to 0.42 nm^2/ns for QCS (C), while the diffusion coefficients of OH^- ions increased from 0.011 to 0.026 nm^2/ns.

Table 6.3: Diffusion coefficients of OH^- ions across different QCS structures and HLs.

D, nm^2/ns, (SE)		HL values		
		3	9	15
OH^-	(A)	0.011 (0.004)	0.017 (0.005)	0.027 (0.003)
	(B)	0.011 (0.003)	0.016 (0.006)	0.026 (0.002)
	(C)	0.011 (0.001)	0.015 (0.002)	0.026 (0.002)

Table 6.4: Diffusion coefficients of H_2O molecules across different QCS structures and HLs.

D, nm^2/ns, (SE)		HL values		
		3	9	15
H_2O	(A)	0.20 (0.07)	0.40 (0.09)	0.46 (0.07)
	(B)	0.18 (0.04)	0.39 (0.08)	0.43 (0.06)
	(C)	0.13 (0.03)	0.39 (0.05)	0.42 (0.05)

The results show that as HL varies from 3 to 15, the diffusion coefficients of both OH^- ions and H_2O molecules rise monotonically. Essentially, there is a positive correlation between the diffusion coefficients of both entities and the QCS HLs. Remarkably, the RDF data from Appendix C shows that the diffusivity of OH^- ions is inversely connected to the

interaction between the nitrogen atom of QCS and the OH^- ion and directly related to the HL. Moreover, QCS (A), QCS (B), and QCS (C) show comparable OH^- ion transit over various HLs. In our earlier study, we used the BTMA and TMHA head groups of AEM under various HLs to investigate the diffusion of OH^- ions. We discovered that the BTMA and TMHA head groups of the AEM displayed diffusion coefficients for the OH^- ion that were similar to those of different trimethyl ammonium head groups of chitosan after comparing the diffusion coefficients from our earlier study with those from our current investigation [1-3]. Moreover, our MD work's OH^- ion diffusion coefficients closely matched those reported in other investigations [95-110]. The diffusion coefficients of OH^- ions and water molecules obtained from our MD simulations were validated against values reported in the literature [95-110]. For OH^- ions, the diffusion coefficient typically ranges from 0.010 to 0.028 nm^2/ns, while for water molecules, it varies between 0.011 and 0.48 nm^2/ns, depending on the HL from 3 to 15, aligning well with our simulation results and confirming their accuracy [95-110].

6.3.2.2 Effect of temperatures on radial distribution functions

This section presents a detailed study of the effects of temperatures between 298 K and 350 K on the RDF between the nitrogen atom of QCS (types A, B, and C) and the oxygen atom of the OH^- ion. **Figure 6.9** shows the findings of a conventional all-atom MD simulation that served as the basis for the detailed investigation at HL 3.

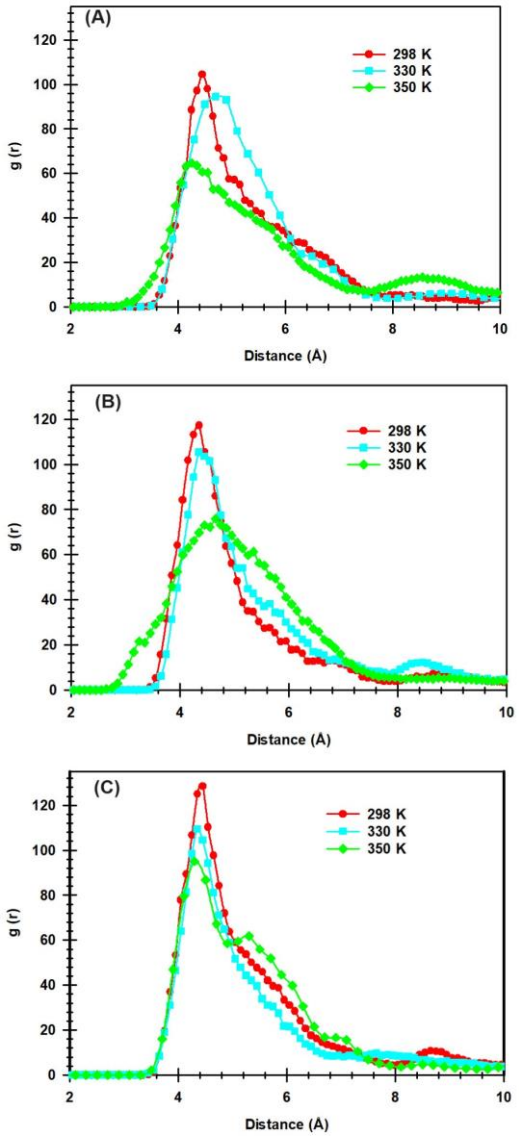

Figure 6.9: RDFs for N atom of QCS(type A, B, and C) with OH^- ion at the different temperatures.

Afterward, RDF profiles were calculated at different temperature values between 298 K and 350 K for the oxygen atom of the OH^- ion and the nitrogen atom of QCS, as shown in **Figure 6.9**. The RDFs of the OH^- ion around the nitrogen atoms of the QCS with explicit water molecules present at several temperatures are depicted in **Figure 6.9**.

Interestingly, the correlation of the OH^- ion close to the nitrogen atom of a QCS (A) at 350 K corresponds to the third-highest radial distribution peak value, which is 64.69 at about 4.35 Å. For instance, **Figure 6.9** shows that the second-highest peak value is 94.79 at 4.50 Å, or 330 K for QCS (A). At 4.45 Å for QCS (A), the first-highest peak value is 104.67, suggesting a stronger OH^- to QCS bound that was seen at 298 K. The correlation between the

OH^- ion and the N atom of QCS (B) and QCS (C) showed similar trends, with peak values for QCS (B) being 74.13 at 4.45 Å (350 K), 105.32 at 4.55 Å (330 K), and 117.19 at 4.45 Å (298 K), and for QCS (C) being 95.06 at 4.35 Å (350 K), 109.24 at 4.45 Å (330 K), and 128.68 at 4.55 Å (298 K). This finding suggests that a larger interaction between the OH^- ion and the QCS occurs at lower temperatures in AEM.

6.3.2.2 Effect of temperatures on diffusion of OH^- ion

For additional molecular structural analysis, **Figure 6.10** shows a typical snapshot of an AEM with QCS (CPK representation), OH^- ion (VDM representation), and water molecules (Quick Surface representation). Consequently, it was discovered that the molecular structure of QCS is probably going to form a bicontinuous network through self-assembly at 298 K - 350 K using water clusters.

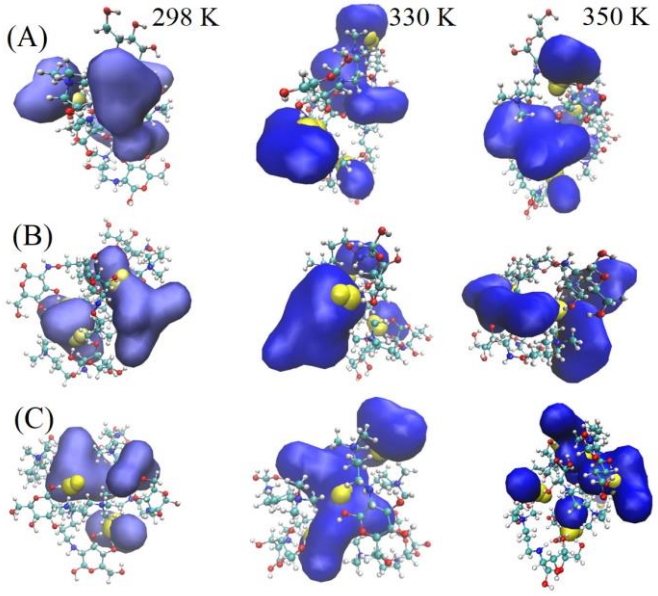

Figure 6.10: Snapshot of water clusters surrounding QCS type (A), type (B), and type (C) AEM at various temperatures. Drawing method for water: Quick Surface and color scheme for water: blue; Drawing method for OH^- ion: VdW representation and color scheme for OH− ion: yellow (oxygen), grey (hydrogen); Drawing method for QCS: CPK representation and color scheme for QCS: violet (carbon), grey (hydrogen), red (oxygen), blue (nitrogen).

It was discovered from the literature that variations in temperature could affect the OH^- ion diffusion for different chemical configurations in the QCS of AEM. Therefore, to investigate the OH^- ion diffusion for different chemical structures of QCS of AEM, temperature ranges spanning from 298 K to 350 K were investigated. The conventional all-

atom MD simulation results presented in this part address the temperature-dependent movement of OH^- ions via QCS (A), (B), and (C). This section presents the results of the calculation of diffusion coefficients from MSD versus time curves using the conventional all-atom MD simulations.

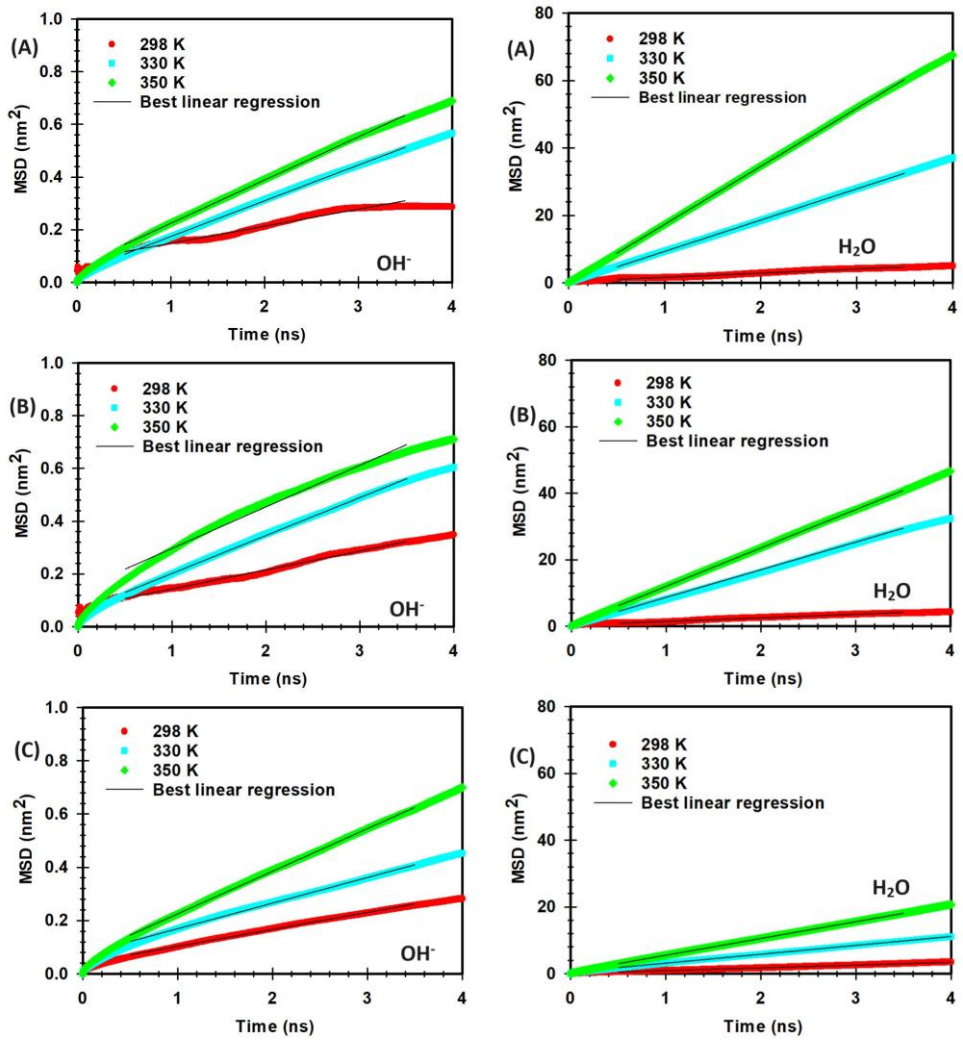

Figure 6.11: MSD vs. time curves at different temperature values for OH^- ions, and H_2O in systems with QCS type (A), (B) and (C), respectively.

To reduce statistical uncertainty, 10 independent classical all-atom MD simulations were performed for each system. **Figures C24** to **C41** (Appendix C) show the complete MSD vs. time curves for OH^- ions and water molecules at different temperatures, with the linear fitting based on the diffusive regime, as depicted in **Figure 6.11**.

The MSD for OH^- ions and H_2O at the various QCS structures for AEM at the various temperatures are displayed in **Figure 6.11**, respectively. Additionally, the diffusion

coefficients were computed using the slope of the H_2O and OH^- ion MSD curves for the various QCS structures and temperatures. **Tables 6.5** and **6.6** present the diffusion coefficient results that were obtained. According to **Tables 6.5** and **6.6**, the mobility of the H_2O and OH^- ions increased from 298 K to 350 K at the various QCS structures for different temperature ranges.

The temperature-dependent diffusion coefficients of the OH^- ion and H_2O molecules rose from 0.20 to 2.86 nm^2/ns and from 0.011 to 0.027 nm^2/ns, respectively, when the QCS (A) of AEM was present. Then, when the temperature increased, the presence of QCS (B) increased the diffusion coefficients of the H_2O and OH^- ion molecules from 0.18 to 1.92 nm^2/ns and 0.011 to 0.026 nm^2/ns, respectively. Furthermore, in the presence of QCS (C), the diffusion coefficients of the H_2O and OH^- ion molecules increased as temperatures rose, rising from 0.13 to 0.83 nm^2/ns and 0.011 to 0.026 nm^2/ns, respectively. It is noteworthy that there was a correlation between temperature and the mobility of OH^- ions in this context. High temperatures increased the kinetic energy of molecules, and thus the OH^- ions moved a further distance. The diffusion coefficients of OH^- ions and water molecules obtained from our MD simulations at different temperatures were validated against values reported in the literature [34-37, 97, 105]. For OH^- ions, the diffusion coefficient typically ranges from 0.011 to 0.028 nm^2/ns, while for water molecules, it varies between 0.012 and 2.96 nm^2/ns, depending on temperatures ranging from 298 to 350 K [34-37, 97, 105]. These values align well with our simulation results, confirming their accuracy [34-37, 97, 105].

Table 6.5: Diffusion coefficients of OH^- ions across various QCS structures at different temperatures.

D, nm^2/ns, (SE)		Temperature values (K)		
		298	330	350
OH^-	(A)	0.011 (0.004)	0.023 (0.003)	0.027 (0.003)
	(B)	0.011 (0.003)	0.023 (0.003)	0.026 (0.003)
	(C)	0.011 (0.001)	0.016 (0.002)	0.026 (0.003)

Table 6.6: Diffusion coefficients of H_2O molecules across various QCS structures at different temperatures.

D, nm^2/ns, (SE)		Temperature values (K)		
		298	330	350
H_2O	(A)	0.20 (0.07)	1.54 (0.04)	2.86 (0.25)
	(B)	0.18 (0.04)	1.38 (0.06)	1.92 (0.20)
	(C)	0.13 (0.03)	0.44 (0.05)	0.84 (0.09)

Tables 6.5 and **6.6** provide examples of the diffusion coefficients of OH^- ions and water molecules, whose movement is crucial to the use of an AEM in alkaline fuel cells. It is clear that for different QCS at different HLs and temperatures, the diffusion of water molecules is greater than that of OH^- ions. Furthermore, we investigate the OH^- ion vehicle transport by different trimethylammonium head groups of chitosan, and our non-reactive all-atom MD simulation does not exhibit the Grotthuss mechanism, which is caused by interactions between OH^- ions and water molecules. According to the literature, it has been shown that the contribution of vehicular diffusion to the diffusion of OH^- ions is lower compared to the Grotthuss mechanism in bulk water [34-37]. Simulation studies incorporating the Grotthuss mechanism using ab initio MD were reported in the next chapter.

While we acknowledge that QCS (A) has been extensively explored in the context of AEM applications, with numerous studies available [185-187], it is important to emphasize that there is currently no direct experimental evidence to definitively establish the superiority of QCS (A) over the other variants (QCS B and QCS C [188]). Our research primarily focused on theoretical modeling and computational simulations. However, we used DFT, and conventional all-atom MD methods to investigate the chemical stability and diffusion of OH^- ion via distinct QA head groups in our earlier chapters. Consequently, the following sequence for chemical stability was discovered in the absolute values of the LUMO energies for each of the six QA head groups: pyridinium < DABCO ~ BTMA < n-methyl piperidinium < guanidium < TMHA. A more thorough comparison of our new findings with our earlier findings suggests that QCS was the most stable QA head group under investigation, as evidenced by the highest LUMO energy. In addition, QCS has a higher activation energy compared to QA head groups from our previous chapters. Moreover, QCS head groups

yielded compatible OH^- ion diffusion compared to QA head groups from our previous chapters.

6.4. Conclusions

From this study, the following conclusions can be made:

- Both DFT calculations and conventional all-atom MD simulations have provided insights into the chemical degradation and diffusion mechanisms of OH^- ions in QCS-based AEMs.
- The optimized structures of DFT calculations yielded LUMO energy results that show an increasing trend of stability, as follows: (A) 2-hydroxy propyl trimethyl ammonium chitosan < (B) oxy propyl trimethyl ammonium chitosan < (C) protonated chitosan.
- Values for $\Delta E_{activation,}$ $\Delta G_{activation}$, $\Delta G_{reaction}$ and $\Delta E_{reaction}$ were found for different trimethylammonium head groups of chitosan in the presence of OH^- ion within HL 0 and HL 3, after predicting the transition state using DFT calculations.
- The DFT results suggest that the QCS (A) head group exhibits higher chemical stability compared to QCS (B) and QCS (C) at different HLs from 0 to 3.
- From conventional all-atom MD simulations, the diffusion coefficients, as discerned from MSD vs time plots, showed analogous vehicular diffusion behavior of OH^- ion in QCS (A), QCS (B), and QCS (C) at different HLs and temperatures.
- Furthermore, the vehicular diffusion of OH^- ion for various trimethyl ammonium head groups of chitosan increased monotonically with an increase in HL from 3 to 15 and a temperature rise from 298 K to 350 K.
- The findings underscore the significance of choosing the right QCS structures with the appropriate HLs and temperatures to achieve optimal chemical stability and OH^- ion diffusion properties.
- This molecular modeling work on head groups-based AEMs offers insights into the field of advanced electrolytes and underscores the value of computational modeling and simulations to gain insights into the properties of AEMs.

Chapter 7: Chemical stability and hydroxide ion transport properties of deep eutectic solvent supported quaternized chitosan head groups for anion exchange membranes applications

In this chapter, DFT calculation, and ab initio MD simulations were used to study the chemical stability and OH^- ion diffusion of DES supported QCS head groups within AEM at the atomistic level at different HLs, and temperatures.

The work presented in this chapter is being prepared for submission to a Q1/Q2 journal.

7.1. Introduction

Implementation of DESs to the QA head group is a viable way to enhance their characteristics and perhaps boost AEM performance. On the other hand, not much is known about the OH^- ion diffusion pathways and the degradation mechanism of QA head groups in AEM supported by DES. The goal of this work is to build highly performance QA head groups-based AEM that are supported by DESs, with an emphasis on enhanced OH^- ion diffusion and chemical stability. Ab initio MD simulation techniques are used to accomplish this. DESs are Lewis or Brønsted acid and base eutectic mixes that contain a variety of cationic and anionic species. They are promising solvents for large-scale applications because they have low vapor pressure, biodegradability, non-toxicity, and non-flammability [194-196].

The low melting point of DESs is a crucial feature that can be adjusted to fit particular applications. As a result, our understanding of the chemical mechanism underlying the diffusion of OH^- ions via QCS head groups in the presence and absence of DESs is still lacking [195-199]. To investigate OH^- ion diffusion via QA head groups of AEMs, computational modeling, and simulations have become indispensable techniques. Although OH^- ion diffusion and chemical stability of several QA in AEM have been reported in our

earlier reviews and studies, a comprehensive computational modeling analysis of DES-supported QCS head group of AEMs is noticeably lacking.

To bridge this gap, we performed ab initio MD methods to evaluate the OH^- ion diffusion mechanism and chemical stability of the DES-supported QCS. The subsequent sections offer a comprehensive overview of our computational models, DFT, and ab initio MD techniques and results regarding the chemical stability and OH^- ion diffusion for DES supported QCS at different temperatures, and HLs.

7.2. Models and methods

7.2.1 System of interest

To build computer models of DESs, the structure of choline chloride with ethylene glycol-based DESs was designed in a 1:2 ratio (**Figure 7.1**). In addition, water molecules, OH^- ions, and QCS were added to the DES as a theoretical model to investigate the OH^- ion diffusion and chemical stability of QCS using ab initio MD techniques (**Figure 7.1**).

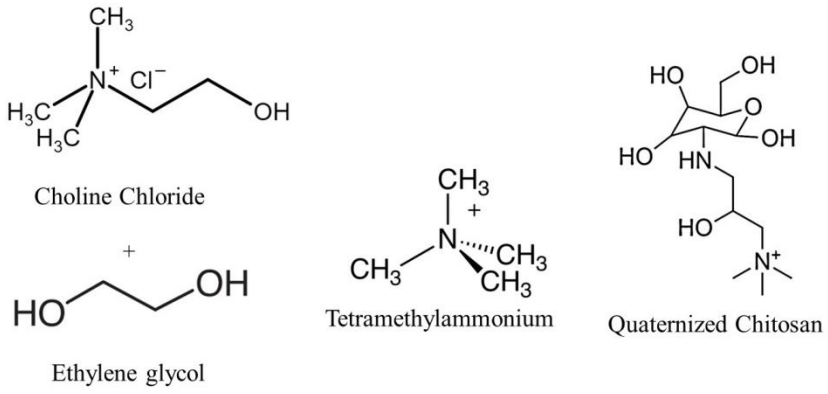

Figure 7.1: Structure of DES and AEM components including choline chloride with ethylene glycol, tetramethylammonium-based head group, and 2-hydroxy propyl trimethylammonium chitosan head group.

To investigate the chemical stability of tetramethylammonium, it was first decided to use ab initio MD simulations to study the AEM segment with OH^- ions in the presence of water and DES components. This was done using tetramethylammonium-based head groups as a computational model for DES-supported AEM, as illustrated in **Figure 7.1**.

Then, as seen in **Figure 7.1**, QCS head group was created in the presence of DES components, water molecules, and OH^- ions to investigate the QA-based chitosan head

group's chemical stability and the OH^- ions diffusion processes using ab initio MD simulations.

7.2.2 DFT calculations

The electronic ground state geometries were optimized by DFT calculations. The positively charged tetramethylammonium head group of the AEM interacted with the OH^- ions in the aqueous phase through both covalent and noncovalent interactions. The tetramethylammonium segment was optimized using DFT with the B3LYP functional in the PCM in both the presence and absence of OH^- ions [150, 151]. As discussed in section 3.4, our choice of the B3LYP functional was influenced by the validation adopted from Dario Dekel's work [88].

The transition states for the YF and S_N2 degradation mechanism reactions of the tetramethylammonium head group in the presence of OH^- ions were optimized in implicit DMSO using the B3LYP 6-311++g(2d,p) DFT level of theory to take into account the effects of explicitly hydrated water molecules [152-155]. DFT calculations for the transition state structure of OH^- ions, tetramethylammonium, in the implicit DMSO model, were used to calculate $\Delta E_{activation}$, $\Delta G_{activation}$, $\Delta E_{reaction}$, and $\Delta G_{reaction}$ for the YF and S_N2 degradation mechanism reaction. Moreover, HL is demonstrated by the quantity of water molecules per OH^- ion.

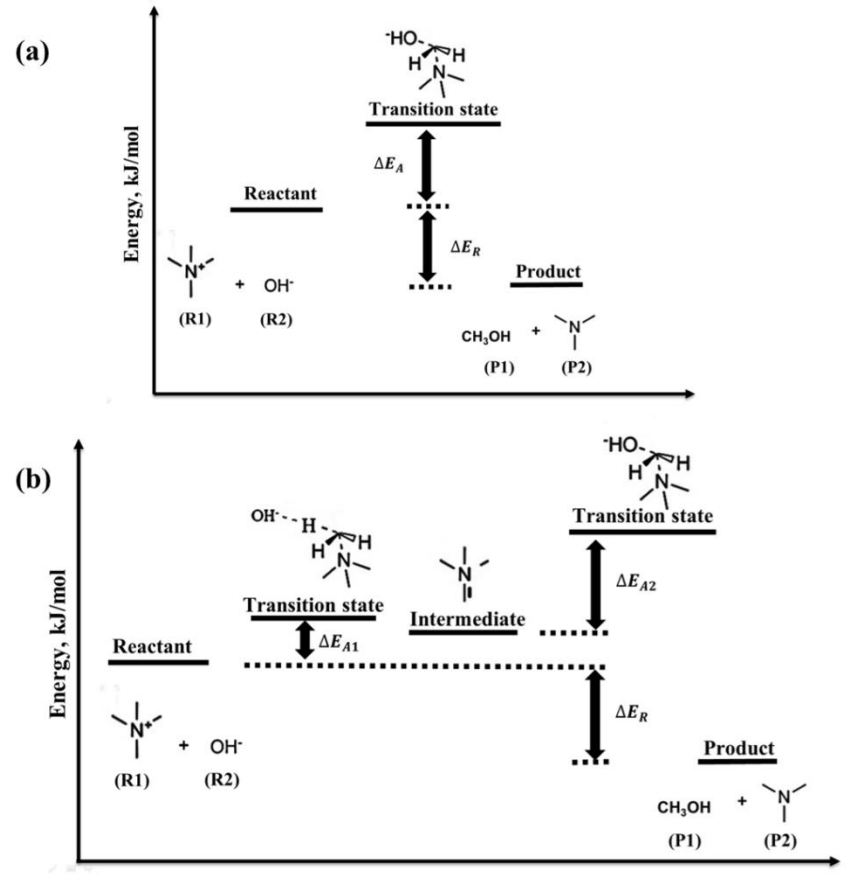

Figure 7.2: Illustration of the representative segment of tetramethylammonium head group for the (a) YF and (b) S_N2 degradation mechanism reaction.

Here, the systems shown in **Figure 7.2** were utilized to evaluate the $\Delta E_{reaction}$ and $\Delta E_{activation}$. In ylide formation, the hydroxide ion attacks the hydrogen atom of the tetramethylammonium head group (**Figure 7.2a**), while in the nucleophilic substitution mechanism, the hydroxide ion attacks the carbon atom of the tetramethylammonium head group (**Figure 7.2b**). Both electrophile and nucleophile fragments were present in the transition state, and the counterpoise correction method was used to estimate the BSSE.

All stationary locations were proved to be absolute minima on their respective potential energy surfaces by further computations of the second energy derivatives. The GaussView (v6.0) program and GAUSSIAN16 were adopted for all DFT analysis and calculations [156].

7.2.3 Ab initio MD simulation

Representative models of AEM, including a tetramethylammonium-based head group, QA-based chitosan head group, OH^- ion, and water, were used in both the absence and presence of DES, as depicted in **Figure 7.1**. As indicated in **Table D1** of Appendix D, the

QA-based head group, OH^- ion, and water molecules at an HL ranging from 1 to 5 comprised the initial configuration of each ab initio MD simulation. Energy minimization was carried out by building a cubic box with edges of 1.2 Å to optimize the initial configuration under circumstances ranging from 298 to 350 K, 1 bar pressure, and both NVE and NPT ensembles for 5-10 ps after the first simulation box for the intended system was created. Using an NVT ensemble, ab initio MD simulations were run for 50 ps after the system attained equilibrium, using a reference temperature of 298/320/350 K.

Atomic forces were computed using DFT calculations with the BLYP functional. Kohn-Sham orbitals were represented using a combination of hybrid Gaussian and plane-wave basis functions. Our choice of the BLYP functional was influenced by the methodology outlined in Zelovich et al.'s work [34]. These parameters were selected based on validations available in the literature [34-37]. This approach, known as the hybrid GPW scheme, was specifically developed for ab initio MD simulations. The key advantage of the GPW method lies in its ability to construct the Kohn-Sham matrix [200-203].

In this study, pseudopotentials of the GTH type were used, initially designed for the local density approximation and adjusted for various density functionals employed. To enhance computational efficiency, elements of the Kohn-Sham and overlap matrix smaller than 10^{-10} were disregarded, and a density grid of 400 Ry was employed [204-206]. The Grimme D3 approximation was incorporated to account for dispersion forces and a stringent convergence criterion for the electronic gradient (SCF) of around 10^{-6} was applied. Furthermore, the GLE method was implemented to maintain temperature, as described in [37-39]. Periodic boundary conditions were applied in all directions. The densities obtained from classical all-atom MD simulations were 1.19 g/cm³, 1.17 g/cm³, and 1.15 g/cm³ for HLs of 1, 3, and 5, respectively. These values closely match the experimental densities reported in the literature [34-37], which were 1.18 g/cm³ for HL 1, 1.16 g/cm³ for HL 3, and 1.10 g/cm³ for HL 5. Ab initio MD simulations were conducted using the CP2K software. Furthermore, VMD was employed to visualize the simulated box, after which the RDF, bond distances, and diffusion coefficients (from the MSD vs. time curve) were analyzed.

7.3. Results and discussion

7.3.1 DFT results

Basically, the OH^- ions, which are not solvated by water molecules, become aggressive, leading to the degradation of the tetramethylammonium head groups of AEMs. This implies that water molecules, when solvated around the OH^- ion, reduce its nucleophilicity and subsequently its ability to degrade the tetramethylammonium head group.

In this study, we employed the B3LYP DFT method to explore the chemical degradation reactions between OH^- ions and the tetramethylammonium head group (**Tables D2-D5**, Appendix D). The analysis primarily focused on evaluating the $\Delta E_{reaction}$, $\Delta G_{reaction}$, $\Delta E_{activation}$, and $\Delta G_{activation}$ for these reactions in both the absence and presence of DES (**Table 7.1**, **Figures 7.3**, and **Figure 7.4**). The findings provide crucial insights into the degradation mechanisms of tetramethylammonium-based AEMs in alkaline environments.

Table 7.1: $\Delta E_{reaction}$, $\Delta G_{reaction}$, $\Delta E_{activation}$, and $\Delta G_{activation}$ values for our designed systems, in the absence and presence of DES. Unit kJ/mol.

	S_N2		YF (step 1)		YF (step 2)	
	Without DES	With DES	Without DES	With DES	Without DES	With DES
$\Delta E_{reaction}$	-105.47	-68.98	16.95	27.66	-135.21	-96.64
$\Delta E_{activation}$	48.18	54.62	18.02	27.64	31.02	39.97
$\Delta G_{reaction}$	-148.70	-81.29	26.81	36.73	-175.52	-118.02
$\Delta G_{activation}$	64.00	100.43	36.63	56.85	37.19	63.69

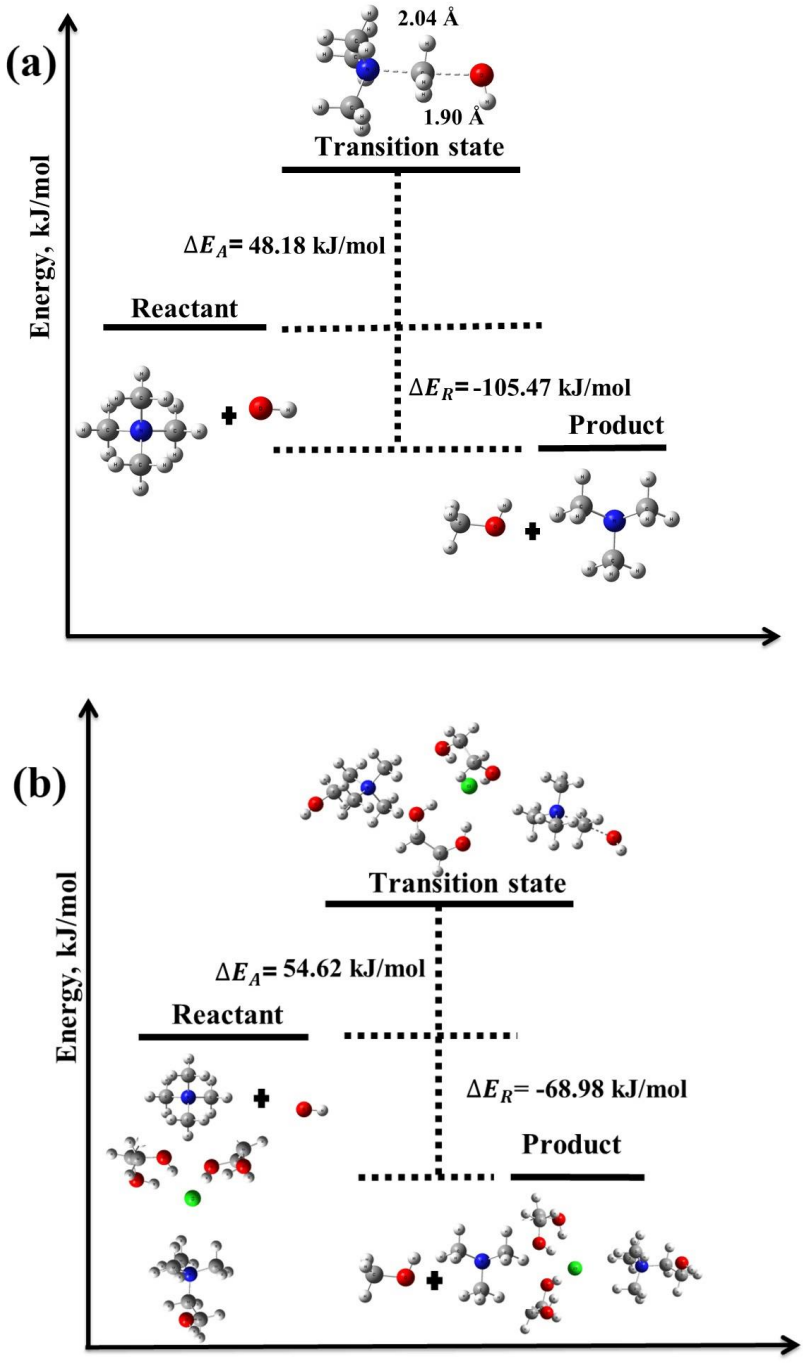

Figure 7.3: Depiction of the S_N2 degradation mechanism for tetramethylammonium head group segments in the (a) absence and (b) presence of DES.

These results align with previous research by Chempath *et al.* [89, 90], which identified the S_N2 and YF mechanisms as key degradation pathways for tetramethylammonium in the presence of OH^- ions (**Table 7.1**, **Figures 7.3**, and **Figure 7.4**). The lower activation energy barriers observed for the YF mechanism, especially in the second step, suggest that this pathway may dominate in the absence of DES. When the

tetramethylammonium head group is supported by DES, a notable increase in activation energy barriers is observed for both the S_N2 and YF mechanisms (**Table 7.1**, **Figures 7.3**, and **Figure 7.4**).

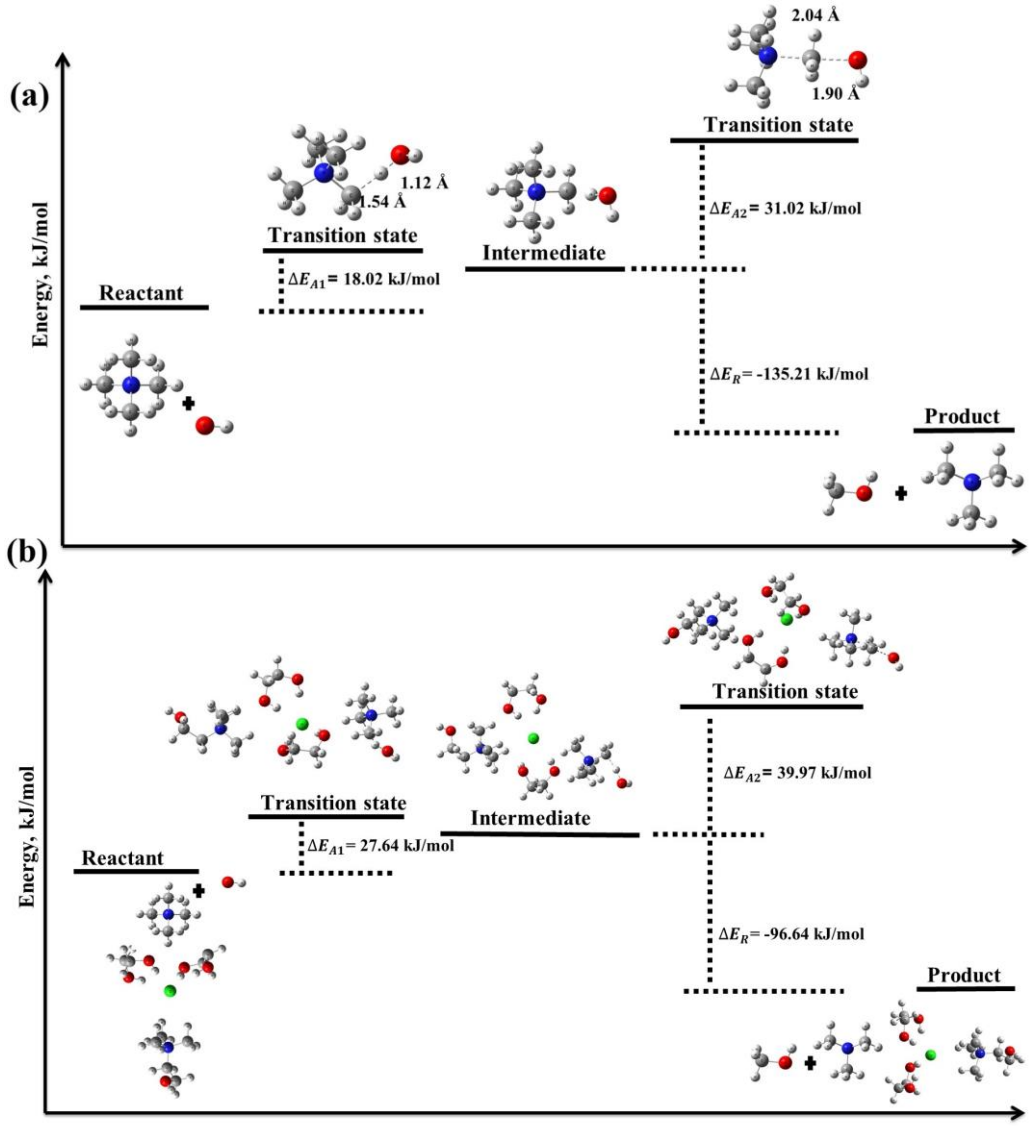

Figure 7.4: Depiction of the YF degradation mechanism for tetramethylammonium head group segments in the (a) absence and (b) presence of DES.

The enhancement in stability provided by DES can be attributed to its interaction with the tetramethylammonium head group, which likely alters the local electrostatic potential and increases the energy barrier for degradation reactions. This stabilization effect is particularly notable given the higher activation energy barriers observed for both degradation mechanisms when DES is present. This suggests that DES can effectively mitigate the

degradation of tetramethylammonium head groups, thereby improving the chemical stability of AEMs in alkaline media.

The increased stability of tetramethylammonium head groups in the presence of DES has significant implications for the longevity and performance of AEMs, particularly in alkaline environments. The higher activation energy barriers observed suggest that incorporating DES into AEM systems could enhance their durability, making them more effective for long-term applications such as fuel cells and other electrochemical devices.

Moreover, the insights gained from this study can guide the design of new DES-supported systems with optimized stability profiles. By understanding the molecular interactions and energy barriers involved, researchers can develop more robust materials tailored to specific applications. Future work should focus on achieving quantitative agreement with experimental data to further validate these findings and explore the potential of DES in other contexts, such as improving the stability of different quaternary ammonium head groups or in various electrochemical applications.

Our study underscores the potential of DES to enhance the chemical stability of tetramethylammonium head groups. The results provide a foundation for further exploration and optimization of DES-supported systems, with the goal of developing advanced materials with superior stability and performance in alkaline environments. These findings not only contribute to the understanding of degradation mechanisms in AEMs but also open new avenues for the development of more durable and efficient materials for energy applications.

7.3.2 Results from ab initio MD simulations

7.3.2.1 Tetramethylammonium head group at different temperatures

In this section, our objective is to delve into the dynamics of bond-breaking events within the tetramethylammonium head group in AEMs as OH^- ions approach, with a focus on potential S_N2 and YF reactions leading to methanol and trimethylammonium formation. Our investigation spans temperatures of 298 K, 320 K, and 350 K, in both the absence and presence of DES. Key attention is given to the bond distances for the C/N and H/C atoms of the TMA head group, as depicted in **Figure 7.5**.

At 298 K and HL 3, the bond distance between the C and N atoms of the TMA head group remains stable at approximately 1.5 Å, regardless of DES presence, indicating the absence of bond-breaking events conducive to S_N2 reactions (**Figure 7.5a**). However, the

bond distance between the H and C atoms increases significantly from 1.20 to 2.61 Å without DES, hinting at potential YF mechanism activation. Interestingly, DES presence maintains a relatively constant bond distance around 1.10 Å, suggesting DES's inhibitory effect on the YF mechanism (**Figure 7.5a**).

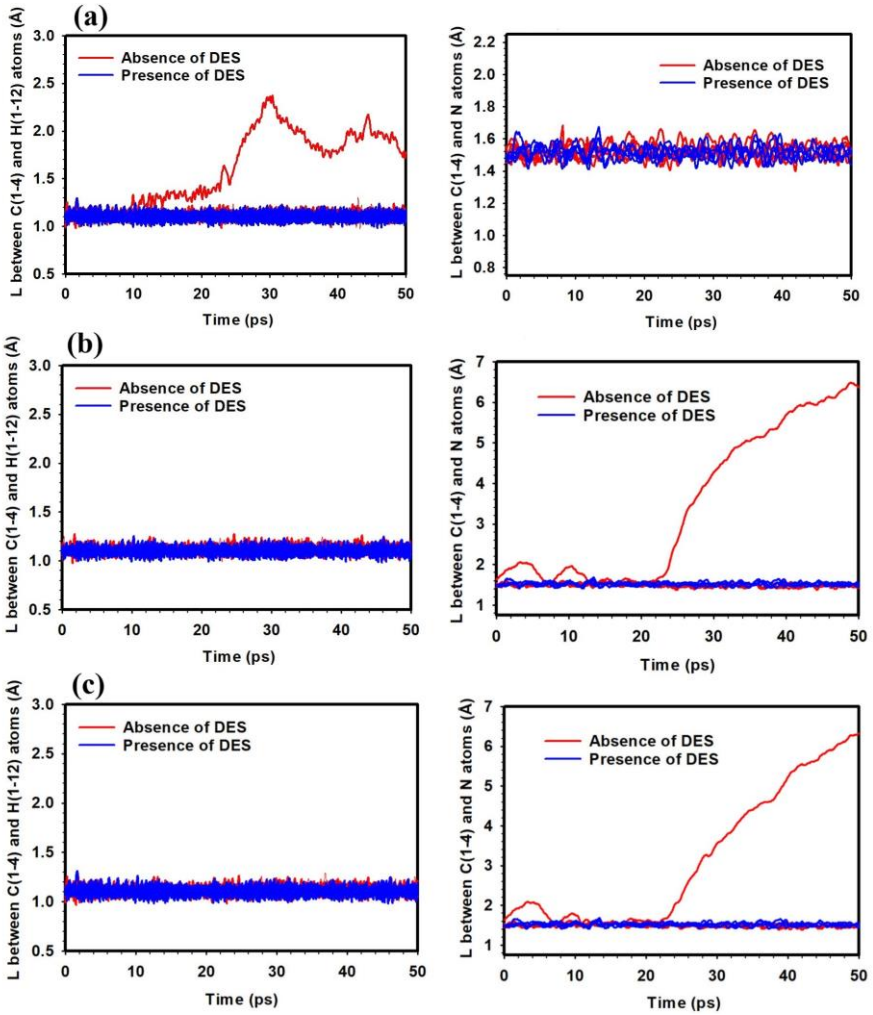

Figure 7.5: Bond distance between C and H atom of tetramethylammonium, and bond distance between C and N atom of tetramethylammonium in the absence and presence of DES at different temperatures ((a) 298 K, (b) 320 K, and (c) 350 K).

Moving to 320 K at HL 3, in the absence of DES, a notable increase in the C/N bond distance to 6.3 Å signals bond-breaking and potential S_N2 reaction initiation (**Figure 7.5b**). Conversely, DES stabilizes the bond distance at approximately 1.55 Å, indicating prevention of bond-breaking events. Notably, the H/C bond distance remains consistent around 1.1 Å, irrespective of DES presence (**Figures 7.5b, 7.5c**), suggesting minimal YF mechanism activity at this temperature.

At 350 K and HL 3, without DES, the C/N bond distance escalates to 6.56 Å, indicating bond-breaking events and S_N2 reaction potential (**Figure 7.5c**). In contrast, DES maintains stability with a bond distance around 1.58 Å. Similar to lower temperatures, the H/C bond distance exhibits stability around 1.1 Å in both DES absence and presence (**Figures 7.5b, 7.5c**), indicating minimal YF mechanism influence.

These findings underscore temperature's primary influence on degradation mechanisms, with DES notably suppressing bond-breaking events and S_N2/YF reactions. Lower temperatures favor the YF mechanism, while higher temperatures enhance S_N2 reaction likelihood. This study provides comprehensive insights into bond-breaking dynamics within the TMA head group in AEMs, shedding light on potential S_N2 and YF reactions.

7.3.2.2 Tetramethylammonium head group at different hydration levels

This study delves into the occurrence of bond-breaking events within the tetramethylammonium head group of AEMs as OH^- ions approach, signaling potential S_N2 and YF reactions leading to methanol and trimethylammonium production. Our investigation covers different HLs: HL 1, HL 3 (corresponding to AEMs' operating conditions), and HL 5, in both the absence and presence of DES. We focus on the bond distances for the C/N and H/C atoms of the TMA head group to gauge the propensity for S_N2 and YF mechanism-induced bond-breaking events, as depicted in **Figure 7.6**.

At HL 1 and a temperature of 298 K, the C/N bond distance of the TMA head group remained remarkably stable at approximately 1.50 Å, regardless of DES presence, suggesting minimal bond-breaking events and S_N2 reaction potential (**Figure 7.6a**). However, the H/C bond distance experienced a notable increase from 1.10 Å to 2.12 Å without DES, hinting at potential YF activation. In contrast, DES presence maintained a stable bond distance around 1.10 Å, indicating effective YF mechanism suppression (**Figure 7.6a**).

Similarly, at HL 3 and 298 K, the C/N bond distance remained stable, indicating minimal S_N2 reaction potential under these conditions (**Figure 7.6b**). However, the H/C bond distance increased to 2.61 Å without DES, suggesting YF mechanism propensity, while DES presence stabilized the bond distance at around 1.10 Å, inhibiting the YF mechanism (**Figure 7.6b**).

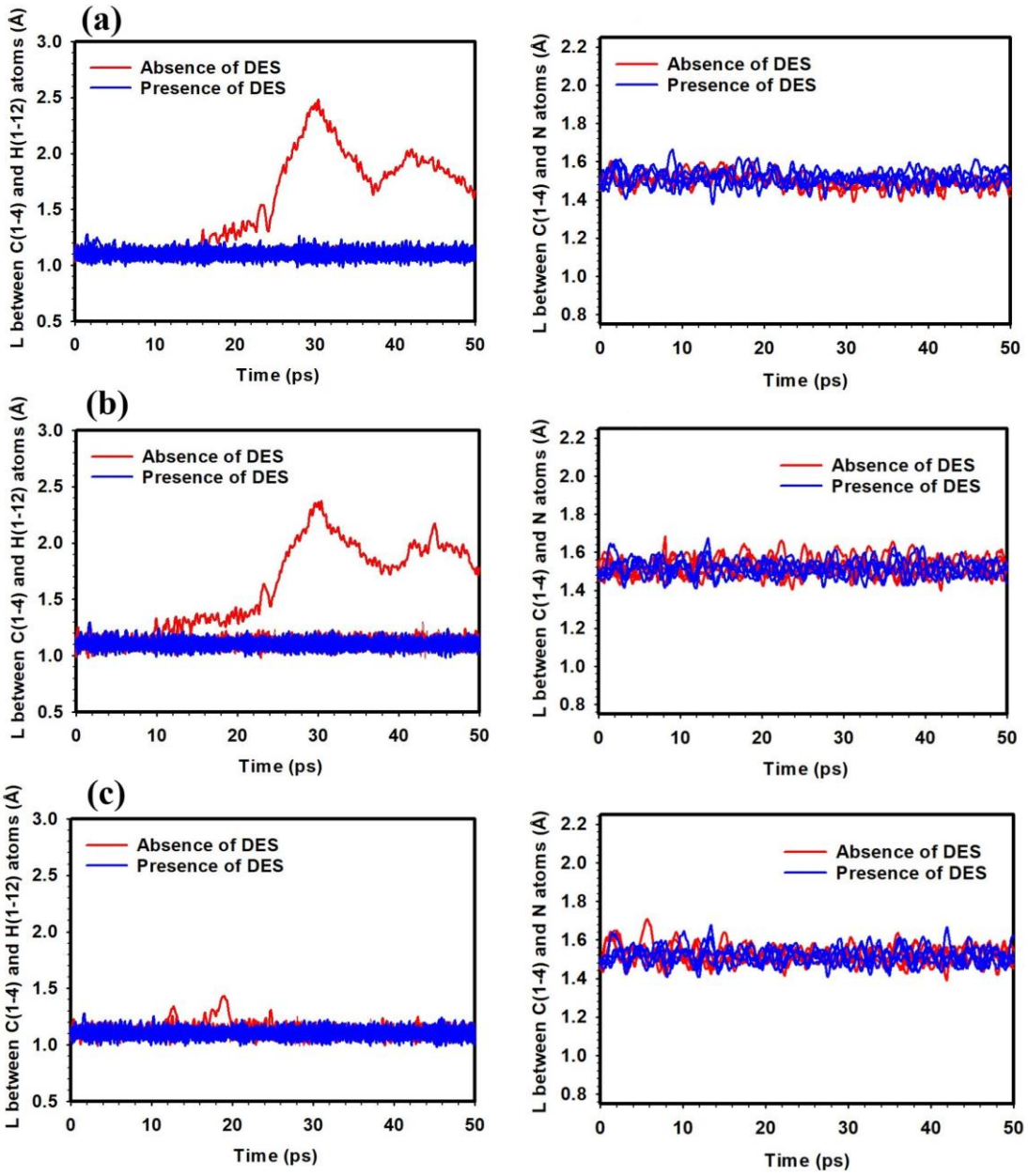

Figure 7.6: Bond distance between C and H atom of tetramethylammonium, and bond distance between C and N atom of tetramethylammonium in the absence and presence of DES at different temperatures ((a) HL 1, (b) HL 3, and (c) HL 5).

At HL 5 and 298 K, stable C/N bond distances were observed, signifying low S_N2 reaction likelihood (**Figure 7.6c**). The H/C bond distance remained consistent around 1.1 Å, regardless of DES presence, indicating minimal YF mechanism activity at this HL and temperature (**Figure 7.6c**).

Our investigation unveils insights into bond-breaking events in the TMA head group of AEMs. At 298 K across various HLs, minimal bond-breaking events were observed, translating to a low likelihood of S_N2 reactions. The YF mechanism, influenced by

temperature and DES presence, shows a greater potential at lower temperatures, effectively suppressed by DES. At higher HLs, the YF mechanism remains subdued, irrespective of DES presence.

7.3.2.3 QCS head group at different temperatures

The focus of this study is on understanding how the presence of DES affects these intermolecular interactions with the QCS head group at various temperatures ranging from 298 K to 350 K. The research employs RDFs to quantify the proximity and strength of the interactions between QCS nitrogen atoms and OH^- ion oxygen atoms. **Figure 7.6** displays the RDF profiles, providing a visual representation of these interactions under different conditions.

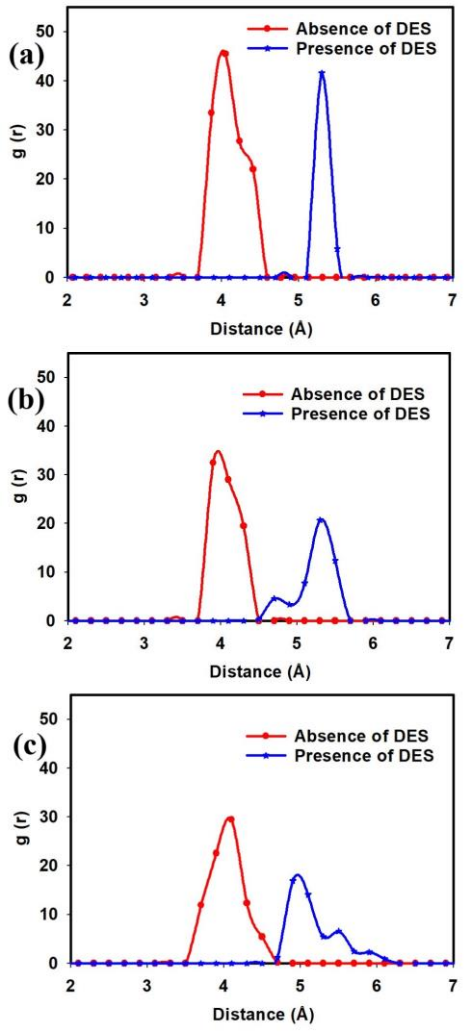

Figure 7.7: RDFs for N atom of QCS with OH^- ion in the absence and presence of the DES at the different temperatures including (a) 298 K, (b) 320 K, and (c) 350 K.

As seen in **Figure 7.7**, at 350 K, in the absence of DES, the RDF peak value of 29.49 at 4.10 Å signifies a strong interaction between the oxygen of the OH^- ion and the nitrogen atom of QCS head groups. However, in the presence of DES, this peak value decreases to 16.88 at 4.90 Å, indicating a slight increase in distance between the two species. This suggests that DES may influence the proximity and strength of the interaction between QCS head groups and OH^- ions at higher temperatures. At 320 K, the RDF peak value without DES reaches 32.49 at 3.90 Å, indicating a more pronounced interaction compared to 350 K. Conversely, in the presence of DES, the peak value decreases to 5.30 at 4.8 Å and 20.68 at 5.3 Å, suggesting a weakening of the interaction at moderate temperatures when DES is involved. Further elevation of temperature to 298 K results in a significant increase in the RDF peak value without DES, reaching 45.48 at 4.05 Å. This indicates a stronger interaction between QCS head groups and OH^- ions at this temperatures. In contrast, the presence of DES at 298 K leads to a peak value of 41.58 at 5.3 Å, signifying a reduction in the strength of the interaction compared to the absence of DES at the same temperature. These findings highlight the complex interplay between temperature, DES presence, and the interaction between QCS head groups and OH^- ions. The results suggest that DES can modulate the strength and distance of these intermolecular interactions of QCS head group based AEMs. Overall, the study provides valuable insights into the molecular level mechanisms governing the behavior of QCS-based AEM in the presence of DES.

Moreover, the study explores the influence of vehicular diffusion and Grotthuss diffusion mechanisms on OH^- ion diffusion, as depicted in **Figures 7.8** and **7.9**. These figures provide a visual representation of these diffusion processes within AEMs, specifically highlighting the dynamics of OH^- ions interacting with QCS head groups in the presence and absence of DES.

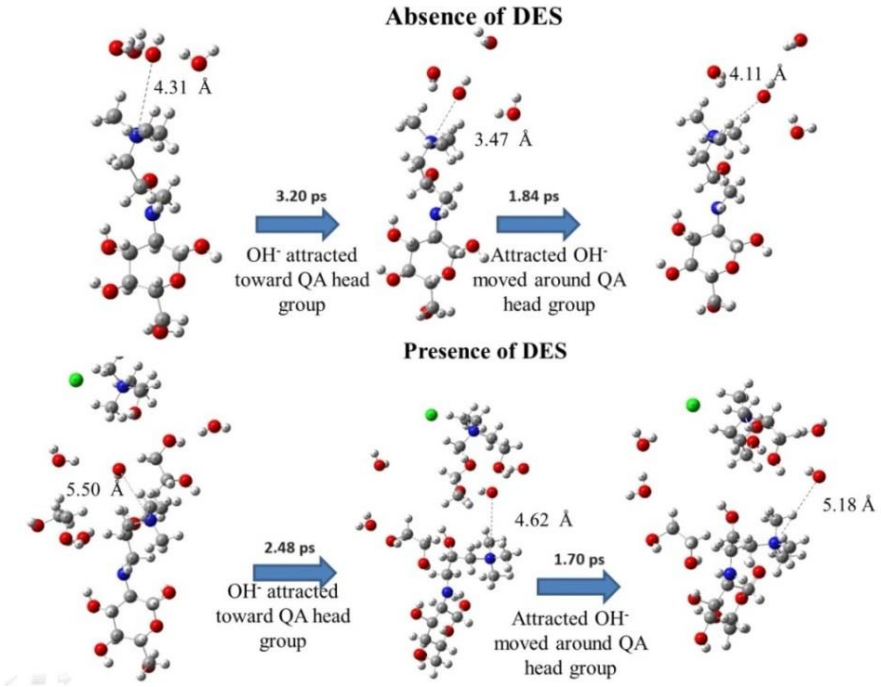

Figure 7.8: Snapshot of vehicular diffusion mechanism surrounding QCS head group in the presence and absence of DES at various temperatures.

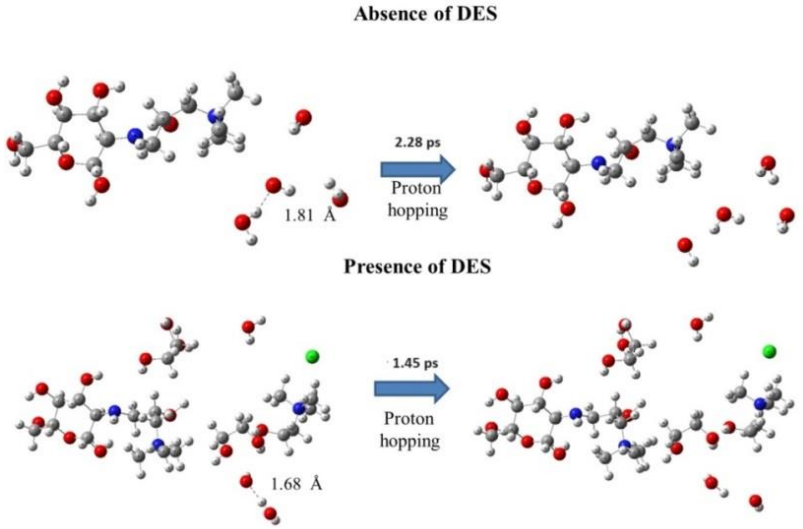

Figure 7.9: Snapshot of Grotthuss diffusion mechanism surrounding QCS head group in the presence and absence of DES at various temperatures.

In the absence of DES, it was observed that OH^- ions took approximately 3.20 ps to reach the vicinity of QCS head groups and 1.84 ps to maneuver around them as can be seen in **Figure 7.8**. This indicates a relatively slower diffusion process due to the absence of a facilitating solvent environment. Conversely, in the presence of DES, the time taken for OH^- ions to reach QCS head groups reduced to 2.48 ps, and the time to move around them

decreased to 1.70 ps. This suggests that DES enhances the efficiency of OH^- ion diffusion by reducing the time required for both reaching and maneuvering around QCS head groups.

The enhancement of OH^- ion diffusion in the presence of DES can be attributed to the unique molecular interactions within the DES system. Our DES is composed of one choline chloride and two ethylene glycol molecules. The choline ion and the chloride ion create a network of hydrogen bonds with ethylene glycol, forming a dynamic solvent environment that facilitates ion mobility. In the DES system, the ethylene glycol molecules act as hydrogen bond donors, creating a more fluidic environment around the OH^- ions compared to the more rigid structure of QCS alone. The hydrogen bonding network in DES not only stabilizes the OH^- ions but also reduces the energy barriers for ion movement, leading to a faster diffusion process. Additionally, the choline ions may interact with the OH^- ions through weak electrostatic interactions, further enhancing their mobility. This combination of hydrogen bonding and electrostatic interactions provides a pathway for easier and faster OH^- ion movement, thereby reducing the time required for the ions to reach and maneuver around the QCS head groups.

Furthermore, **Figure 7.9** delves into the proton hopping time, which is a key aspect of Grotthuss diffusion. In the absence of DES, the proton hopping time was observed to be 2.28 ps, indicating a moderate rate of proton transfer within the membrane. However, in the presence of DES, this time significantly decreased to 1.45 ps, highlighting the enhanced diffusivity facilitated by DES molecules. These findings underscore the significant impact of DES on improving OH^- ion diffusion efficiency and enhancing proton hopping rates within AEMs. The reduced times observed in the presence of DES suggest a more favorable environment for ion transport, which is crucial for the development of efficient AEM for various electrochemical applications.

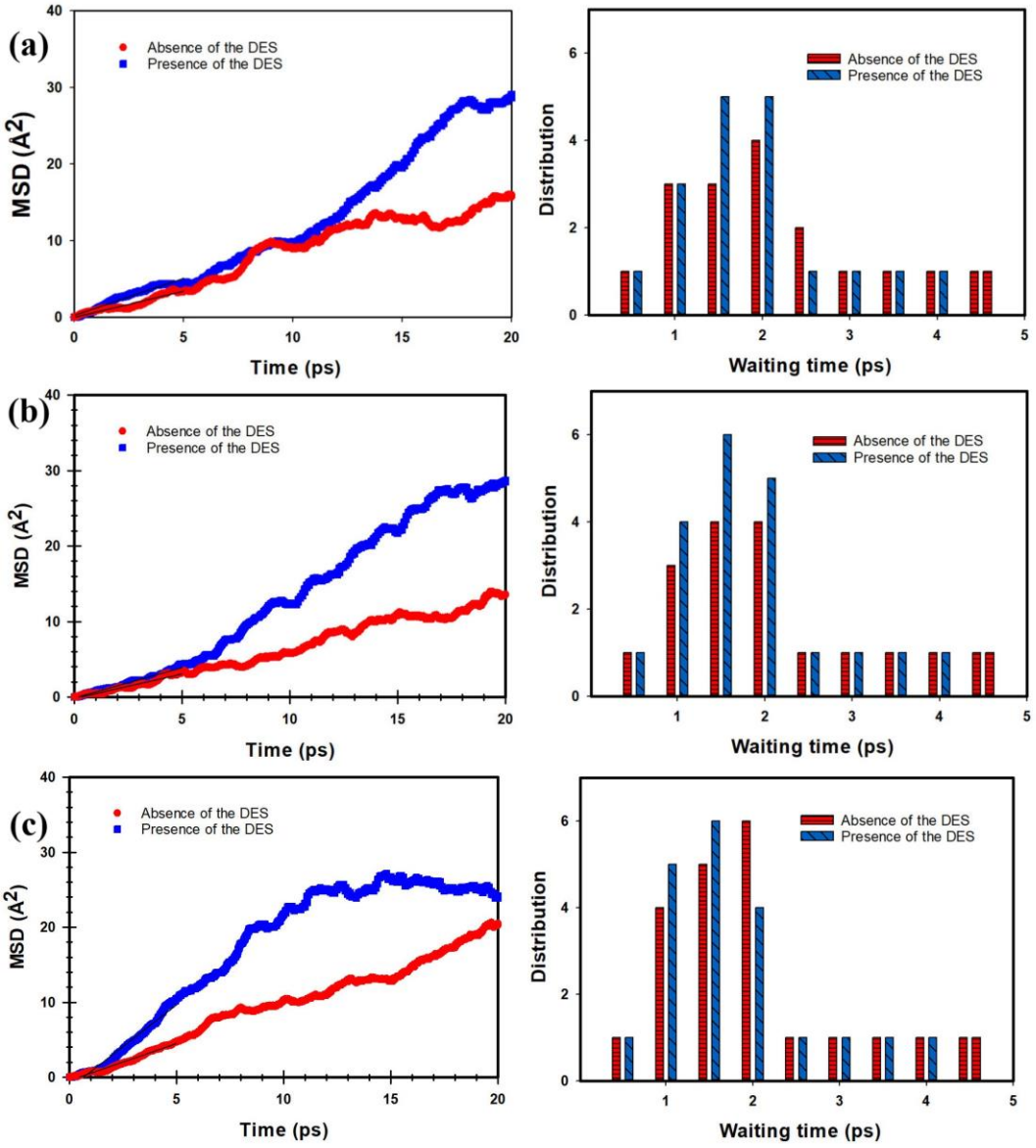

Figure 7.10: MSD vs. time curves and waiting time distribution histogram at different temperatures ((a) 298 K, (b) 320 K, and (c) 350 K) for OH^- ions for QCS head group in the absence and presence of DES.

Next, the analysis focuses on understanding how temperature and the presence of DES affect OH^- ion diffusion and the initiation of Grotthuss diffusion mechanisms. From the MSD curves (**Figure D1-D6**, Appendix D, **Figure 7.10**), it was observed that as the temperature increased, the MSD values also rose, indicating greater OH^- ion mobility. At lower temperatures (e.g., 298 K), the OH^- ions exhibited a similar MSD trend regardless of the presence or absence of DES. However, at higher temperatures, OH^- ion mobility was significantly greater in the presence of DES, as shown by the MSD vs. time curves. The diffusion coefficients (**Table 7.2**) were calculated from the slope of the MSD curves in

Figure 7.10. The temperature-dependent diffusion coefficients of the OH^- ion increased from 0.011 to 0.016 Å²/ps in the absence of DES, and from 0.016 to 0.037 Å²/ps in the presence of DES. The diffusion coefficients of OH− ions from our ab initio MD simulations at different temperatures were validated against literature values [34-37]. Reported diffusion coefficients for OH− ions typically range from 0.004 to 0.042 Å²/ps for temperatures between 298 and 350 K, and this agreement confirms the accuracy of our results. This demonstrates a clear correlation between temperature and OH^- ion mobility. Higher temperatures increased the kinetic energy of the molecules, causing the OH^- ions to travel greater distances. These results suggest that DES significantly enhances OH^- ion diffusion, particularly at elevated temperatures. The diffusion coefficients of OH^- ions from our ab initio MD simulations at different temperatures were validated against literature values [34-37]. Reported diffusion coefficients for OH^- ions typically range from 0.010 to 0.042 Å²/ps for temperatures between 298 and 350 K, and this agreement confirms the accuracy of our results.

Table 7.2: Diffusion coefficients of OH^- ions for DES supported QCS head groups of AEM at the different temperatures.

Diffusion coefficient, $Å^2$/ps, (SE)	Temperature values (K)		
	298 K	320 K	350 K
Absence of the DES	0.011 (0.0002)	0.013 (0.0003)	0.016 (0.0004)
Presence of the DES	0.016 (0.0005)	0.018 (0.0007)	0.037 (0.0015)

Furthermore, the waiting time distribution histogram for proton hopping to initiate Grotthuss diffusion is illustrated in **Figure 7.10**. The the waiting time decreased from 2 ps to 1.5 ps in the absence of DES, and from 2 ps to 1 ps in the presence of DES. These findings suggest that DES facilitates the initiation of Grotthuss diffusion mechanisms by reducing the waiting time for proton hopping. The temperature-dependent effects on proton hopping further highlight the complex interplay between temperature, solvent environment, and OH^- ion dynamics within AEMs.

7.3.2.3 QCS head group at different hydration levels

Ab initio MD simulations, coupled with RDF analysis, were employed to delve into intermolecular interactions of DES supported QCS head groups. The RDF profiles depicted in **Figure 7.11**, present a comprehensive view of the distances between QCS nitrogen atoms

and OH^- ion oxygen atoms at different HLs ranging from 1 to 5, both in the presence and absence of DES.

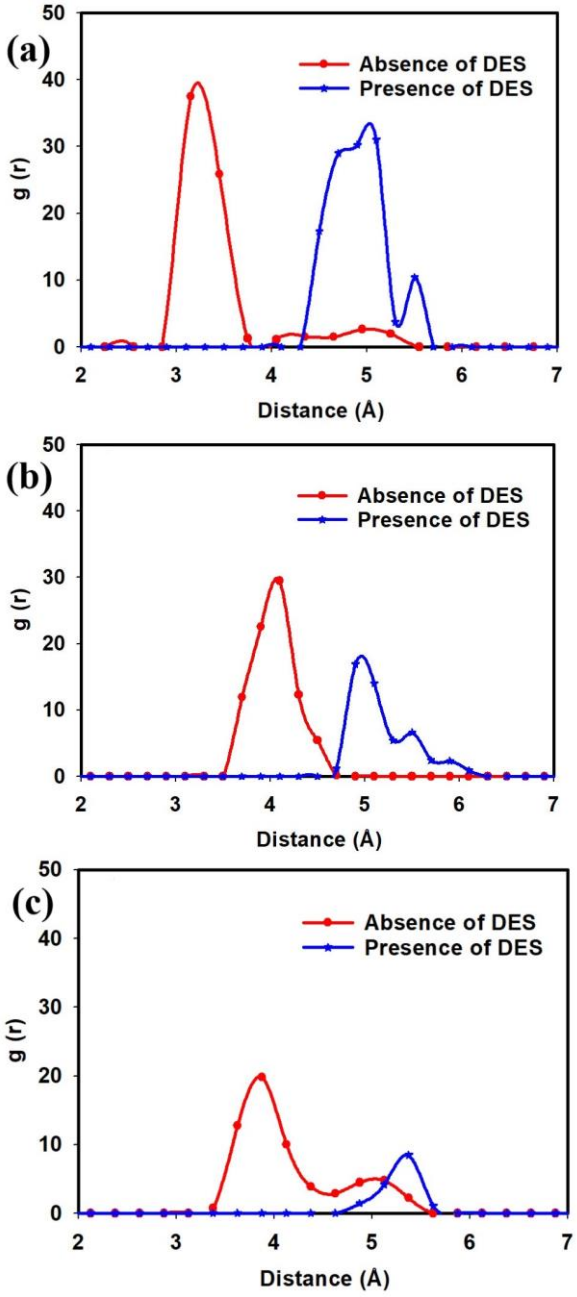

Figure 7.11: RDFs for N atom of QCS with OH^- ion in the absence and presence of the DES at the different HLs including (a) HL 1 K, (b) HL 3, and (c) HL 5.

At HL 1, in the absence of DES, the RDF peak value of 37.50 at 3.15 Å signifies a strong interaction between the OH^- ion oxygen and the nitrogen atom of QCS head groups. However, with DES present, this peak value decreases to 31.01 at 5.10 Å, indicating a weakened interaction under the influence of DES at this hydration level.

Moving to HL 3, the RDF peak value without DES is 29.49 at 4.10 Å, suggesting a moderate interaction between QCS head groups and OH^- ions. In contrast, with DES, the peak value reduces to 16.88 at 4.90 Å, indicating a significant decrease in the strength of interaction compared to the absence of DES at this hydration level.

At HL 5, the RDF peak value in the absence of DES is 19.82 at 3.85 Å, indicating a relatively weaker interaction between QCS head groups and OH^- ions compared to lower hydration levels. Interestingly, in the presence of DES at HL 5, the peak value drops substantially to 8.45 at 5.37 Å, signifying a drastic reduction in the strength of interaction, possibly due to the influence of DES molecules on the hydration environment and ion interactions.

These results highlight the intricate relationship between HLs, DES presence, and the nature of interactions between QCS head groups and OH^- ions. The findings suggest that higher HLs may lead to weaker interactions, and the presence of DES can further modulate these intermolecular interactions.

Moreover, this study delves into the effects of vehicular diffusion and Grotthuss diffusion mechanisms on OH^- ion diffusion within AEMs, as highlighted in **Figures 7.12** and **7.13**. These figures offer a detailed representation of these diffusion processes and provide additional insight into the dynamics of OH^- ions interacting with QCS head groups, particularly in the presence or absence of DES.

In the absence of DES, it was observed that OH^- ions required approximately 3.76 ps to reach the vicinity of QCS head groups and 2.40 ps to navigate around them. This indicates a relatively slower diffusion process due to the absence of a facilitating solvent environment. On the other hand, in the presence of DES, the time taken for OH^- ions to reach QCS head groups was reduced to 3.15 ps, with a corresponding decrease in the time required to move around the head groups to 2.16 ps. This suggests that DES contributes to enhancing the efficiency of OH^- ion diffusion by reducing both the reaching time and maneuvering time around QCS head groups.

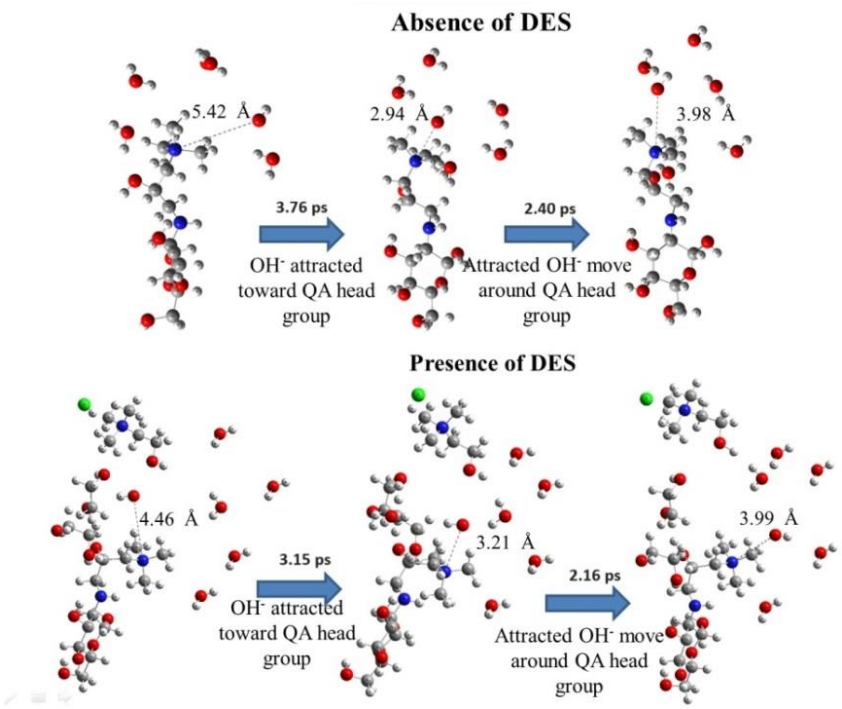

Figure 7.12: Snapshot of vehicular diffusion mechanism surrounding QCS head group in the presence and absence of DES at various HLs.

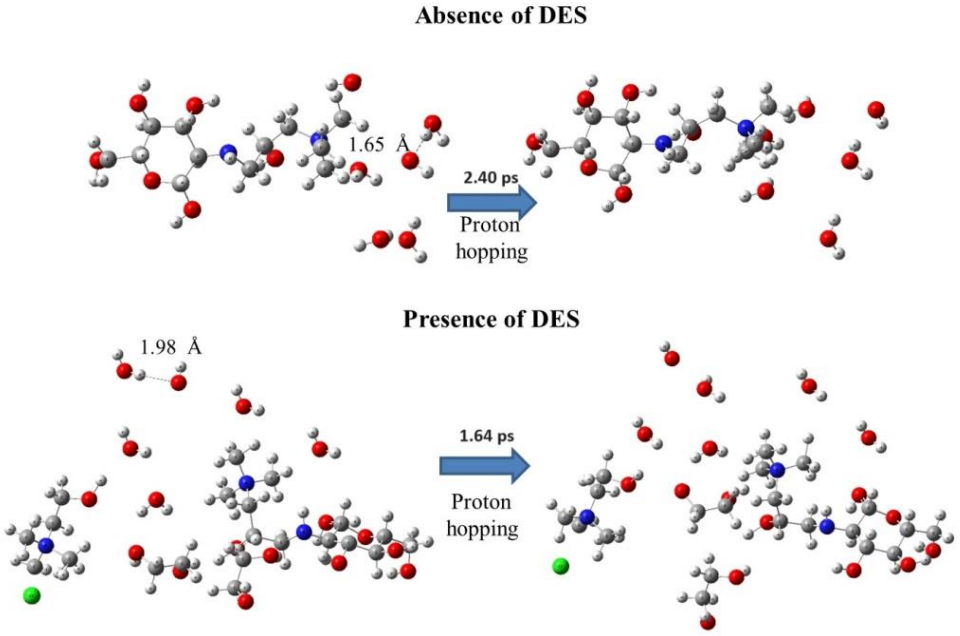

Figure 7.13: Snapshot of Grotthuss diffusion mechanism surrounding QCS head group in the presence and absence of DES at various HLs.

Additionally, **Figure 7.13** explores the proton hopping time, a critical aspect of Grotthuss diffusion. In the absence of DES, the proton hopping time was observed to be 2.40

ps, indicating a moderate rate of proton transfer within the AEM. However, in the presence of DES, this time significantly decreased to 1.64 ps, demonstrating the enhanced OH^- ion mobility facilitated by DES molecules.

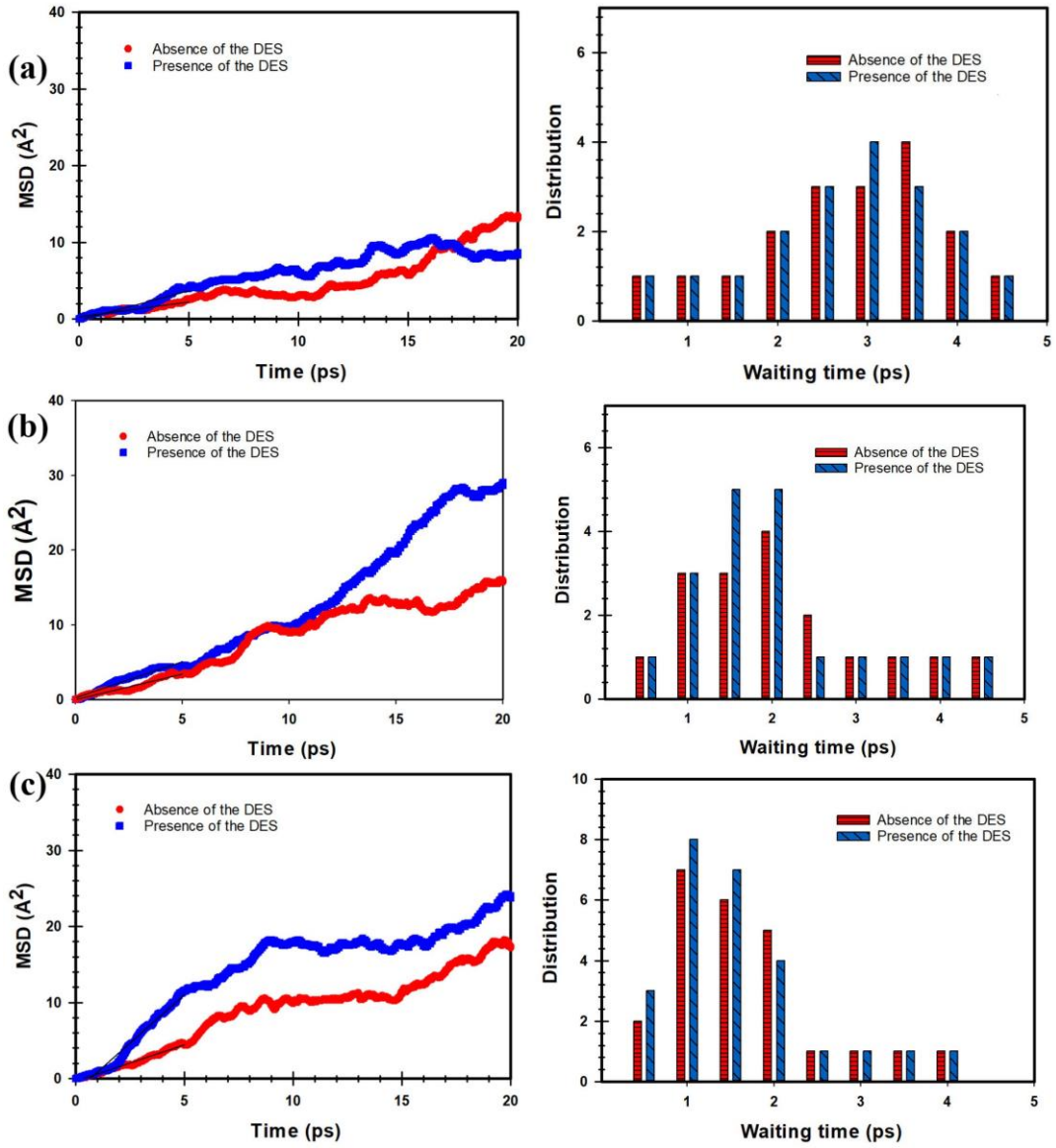

Figure 7.14: MSD vs. time curves and waiting time distribution histogram at different HLs ((a) 298 K, (b) 320 K, and (c) 350 K) for OH^- ions for QCS head group in the absence and presence of DES.

From the MSD curves (**Figure D7-D12**, Appendix D, **Figure 7.14**), it was observed that as the hydration level (HL) increased, the MSD values also rose, indicating enhanced OH- ion diffusion. At lower HLs, such as HL 1 and 3, the OH- ions displayed a similar diffusion trend regardless of the presence or absence of DES. However, at higher HLs, particularly at HL 5, OH- ion diffusion was significantly greater in the presence of DES

compared to its absence. The diffusion coefficients (**Table 7.3**) were derived from the slopes of the MSD curves in **Figure 7.14**. As HLs increased, the diffusion coefficients of the OH- ion steadily rose from 0.006 to 0.015 Å²/ps without DES, and from 0.012 to 0.042 Å²/ps with DES. This suggests that DES plays a key role in promoting OH- ion diffusion, especially at higher hydration levels. The diffusion coefficients of OH^- ions from our ab initio MD simulations at different HLs were validated against literature values [34-37]. Reported diffusion coefficients for OH^- ions typically range from 0.004 to 0.069 Å²/ps for different HLs (HL < 6), and this agreement confirms the accuracy of our results.

Table 7.3: Diffusion coefficients of OH^- ions for DES supported QCS head groups of AEM at the different HLs.

Diffusion coefficient, $Å^2$/ps, (SE)	HL values		
	1	3	5
Absence of the DES	0.006 (0001)	0.011 (0.0002)	0.015 (0.004)
Presence of the DES	0.012 (0.002)	0.016 (0.0005)	0.042 (0.02)

Additionally, the waiting time distribution histogram for proton hopping to initiate Grotthuss diffusion is depicted in **Figure 7.14**. Additionally, the waiting time distribution histogram for proton hopping, which initiates Grotthuss diffusion, is shown in **Figure 7.14**. The waiting time decreased from 3.5 ps to 1.5 ps in the absence of DES, and from 3 to 1 ps in the presence of DES.

These results highlight the significant impact of HLs and DES presence on OH^- ion vehicular diffusion and Grotthuss diffusion initiation. The enhanced diffusion and reduced waiting times observed in the presence of DES at higher HLs suggest a synergistic effect between the hydration environment and solvent properties in promoting efficient ion transport within AEM.

In this research, it was discovered that the addition of DES enhanced the chemical stability of head groups, as observed in DFT, and ab initio MD methods. Subsequent investigations revealed that the inclusion of DES resulted in comparable diffusion patterns of OH^- ions across QCS head groups under varying HLs and temperatures, as observed in ab initio MD methods. This finding is particularly intriguing, emphasizing the necessity for future experimental validation, which is currently underway by our experimental group.

7.4. Conclusions

From this study, the following conclusions can be made:

- DFT and ab initio MD methods were implemented to study the YF, and S_N2 reaction mechanisms within the DES supported tetramethylammonium head group at the different HLs, temperatures, and the diffusion mechanism of OH^- ion via QCS head group supported by DES.
- DFT calculations of transition state ($\Delta E_{activation}$, $\Delta G_{activation}$, $\Delta E_{reaction}$, and $\Delta G_{reaction}$) for key degradation mechanisms, YF and S_N2, suggested that the presence of DES enhances the stability of the tetramethylammonium head groups compared to systems without DES.
- From the results of ab initio MD simulation, it was found that, in the absence of DES, the S_N2 mechanism predominated at HL 3 and 310-350 K, while YF emerged as the major degradation mechanism pathway at the various HLs, including 1 and 3 and 298 K.
- Ab initio MD simulation studies showed that the addition of DES improved the chemical stability of head groups.
- It was found that including DES led to compatible OH^- ion diffusion across QCS head groups at different HLs and temperatures, in comparison to situations without DES.
- This study underscores the importance of temperature, HL, and DES presence in modulating the chemical stability behavior and diffusion of OH^- ions within AEMs.
- These insights are invaluable for the design and optimization of AEM-based systems, offering new avenues for enhancing their performance and stability in various applications.

Chapter 8: Conclusion & outlook

8.1. Summary of main findings

The DFT, ab initio MD, and conventional all-atom MD methods were performed to study the chemical stability, degradation mechanism of head groups, and OH^- ion diffusion via QCS head groups.

Regarding the DFT, ab initio MD, and conventional all-atom MD methods, the DFT method is allowed us to understand S_N2/YF degradation mechanism for head groups of AEM at the different HLs via calculating reaction energy, activation energy, and transition states. Next, ab initio MD method allowed us to explore the chemical bond formation and breaking events in AEM system to understand the S_N2/YF degradation mechanisms of QCS head groups, and vehicular/Grotthuss diffusion mechanism of OH^- ion via DES supported QCS head group of AEM at the different HLs, and temperatures. Next, conventional all-atom MD method allowed us to calculate diffusion coefficient for OH^- ion diffusion around head groups of AEM from MSD vs time plot.

Then, four different objectives were studied in this work as a four different parts. Herein, the main findings can be summarized as follows for each part:

The first part was devoted to explore the effect of HLs on the chemical stability and degradation mechanism of various QA head groups of AEM via DFT method. In this regard, LUMO energy, $\Delta E_{reaction}$, $\Delta G_{reaction}$, $\Delta E_{activation}$ and $\Delta G_{activation}$ values indicated a trend of increasing chemical stability as: (a) pyridinium < (b) 1,4-diazabicyclo [2.2.2] octane ~(c) benzyltrimethylammonium < (d) n-methyl piperidinium ~ (e) guanidium < (f) trimethylhexylammonium for HL 0. In addition, transition state calculations were performed for the QA (c) and (f) head groups at different HLs ranging from 0 to 3. The results suggest that the QA (f) head group exhibits higher chemical stability compared to QA (c) across these HLs. These DFT results were consistent with experimental findings, offering crucial insights into AEM degradation mechanism.

The second part was devoted to study the effect of HLs on the vehicular diffusion mechanism of OH^- ions via different QA head groups by conventional all-atom MD method. Considering conventional all-atom MD simulations for various QA head groups, QA (c), and (f) variations exhibited similar OH^- ion vehicular diffusion coefficients from MSD vs time curve at the varied HLs from 3 to 15. Higher water content was found to enhance OH^- ion

mobility, emphasizing the importance of considering water content in QA (c), and (f) head groups.

The third part was to study the chemical stability, degradation mechanism of QCS head groups, and vehicular diffusion of OH^- ions at various HLs and temperatures via DFT, and conventional all-atom MD methods. As a result of the LUMO energy, $\Delta E_{reaction}$, $\Delta G_{reaction}$, $\Delta E_{activation}$ and $\Delta G_{activation}$ values, QCS (A) exhibited greater chemical stability compared to QCS (B) and QCS (C) at the HL 0, and 3. Next, from the results of conventional all-atom MD simulations, the diffusion coefficients of MSD vs time curve revealed similar vehicular diffusion behavior of OH^- ions in different QCS systems at the different HLs, and temperatures.

The last part was to understand the chemical stability, and degradation mechanism of DES supported QCS head groups and vehicular/Grotthuss diffusion mechanisms of OH^- ion of AEM at different HLs, temperatures via DFT and ab initio MD methods. The DFT calculations of transition state for key degradation mechanisms, YF and S_N2, suggested that the presence of DES enhances the stability of the tetramethylammonium head groups compared to systems without DES. Next, from the results of ab initio MD simulation, it was found that, in the absence of DES, the S_N2 mechanism predominated at HL 3 and 310-350 K, while YF emerged as the major degradation mechanism pathway at the various HLs, including 1 and 3 and 298 K. Nevertheless, DFT calculations and ab initio MD simulation studies showed that the addition of DES improved the chemical stability of head groups. Later on, it was found that including DES led to compatible diffusion of OH^- ions across QCS head groups under different HLs and temperatures, in contrast to situations without DES. This might be attributed to the reduced waiting time of the Grotthuss mechanism for QCS head groups supported by DES, compared to those without such support.

In general, as it was hypothesized, multiple factors, such as various structures of QCS head groups, HLs, and temperatures altered the degradation mechanism and diffusion of OH^- ions. Moreover, the addition of DES improved the chemical stability of head groups of AEM at higher HLs, and lower temperatures. Addition of DES is also lead to compatible vehicular/Grotthuss diffusion mechanisms of OH^- ions at higher HLs and temperatures compared with absence of DES case, for QCS head groups.

8.2. Limitations of the present work

Based on the DFT, ab initio MD, and conventional all-atom MD works conducted in the previous chapters, the following limitations can be mentioned:

- The simulations in this work are based on monomers or oligomers rather than the complete polymer structure. While this approach allows for detailed analysis at the molecular level, it may not fully represent the complexities of the actual polymer system.
- The MD methods conducted in this study were performed under equilibrium conditions. However, real AEMFCs operate under external voltage during operation, leading to non-equilibrium states.

8.3. Recommendations and outlook

Based on the findings from the preceding chapters, the following recommendations are suggested:

- Based on the findings of this work, future research should focus on designing AEM materials with enhanced chemical stability by carefully selecting and modifying head group structures. Specifically, incorporating head groups with steric hindrance, protective groups, higher LUMO energy, higher activation energies, lower reaction energies, and increased hydration levels can significantly improve the chemical stability of AEMs. Additionally, the integration of DES has shown potential in stabilizing head groups, even under varying hydration levels and temperatures. Future material design should explore the synergy between DES and optimized quaternary ammonium structures to develop AEMs with superior performance and durability under alkaline conditions. Advancements in multiscale molecular modeling and simulation techniques can further aid in predicting and tailoring these properties at the molecular level, ultimately leading to the next generation of high-performance AEM fuel cells.
- The outcomes highlighted here consider the impact of various structure of head groups, HLs, and temperatures on chemical stability and degradation mechanism of QCS, diffusion of OH^- ion using DFT, ab initio MD, and conventional all-atom MD methods. Future research should delve deeper into the chemical stability of QCS head groups, and diffusion of OH^- ions, especially focusing on understanding the

mechanisms behind the observed differences in stability among various head group structures, HLs, and temperatures.

- Further possible experimental validations are needed to confirm the multiscale molecular modeling and simulation findings. While computational modeling has provided valuable insights, integrating experimental validation, especially regarding ion transport and chemical stability, would enhance the reliability and applicability of the findings. Collaborative efforts between computational and experimental researchers can bridge the gap between micro- and real-world performances.
- Investigating novel materials, such as alternative QCS structures or innovative membrane compositions, could lead to advancements in AEM technology. Computational screening methods coupled with experimental testing can identify promising candidates for improved AEM performance.
- Given the positive and compatible impact of DES on chemical stability and OH^- ion diffusion observed in this study, further optimization and exploration of DES-supported systems are warranted. Understanding the interaction mechanisms between DES and AEM components can guide the design of more effective and stable membrane materials.
- Collaboration across disciplines, including materials science, computational modeling, electrochemistry, and engineering, can foster innovative solutions and accelerate the development of next-generation AEMFCs. Joint research efforts can leverage diverse expertise to address complex challenges in AEM technology.

Reference list

[1] H. Zhou, J. Dai, X. Chen, B. Hu, H. Wei, and H. H. Cai, “Understanding innovation of new energy industry: Observing development trend and evolution of hydrogen fuel cell based on patent mining,” *International Journal of Hydrogen Energy*, vol. 52, pp. 548-560, 2024

[2] T. Li, N. Tsubaki, and Z. Jin, “S-scheme heterojunction in photocatalytic hydrogen production,” *Journal of Materials Science & Technology*, vol. 169, pp. 82-104, 2024.

[3] A. A. Alabbadi, O. A. Obaid, and A. A. AlZahrani, “A comparative economic study of nuclear hydrogen production, storage, and diffusion”. *International Journal of Hydrogen Energy*, vol. 54, pp. 849-863, 2024.

[4] J. E. G. Baquero, and D. B. Monsalve, “From fossil fuel energy to hydrogen energy: Transformation of fossil fuel energy economies into hydrogen economies through social entrepreneurship” *International Journal of Hydrogen Energy*, vol. 54, pp. 574-585, 2024.

[5] K. Yassin, I. G. Rasin, S. Brandon, and D. R. Dekel, “How can we design anion-exchange membranes to achieve longer fuel cell lifetime?” *Journal of Membrane Science*, vol. 690, pp. 122164, 2024.

[6] F. Li, S. H. Chan, and Z. Tu, “Recent Development of Anion Exchange Membrane Fuel Cells and Performance Optimization Strategies: A Review,” *The Chemical Record*, vol. 24, e202300067, 2014.

[7] D. R. Dekel, "Review of cell performance in anion exchange membrane fuel cells," *Journal of Power Sources*, vol. 375, pp. 158-169, 2018.

[8] Z. Sun, B. Lin, and F. Yan, "Anion-exchange membranes for alkaline fuel-cell applications: the effects of cations," *ChemSusChem*, vol. 11, no. 1, pp. 58-70, 2018.

[9] L. Osmieri, L. Pezzolato, and S. Specchia, "Recent trends on the application of PGM-free catalysts at the cathode of anion exchange membrane fuel cells," *Current Opinion in Electrochemistry*, vol. 9, pp. 240-256, 2018.

[10] F. Nessa, S. M. Masum, M. Asaduzzaman, S. Roy, M. Hossain, and M. Jahan, "A process for the preparation of chitin and chitosan from prawn shell waste," *Bangladesh Journal of Scientific and Industrial Research*, vol. 45, no. 4, pp. 323-330, 2010.

[11] Y. Xiong, Q. L. Liu, Q. G. Zhang, and A. M. Zhu, "Synthesis and characterization of cross-linked quaternized poly (vinyl alcohol)/chitosan composite anion exchange membranes for fuel cells," *Journal of Power Sources*, vol. 183, no. 2, pp. 447-453, 2008.

[12] Y. Wan, B. Peppley, K. A. Creber, and V. T. Bui, "Anion-exchange membranes composed of quaternized-chitosan derivatives for alkaline fuel cells," *Journal of power sources*, vol. 195, no. 12, pp. 3785-3793, 2010.

[13] V. Vijayakumar and S. Y. Nam, "A Review of Recent Chitosan Anion Exchange Membranes for Polymer Electrolyte Membrane Fuel Cells," *Membranes*, vol. 12, no. 12, p. 1265, 2022.

[14] F. Song *et al.*, "Novel alkaline anion-exchange membranes based on chitosan/ethenylmethylimidazoliumchloride polymer with ethenylpyrrolidone composites for

low temperature polymer electrolyte fuel cells," *Electrochimica Acta,* vol. 177, pp. 137-144, 2015.

[15] J. Li, C. Liu, J. Ge, W. Xing, and J. Zhu, "Challenges and Strategies of Anion Exchange Membranes in Hydrogen-electricity Energy Conversion Devices," *Chemistry–A European Journal,* vol. 29, no. 26, p. e202203173, 2023.

[16] U. Salma and N. Shalahin, "A mini-review on alkaline stability of imidazolium cations and imidazolium-based anion exchange membranes," *Results in Materials,* p. 100366, 2023.

[17] Q. Hassan, "Optimisation of solar-hydrogen power system for household applications," *International journal of hydrogen energy,* vol. 45, no. 58, p. 33111-33127 2020.

[18] R. Gutru *et al.*, "Recent progress in heteroatom doped carbon based electrocatalysts for oxygen reduction reaction in anion exchange membrane fuel cells," *international journal of hydrogen energy,* vol. 48, no. 9, pp. 3593-3631, 2023.

[19] B. Yang and Z. Cunman, "Progress in constructing high-performance anion exchange Membrane: Molecular design, microphase controllability and In-device property," *Chemical Engineering Journal,* vol. 457, p. 141094, 2023.

[20] M. M. Hossen, M. S. Hasan, M. R. I. Sardar, J. bin Haider, K. Tammeveski, and P. Atanassov, "State-of-the-art and developmental trends in platinum group metal-free cathode catalyst for anion exchange membrane fuel cell (AEMFC)," *Applied Catalysis B: Environmental,* vol. 325, p. 121733, 2023.

[21] L. Marin *et al.*, "Quaternized chitosan (nano) fibers: A journey from preparation to high performance applications," *International Journal of Biological Macromolecules,* p. 125136, 2023.

[22] A. Akhmetova, B. Myrzakhmetov, Y. Wang, Z. Bakenov, and A. Mentbayeva, "Development of Quaternized Chitosan Integrated with Nanofibrous Polyacrylonitrile Mat as an Anion-Exchange Membrane," *ACS omega,* vol. 7, no. 49, pp. 45371-45380, 2022.

[23] A. M. Samsudin, M. Bodner, and V. Hacker, "A brief review of poly (vinyl alcohol)-based anion exchange membranes for alkaline fuel cells" *Polymers*, *14*(17), pp. 3565, 2022.

[24] H. Zhao, Y. Yang, X. Shu, Y. Wang, and Q. Ran, "Adsorption of organic molecules on mineral surfaces studied by first-principle calculations: A review," *Advances in Colloid and Interface Science,* vol. 256, pp. 230-241, 2018.

[25] R. Tsuchitani, H. Nakanishi, H. Shishitani, S. Yamaguchi, H. Tanaka, and H. Kasai, "A theoretical study of how C2-substitution affects alkaline stability in imidazolium-based anion exchange membranes," *Solid State Ionics,* vol. 278, pp. 5-10, 2015.

[26] I. Dance, "The pathway for serial proton supply to the active site of nitrogenase: enhanced density functional modeling of the Grotthuss mechanism," *Dalton Transactions,* vol. 44, no. 41, pp. 18167-18186, 2015.

[27] C. E. Diesendruck and D. R. Dekel, "Water–a key parameter in the stability of anion exchange membrane fuel cells," *Current Opinion in Electrochemistry,* vol. 9, pp. 173-178, 2018.

[28] G. F. Mangiatordi, V. Butera, N. Russo, D. Laage, and C. Adamo, "Charge transport in poly-imidazole membranes: a fresh appraisal of the Grotthuss mechanism," *Physical Chemistry Chemical Physics,* vol. 14, no. 31, pp. 10910-10918, 2012.

[29] A. I. Persson, M. W. Larsson, S. Stenström, B. J. Ohlsson, L. Samuelson, and L. R. Wallenberg, "Solid-phase diffusion mechanism for GaAs nanowire growth," *Nature materials,* vol. 3, no. 10, pp. 677-681, 2004.

[30] Z. Xu, X. Lv, J. Chen, L. Jiang, Y. Lai, and J. Li, "Dispersion-corrected DFT investigation on defect chemistry and potassium migration in potassium-graphite intercalation compounds for potassium ion batteries anode materials," *Carbon,* vol. 107, pp. 885-894, 2016.

[31] B. Song, T. Yu, X. Jiang, W. Xi, and X. Lin, "The relationship between convection mechanism and solidification structure of the iron-based molten pool in metal laser direct deposition," *International Journal of Mechanical Sciences,* vol. 165, p. 105207, 2020.

[32] C. Chen, Y.-L. S. Tse, G. E. Lindberg, C. Knight, and G. A. Voth, "Hydroxide solvation and transport in anion exchange membranes," *Journal of the American Chemical Society,* vol. 138, no. 3, pp. 991-1000, 2016.

[33] D. Munoz-Santiburcio and D. Marx, "On the complex structural diffusion of proton holes in nanoconfined alkaline solutions within slit pores," *Nature Communications,* vol. 7, no. 1, p. 12625, 2016.

[34] T. Zelovich, Z. Long, M. Hickner, S. J. Paddison, C. Bae, and M. E. Tuckerman, "Ab initio molecular dynamics study of hydroxide diffusion mechanisms in nanoconfined structural mimics of anion exchange membranes," *The Journal of Physical Chemistry C,* vol. 123, no. 8, pp. 4638-4653, 2019.

[35] T. Zelovich *et al.*, "Hydroxide ion diffusion in anion-exchange membranes at low hydration: insights from ab initio molecular dynamics," *Chemistry of Materials,* vol. 31, no. 15, pp. 5778-5787, 2019.

[36] T. Zelovich and M. E. Tuckerman, "Water layering affects hydroxide diffusion in functionalized nanoconfined environments," *The Journal of Physical Chemistry Letters,* vol. 11, no. 13, pp. 5087-5091, 2020.

[37] T. Zelovich *et al.*, "Non-monotonic temperature dependence of hydroxide ion diffusion in anion exchange membranes," *Chemistry of Materials,* vol. 34, no. 5, pp. 2133-2145, 2022.

[38] S. Faucher *et al.*, "Critical knowledge gaps in mass transport through single-digit nanopores: A review and perspective," *The Journal of Physical Chemistry C,* vol. 123, no. 35, pp. 21309-21326, 2019.

[39] D. Munoz-Santiburcio and D. Marx, "Confinement-controlled aqueous chemistry within nanometric slit pores: Focus review," *Chemical Reviews,* vol. 121, no. 11, pp. 6293-6320, 2021.

[40] X. Luo, H. Liu, C. Bae, M. E. Tuckerman, M. A. Hickner, and S. J. Paddison, "Mesoscale simulations of quaternary ammonium-tethered triblock copolymers: Effects of the degree of functionalization and styrene content," *The Journal of Physical Chemistry C,* vol. 124, no. 30, pp. 16315-16323, 2020.

[41] D. Dong, W. Zhang, A. C. Van Duin, and D. Bedrov, "Grotthuss versus vehicular transport of hydroxide in anion-exchange membranes: insight from combined reactive and nonreactive molecular simulations," *The Journal of Physical Chemistry Letters,* vol. 9, no. 4, pp. 825-829, 2018.

[42] K. Chand and O. Paladino, "Recent developments of membranes and electrocatalysts for the hydrogen production by anion exchange membrane water electrolysers: A review," *Arabian Journal of Chemistry,* vol. 16, no. 2, p. 104451, 2023.

[43] Y. Zhao *et al.*, "Rational design protocols to tune the morphology and conductivity of poly (arylene alkylene)-based anion exchange membranes," *Journal of Membrane Science,* vol. 688, p. 122132, 2023.

[44] K. Takahashi and L. Takahashi, "Toward the Golden Age of Materials Informatics: Perspective and Opportunities," *The Journal of Physical Chemistry Letters,* vol. 14, pp. 4726-4733, 2023.

[45] T. Wan, B. Shao, S. Ma, Y. Zhou, Q. Li, and Y. Chai, "In-sensor computing: materials, devices, and integration technologies," *Advanced materials,* vol. 35, no. 37, p. 2203830, 2023.

[46] M. Neubauer, C. Reiff, M. Walker, S. Oechsle, A. Lechler, and A. Verl, "Cloud-based evaluation platform for software-defined manufacturing: Cloud-basierte Evaluierungsplattform für Software-defined Manufacturing," *at-Automatisierungstechnik,* vol. 71, no. 5, pp. 351-363, 2023.

[47] C. Xie and H. Li, "Multiscale simulations of nanofluidics: Recent progress and perspective," *Wiley Interdisciplinary Reviews: Computational Molecular Science,* p. e1661, 2023.

[48] F. Wang and J. Cheng, "Understanding the solvation structures of glyme-based electrolytes by machine learning molecular dynamics," *Chinese Journal of Structural Chemistry,* p. 100061, 2023.

[49] Y. Liao, L. A. R. Pestana, and W. Xia, "Multiscale modeling of supramolecular assemblies of 2D materials," in *Fundamentals of Multiscale Modeling of Structural Materials*: Elsevier, 2023, pp. 389-423.

[50] J. Bi *et al.*, "Multiscale modeling for the science and engineering of materials," *International Journal for Multiscale Computational Engineering,* vol. 19, no. 3, 2021.

[51] J. Fish, G. J. Wagner, and S. Keten, "Mesoscopic and multiscale modelling in materials," *Nature materials,* vol. 20, no. 6, pp. 774-786, 2021.

[52] G. C. Peng *et al.*, "Multiscale modeling meets machine learning: What can we learn?," *Archives of Computational Methods in Engineering,* vol. 28, pp. 1017-1037, 2021.

[53] E. Van Der Giessen *et al.*, "Roadmap on multiscale materials modeling," *Modelling and Simulation in Materials Science and Engineering,* vol. 28, no. 4, p. 043001, 2020.

[54] A. A. Franco *et al.*, "Boosting rechargeable batteries R&D by multiscale modeling: myth or reality?," *Chemical reviews,* vol. 119, no. 7, pp. 4569-4627, 2019.

[55] N. E. Jackson, M. A. Webb, and J. J. de Pablo, "Recent advances in machine learning towards multiscale soft materials design," *Current Opinion in Chemical Engineering,* vol. 23, pp. 106-114, 2019.

[56] D. Dong *et al.*, "Multiscale modeling of structure, transport and reactivity in alkaline fuel cell membranes: Combined coarse-grained, atomistic and reactive molecular dynamics simulations," *Polymers,* vol. 10, no. 11, p. 1289, 2018.

[57] A. Agrawal and A. Choudhary, "Perspective: Materials informatics and big data: Realization of the “fourth paradigm” of science in materials science," *Apl Materials,* vol. 4, no. 5, 2016.

[58] J. LLorca *et al.*, "Multiscale modeling of composite materials: a roadmap towards virtual testing," *Advanced materials,* vol. 23, no. 44, pp. 5130-5147, 2011.

[59] T. Murtola, A. Bunker, I. Vattulainen, M. Deserno, and M. Karttunen, "Multiscale modeling of emergent materials: biological and soft matter," *Physical Chemistry Chemical Physics,* vol. 11, no. 12, pp. 1869-1892, 2009.

[60] M. M. Koleini, M. F. Mehraban, and S. Ayatollahi, "Effects of low salinity water on calcite/brine interface: A molecular dynamics simulation study," *Colloids and Surfaces A: Physicochemical and Engineering Aspects,* vol. 537, pp. 61-68, 2018.

[61] G. Kumar, T. R. Kartha, and B. S. Mallik, "Novelty of lithium salt solution in sulfone and dimethyl carbonate-based electrolytes for lithium-ion batteries: A conventional molecular dynamics simulation study of optimal ion diffusion," *The Journal of Physical Chemistry C,* vol. 122, no. 46, pp. 26315-26325, 2018.

[62] Y. Hori *et al.*, "Local Structures and Dynamics of Imidazole Molecules in Poly (vinylphosphonic acid)–Imidazole Composite Investigated by Molecular Dynamics," *ACS Applied Polymer Materials,* vol. 2, no. 4, pp. 1561-1568, 2020.

[63] S. G. Poulopoulos, G. Ulykbanova, and C. J. Philippopoulos, "Photochemical mineralization of amoxicillin medicinal product by means of UV, hydrogen peroxide, titanium dioxide and iron," *Environmental Technology,* vol. 42, no. 19, pp. 2941-2949, 2021.

[64] M. Mehana, Q. Kang, H. Nasrabadi, and H. Viswanathan, "Molecular modeling of subsurface phenomena related to petroleum engineering," *Energy & Fuels,* vol. 35, no. 4, pp. 2851-2869, 2021.

[65] H. Yu, H. Xu, J. Fan, Y.-B. Zhu, F. Wang, and H. Wu, "Transport of shale gas in microporous/nanoporous media: molecular to pore-scale simulations," *Energy & Fuels,* vol. 35, no. 2, pp. 911-943, 2020.

[66] K. Gharbi, K. Benyounes, and M. Khodja, "Removal and prevention of asphaltene deposition during oil production: A literature review," *Journal of Petroleum Science and Engineering,* vol. 158, pp. 351-360, 2017.

[67] I. Babich and J. Moulijn, "Science and technology of novel processes for deep desulfurization of oil refinery streams: a review☆," *Fuel,* vol. 82, no. 6, pp. 607-631, 2003.

[68] S. A. Adcock and J. A. McCammon, "Molecular dynamics: survey of methods for simulating the activity of proteins," *Chemical reviews,* vol. 106, no. 5, pp. 1589-1615, 2006.

[69] D. Lu, Z. Liu, and J. Wu, "Structural transitions of confined model proteins: molecular dynamics simulation and experimental validation," *Biophysical Journal,* vol. 90, no. 9, pp. 3224-3238, 2006.

[70] N. Hu, H. Fukunaga, C. Lu, M. Kameyama, and B. Yan, "Prediction of elastic properties of carbon nanotube reinforced composites," *Proceedings of the Royal Society A: Mathematical, Physical and Engineering Sciences,* vol. 461, no. 2058, pp. 1685-1710, 2005.

[71] S. Sahmani and A. Fattahi, "An anisotropic calibrated nonlocal plate model for biaxial instability analysis of 3D metallic carbon nanosheets using molecular dynamics simulations," *Materials Research Express,* vol. 4, no. 6, p. 065001, 2017.

[72] R. Tebeta, A. Fattahi, and N. Ahmed, "Experimental and numerical study on HDPE/SWCNT nanocomposite elastic properties considering the processing techniques effect," *Microsystem Technologies,* vol. 26, pp. 2423-2441, 2020.

[73] M. Konishi and H. Washizu, "Understanding the effect of the base oil on the physical adsorption process of organic additives using molecular dynamics," *Tribology International,* vol. 149, p. 105568, 2020.

[74] M. Amouei Torkmahalleh, M. Karibayev, D. Konakbayeva, M. Fyrillas, and A. M. Rule, "Aqueous chemistry of airborne hexavalent chromium during sampling," *Air Quality, Atmosphere & Health,* vol. 11, pp. 1059-1068, 2018.

[75] E. Benassi and P. S. Sherin, "Theoretical study of solvent influence on the electronic absorption and emission spectra of kynurenine," *International Journal of Quantum Chemistry,* vol. 111, no. 14, pp. 3799-3804, 2011.

[76] L. Riccardi, V. Genna, and M. De Vivo, "Metal–ligand interactions in drug design," *Nature Reviews Chemistry,* vol. 2, no. 7, pp. 100-112, 2018.

[77] J. H. Panchal, S. R. Kalidindi, and D. L. McDowell, "Key computational modeling issues in integrated computational materials engineering," *Computer-Aided Design,* vol. 45, no. 1, pp. 4-25, 2013.

[78] G. B. Olson, "Computational design of hierarchically structured materials," *Science,* vol. 277, no. 5330, pp. 1237-1242, 1997.

[79] W. J. Joost, "Reducing vehicle weight and improving US energy efficiency using integrated computational materials engineering," *Jom,* vol. 64, pp. 1032-1038, 2012.

[80] T. Ogawa, M. Takeuchi, and Y. Kajikawa, "Comprehensive analysis of trends and emerging technologies in all types of fuel cells based on a computational method," *Sustainability,* vol. 10, no. 2, p. 458, 2018.

[81] R. G. Parr, "Density functional theory," *Annual Review of Physical Chemistry,* vol. 34, no. 1, pp. 631-656, 1983.

[82] A. J. Cohen, P. Mori-Sánchez, and W. Yang, "Challenges for density functional theory," *Chemical reviews,* vol. 112, no. 1, pp. 289-320, 2012.

[83] R. Tsuchitani, H. Nakanishi, and H. Kasai, "An Initial Degradation mechanism Reaction before Ring-Opening in Imidazolium-Based Anion Exchange Membranes: A DFT Study," *e-Journal of Surface Science and Nanotechnology,* vol. 11, pp. 138-141, 2013.

[84] H. Long, K. Kim, and B. S. Pivovar, "Hydroxide degradation mechanism pathways for substituted trimethylammonium cations: a DFT study," *The Journal of Physical Chemistry C,* vol. 116, no. 17, pp. 9419-9426, 2012.

[85] H. Long and B. Pivovar, "Hydroxide degradation mechanism pathways for imidazolium cations: A DFT study," *The Journal of Physical Chemistry C,* vol. 118, no. 19, pp. 9880-9888, 2014.

[86] G. Yang *et al.*, "Hydroxide ion transfer in anion exchange membrane: A density functional theory study," *International Journal of Hydrogen Energy,* vol. 41, no. 16, pp. 6877-6884, 2016.

[87] T. Xiang and H. Si, "Theoretical study of the degradation mechanism mechanisms of substituted phenyltrimethylammonium cations," *Computational and Theoretical Chemistry,* vol. 1065, pp. 12-17, 2015.

[88] D. R. Dekel, M. Amar, S. Willdorf, M. Kosa, S. Dhara, and C. E. Diesendruck, "Effect of water on the stability of quaternary ammonium groups for anion exchange membrane fuel cell applications," *Chemistry of Materials,* vol. 29, no. 10, pp. 4425-4431, 2017.

[89] S. Chempath, J. M. Boncella, L. R. Pratt, N. Henson, and B. S. Pivovar, "Density functional theory study of degradation mechanism of tetraalkylammonium hydroxides," *The Journal of Physical Chemistry C,* vol. 114, no. 27, pp. 11977-11983, 2010.

[90] S. Chempath *et al.*, "Mechanism of tetraalkylammonium headgroup degradation mechanism in alkaline fuel cell membranes," *The Journal of Physical Chemistry C,* vol. 112, no. 9, pp. 3179-3182, 2008.

[91] W. Wang, S. Wang, X. Xie, and V. Ramani, "Density functional theory study of hydroxide-ion induced degradation mechanism of imidazolium cations," *International journal of hydrogen energy,* vol. 39, no. 26, pp. 14355-14361, 2014.

[92] R. Espiritu, J. L. Tan, L. H. Lim, and S. Arco, "Density functional theory study on the degradation mechanism of fuel cell anion exchange membranes via removal of vinylbenzyl quaternary ammonium head group," *Journal of Physical Organic Chemistry,* vol. 33, no. 5, p. e4049, 2020.

[93] D. A. Salvatore *et al.*, "Designing anion exchange membranes for CO2 electrolysers," *Nature Energy,* vol. 6, no. 4, pp. 339-348, 2021.

[94] S. Castañeda and R. Ribadeneira, "Theoretical description of the structural characteristics of the quaternized SEBS Anion-Exchange Membrane Using DFT," *The Journal of Physical Chemistry C,* vol. 119, no. 51, pp. 28235-28246, 2015.

[95] J. Parrondo, Z. Wang, M.-S. J. Jung, and V. Ramani, "Reactive oxygen species accelerate degradation mechanism of anion exchange membranes based on polyphenylene oxide in alkaline environments," *Physical chemistry chemical physics,* vol. 18, no. 29, pp. 19705-19712, 2016.

[96] D. R. Dekel *et al.*, "The critical relation between chemical stability of cations and water in anion exchange membrane fuel cells environment," *Journal of Power Sources,* vol. 375, pp. 351-360, 2018.

[97] N. Zhang *et al.*, "Understanding of imidazolium group hydration and polymer structure for hydroxide anion conduction in hydrated imidazolium-g-PPO membrane by molecular dynamics simulations," *Chemical Engineering Science,* vol. 192, pp. 1167-1176, 2018.

[98] W. Zhang and A. C. Van Duin, "ReaxFF reactive molecular dynamics simulation of functionalized poly (phenylene oxide) anion exchange membrane," *The Journal of Physical Chemistry C,* vol. 119, no. 49, pp. 27727-27736, 2015.

[99] W. Zhang, D. Dong, D. Bedrov, and A. C. Van Duin, "Hydroxide transport and chemical degradation mechanism in anion exchange membranes: a combined reactive and non-reactive molecular simulation study," *Journal of Materials Chemistry A,* vol. 7, no. 10, pp. 5442-5452, 2019.

[100] L. Wu *et al.*, "Tunable OH–transport and alkaline stability by imidazolium-based groups of poly (2, 6-dimethyl-1, 4-phenylene oxide) anion exchange membranes: a molecular dynamics simulation," *Industrial & Engineering Chemistry Research,* vol. 60, no. 6, pp. 2481-2491, 2021.

[101] Y.-L. S. Tse *et al.*, "Chloride enhances fluoride mobility in anion exchange membrane/polycationic systems," *The Journal of Physical Chemistry C,* vol. 118, no. 2, pp. 845-853, 2014.

[102] V. Dubey, A. Maiti, and S. Daschakraborty, "Predicting the solvation structure and vehicular diffusion of hydroxide ion in an anion exchange membrane using nonreactive molecular dynamics simulation," *Chemical Physics Letters,* vol. 755, p. 137802, 2020.

[103] D. J. Kim, C. H. Park, and S. Y. Nam, "Molecular dynamics simulations of modified PEEK polymeric membrane for fuel cell application," *international journal of hydrogen energy,* vol. 41, no. 18, pp. 7641-7648, 2016.

[104] H. Takaba, T. Hisabe, T. Shimizu, and M. K. Alam, "Molecular modeling of OH− transport in poly (arylene ether sulfone ketone) s containing quaternized ammonio-substituted fluorenyl groups as anion exchange membranes," *Journal of Membrane Science,* vol. 522, pp. 237-244, 2017.

[105] K. W. Han, K. H. Ko, K. Abu-Hakmeh, C. Bae, Y. J. Sohn, and S. S. Jang, "Molecular dynamics simulation study of a polysulfone-based anion exchange membrane in comparison with the proton exchange membrane," *The Journal of Physical Chemistry C,* vol. 118, no. 24, pp. 12577-12587, 2014.

[106] J. L. Di Salvo, G. De Luca, A. Cipollina, and G. Micale, "Effect of ion exchange capacity and water uptake on hydroxide transport in PSU-TMA membranes: A DFT and molecular dynamics study," *Journal of Membrane Science,* vol. 599, p. 117837, 2020.

[107] X. Tongwen and Y. Weihua, "Fundamental studies of a new series of anion exchange membranes: membrane preparation and characterization," *Journal of Membrane Science,* vol. 190, no. 2, pp. 159-166, 2001.

[108] C. Wang *et al.*, "Crosslinked norbornene copolymer anion exchange membrane for fuel cells," *Journal of Membrane Science,* vol. 556, pp. 118-125, 2018.

[109] C. Wang *et al.*, "Hydroxide ions diffusion in polynorbornene anion exchange membrane," *Polymer,* vol. 138, pp. 363-368, 2018.

[110] S. Kim, S. Yang, and D. Kim, "Poly (arylene ether ketone) with pendant pyridinium groups for alkaline fuel cell membranes," *International journal of hydrogen energy,* vol. 42(17), pp. 12496-12506, 2017.

[111] D. J. Kim, B. N. Lee, and S. Y. Nam, "Synthesis and characterization of PEEK containing imidazole for anion exchange membrane fuel cell," *International journal of hydrogen energy*, vol. 42(37), pp. 23759-23767, 2017.

[112] Q. Yang, C. X. Lin, F. H. Liu, L. Li, Q. G. Zhang, A. M. Zhu, and Q. L. Liu, "Poly (2, 6-dimethyl-1, 4-phenylene oxide)/ionic liquid functionalized graphene oxide anion exchange membranes for fuel cells," *Journal of membrane science*, vol. 552, pp. 367-376, 2018.

[113] Y. Gong, X. Liao, J. Xu, D. Chen and H. Zhang, "Novel anion-conducting interpenetrating polymer network of quaternized polysulfone and poly (vinyl alcohol) for alkaline fuel cells," *International journal of hydrogen energy*, vol 41(13), pp. 5816-5823, 2016.

[114] Y. Wang, Y. Long, Z. Yang, and D. Zhang, "A novel ion-exchange strategy for the fabrication of high strong BiOI/BiOBr heterostructure film coated metal wire mesh with tunable visible-light-driven photocatalytic reactivity," *Journal of hazardous materials*, vol. 351, pp. 11-19, 2018.

[115] A. N. Lai, D. Guo, C. X. Lin, Q. G. Zhang, A. M. Zhu, M. L. Ye and Q. L. Liu, "Enhanced performance of anion exchange membranes via crosslinking of ion cluster regions for fuel cells," *Journal of Power Sources*, vol. 327, pp. 56-66, 2016.

[116] A. N. Lai, K. Zhou, Y. Z. Zhuo, Q. G. Zhang, A. M. Zhu, M. L. Ye and Q. L. Liu "Anion exchange membranes based on carbazole-containing polyolefin for direct methanol fuel cells," *Journal of Membrane Science*, vol. 497, pp. 99-107, 2016.

[117] Z. Luo, Y. Gong, X. Liao, Y. Pan and H. Zhang, H, "Nanocomposite membranes modified by graphene-based materials for anion exchange membrane fuel cells," *RSC advances*, vol. *6*(17), pp. 13618-13625, 2016.

[118] R. Hussain *et al.*, "Density functional theory study of palladium cluster adsorption on a graphene support," *RSC advances*, vol. 10, no. 35, pp. 20595-20607, 2020.

[119] A. D. Mohanty and C. Bae, "Mechanistic analysis of ammonium cation stability for alkaline exchange membrane fuel cells," J. Mater. Chem. A, vol. 2, pp. 17314–17320, 2014.

[120] Y. Tsutsumi, "Schrodinger equation," *Funkcialaj Ekvacioj*, vol. 30, pp. 115-125, 1987.

[121] M. Born, R. Oppenheimer "Zur Quantentheorie der Molekeln," *Annalen der Physik*, vol. 84, pp. 457, 1927.

[122] P. Hohenberg, W. Kohn, "Inhomogeneous electron gas," *Physical Review*, vol. 136, pp. 864, 1964.

[123] J. L. Durant, "Evaluation of transition state properties by density functional theory," *Chemical physics letters*, vol. 256(6), pp. 595-602, 1996.

[124] S. Schenker, C. Schneider, S. B. Tsogoeva, and T. Clark, "Assessment of popular DFT and semiempirical molecular orbital techniques for calculating relative transition state energies and kinetic product distributions in enantioselective organocatalytic reactions," *Journal of Chemical Theory and Computation*, vol. 7(11), pp. 3586-3595, 2011.

[125] M. Saeys, M. F. Reyniers, G. B. Marin, V. Van Speybroeck, and M. Waroquier, "Ab initio calculations for hydrocarbons: enthalpy of formation, transition state geometry, and

activation energy for radical reactions," *The Journal of Physical Chemistry A*, vol. 107(43), pp. 9147-9159, 2003.

[126] J. Hafner, "Ab-initio simulations of materials using VASP: Density-functional theory and beyond," *Journal of computational chemistry*, vol. 29(13), pp. 2044-2078, 2008.

[127] A. Bayrakdar, H. H. Kart, S. Elcin, H. Deligoz, and M. Karabacak, "Synthesis and DFT calculation of a novel 5, 17-di (2-antracenylazo)-25, 27-di (ethoxycarbonylmethoxy)-26, 28-dihydroxycalix [4] arene," *Spectrochimica Acta Part A: Molecular and Biomolecular Spectroscopy*, vol. 136, pp. 607-617, 2015.

[128] L. Malakkal, B. Szpunar, J. C. Zuniga, R. K. Siripurapu, and J. A. Szpunar, "First principles calculation of thermo-mechanical properties of thoria using Quantum ESPRESSO," *International Journal of Computational Materials Science and Engineering*, vol. *5*(02), pp. 1650008, 2016.

[129] Y. Huang, C. Rong, R. Zhang, and S. Liu, "Evaluating frontier orbital energy and HOMO/LUMO gap with descriptors from density functional reactivity theory," *Journal of molecular modeling*, vol. 23, pp. 1-12, 2017.

[130] D. D. Méndez-Hernández, P. Tarakeshwar, D. Gust, T. A. Moore, A. L. Moore, and V. Mujica, "Simple and accurate correlation of experimental redox potentials and DFT-calculated HOMO/LUMO energies of polycyclic aromatic hydrocarbons," *Journal of molecular modeling*, *19*, 2845-2848, 2013.

[131] C. Parks, E. Alborzi, M. Akram, and M. Pourkashanian, "DFT studies on thermal and oxidative degradation of monoethanolamine," *Industrial & Engineering Chemistry Research*, vol. 59(34), pp. 15214-15225, 2020.

[132] T. Joutsuka, "Molecular Mechanism of Autodissociation in Liquid Water: Ab Initio Molecular Dynamics Simulations," *The Journal of Physical Chemistry B*, vol. 126, no. 24, pp. 4565-4571, 2022.

[133] S. Yamabe, N. Tsuchida, S. Yamazaki, and S. Sakaki, "Frontier orbitals and transition states in the oxidation and degradation of l-ascorbic acid: a DFT study," *Organic & biomolecular chemistry*, vol. 13(13), pp. 4002-4015, 2015.

[134] A. H. Mazurek, L. Szeleszczuk, and D. M. Pisklak, "Periodic DFT calculations—review of applications in the pharmaceutical sciences," *Pharmaceutics*, vol. 12(5), pp. 415, 2020.

[135] M. Orio, D. A. Pantazis, and F. Neese, "Density functional theory," *Photosynthesis research*, vol. 102, pp. 443-453, 2009.

[136] M. C. Zwier and L. T. Chong, "Reaching biological timescales with all-atom molecular dynamics simulations," *Current opinion in pharmacology*, vol. 10, no. 6, pp. 745-752, 2010.

[137] E. R. Henry, R. B. Best, and W. A. Eaton, "Comparing a simple theoretical model for protein folding with all-atom molecular dynamics simulations," *Proceedings of the National Academy of Sciences*, vol. 110, no. 44, pp. 17880-17885, 2013.

[138] G. Shahane, W. Ding, M. Palaiokostas, and M. Orsi, "Physical properties of model biological lipid bilayers: insights from all-atom molecular dynamics simulations," *Journal of molecular modeling*, vol. 25, pp. 1-13, 2019.

[139] A. Hospital, J. R. Goñi, M. Orozco, and J. L. Gelpí, "Molecular dynamics simulations: advances and applications," *Advances and Applications in Bioinformatics and Chemistry,* pp. 37-47, 2015.

[140] J. Whittaker and L. Delle Site, "Investigation of the hydration shell of a membrane in an open system molecular dynamics simulation," *Physical Review Research,* vol. 1, no. 3, p. 033099, 2019.

[141] D. Jones *et al.*, "Accelerators for conventional molecular dynamics simulations of biomolecules," *Journal of chemical theory and computation,* vol. 18, no. 7, pp. 4047-4069, 2022.

[142] Y. V. Sereda and P. J. Ortoleva, "Temporally Coarse-Grained All-Atom Molecular Dynamics Achieved via Stochastic Padé Approximants," *The Journal of Physical Chemistry B,* vol. 124, no. 8, pp. 1392-1410, 2020.

[143] V. Monje-Galvan, L. Warburton, and J. B. Klauda, "Setting up all-atom molecular dynamics simulations to study the interactions of peripheral membrane proteins with model lipid bilayers," *Intracellular Lipid Transport: Methods and Protocols,* pp. 325-339, 2019.

[144] B. Qiao and W. Jiang, "All-Atom Molecular Dynamics Study of Water–Dodecane Interface in the Presence of Octanol," *The Journal of Physical Chemistry C,* vol. 122, no. 1, pp. 687-693, 2018.

[145] B. Hess, C. Kutzner, D. Van Der Spoel, and E. Lindahl, "GROMACS 4: algorithms for highly efficient, load-balanced, and scalable molecular simulation," *Journal of chemical theory and computation,* vol. 4, no. 3, pp. 435-447, 2008.

[146] N. Aho, P. Buslaev, A. Jansen, P. Bauer, G. Groenhof, and B. Hess, "Scalable constant pH molecular dynamics in GROMACS," *Journal of Chemical Theory and Computation,* vol. 18, no. 10, pp. 6148-6160, 2022.

[147] M. Karibayev, B. Myrzakhmetov, S. Kalybekkyzy, Y. Wang, and A. Mentbayeva, "Binding and Degradation mechanism Reaction of Hydroxide Ions with Several Quaternary Ammonium Head Groups of Anion Exchange Membranes Investigated by the DFT Method," *Molecules,* vol. 27, no. 9, p. 2686, 2022.

[148] M. Karibayev, B. Myrzakhmetov, D. Bekeshov, Y. Wang, and A. Mentbayeva, "Atomistic Modeling of Quaternized Chitosan Head Groups: Insights into Chemical Stability and Ion Transport for Anion Exchange Membrane Applications," *Molecules,* vol. *29, no.* 13, p.3175, 2024.

[149] P. J. Stephens, F. J. Devlin, C. F. Chabalowski, and M. J. Frisch, "Ab Initio Calculation of Vibrational Absorption and Circular Dichroism Spectra Using Density Functional Force Fields," J. Phys. Chem., vol. 98, pp. 11623–11627, 1994.

[150] B. Mennucci, "Polarizable continuum model," WIREs Comput. Mol. Sci., vol. 2, pp. 386–404, 2012.

[151] S. Seenithurai, J. D. Chai, "TAO-DFT with the Polarizable Continuum Model," Nanomaterials, vol. 13, no. 10, pp. 1593, 2023.

[152] K. B. Koziara, M. Stroet, A. K. Malde, and A. E. Mark, "Testing and validation of the Automated Topology Builder (ATB) version 2.0: Prediction of hydration free enthalpies," J. Comput. Mol. Des., vol. 28, pp. 221–233, 2014.

[153] A. D. Becke, "A new mixing of Hartree-Fock and local density-functional theories," J. Chem. Phys., vol. 98, pp. 1372–1377, 1993.

[154] P. M. Gill, B. G. Johnson, J. A. Pople, and M. J. Frisch, "The performance of the Becke-Lee-Yang-Parr (B-LYP) density functional theory with various basis sets," Chem. Phys. Lett., vol. 197, pp. 499–505, 1992.

[155] E. V. R. De Castro and F. E. Jorge, "Accurate universal Gaussian basis set for all atoms of the Periodic Table," J. Chem. Phys., vol. 108, pp. 5225–5229, 1998. [CrossRef]

[156] M. J. Frisch et al., "G16_C01, Gaussian 16, Revision, C.01," Gaussian, Inc., Wallingford, CT, USA, 2016.

[157] S. Noh, J. Y. Jeon, S. Adhikari, Y. S. Kim, and C. Bae, "Molecular Engineering of Hydroxide Conducting Polymers for Anion Exchange Membranes in Electrochemical Energy Conversion Technology," Acc. Chem. Res., vol. 52, pp. 2745–2755, 2019.

[158] J. E. Chae, S. Y. Lee, S. J. Yoo, J. Y. Kim, J. H. Jang, H. Y. Park, et al. "Polystyrene-based hydroxide-ion-conducting ionomer: binder characteristics and performance in anion-exchange membrane fuel cells," *Polymers*, vol. *13*(5), pp. 690, 2021.

[159] M. Karibayev *et al.*, "Effect of hydration on the intermolecular interaction of various quaternary ammonium based head groups with hydroxide ion of anion exchange membrane studied at the molecular level," *Eurasian Chemico-Technological Journal,* vol. 25, no. 2, pp. 89-102, 2023.

[160] P. Podio-Guidugli, "On (Andersen–) Parrinello–Rahman molecular dynamics, the related metadynamics, and the use of the Cauchy–Born rule," *Journal of Elasticity,* vol. 100, pp. 145–153, 2010.

[161] H. J. C. Berendsen, "Transport properties computed by linear response through weak coupling to a bath," in *Computer Simulation in Materials Science: Interatomic Potentials, Simulation Techniques and Applications,* pp. 139–155, Springer Netherlands, 1991.

[162] W. Humphrey, A. Dalke, and K. Schulten, "VMD: Visual Molecular Dynamics," *Journal of Molecular Graphics,* vol. 14, no. 1, pp. 33–38, 1996.

[163] C. Johansson et al., "Renewable fibers and bio-based materials for packaging applications–a review of recent developments," *BioResources,* vol. 7, no. 2, pp. 2506–2552, 2012.

[164] A. Gandini, "Polymers from renewable resources: a challenge for the future of macromolecular materials," *Macromolecules,* vol. 41, no. 24, pp. 9491–9504, 2008.

[165] Y. Shchipunov, N. Ivanova, and V. Silant'ev, "Bionanocomposites formed by in situ charged chitosan with clay," *Green Chemistry,* vol. 11, no. 11, pp. 1758–1761, 2009.

[166] A. Giannakas et al., "Preparation, characterization, mechanical and barrier properties investigation of chitosan–clay nanocomposites," *Carbohydrate Polymers,* vol. 108, pp. 103–111, 2014.

[167] D. H. Kang et al., "A composite anion conducting membrane based on quaternized cellulose and poly(phenylene oxide) for alkaline fuel cell applications," *Polymers,* vol. 12, no. 11, 2020.

[168] Y. Lu et al., "A cellulose nanocrystal-based composite electrolyte with superior dimensional stability for alkaline fuel cell membranes," *J. Mater. Chem. A,* vol. 3, pp. 13350–13356, 2015.

[169] J. Ryu et al., "Quaternized chitosan-based anion exchange membrane for alkaline direct methanol fuel cells," *Journal of Industrial and Engineering Chemistry*, vol. 73, pp. 254–259, 2019.

[170] S. Muhmed et al., "Emerging chitosan and cellulose green materials for ion exchange membrane fuel cell: a review," *Energy, Ecology and Environment,* 2019.

[171] P. Kumar Dutta, J. Dutta, and V. Tripathi, "Chitin and chitosan: Chemistry, properties and applications," *Journal of scientific & industrial research,* vol. 63, pp. 20–31, 2004.

[172] H. Wu et al., "Surface-modified zeolite-filled chitosan membrane for direct methanol fuel cell," *J. Power Sources,* vol. 173, no. 2, pp. 842–852, 2007.

[173] Z. Cui et al., "Ionic interactions between sulfuric acid and chitosan membranes," *Carbohydr. Polym.,* vol. 73, no. 1, pp. 111–116, 2008.

[174] S. Ojha et al., "Fabrication and characterization of electrospun chitosan nanofibers formed via templating with polyethylene oxide," *Biomacromolecules,* vol. 9, no. 9, pp. 2523–2529, 2008.

[175] A. Tiraferri et al., "Mechanism of chitosan adsorption on silica from aqueous solutions," *Langmuir,* vol. 30, no. 17, pp. 4980–4988, 2014.

[176] H, Lu, J. Chen, S. Gao, C. Shen, "N and non-N site grafting piperidinium group to chitosan for anion exchange membrane," *Ionics.*, vol. 29, no. 5, p. 1831-1845, 2023.

[177] A. Dias et al., "Development of greener multi-responsive chitosan biomaterials doped with biocompatible ammonium ionic liquids," *ACS Sustain. Chem. Eng.,* vol. 1, no. 11, pp. 1480–1492, 2013.

[178] H. Vaghari et al., "Recent advances in the application of chitosan in fuel cells," *Sustain. Chem. Process.,* vol. 1, no. 1, pp. 1–12, 2013.

[179] P. Murugaraj et al., "Probing the dynamics of water in chitosan polymer films by dielectric spectroscopy," *J. Appl. Polym. Sci.,* vol. 120, no. 3, pp. 1307–1315, 2011.

[180] J. Wang et al., "Proton exchange membrane based on chitosan and solvent-free carbon nanotube fluids for fuel cells applications," *Carbohydr. Polym.,* vol. 186, pp. 200–207, 2018.

[181] B. Smitha, S. Sridhar, and A. Khan, "Chitosan–poly (vinyl pyrrolidone) blends as membranes for direct methanol fuel cell applications," *J. Power Sources,* vol. 159, no. 2, pp. 846–854, 2006.

[182] J. Wang et al., "Effect of zeolites on chitosan/zeolite hybrid membranes for direct methanol fuel cell," *J. Power Sources,* vol. 178, no. 1, pp. 9–19, 2008.

[183] P. O. Osifo and A. Masala, "Characterization of direct methanol fuel cell (DMFC) applications with H2SO4 modified chitosan membrane," *J. Power Sources,* vol. 195, no. 15, pp. 4915–4922, 2010.

[184] E. Tomasino, B. Mukherjee, N. Ataollahi, P. Scardi, "Water Uptake in an Anion Exchange Membrane Based on Polyamine: A First-Principles Study," *The Journal of Physical Chemistry B,* vol. 126(38), pp. 7418-7428, 2022.

[185] H. Zhang, X. Wang, Y. Wang, Y. Zhang, W. Zhang, W. You, "Alkaline-Stable Anion-Exchange Membranes with Barium [2.2. 2] Cryptate Cations: The Importance of High Binding Constants," *Angewandte Chemie*, vol. 135(15), pp. 202217742, 2023.

[186] S.-C. Jang, W.-C. Tsen, F.-S. Chuang, and C. Gong, "Simultaneously enhanced hydroxide conductivity and mechanical properties of quaternized chitosan/functionalized carbon nanotubes composite anion exchange membranes," *Int. J. Hydrog. Energy*, vol. 44, no. 33, pp. 18134–18144, 2019.

[187] L. T. T. Nhung, I. Y. Kim, and Y. S. Yoon, "Quaternized chitosan-based anion exchange membrane composited with quaternized poly (vinylbenzyl chloride)/polysulfone blend," *Polymers*, vol. 12, p. 2714, 2020.

[188] S. Zhao, W.-C. Tsen, and C. Gong, "3D nanoflower-like layered double hydroxide modified quaternized chitosan/polyvinyl alcohol composite anion conductive membranes for fuel cells," *Carbohydr. Polym.*, vol. 256, p. 117439, 2021.

[189] E. López-Chávez et al., "Molecular modeling and simulation of ion conductivity in chitosan membranes," *Polymer*, vol. 46, no. 18, pp. 7519–7527, 2005.

[190] F. Muller-Plathe, "Permeation of polymers—a computational approach," *Acta Polymerica*, vol. 45, no. 4, pp. 259–293, 1994.

[191] Y. Wan et al., "Ionic conductivity and related properties of crosslinked chitosan membranes," *J. Appl. Polym. Sci.*, vol. 89, no. 2, pp. 306–317, 2003.

[192] Y. Wan et al., "Synthesis, characterization and ionic conductive properties of phosphorylated chitosan membranes," *Macromol. Chem. Phys.*, vol. 204, no. 5-6, pp. 850–858, 2003.

[193] Y. Wan et al., "Quaternized-chitosan membranes for possible applications in alkaline fuel cells," *J. Power Sources*, vol. 185, no. 1, pp. 183–187., 2008.

[194] J. Xu, G. Du, Y. Zhai, G. Guan, & Y. Wang. “Synthesis of deep eutectic solvents of N, N, N-trimethyl butylsulphonate ammonium hydrosulfate-urea and their performance investigation as electrolytes in fuel cells”. *Ionics*, 1-10, 2023.

[195] A. Kityk, V. Pavlik, & M. Hnatko. “Exploring deep eutectic solvents for the electrochemical and chemical synthesis of photo-and electrocatalysts for hydrogen evolution” *International Journal of Hydrogen Energy*, 2023.

[196] S. Guan, B. Xu, J. Wu, J. Han, T. Guan, Y. Yang,, et. al. “High-entropy materials based on deep eutectic solvent for boosting oxygen evolution reaction”. *Fuel*, *358*, 130315, 2024.

[197] Q. Ma, W. Fu, L. Zhao, Z. Chen, H. Su, & Q. Xu. “A double-layer electrode for the negative side of deep eutectic solvent electrolyte-based vanadium-iron redox flow battery”. *Energy*, *265*, 126291, 2023.

[198] J. Xu, J. Hao, Y. Zhai, & Y. Wang. “Deep eutectic solvents based on N, N, N-trimethyl propylsulphonate ammonium hydrosulfate-urea as potential electrolytes for proton exchange membrane fuel cell”. *Journal of Power Sources*, *580*, 233385, 2023

[199] Y. Hariyanto, Y. K. Ng, Z. Z. Siew, C. Y. Soon, A. C. Fisher, *et. al.* “Deep Eutectic Solvents for Batteries and Fuel Cells: Biosubstitution, Advantages, Challenges, and Future Directions”. *Energy & Fuels*. 2023.

[200] R. Devanathan, N. Idupulapati, M. D. Baer, C. J. Mundy, and M. Dupuis, "Ab initio molecular dynamics simulation of proton hopping in a model polymer membrane," The Journal of Physical Chemistry B, vol. 117, no. 51, pp. 16522-16529, 2013.

[201] A. Govind Rajan, M. S. Strano, and D. Blankschtein, "Ab initio molecular dynamics and lattice dynamics-based force field for modeling hexagonal boron nitride in mechanical and interfacial applications," The Journal of Physical Chemistry Letters, vol. 9, no. 7, pp. 1584-1591, 2018.

[202] G. Tocci, L. Joly, and A. Michaelides, "Friction of water on graphene and hexagonal boron nitride from ab initio methods: very different slippage despite very similar interface structures," Nano Letters, vol. 14, no. 12, pp. 6872-6877, 2014.

[203] B. Grosjean, A. Robert, R. Vuilleumier, and M. L. Bocquet, "Spontaneous liquid water dissociation on hybridised boron nitride and graphene atomic layers from ab initio molecular dynamics simulations," Physical Chemistry Chemical Physics, vol. 22, no. 19, pp. 10710-10716, 2020.

[204] E. D. Wetzel, R. Balu, and T. D. Beaudet, "A theoretical consideration of the ballistic response of continuous graphene membranes," Journal of the Mechanics and Physics of Solids, vol. 82, pp. 23-31, 2015.

[205] J. K. Shah, "Ab initio molecular dynamics simulations of ionic liquids," in Annual Reports in Computational Chemistry, vol. 14, pp. 95-122, Elsevier, 2018.

[206] C. J. Mundy, "Ab initio approach to interfacial processes in hydrogen bonded fluids," in Airlie Conference Center Warrenton Virginia October 19-22, 2008, p. 179, October 2008.

Appendix A

Molecular Electrostatic Potential Maps (MEPs)

The MEPs for binding of OH^- ion with different QA head groups are illustrated in **Figure A1**.

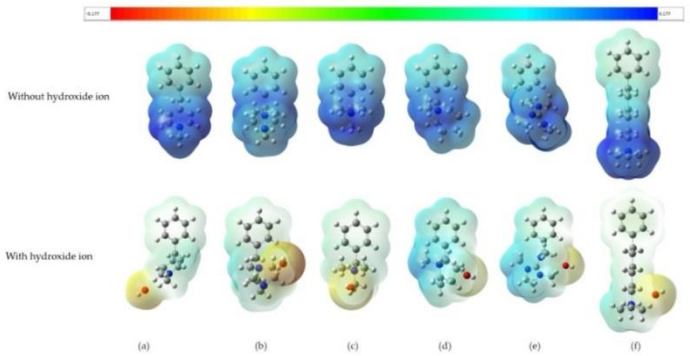

Figure A1. Representation of MEPs for different QA head groups with OH^- ion.

Initially, OH^- ion was placed near trimethyl ammonium part of QA. It is important to note that OH^- ion interacts with trimethylammonium part of QA to stabilize the positive charge (**Figure A1**).

Binding Energies

$E_{Binding}$ for OH^- ions with different QA head groups is illustrated in **Figure A2** and **Table A1**.

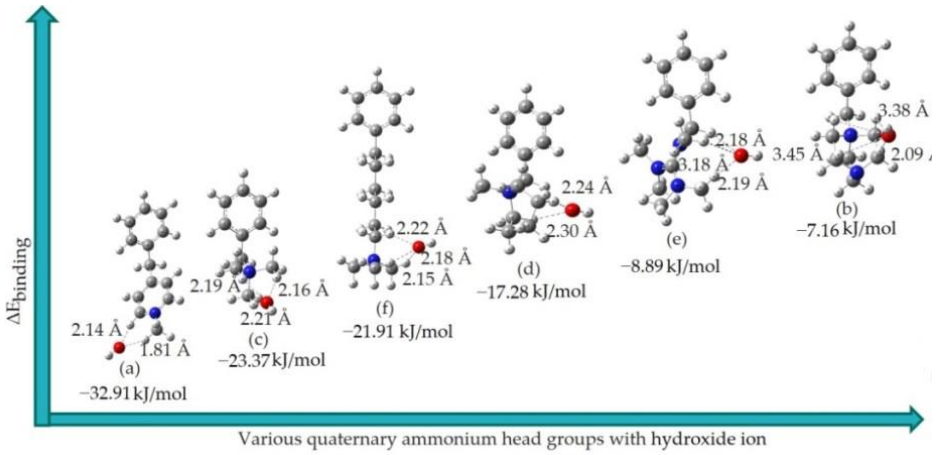

Figure A2. Different QA head groups with OH^- ion.

As depicted in **Table A1**, there is a noteworthy variation in the the $\Delta E_{Binding}$ among various QA head groups when binding to OH^- ions.

Table A1: The binding energies $\Delta E_{Binding}$ of QA with OH^- ion, $\Delta E_{binding} = E_{QA\ with\ OH^-} - (E_{QA} + E_{OH^-})$.

QA	E (OH^-) (kJ/mol)	E (QA) (kJ/mol)	E (QA with OH^-) (kJ/mol)	$\Delta E_{binding}$ (kJ/mol)
(a)	−199431.16	−1466500.19	−1665964.27	−32.91
(c)	−199431.16	−1169420.80	−1368875.34	−23.37
(f)	−199431.16	−1685662.20	−1885115.30	−21.91
(d)	−199431.16	−1475970.88	−1675419.33	−17.28
(e)	−199431.16	−1766722.23	−1966162.29	−8.89
(b)	−199431.16	−1618116.55	−1817554.88	−7.16

The values of energies and free energies for DFT calculation are illustrated in **Table A2** and **A3**.

Table A2: Energy values for S_N2 degradation mechanism of QA (a)-(f). Unit: kJ/mol.

QA	HL	E(R1)	E(R2)	E(TS)	E(P1)	E(P2)	E(P3)
(a)	0	-1466500.19	-199429.14	-1665901.36	-1362124.64	-303952.44	-
(b)	0	-1618116.55	-199429.14	-1817513.49	-906940.79	-910733.09	-
(c)	0	-1169446.34	-199429.14	-1368822.03	-910761.97	-458238.23	-
	1	-1169446.34	-400248.63	-1569632.52	-910761.97	-458238.23	-200764.45
	2	-1169446.34	-601059.62	-1770433,28	-910761.97	-458238.23	-401545.78
	3	-1169446.34	-801864.08	-1971217.59	-910761.97	-458238.23	-602329.96
(d)	0	-1475026.77	-199429.14	-1674412.18	-910761.97	-763816.78	-
(e)	0	-1765546.15	-199429.14	-1964922.09	-910761.97	-1054335.46	-
(f)	0	-1685699.31	-199429.14	-1885054.44	-1427011.42	-458238.23	-
	1	-1685699.31	-400248.63	-2085861.6	-1427011.42	-458238.23	-200764.45
	2	-1685699.31	-601059.62	-2286662.47	-1427011.42	-458238.23	-401545.78
	3	-1685699.31	-801864.08	-2487450.75	-1427011.42	-458238.23	-602329.96

Table A3: Free energy values for S_N2 degradation mechanism of QA (a)-(f). Unit: kJ/mol.

QA	HL	E(R1)	E(R2)	E(TS)	E(P1)	E(P2)	E(P3)
(a)	0	-1465874.27	-199448.95	-1665281.15	-1361665.83	-303876.72	-
(b)	0	-1617332.27	-199448.95	-1816705.39	-906509.72	-910465.22	-
(c)	0	-1168905.64	-199448.95	-1368263.58	-910498.05	-457996.09	-
	1	-1168905.64	-400225.92	-1569027.47	-910498.05	-457996.09	-200755.16
	2	-1168905.64	-600989.69	-1769784.67	-910498.05	-457996.09	-401494.66
	3	-1168905.64	-801747.98	-1970507.84	-910498.05	-457996.09	-602231.89
(d)	0	-1474925.89	-199448.95	-1674267.24	-910498.05	-764012.46	-
(e)	0	-1765136.78	-199448.95	-1964459.27	-910498.05	-1054221.03	-
(f)	0	-1685005.72	-199448.95	-1884324.57	-1426590.37	-457996.09	-
	1	-1685225.72	-400225.92	-2085316.17	-1426590.37	-457996.09	-200755.16
	2	-1685225.72	-600989.69	-2286068.68	-1426590.37	-457996.09	-401494.66
	3	-1685225.72	-801747.98	-2486807.7	-1426590.37	-457996.09	-602231.89

Appendix B

The designed systems for conventional all-atom MD simulation are illustrated in **Table B1**.

Table B1: Description for our designed systems at 298 K and 1 bar.

	QA	OH^-	H_2O	Number of atoms	Box size (nm^3)
(a)	1	1	3	39	0.76×0.76×0.76
(b)	1	1	3	45	0.87×0.87×0.87
(c)	1	1	3	38	0.74×0.74×0.74
(c)	1	1	9	56	1.08×1.08×1.08
(c)	1	1	15	74	1.15×1.15×1.15
(c)	1	1	500	1529	2.46×2.46×2.46
(c)	5	5	15	190	1.55×1.55×1.55
(c)	5	5	45	280	1.62×1.62×1.62
(c)	5	5	75	370	1.73×1.73×1.73
(d)	1	1	3	45	0.87×0.87×0.87
(e)	1	1	3	49	0.95×0.95×0.95
(f)	1	1	3	53	1.05×1.05×1.05
(f)	1	1	9	71	1.12×1.12×1.12
(f)	1	1	15	89	1.22×1.22×1.22
(f)	1	1	500	1544	2.47×2.47×2.47
(f)	5	5	15	265	1.65×1.65×1.65
(f)	5	5	45	355	1.72×1.72×1.72
(f)	5	5	75	445	1.84×1.84×1.84

Figures B1-B12 shows the MSD at the different HLs.

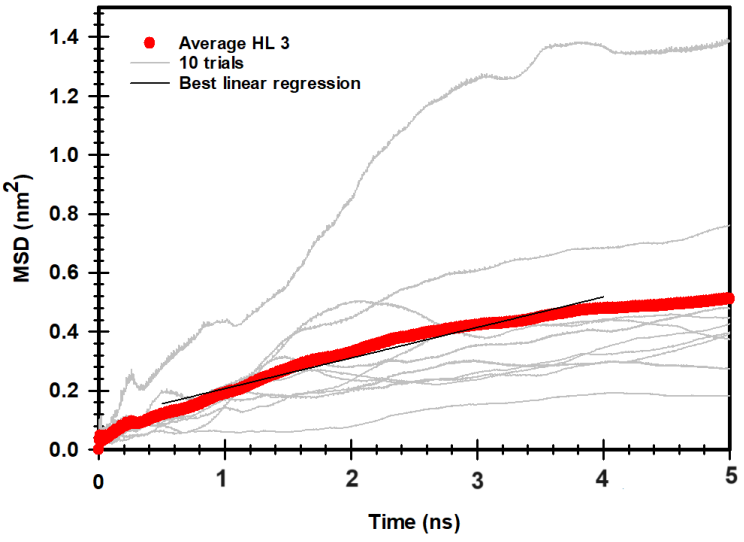

Figure B1: MSD for 10 trials at the HL 3 for OH^- ions around QA (c) of AEM.

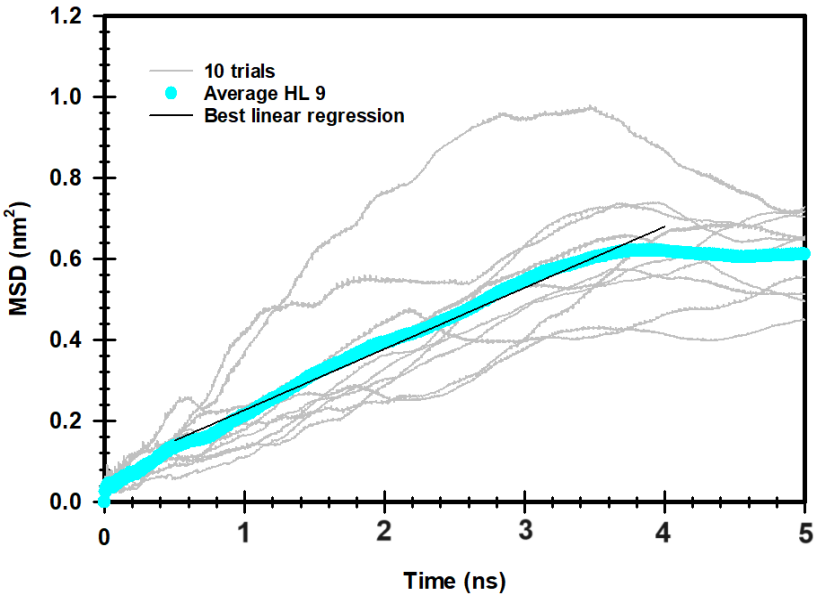

Figure B2: MSD for 10 at the HL 9 for OH^- ions around QA (c) of AEM.

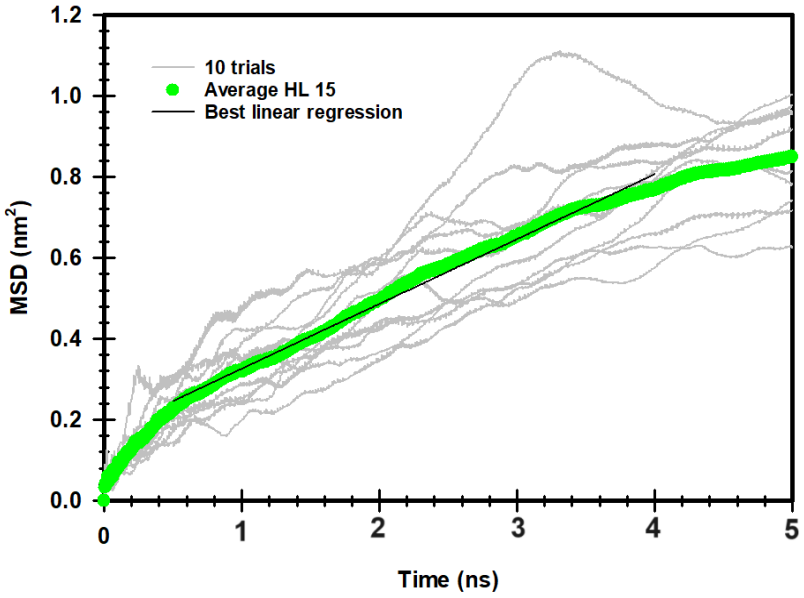

Figure B3: MSD for 10 trials at the HL 15 for OH^- ions around QA (c) of AEM.

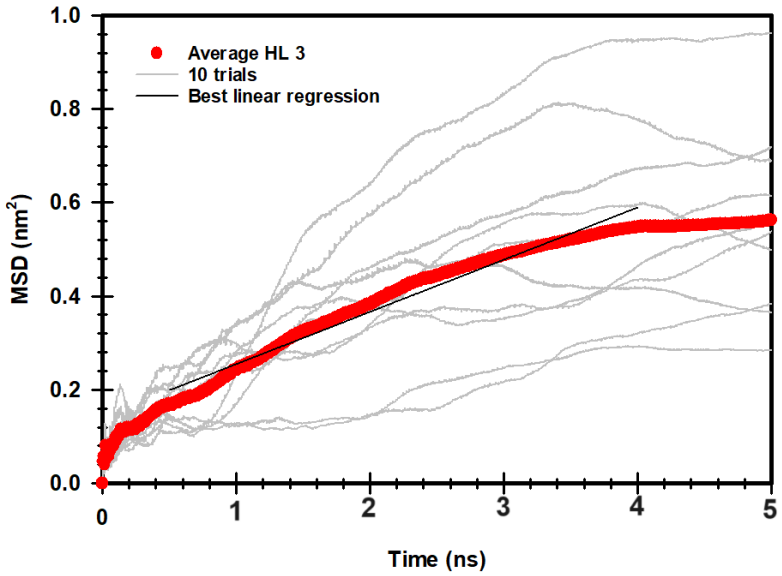

Figure B4: MSD for 10 trials at the HL 3 for water around QA (c) of AEM.

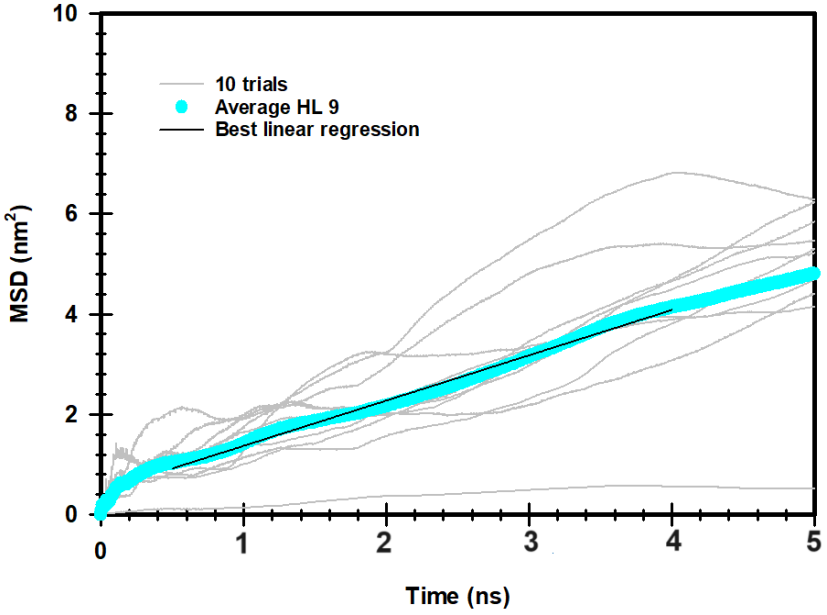

Figure B5: MSD for 10 trials at the HL 9 for water around QA (c) of AEM.

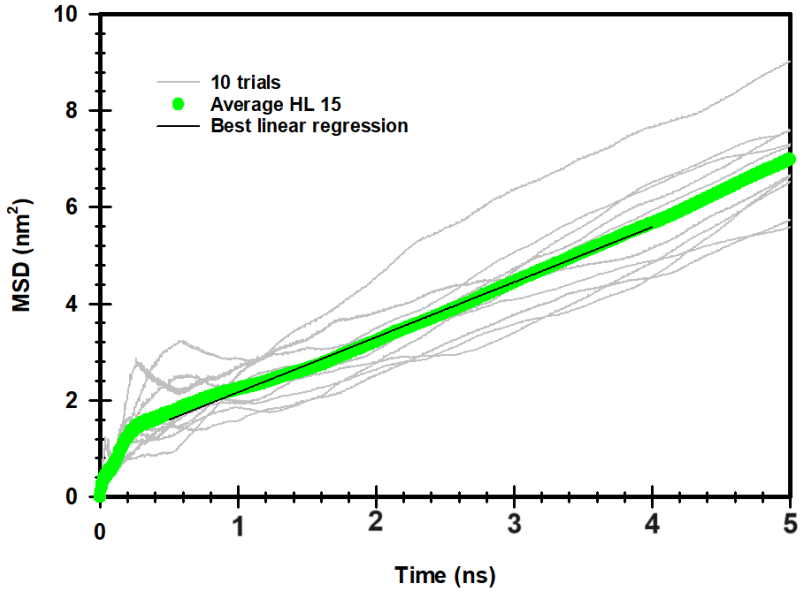

Figure B6: MSD for 10 trials at the HL 15 for water around QA (c) of AEM.

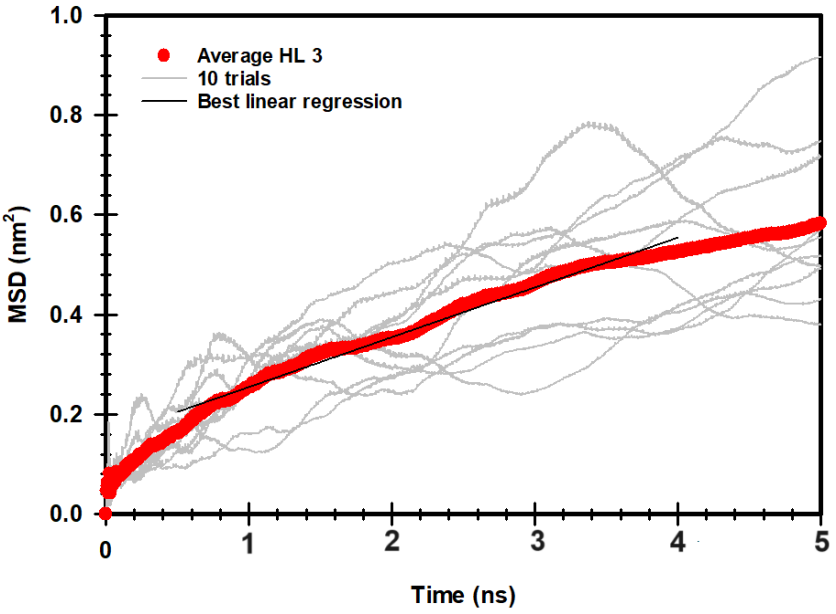

Figure B7: MSD for 10 trials at the HL 3 for OH^- ions around QA (f) of AEM.

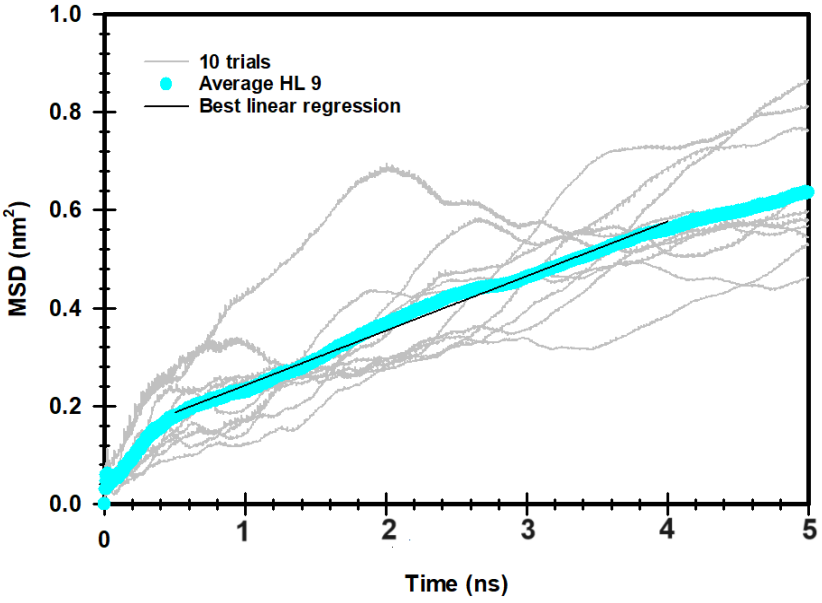

Figure B8: MSD for 10 trials at the HL 9 for OH^- ions around QA (f) of AEM.

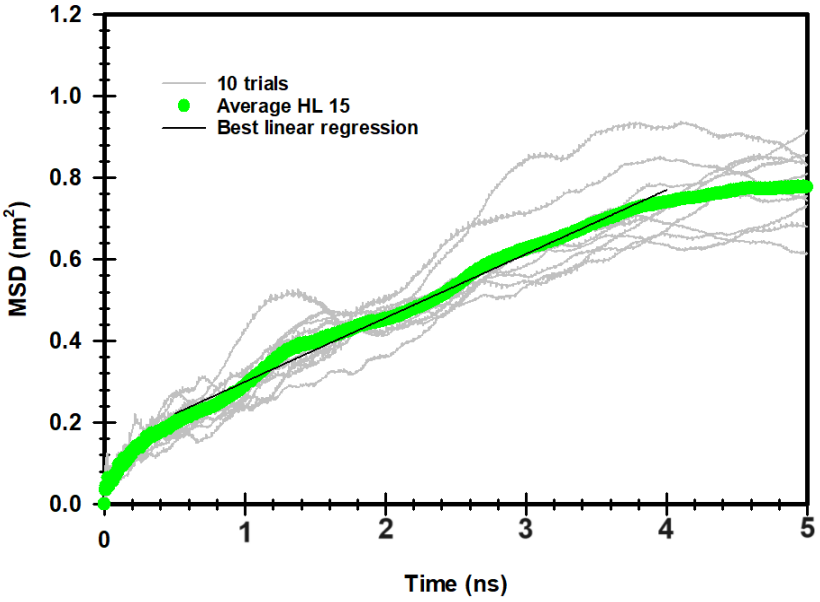

Figure B9: MSD for 10 trials at the HL 15 for OH^- ions around QA (f) of AEM.

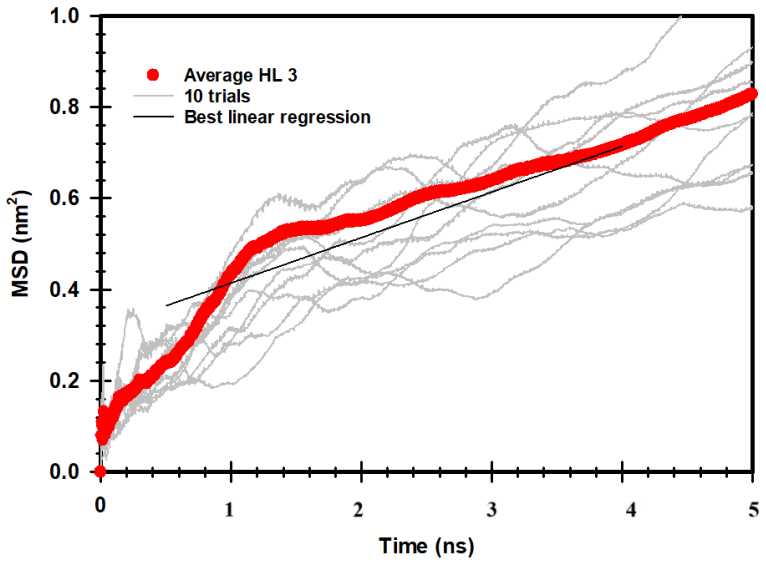

Figure B10: MSD for 10 at the HL 3 for water around QA (f) of AEM.

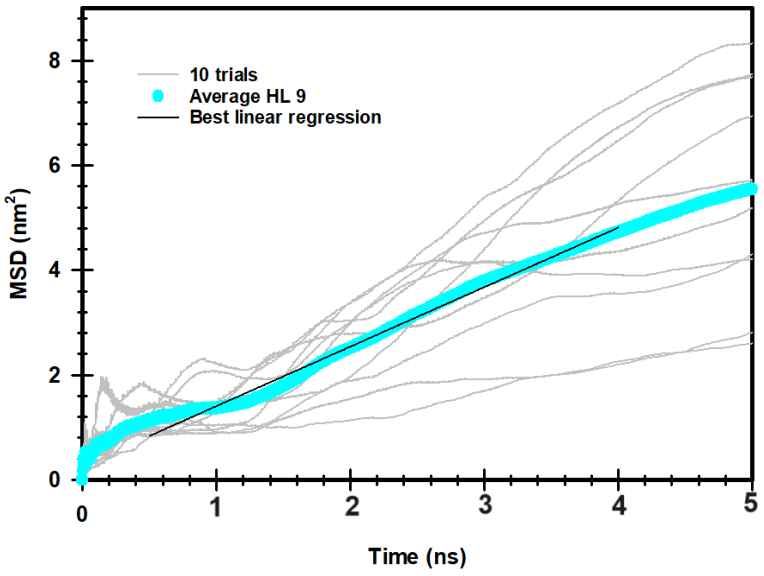

Figure B11: MSD for 10 trials at the HL 9 for water around QA (f) of AEM.

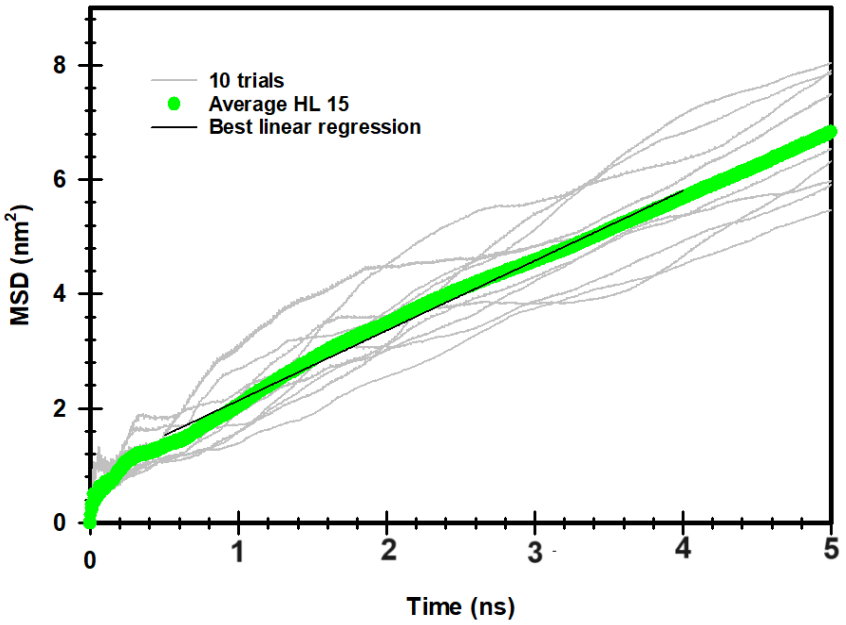

Figure B12: MSD for 10 trials at the HL 15 for water around QA (f) of AEM.

Appendix C

The 2D representations for the S_N2 degradation mechanism of the QCS (A), QCS (B), and QCS (C) were presented in **Figures C1-C3**.

The classical all-atom MD method setup was created by placing five QCS (labeled A-C) and five negatively charged OH^- ions, along with 15, 45, or 75 water molecules at 298 K, as shown in **Table C1**.

A theoretical model of QCS (A), (B), and (C) of AEM was established by using 5 QCS, 5 OH^- ions, and 15 water molecules to study the impact of the temperatures from 298 K to 350 K.

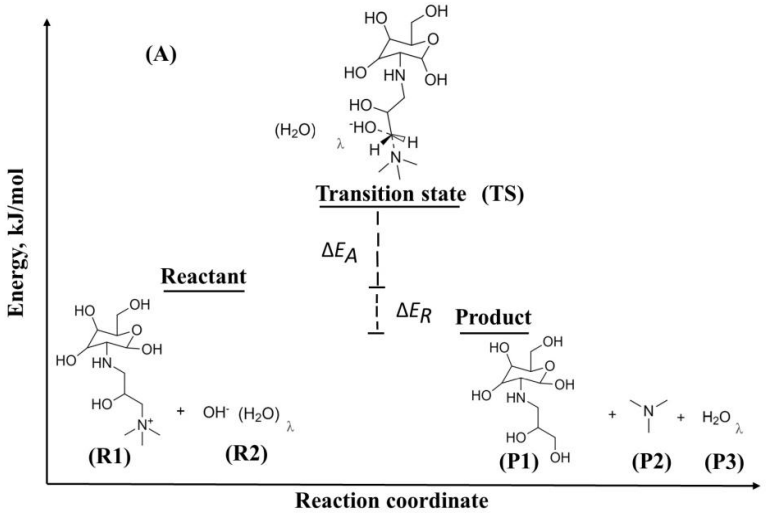

Figure C1: 2D representation for S_N2 mechanism for QCS (A).

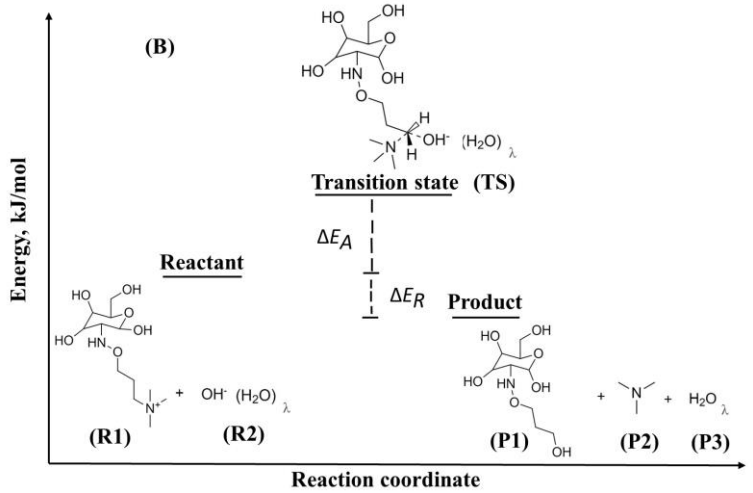

Figure C2: 2D representation for S_N2 mechanism for QCS (B).

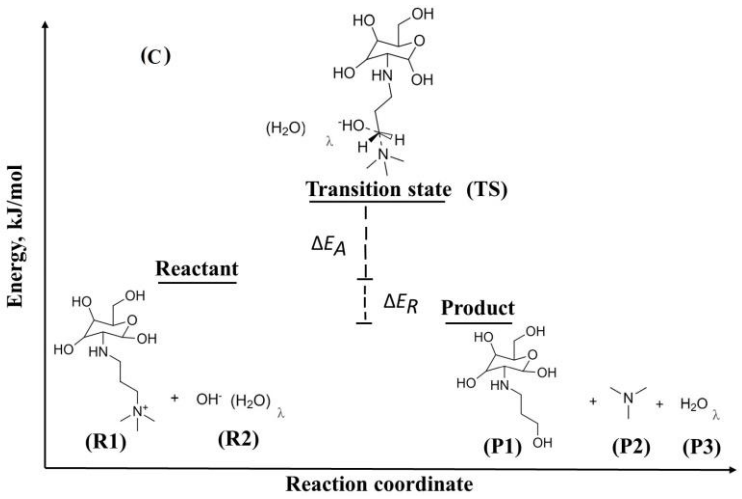

Figure C3: 2D representation for S_N2 mechanism for QCS (C).

Table C1: Designed systems for QCS based AEM at the different HLs, and temperatures.

	AEM	OH^-	Water	Number of atoms	Box size
(A)	5	5	15	290	$1.45\times1.45\times1.45$ nm^3
(A)	5	5	45	380	$1.61\times1.61\times1.61$ nm^3
(A)	5	5	75	470	$1.74\times1.74\times1.74$ nm^3
(B)	5	5	15	290	$1.45\times1.45\times1.45$ nm^3
(B)	5	5	45	380	$1.61\times1.61\times1.61$ nm^3
(B)	5	5	75	470	$1.74\times1.74\times1.74$ nm^3
(C)	5	5	15	290	$1.44\times1.44\times1.44$ nm^3
(C)	5	5	45	380	$1.60\times1.60\times1.60$ nm^3
(C)	5	5	75	470	$1.73\times1.73\times1.73$ nm^3

Figure C4 shows the MEPs for the binding of QCS segments with OH^- ions and the charge distribution. The positive charge of the QCS segment was stabilized by placing OH^- ion near the nitrogen atom. The net charges of OH^- ions and QCS segments are -1 and +1, respectively. It is evident that OH^- ions stabilize the positive charge of QCS of the AEM by networking with the nitrogen atom.

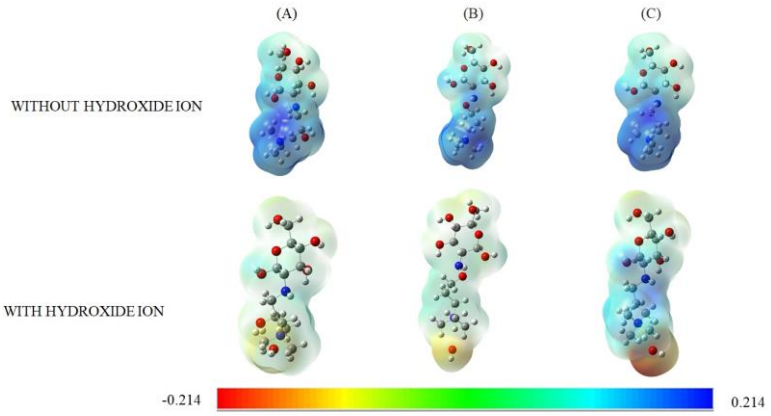

Figure C4: Representation of molecular electrostatic potential maps for various QCS segments, and their complexes with OH^- ions.

Through three branched H-bonds between the OH^- ion and the QCS of AEM, the OH^- ion was positioned close to the distinct QCS of AEM in the structures (**Figure C5**). As a result, calculation of binding energy by B3LYP DFT was implemented to characterize the OH^- ion diffusion process in AEMs (see **Table C2** and **Figure C5**).

Table C2: Energy values for our designed systes at 298 K and 1 bar.

QCS	E (OH^-)	E (QA)	E (QA with OH^-)	$E_{binding}$, kJ/mol
(A)	-199432.19	-2716167.23	-2915620.89	-21.40
(B)	-199432.19	-2716040.05	-2915495.66	-23.40
(C)	-199432.19	-2518620.95	-2718076.76	-23.60

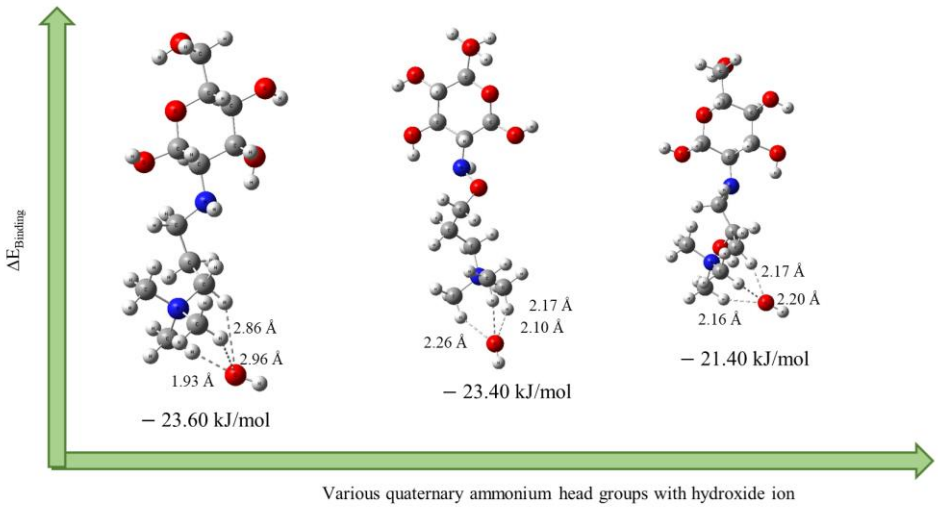

Figure C5: Complexes of three different QCS segments with OH^- ions.

Table C2 and **Figure C5** display the outcomes of the corresponding binding energy with optimal structures for complexes of OH^- ions with the different QCS of AEM.

The values of total energies and free energies for our designed systems of AEM studied by the DFT calculations are listed in **Table C3, C4, C5** and **C6**.

Table C3: Energy values for our designed systems of AEM studied by the DFT calculations.

QCS	E (R1)	E (R2)	E (TS)	E (P1)	E (P2)
(A)	-2716186.58	-199432.19	-2915537.13	-2457504.02	-458238.23
(B)	-2716037.74	-199432.19	-2915417.54	-2457362.32	-458238.23
(C)	-2518618.59	-199432.19	-2717999.49	-2259945.49	-458238.23

Table C4: Free energy values for our designed systems of AEM studied by the DFT calculations.

QCS	G (R1)	G (R2)	G (TS)	G (P1)	G (P2)
(A)	-2715551.06	-199448.95	-2914893.18	-2457230.85	-457996.09
(B)	-2715392.23	-199448.95	-2914754.11	-2457027.48	-457996.09
(C)	-2518082.53	-199448.95	-2717455.18	-2259691.43	-457996.09

Table C5: Energy values for our designed systems of AEM studied by the DFT calculations.

QCS	E (R1)	E (R2)	E (TS)	E (P1)	E (P2)	E (P3)
(A)	-2716186.58	-801864.08	-3517891.91	-2457504.02	-458238.23	-602329.96
(B)	-2716037.74	-801864.08	-3517790.24	-2457362.32	-458238.23	-602329.96
(C)	-2518618.59	-801864.08	-3320373.26	-2259945.49	-458238.23	-602329.96

Table C6: Free energy values for our designed systems of AEM studied by the DFT calculations.

QCS	G (R1)	G (R2)	G (TS)	G (P1)	G (P2)	G (P3)
(A)	-2715551.06	-801747.98	-3517135.88	-2457230.85	-457996.09	-602231.89
(B)	-2715392.23	-801747.98	-3517014.05	-2457027.48	-457996.09	-602231.89
(C)	-2518082.53	-801747.98	-3319707.57	-2259691.43	-457996.09	-602231.89

The MSD for OH^- ions and water at various QCS structures, at the different HLs, and at the different temperatures are depicted in **Figures C6-C41** below.

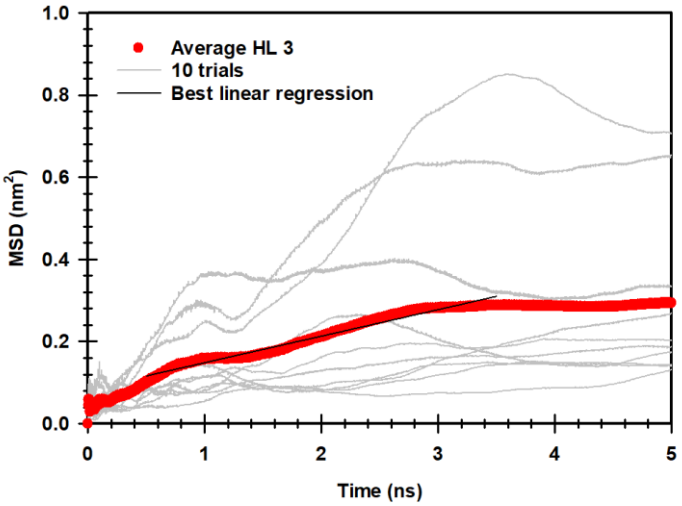

Figure C6: MSD plot at the HL 3 for OH^- ions around QCS (A) of AEM.

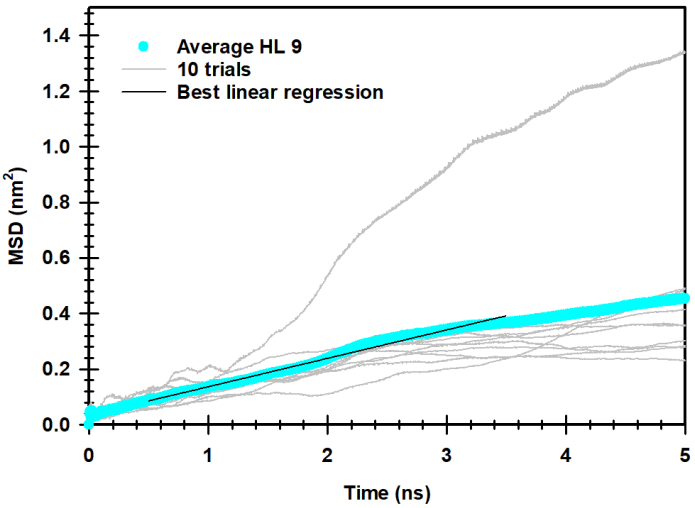

Figure C7: MSD plot at the HL 9 for OH^- ions around QCS (A) of AEM.

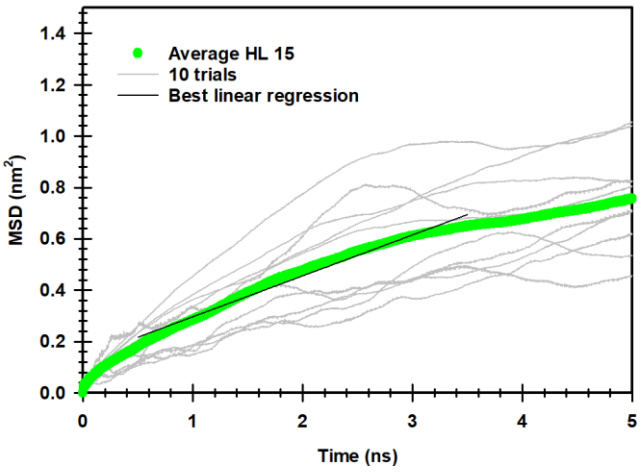

Figure C8: MSD plot at the HL 15 for OH^- ions around QCS (A) of AEM.

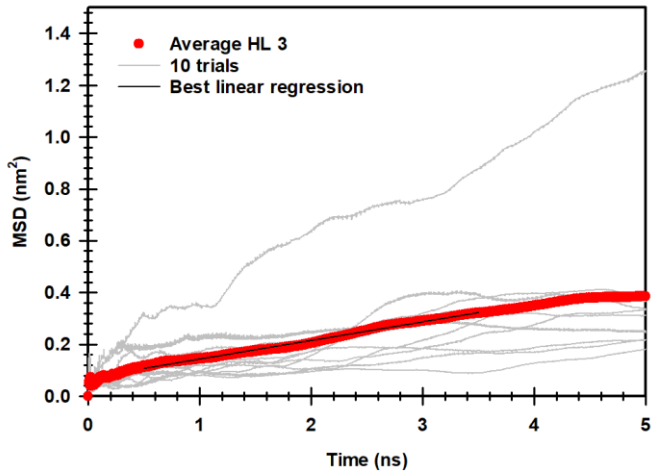

Figure C9: MSD plot at the HL 3 for OH^- ions around QCS (B) of AEM.

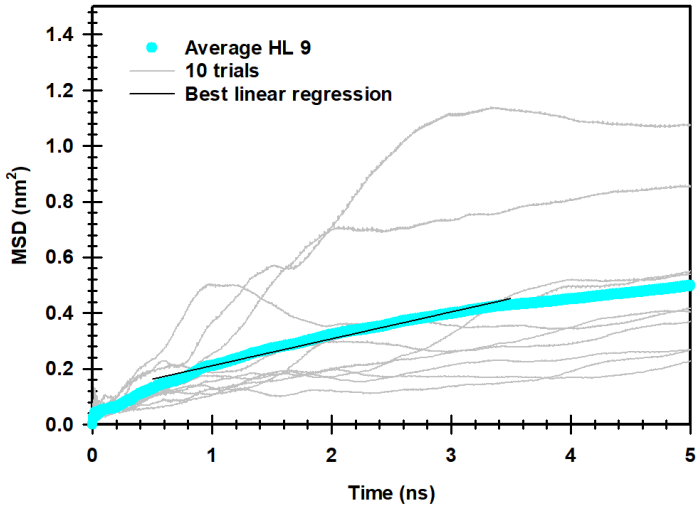

Figure C10: MSD plot at the HL 9 for OH^- ions around QCS (B) of AEM.

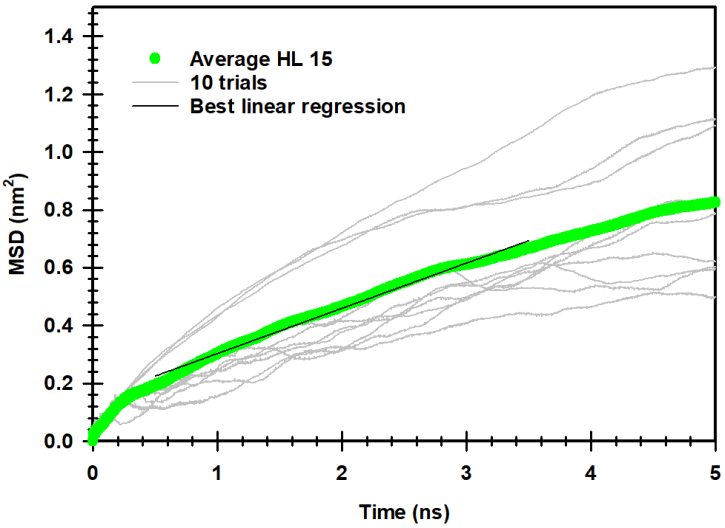

Figure C11: MSD plot at the HL 15 for OH^- ions around QCS (B) of AEM.

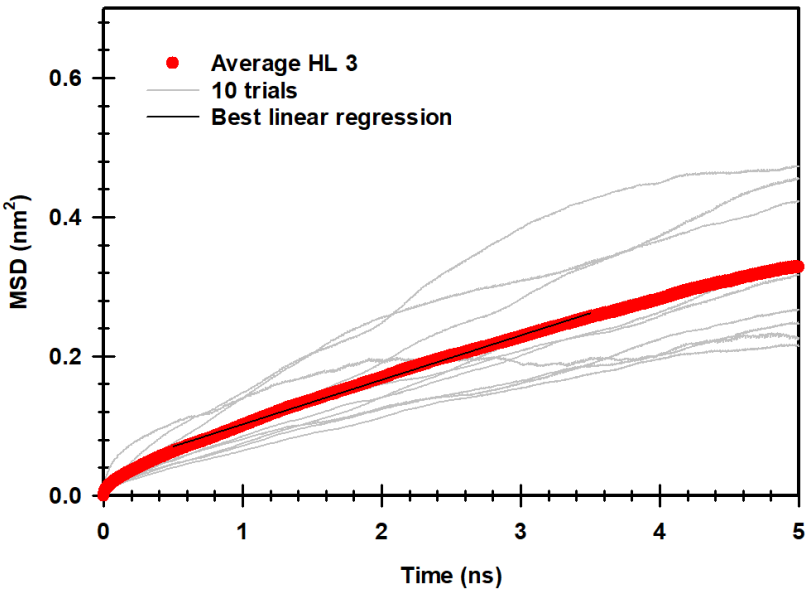

Figure C12: MSD plot at the HL 3 for OH^- ions around QCS (C) of AEM.

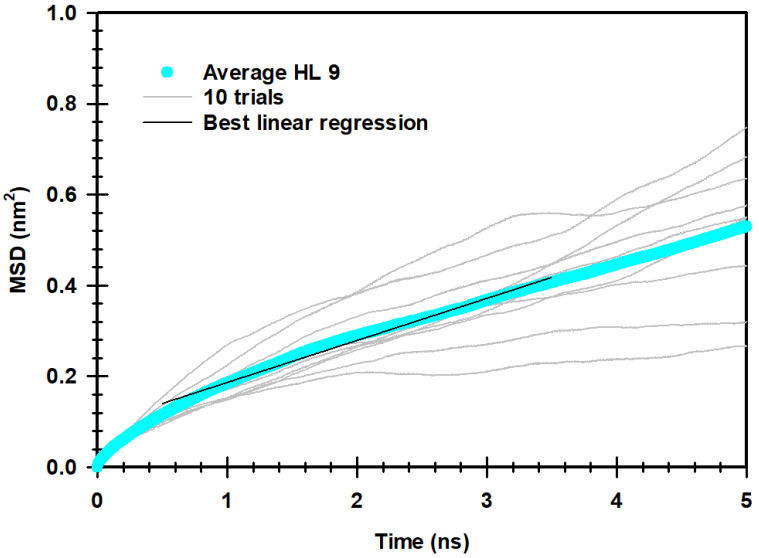

Figure C13: MSD plot at the HL 9 for OH^- ions around QCS (C) of AEM.

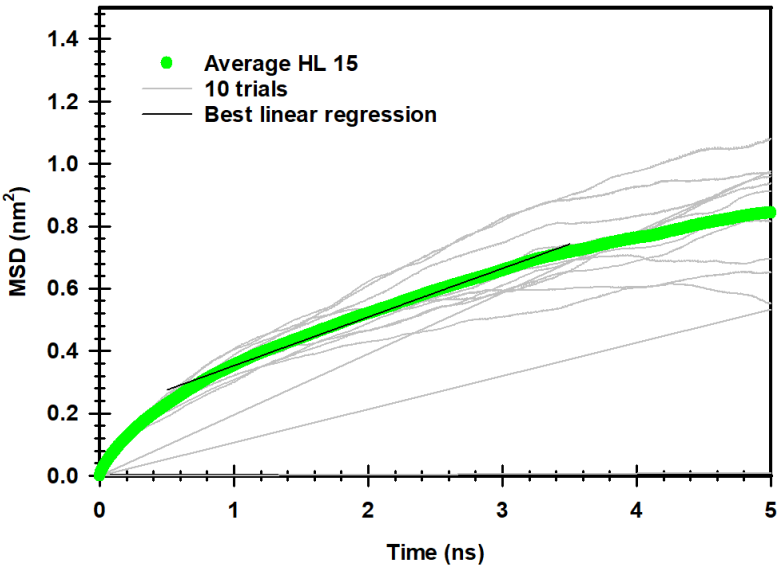

Figure C14: MSD plot at the HL 15 for OH^- ions around QCS (C) of AEM.

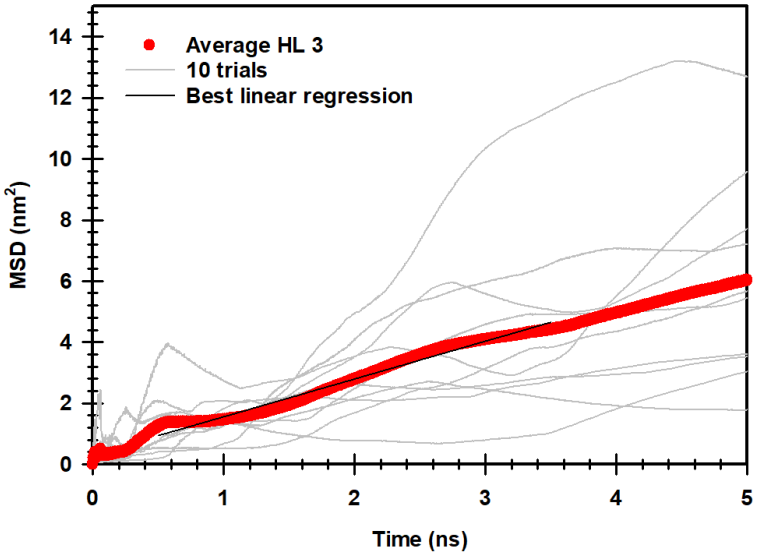

Figure C15: MSD plot at the HL 3 for water around QCS (A) of AEM.

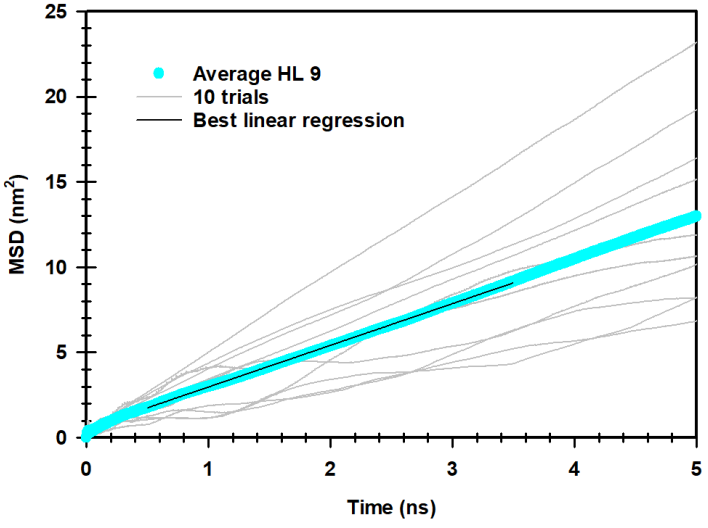

Figure C16: MSD plot at the HL 9 for water around QCS (A) of AEM.

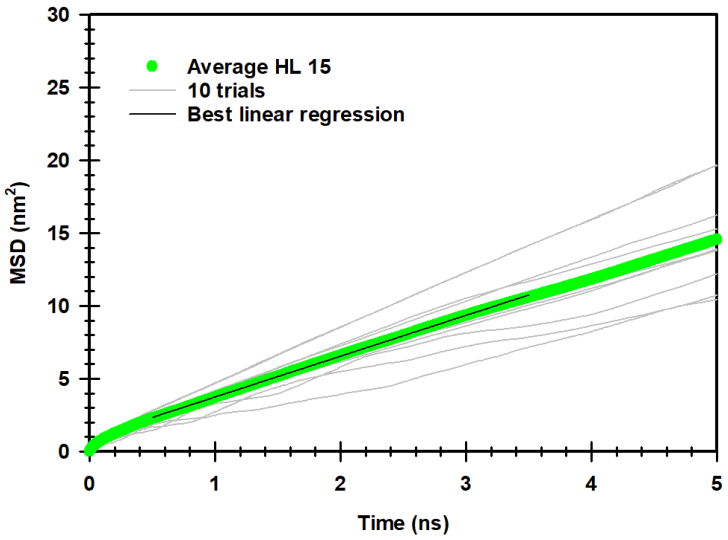

Figure C17: MSD plot at the HL 15 for water around QCS (A) of AEM.

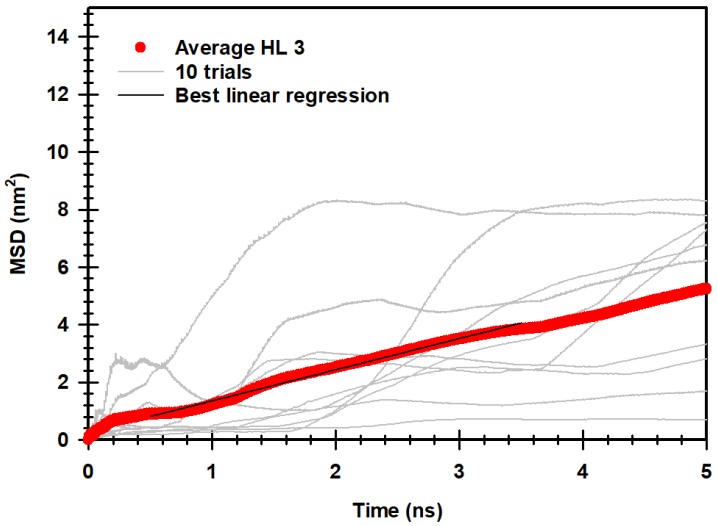

Figure C18: MSD plot at the HL 3 for water around QCS (B) of AEM.

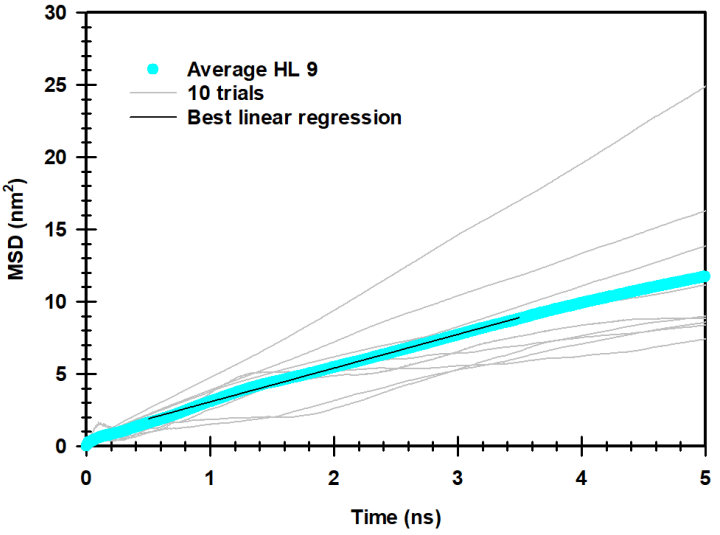

Figure C19: MSD plot and the trend line at the HL 9 for water in the presence of QCS (B) of AEM.

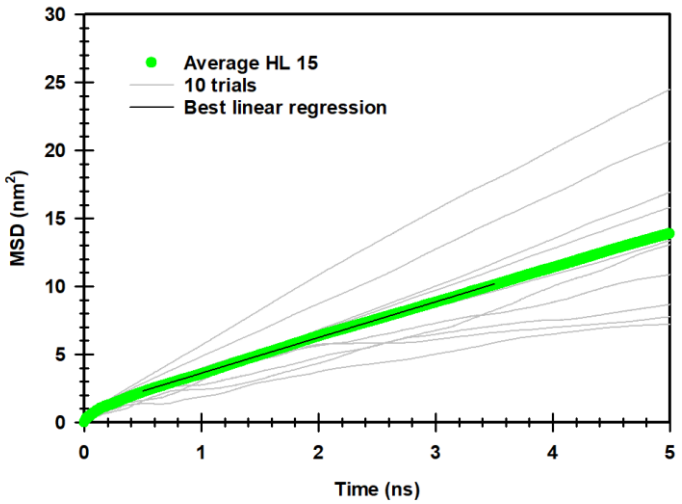

Figure C20: MSD plot at the HL 15 for water around QCS (B) of AEM.

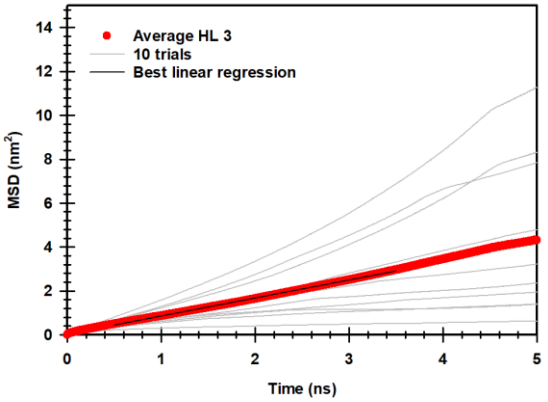

Figure C21: MSD plot at the HL 3 for water around QCS (C) of AEM.

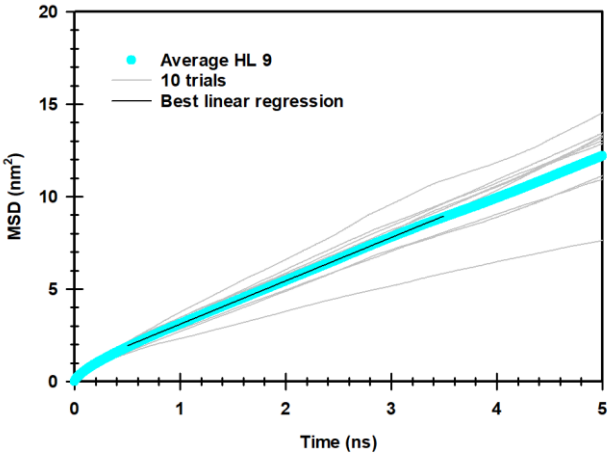

Figure C22: MSD plot at the HL 9 for water around QCS (C) of AEM.

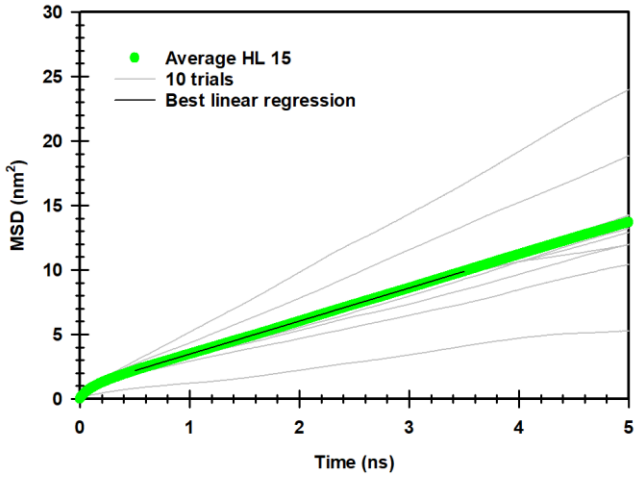

Figure C23: MSD plot at the HL 15 for water around QCS (C) of AEM.

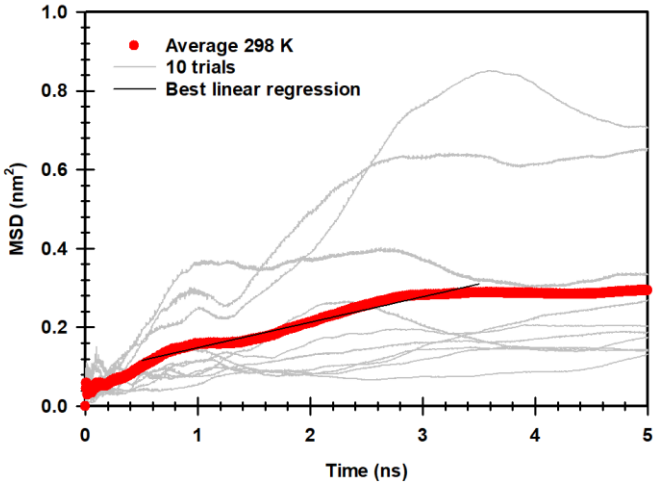

Figure C24: MSD plot at the HL 3 for OH^- ions around QCS (A) of AEM at 298 K.

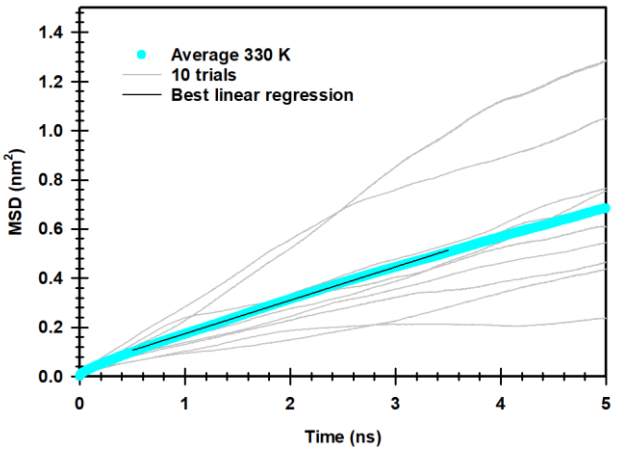

Figure C25: MSD plot at the HL 3 for OH^- ions around QCS (A) of AEM at the 330 K.

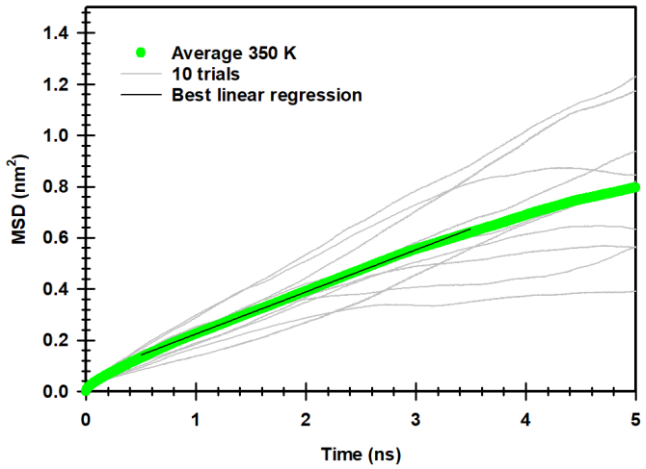

Figure C26: MSD plot at the HL 3 for OH^- ions around QCS (A) of AEM at the 350 K.

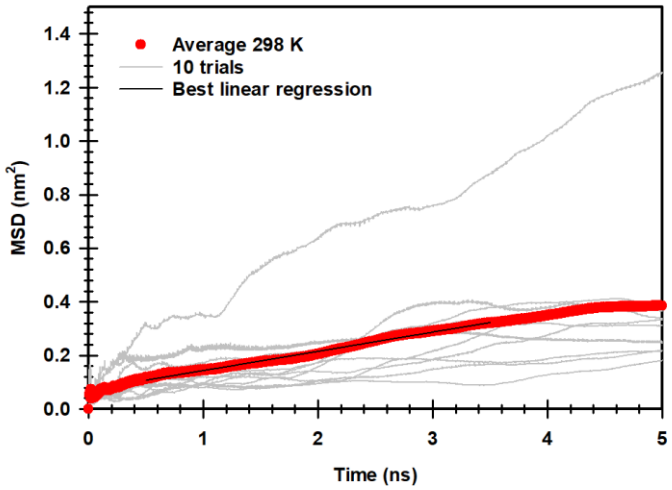

Figure C27: MSD plot at the HL 3 for OH^- ions around QCS (B) of AEM at the 298 K.

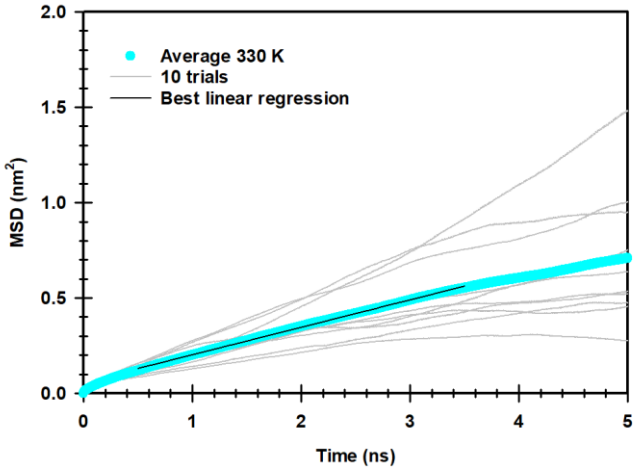

Figure C28: MSD plot at the HL 3 for OH^- ions around QCS (B) of AEM at the 330 K.

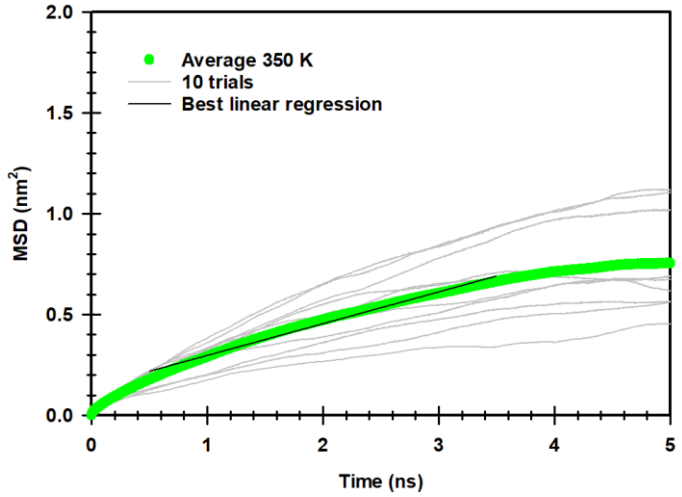

Figure C29: MSD plot at the HL 3 for OH^- ions around QCS (B) of AEM at the 350 K.

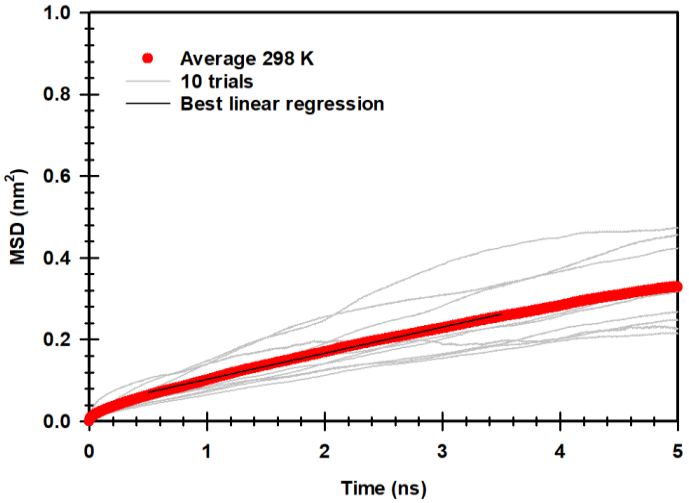

Figure C30: MSD plot at the HL 3 for OH^- ions around QCS (C) of AEM at the 298 K.

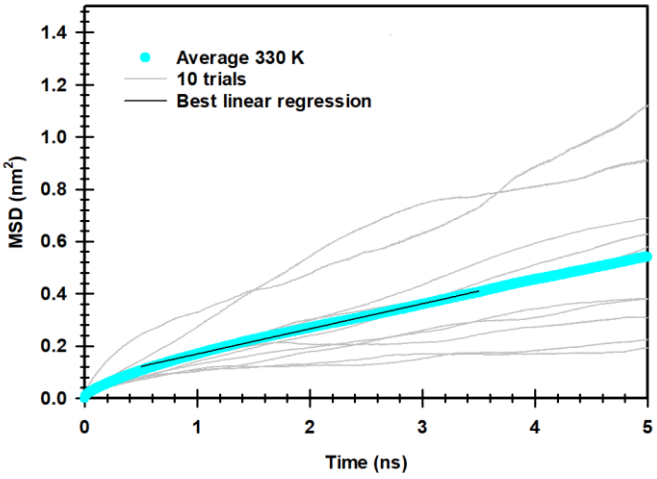

Figure C31: MSD plot at the HL 3 for OH^- ions around QCS (C) of AEM at the 330 K.

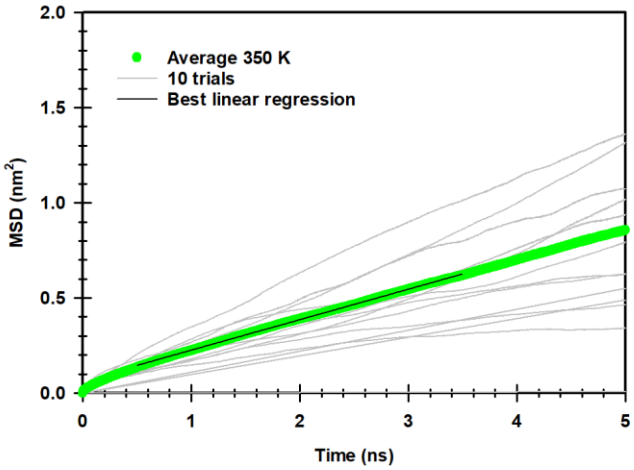

Figure C32: MSD plot at the HL 3 for OH^- ions around QCS (C) of AEM at the 350 K.

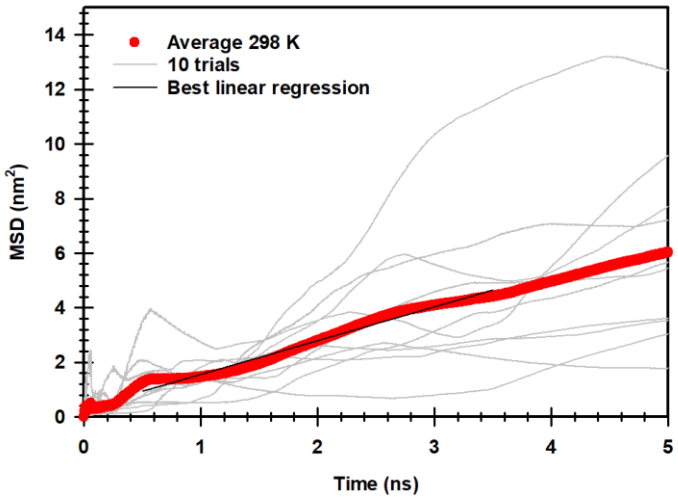

Figure C33: MSD plot at the HL 3 for water around QCS (A) of AEM at the 298 K.

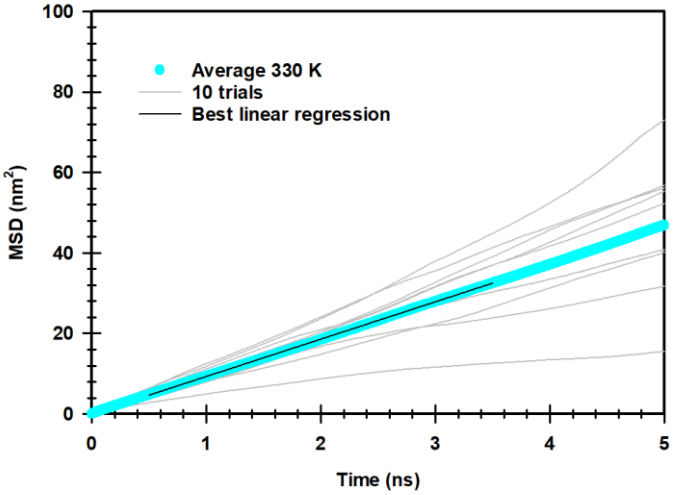

Figure C34: MSD plot at the HL 3 for water around QCS (A) of AEM at the 330 K.

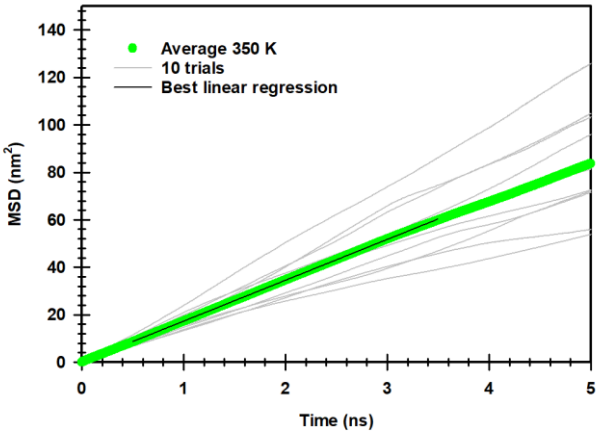

Figure C35: MSD plot at the HL 3 for water around QCS (A) of AEM at the 350 K.

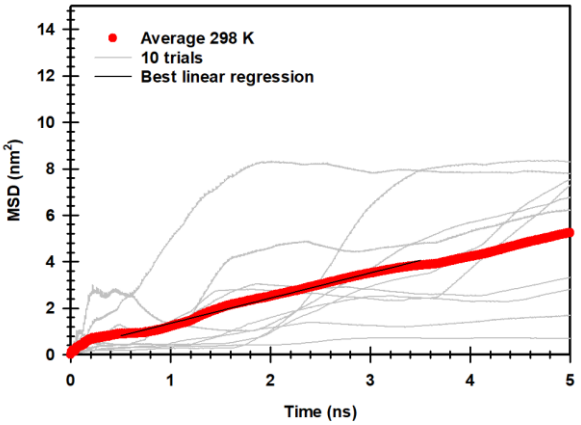

Figure C36: MSD plot at the HL 3 for water around QCS (B) of AEM at the 298 K.

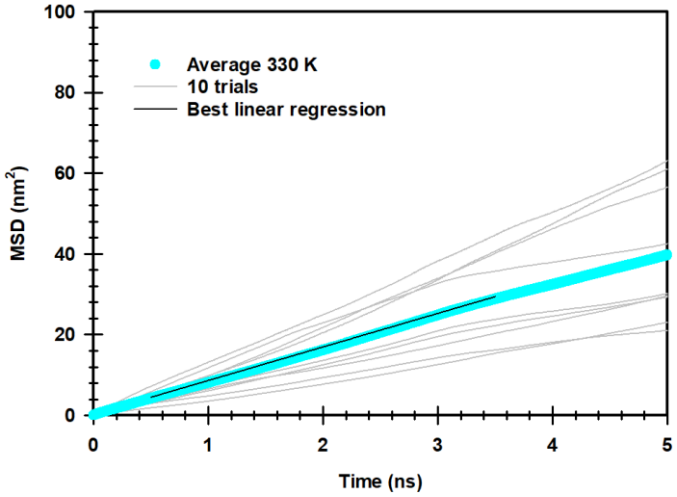

Figure C37: MSD plot at the HL 3 for water around QCS (B) of AEM at the 330 K.

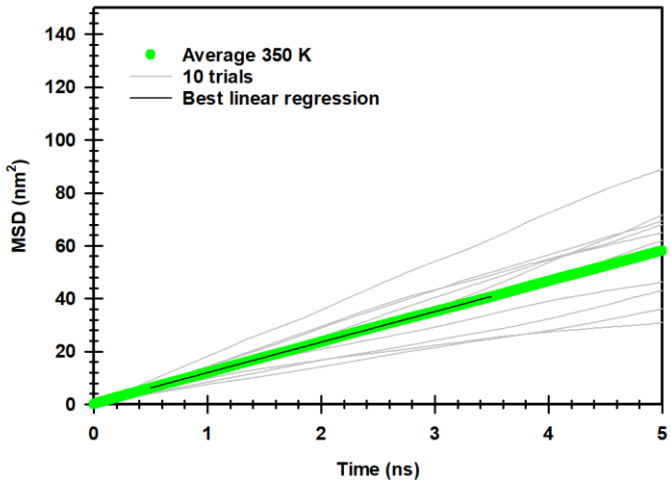

Figure C38: MSD plot at the HL 3 for water around QCS (B) of AEM at the 350 K.

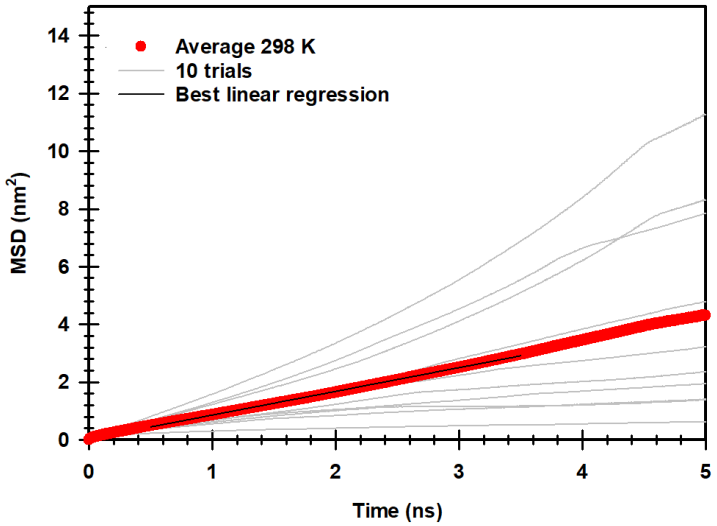

Figure C39: MSD plot at the HL 3 for water around QCS (C) of AEM at the 298 K.

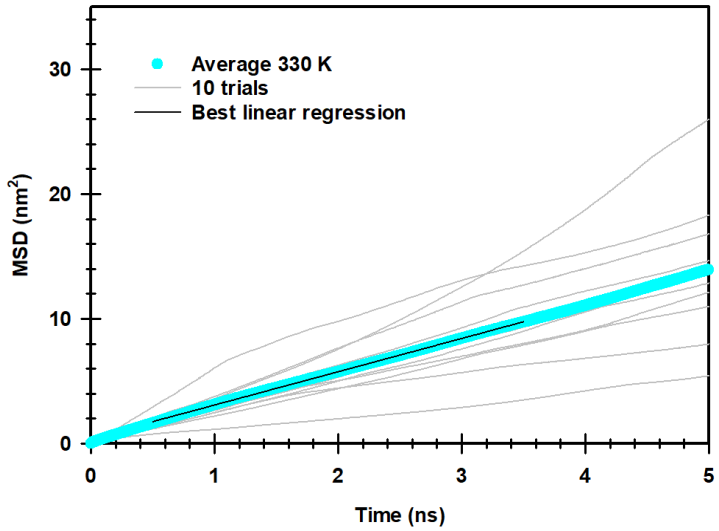

Figure C40: MSD plot at the HL 3 for water around QCS (C) of AEM at the 330 K.

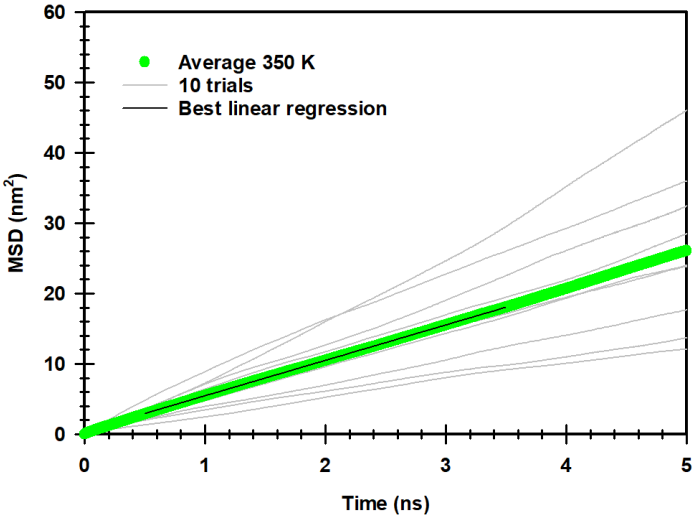

Figure C41: MSD plot at the HL 3 for water around QCS (C) of AEM at 350 K

Appendix D

Ab initio MD simulation setup was created by placing one QA-based head group (tetramethylammonium (TMA), and 2-hydroxy propyl trimethyl ammonium chitosan (QCS)) and one negatively charged OH^- ion, along with 1-5 water molecules at 298-350 K, in the absence and presence of choline chloride (ChCl) and ethylene glycol (EGL) based DES as shown in **Table D1**.

Namely, **Table D1** presents a comprehensive overview of our designed systems, each characterized by operating temperatures ranging from 298 K to 350 K. The systems include tetramethylammonium (TMA) and Quaternary quaternized chitosan (QCS) in both pure forms and when supported by Deep Eutectic Solvents (DES). The table outlines the composition of each system in terms of the presence of head groups, hydroxide ions, water molecules, choline chloride (ChCl), ethylene glycol (EGL), and the total number of atoms in the simulation.

Table D1: Description for our designed systems at 298-350 K.

	AEM	OH^-	Water	ChCl	EGL	#, atoms	T (K)	Box size (nm^3)
TMA	1	1	1	-	-	22	298	0.67×0.67×0.67
TMA	1	1	1	1	2	64	298	0.90×0.90×0.90
TMA	1	1	3	-	-	28	298	0.75×0.75×0.75
TMA	1	1	3	1	2	70	298	0.92×0.92×0.92
TMA	1	1	5	-	-	34	298	0.83×0.83×0.83
TMA	1	1	5	1	2	76	298	1.08×1.08×1.08
QCS	1	1	1	-	-	52	298	0.86×0.86×0.86
QCS	1	1	1	1	2	94	298	1.05×1.05×1.05
QCS	1	1	3	-	-	58	298	0.89×0.89×0.89
QCS	1	1	3	1	2	100	298	1.04×1.04×1.04
QCS	1	1	5	-	-	64	298	0.97×0.97×0.97
QCS	1	1	5	1	2	106	298	1.12×1.12×1.12

Distinct configurations are presented for varying water content, demonstrating the influence of hydration on the system. Furthermore, the inclusion of ChCl and EGL in DES-supported systems indicates the role of these components in altering the system's characteristics. The temperature parameter allows for a thorough examination of the systems' behavior under different thermal conditions. This table serves as a valuable reference for understanding the diverse compositions and conditions of the designed systems, offering insights into their structural variations and potential applications in a range of environments.

Tables D2 and **D3** provide energy values for our designed systems with DES supported AEM, as determined through DFT calculations. The table presents various energy components, including reaction energies (E(R1) and E(R2)), transition states, BSSE, and product energies (E(P1) and E(P2). The negative and positive signs indicate the absence and presence of DES, respectively.

Table D2: Energy values for our designed systems of DES supported AEM studied by the DFT calculations.

	(-) DES	(+) DES
E (R1)	-562666.04	-3844567.10
E (R2)	-199429.14	-199429.14
E (TS1)	-762064.38	-4043955.57
E (Interm(P1))	-561301.01	-3843204.12
E (Interm(P2))	-200764.45	-200764.45
E (TS2)	-762036.01	-4043930.35
E (P1)	-458238.23	-3740102.80
E (P2)	-303962.42	-303962.42

Table D3: Energy values for our designed systems of DES supported AEM studied by the DFT calculations.

	(-) DES	(+) DES
E (R1)	-562666.04	-3844567.10
E (R2)	-199429.14	-199429.14
E (TS)	-762036.01	-4043930.35
E (P1)	-458238.23	-3740102.80
E (P2)	-303962.42	-303962.42

Tables D4 and **D5** present the free energy values for the systems we designed with DES-supported AEM, as obtained from DFT frequency calculations. These tables detail several free energy components, including the reaction free energies, transition states, and product free energies. The signs (negative and positive) denote the absence or presence of DES, respectively.

Table D4: Energy values for our designed systems of DES supported AEM studied by the DFT calculations.

	(-) DES	(+) DES
G (R1)	-562286.91	-3843096.68
G (R2)	-199448.95	-199448.95
G (TS1)	-761699.23	-4042428.79
G (Interm(P1))	-560952.15	-3841752.01
G (Interm(P2))	-200756.89	-200756.89
G (TS2)	-761671.85	-4042445.21
G (P1)	-457996.09	-3738738.45
G (P2)	-303888.47	-303888.47

Table D5: Energy values for our designed systems of DES supported AEM studied by the DFT calculations.

	(-) DES	(+) DES
G (R1)	-562286.91	-3843096.68
G (R2)	-199448.95	-199448.95
G (TS)	-761671.85	-4042445.21
G (P1)	-457996.09	-3738738.45
G (P2)	-303888.47	-303888.47

Next, the MSD for OH^- ions and water at various temperatures for QCS are depicted in **Figures D1-D6** below in the absence and presence of DES.

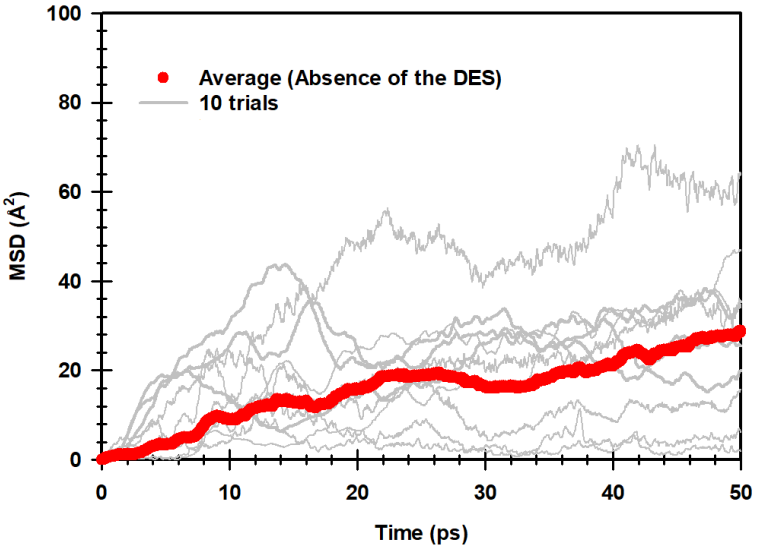

Figure D1: MSD plot at the 298 K for OH^- ions around QCS and absence of DES.

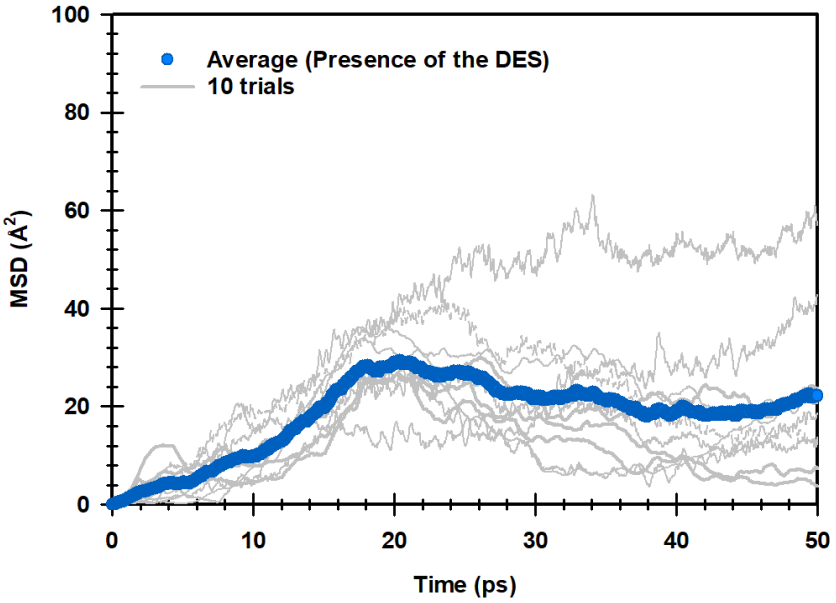

Figure D2: MSD plot at the 298 K for OH^- ions around QCS and presence of DES.

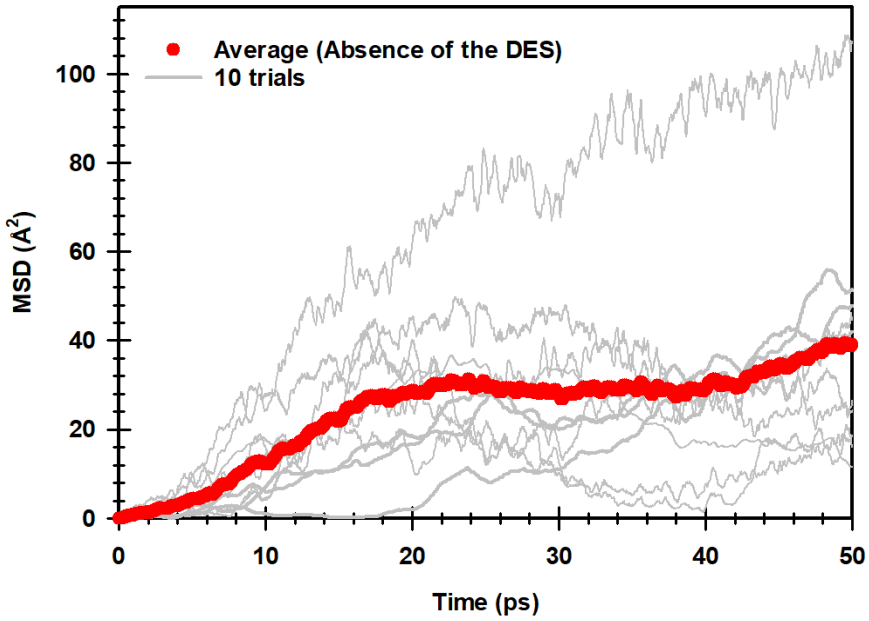

Figure D3: MSD plot around at the 320 K for OH^- ions around QCS and absence of DES.

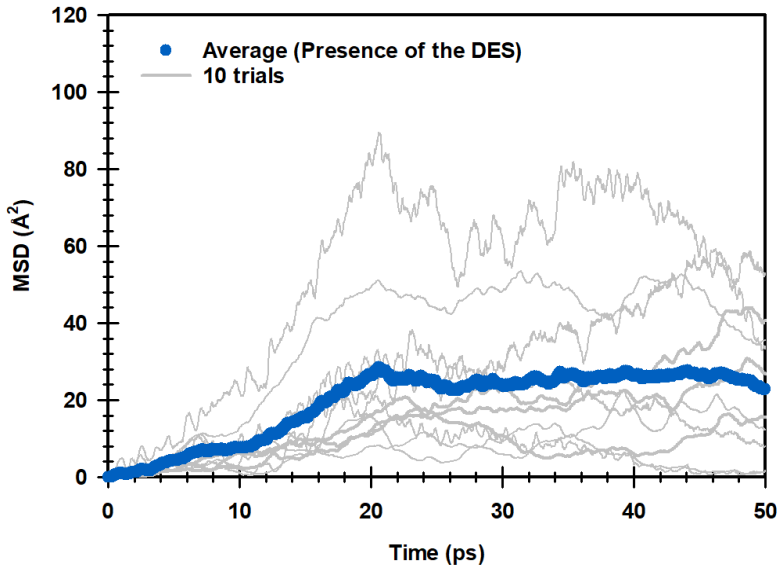

Figure D4: MSD plot at the 320 K for OH^- ions around QCS and presence of DES.

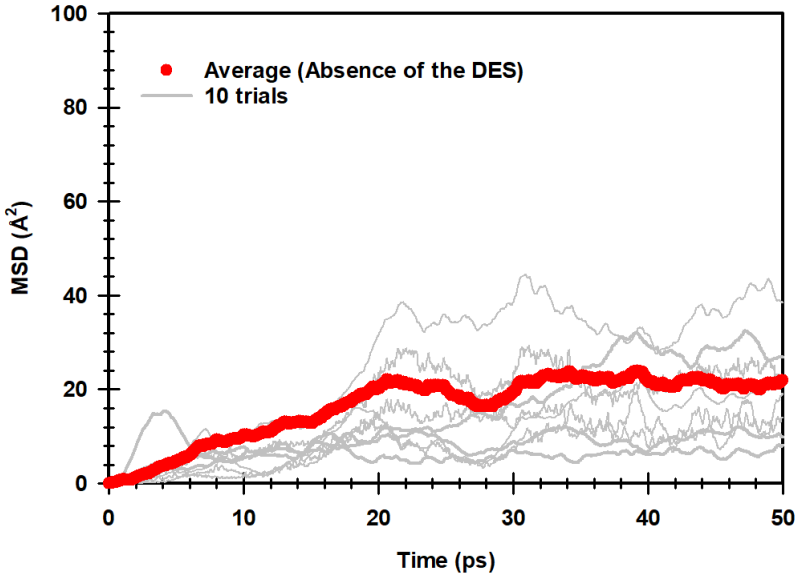

Figure D5: MSD plot at the 350 K for OH^- ions around QCS and absence of DES.

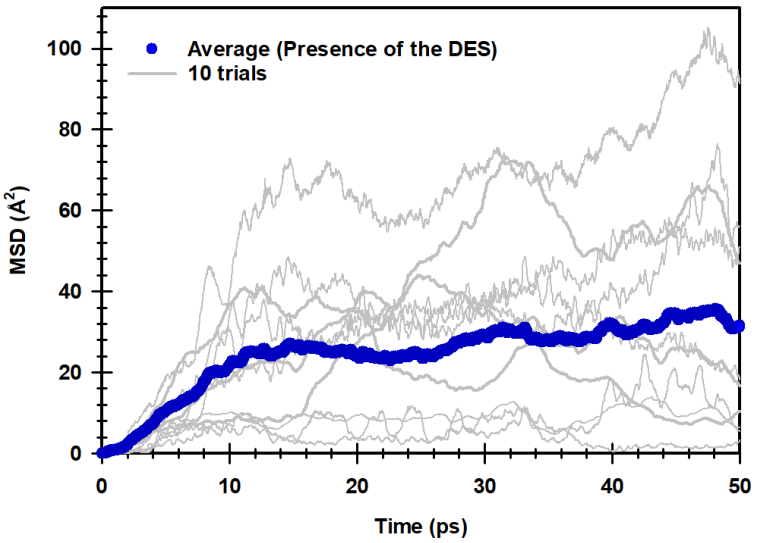

Figure D6: MSD plot at the 350 K for OH^- ions around QCS and presence of DES.

Next, the MSD for OH^- ions and water at various QCS structures, at the different HLs are depicted in **Figures D7-D12** below.

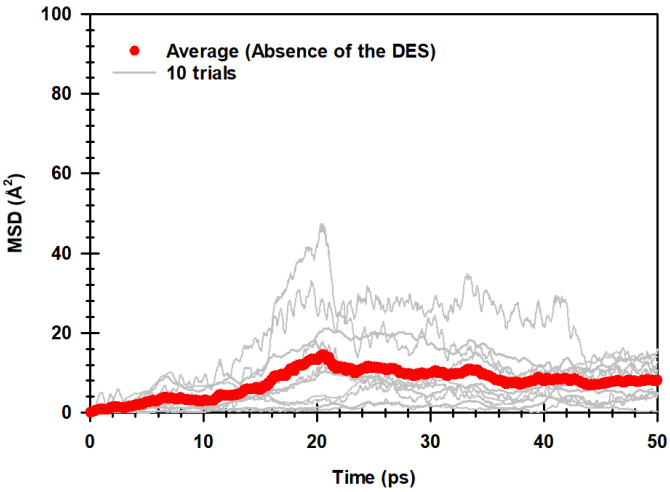

Figure D7: MSD plot at the HL 1 for OH^- ions around QCS and absence of DES.

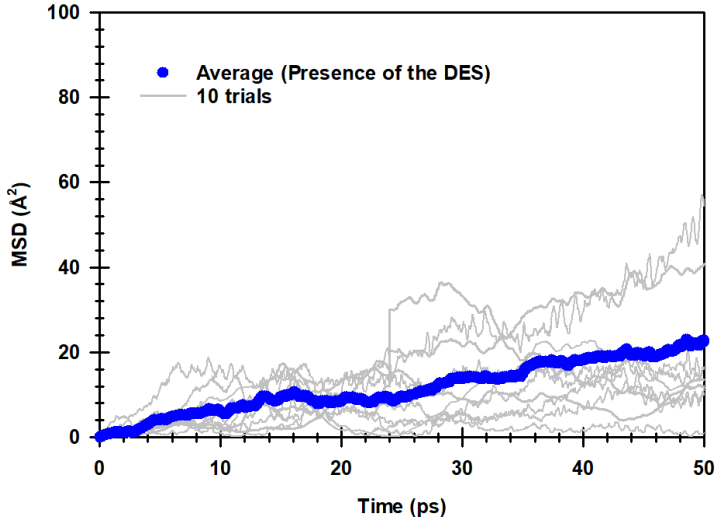

Figure D8: MSD plot at the HL 1 for OH^- ions around QCS and presence of DES.

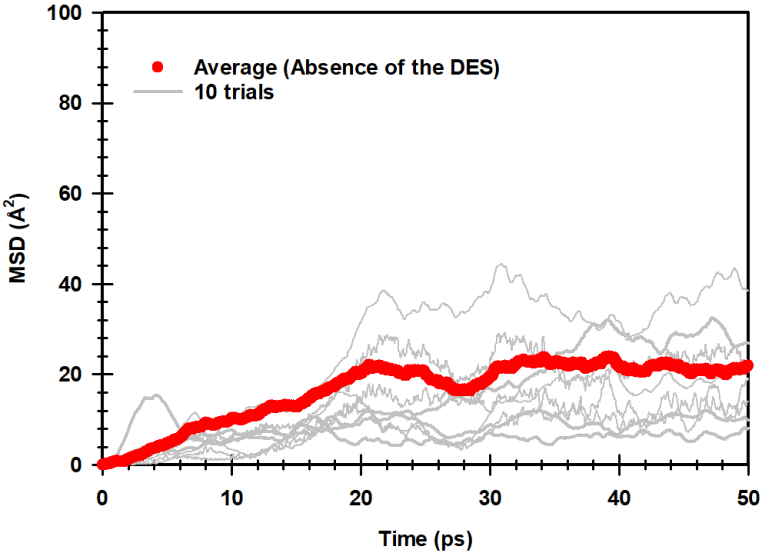

Figure D9: MSD plot at the HL 3 for OH^- ions around QCS and absence of DES.

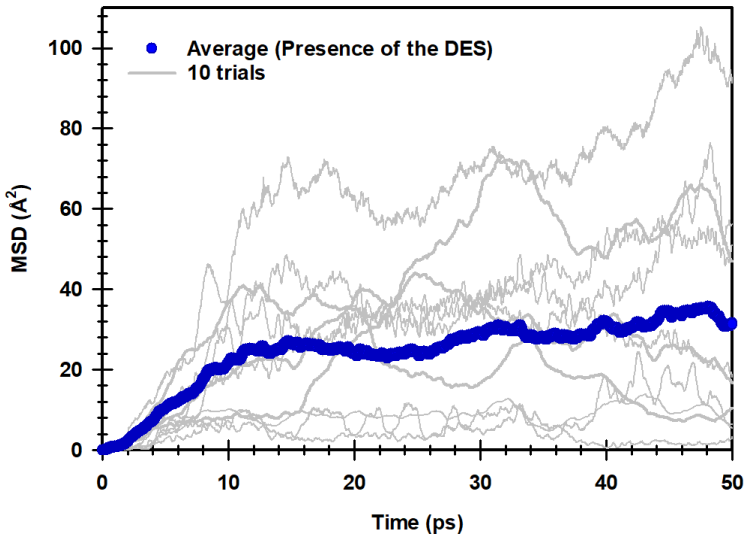

Figure D10: MSD plot at the HL 3 for OH^- ions around QCS and presence of DES.

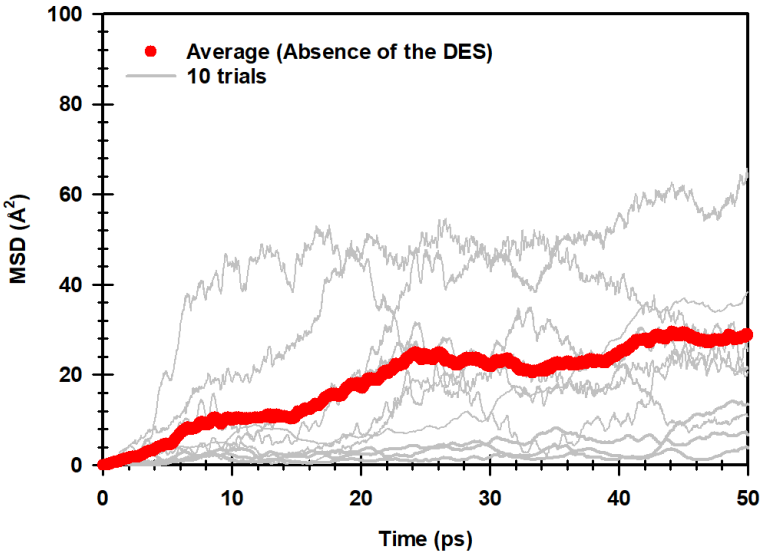

Figure D11: MSD plot at the HL 5 for OH^- ions around QCS and absence of DES.

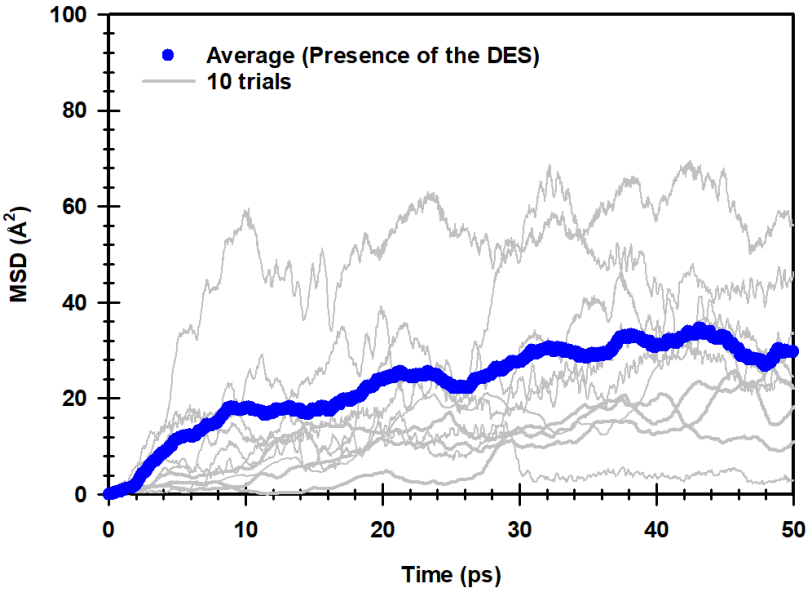

Figure D12: MSD plot at the HL 5 for OH^- ions around QCS and presence of DES.